FISSION RATES IN NISUS - A FAST REACTOR

NEUTRON SPECTRUM GENERATOR

A thesis submitted for the award of the

degree of Doctor of Philosophy of the

University of London

by

Dariush AZIMI-GARAKANI

B.Sc., M.Sc. (Tehran), M.Sc. (London), D.I.C.

University of London Reactor Centre

Department of Mechanical Engineering

Imperial College of Science and Technology

November 1975

"If you split a particle,
You'll see a sun inside"

Hatef-Esfahani, 1700 A.D.

ABSTRACT

Fission rates have been experimentally determined in the standard fast assembly NISUS, installed on the University of London Reactor CONSORT, with double fission chambers and solid-state track recorders. The results are compared with one-dimensional discrete ordinates ANISN calculations using a 37 group UKNDL nuclear data file processed by the GALAXY code. Calculations have also been made to investigate sensitivities of the central NISUS spectrum and reaction rate ratios to uncertainties in the macroscopic configuration and nuclear data file used. The effects of these uncertainties were studied and a comparison between NISUS and MOL-$\Sigma\Sigma$ standard neutron fields has been made.

An accurate and reproducible fission track counting method using the Quantimet 720 was established. The results show that either method of track counting by eye or by Quantimet, is capable of precision of $\pm$ 2% or better in fission rate ratios. A systematic error of $\pm$ 2% in absolute track densities is attributable to the calibration of the fields of view in both methods.

The results of $^{239}Pu/^{238}U$, $^{239}Pu/^{235}U$ and $^{237}Np/^{235}U$ fission ratios in the centre of NISUS show an agreement better than $\pm$ 0.6% compared with those of $\Sigma\Sigma$. The $^{238}U/^{235}U$ fission ratio in NISUS was found to be 1.7% higher than that in $\Sigma\Sigma$, as was predicted by the ANISN transport code.

The optical efficiency of Makrofol SSTR was found to be (94.3 ± .64)% for thin deposits. The measurements of $^{238}U/^{235}U$ fission ratio with SSTR showed a discrepancy of about ±3% compared with those of the fission chamber. The fission rate distribution on the outer and inner surfaces of the NISUS uranium shell was measured in three orthogonal planes using Makrofol SSTR.

ACKNOWLEDGEMENTS

TABLE OF CONTENTS

8

9

13

LIST OF FIGURES

14

17

18

LIST OF TABLES

Page

1. INTRODUCTION

The discovery of nuclear fission altered the prospects of mankind. Nuclear energy can prolong our power-based civilization or it can end it abruptly. The attendant radioactivity can cause disease or it can cure disease. Intelligent social choices must be based on technical as well as political understanding. For his survival man's intelligence is challenged as never before.

Power demands and power needs for modern civilization have vigorously pushed all kinds of effort for energy production to go into nuclear energy. The use of the old-fashioned fossil fuels is still one of the important sources for today's world energy requirements. Exhaustion of these deposits cannot last for many decades at the present rapidly increasing rate of consumption. Whether these estimates prove to be pessimistic, as some previous estimates have been, remains to be seen. The other sources of power, geothermal, tidal, hydro and in practice probably also wind, are not plentiful enough to supply large parts of the future demand. The present idea to use solar energy as a commercial source of power may be far from realisation. It appears that in the long term, on into the centuries, the continuation of industrial civilization will require either fusion power or solar power. Meanwhile, at the threshold of the world energy crisis, the fast breeder reactor is an alternative solution having several contributions to make to the nuclear program. In such a reactor the conversion ratio is in excess of unity, in order

to make significant use of the breeder reaction. The lowest

conversion ratio amongst existing power reactor types is 0.5, that is

for each two nuclei of $^{235}_{92}$U undergoing fission just one $^{239}_{94}$Pu nucleus

is produced. If the plutonium is extracted from the used fuel

elements, as it can be by chemical methods, and used to fuel a reactor

of similar type, neglecting any plutonium losses in the process, and

making the optimistic assumption that all the original fissile material

undergoes fission before removal of the fuel element from the reactor,

the amount of uranium effectively used in two cycles is [1]

$$\underset{\substack{\text{initial } ^{235}_{92}\text{U}}}{0.7\%} + \underset{\substack{^{239}_{94}\text{Pu bred in first cycle}}}{0.5 \times 0.7\%} = 1.05\%$$

If now the plutonium bred in the second cycle is extracted and recycled,

the utilisation becomes

$$0.7\% + (0.5 \times 0.7\%) + (0.5 \times 0.5 \times 0.7\%) = 1.22\%.$$

The third cycle increases this to 1.31%, a fourth cycle to 1.36%, a

fifth to 1.38%, and so on. If it is assumed that the process is

repeated an infinite number of times, the total percentage of initial

uranium eventually undergoing fission is somewhat less than 1.5%.

With the better breeding ratio of 0.8 and the same assumption of zero

loss of plutonium and infinite recycling, the percentage of uranium

eventually undergoes fission is increased to about 3.6%, but when the

breeder ratio reaches unity, each nucleus of initial fissile material

consumed converts one nucleus of $^{238}_{92}U$ to fissile $^{239}_{94}Pu$ so that

eventually all the initial charge of uranium undergoes fission.

On this idealised picture the so-called uranium utilisation, or

percentage of all the uranium present ultimately undergoing

fission, increases dramatically from a few per cent to 100% as

the breeder ratio is increased from just below to slightly above

unity.   In the actual case, considering the percentage of

plutonium loss in extraction and the economic limit to the re-

cycling process, the uranium utilisation remains near 1% for low

conversion ratio reactors and reaches about 70% when the conversion

ratio exceeds unity.   One would consequently expect an increase

in the usable fissile fuel reserves by a factor of about 70 if

high conversion ratio rather than low conversion ratio reactors

are used.

From the economic point of view, for a given rate of

import of uranium fuel, the breeder will enable a larger generating

capacity to be installed than would be possible with thermal reactors

alone.   Then, when low grade ores have to be used towards the end

of the century the breeder will give more useful output and will

not experience a large increase in fuel cycle cost.   Finally, in

the long term, breeders will be able to operate for centuries, if

required, using ^{238}U from stockpile or from ores which were uneconomic

for thermal reactors [2].

1.1 Requirement for integral measurements

Nuclear data used in reactor technology and other applications derive from the sources: theoretical calculations, differential measurements and integral experiments. Theoretical calculations, based on nuclear models, are widely used in evaluations, in interpolation and extrapolation of differential data and have a major role in providing quantitative estimates where no reliable experimental information is available.

The major source of uncertainties in most fast reactor calculations is considered to be nuclear data rather than calculational methods, and also from the relative standardization of calculational methods, therefore, of the form of nuclear data, in this area [3]. The sensitivity of fast reactor performance to nuclear data uncertainties has been studies and led to the conclusion that the differential nuclear data requires very considerable improvements. The achievement of the target accuracy in nuclear data is based on the use of both evaluated differential data and integral information. The integral data uses results from clean-geometry fast lattices to minimise calculational errors, and covers neutron spectrum as well as all the important reaction rates measurable by integral techniques. By using a least-square fitting process the cross sections are adjusted to give the best fit to both the integral and evaluated differential measurements [4]. The alternative is the development of improved techniques and equipment for nuclear data measurements to meet increasing accuracy requirements [5].

The adjustment procedure was used for thermal reactors from the earliest times and began to be applied to the data for fast reactors in the nineteen sixties, when several new methods for cross section adjustment were developed. Use of integral experiments as benchmarks to provide feedback to the evaluators of cross sections was widely employed in the same period in setting up the different nuclear data files. Both differential and integral information is everywhere recognized to be necessary for the timely development of fast breeder reactors, although the way in which to take them into account varies widely from one place to another. In most cases, however, integral experiments both of benchmark and mock-up are carried out in support of specific fast reactor programs.[3]

1.2 Standardization of techniques

The prospects of fast breeder reactors are such that many countries have large research programs for the design and construction of this reactor. Several research groups throughout the world are investigating the improvement of nuclear data and methods for reactor design. It is clearly desirable to compare the results of the investigations with each other. Although intercomparison work may be achieved by building identical special fast reactor cores in different laboratories, it is an enormously expensive method and, in fact, is limited to very few research centres.

In order to standardize the measuring techniques between
different laboratories, a fast neutron standard has been developed
which would be inexpensive and so could be adopted by a large number
of laboratories and universities as an international standard.
The concept of the intermediate energy standard neutron field
has been promoted by CEN/SCK, Mol, Belgium, since 1967 within
the framework of the tripartite German-Dutch-Belgian fast breeder
program.   In 1969, the MOL-$\Sigma\Sigma$[6] facility was proposed as an
international intermediate energy secondary standard neutron field
and was put into operation in early Spring 1970.   In the same
year as a result of collaboration between CEN/SCK, Belgium, UKAEA
and Imperial College such a facility was designed and built to
fulfil the requirements of a standard neutron source.   Similar
efforts were undertaken and are being pursued at the Institute for
Nuclear Technology (ITN), Bucharest, and at the National Bureau
of Standards as the Intermediate Energy Standard Neutron Field
(ISNF), in co-operation with MOL.

The NISUS (Neutron Intermediate Standard Uranium Source)
assembly[7] was installed at the thermal column on the University
of London Research Reactor, CONSORT[8] in December 1971.   The
basic idea of this design was to build an assembly for generating
a neutron spectrum which would simulate the neutron spectrum of
the core and breeder of a fast reactor.   The neutron energy range
which is important in the study of fast breeder reactors is about
50 eV to 5 MeV.

The NISUS facility consists of two concentric spherical shells, are outer driver shell of natural uranium and an inner shell of boron carbide. The shells are supported in the centre of the air filled spherical cavity hollowed out of a 60 cm. cube of graphite. The graphite cube is mounted in a thermal column on a research reactor. The mechanism of spectrum generation in NISUS is that neutrons, originating from the reactor core, are slowed down in the thermal column and provide a well-thermalized source which impinges on the natural uranium shell. This gives rise to a fission distribution which is a maximum at the outer shell edge owing to the attenuation of the thermal flux through the driver shell. Inelastic scattering in the inner region of the shell degrades the spectrum to a characteristic fast reactor shape above 10 keV. The inner boron carbide absorbing shell is used to suppress any unwanted thermal neutron response in the detectors which are located inside an inner air filled cavity at the centre of the shells.

A series of experiments have been carried out in this facility since the installation using threshold detectors, proton-recoil proportional counter, [6]Li sandwich detector, and solid-state track recorders, and some more investigations are still in progress. Some measurements were made in collaboration with Mol, Belgium, to prove this assembly as an intermediate-energy standard neutron field to make it suitable for high-accuracy interlaboratory comparisons and standardizations.

The design, basic requirements and description of NISUS were described by others [9, 10], and, therefore, only the details entirely associated with the present measurements will be discussed in this thesis.

1.3 Objectives of this work

The general aim of this work is to measure absolute fission rates with solid-state track recorders and gas-filled fission chambers in a fast reactor neutron spectrum generator. The central neutron spectrum and reaction rate ratios are the major concern of the Neutron Intermediate Standard Uranium Source (NISUS). Since the NISUS assembly has come into operation, different spectrometry techniques have been used, and some are under investigation, for measurement of the central spectrum including: threshold detectors, proton-recoil proportional counters, and lithium-6 sandwich spectrometers. The central NISUS spectrum has also been calculated by one-dimensional transport code, and comparison made between theoretical prediction and measurements. This comparison revealed a discrepancy of 16-20% (depending on the normalising procedure) above 800 keV, between measured and calculated spectra and it was thought to be due to ill-defined nuclear data of uranium of the particular data set used[11].

Some uncertainties which have not been taken into account are those for the NISUS constituents as well as cross sections. These uncertainties which could have an effect on the shape of the spectrum and the reaction rate ratios may be considered in five main categories:

density, impurity, abundance, tolerance and cross section. In this
work these uncertainties are studied in detail and a comparison is
made between NISUS and MOL-$\Sigma\Sigma$ facility both for the central spectra
and reaction rate ratios.

On the experimental side use has been made of SSTR as
fission track recorders. The investigations have been confined to
use of Mica (Polaron, England) and a polycarbonate resin known as
Makrofol (Bayer, Germany). Makrofol has been found to have[12] one
of the highest efficiencies among the fission track recorders. Two
types of Makrofol were available: Makrofol E and Makrofol KG with
the thicknesses of 0.40 mm and 0.025 mm, respectively. Because of
the flexibility and nominal thickness which are very important
factors in angular measurements, Makrofol KG was chosen in the
routine experiments. An automatic image analyzer was used for
fission track counting and, therefore, the first part of this work
is devoted to study some of the problems and limitations associated
with this technique. A comparison is made between the track counting
by eye and automatically and the accuracy and reproducibility of
each is discussed.

The tasks of this work to be solved may be summarized as
follows:

(1)   To obtain track recorders to meet all requirements of track
counting, either by eye or automatically, i.e. satisfactory track
density, low background, high contrast, and uniformity of the features.

(2)   To establish an accurate and reproducible fission track
counting technique using an automatic image analyzer, the Quantimet 720.

(3)   To find the 'optical efficiency' of the SSTR by calibrating

the solid-state track recorders against fission chamber.

(4)   To measure the absolute fission rates at several positions

in the NISUS natural uranium shell.

(5)   To calculate fast neutron spectra and reaction rates using

available nuclear data set libraries by means of the one-dimensional

transport code.

(6)   To compare calculated and experimental results with the aim

to investigate NISUS as a standard fast neutron field.

1.4   Fission rate measurement techniques

The fission reaction, so basic in many aspects of nuclear

science and engineering, is important in nuclear radiation detection.

In these applications use is made either of the kinetic energy of

the fission products or of their resulting radioactivity, and or the

ability to produce tracks in nuclear emulsions and solid-state track

recorders.

1.4.1 Fission chambers

The ionization produced as the fission products are brought

to rest is utilized extensively in ionization and proportional chambers,

known as fission chambers.   A number of factors contribute to the

utility of fission chambers.   The wide choice of fissionable materials

allows the selection of the energy dependence and of the efficiency.

The large energy released per reaction makes it possible to discriminate

against much larger fluxes of gamma rays than with detectors employing

the (n,α) or similar reactions[13].

Fission chambers containing the thermal-fissionable nuclei
^{233}U, ^{235}U, or ^{239}Pu are efficient thermal neutron detectors. Materials

which are fissionable by only fast neutrons are useful for fast-neutron

measurement, particularly when it is desirable to discriminate against

low and intermediate-energy neutrons. All energies below the threshold

are excluded from the counting. Table 1.1 lists several fissionable

materials of interest for fast-fission chambers, along with their

threshold energies. The fissionable materials are incorporated into

the chambers in the form of thin deposits and the double fission

chambers are most commonly used. These chambers contain back-to-back

fissile deposits in two independent fast ionization chambers. The

electrodes are normally two discs parallel to the fissionable deposits

as the anodes, while the back-to-back positioned deposits serve as

the common grounded electrode. The EHT of about four hundred volts

is usually applied as operating voltage. The chambers are used

either as gas flow or sealed counters and pure methane or P-10 gas

(90% argon, 10% methane)[14] is normally used. However, the chambers

utilizing argon containing 2% nitrogen have also been suggested[15].

The absolute fission rates can be derived from the absolute

counting of the fissions occurring in a known quantity of fissile

material. A particular problem in such a method is the perturbation

introduced from the fission chamber material in the point where the

determination must be made. As a consequence it is tried to reduce

TABLE 1.1

Approximate values of fast-fission thresholds[13]

Material	Threshold (MeV)
^{238}U	1.45
^{237}Np	.75
^{232}Th	1.75
^{232}Pa	.5
^{209}Bi	50

this perturbation by using chamber material compositions similar to those of the media investigated. To reduce neutron absorption and scattering effects, the electrodes and structural elements are usually made up of aluminium, and the insulators are made of a hydrogen-free polymer. The shielding of the access hole for electronic cables and gas tubing against the thermal and epithermal neutron streaming is also necessary for absolute fission rate measurements.

1.4.2 Gamma counting technique

In this technique, use is made of the fission product activity in the foil detectors. If the fission yield of the product is known, the number of fission events can, therefore, be deduced from the gamma activity. There are two different techniques employed in gamma counting: the integral technique and the ^{140}La technique.

In the fission rate measurement by integral technique, the irradiated uranium foils are counted on a counting system in which a threshold energy of 1.28 MeV of a ^{22}Na standard source is set at the discriminator. This threshold is set to discriminate against β-rays produced in ^{238}U capture which have a maximum energy of 1.2 MeV. This method is normally used to obtain fission rate ratios and requires calibration against another technique, usually fission chambers[16].

The absolute values of F_8 and F_5 can be found by counting a particular fission product. Then, knowing the fission yield of this product, the number of fissions which have occurred in the sample can

be calculated. ^{140}La is a common fission product which is usually

selected and its 1.6 MeV gamma ray is detected. ^{140}La is produced

from the decay of ^{140}Ba which is a fission product and has a half-

life of 12.8 days. This is effectively the ^{140}La half-life after

a few days, when ^{140}Ba and ^{140}La reach their equilibrium. ^{140}La

decays to ^{140}Ce with the emission of several gamma rays, 96% of

which is the 1.6 MeV gamma ray.

$$U + n \longrightarrow {}^{140}Ba \xrightarrow[12.8\ d]{\beta^-} {}^{140}La \xrightarrow[40.2\ h]{\beta^-} {}^{140}Ce$$
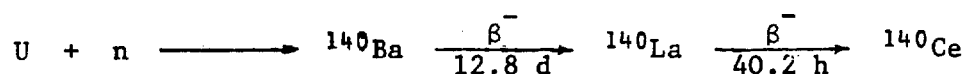
Since the 1.6 MeV gamma ray is superimposed on a very large gamma

background from other fission products, the resolution in counting

is of importance. The number of ^{140}Ba nuclei at the end of irradiation

in the sample is given by[17]:

$$N_{Ba}^0 = \frac{\lambda_{La} - \lambda_{Ba}}{\lambda_{Ba}} N_{La}(t_d)\ exp(\lambda_{Ba} t_d)$$

where,

λ_{La} and λ_{Ba} are the decay constants of ^{140}La and ^{140}Ba

$N_{La}(t_d)$ is the number of ^{140}La in the sample at decay time t_d.

Knowing the ^{140}Ba fission yield, Y, for the spectrum, the number of

fissions is calculated:

$$F = N^o_{Ba}/Y$$

This method requires the use of a calibrated gamma detector, although reaction rate ratios can be obtained without knowledge of the detector efficiency.

1.4.3 Nuclear emulsions

When charged particles pass through photographic emulsions, they can produce latent images along their paths. Upon development of the film, the grains of silver appear along the tracks of the particles. A variety of information can be obtained from the study of the tracks. Counting the individual path gives a measure of the number of nuclear particles entering the plate. A study of the detailed structure of the tracks leads to the determination of the mass, charge, and energy of the particles.

Nuclear track emulsions are widely used in cosmic ray physics, and high-energy particles from accelerators. It is also possible to detect fragments of uranium fission with emulsion despite the presence of a large flux of alpha particles. The techniques, theory and applications of nuclear track emulsion were described by Barkas[18].

1.4.4 Solid-state track recorders (SSTR)

When a heavy charged particle traverses certain materials it leaves a trail of radiation damage which shows up as a "track" when

a sample is viewed by transmission electron microscopy. This
discovery that almost all solid-state materials are capable of
recording the tracks of charged particles passing through the material,
has led to the development of new particle detectors with important
advantages over prior detectors in certain nuclear science application.
These detectors known as Solid-State Track Recorders, SSTR, (or
Solid-State Nuclear Track Detectors, SSNTD, or Nuclear Track Techniques,
NTT) could be natural minerals (e.g. mica or quartz), glasses, plastics
(e.g. polycarbonates or Cellulose compounds), and/or single crystals
(e.g. LiF or AgCl).

Growth in the use of solid-state track recorders has been
much more spectacular than in the understanding of how tracks are
formed. In addition to the obvious application to radiation
dosimetry, fields as diverse as geophysics (dating antique glasses
and ancient minerals and rocks), medical physics (production of bio-
logical filters), autoradiography (measuring the concentration of
fissionable elements such as boron, lithium, and uranium), space
science (determining cosmic, galactic, and solar particle flux
densities), and air and water pollution have been influenced by
tracks.

Fission track studies have an important place among the
numerous applications of SSTR. Fission rate measurements, precise
measurements of sponataneous fission half-lives, absolute fast
neutron fission yields, and environmental neutron intensities are
typical applications of fission track recorders. Gold et al[19]

have developed techniques for measuring absolute fission rates to accuracies approaching ±1% using SSTR. Besant and Ipson[20] measured the $^{238}U/^{235}U$ fission ratios in the fast reactor ZEBRA with SSTR and found the agreement to within the errors of ±4.2% with fission chamber measurements. The agreement in the same types of measurements has been improved to within ±3%[21]. Measurements of the $^{238}U/^{235}U$ fission ratio by SSTR in several assemblies in a zero power fast reactor have shown an estimated accuarcy similar to that using the more conventional foil activation technique[22]. However, it is notable that accuracies of the order reported by Gold et al[19] in 1968 for absolute fission rates have not appeared in the subsequent literature, nor has the technique had the impact in the dosimetry field which one would expect if such accuracies were routinely obtainable.

The important features of solid-state track recorders can be summarized as follows:

(a)   The detectors are simple in construction and use.

(b)   They are insensitive to light, unlike nuclear emulsions.

(c)   The exposed and etched detectors can usually be stored for long periods of time under various extreme environmental conditions of temperature, humidity, mechanical vibrations or pressure, etc.

(d)   Heavy charged particles such as fission fragments can be recorded and distinguished from a very high background of lighter charged particles like ^{4}He, ^{3}He, ^{2}H, ^{1}H, beta particles, X-rays, gamma-rays and even neutrons.

(e)   Since the detectors can be placed in direct contact with

fissile sources, a very high efficiency and sensitivity can be obtained.

(f)   The detectors have a considerable amount of geometric flexibility, and are therefore, particularly useful in angular distributions measurements.

1.5   Previous work on SSTR

In 1959, when E.C.H. Silk and R.S. Barnes[23] working at Harwell, published the first observation of fission fragment damage in mica by electron microscope, they probably did not expect that these tracks would become useful tools in many fields of science and engineering.   They alternated sheets of muscovite mica with sheets of aluminium upon which a layer of uarnium, less than one micron thick, had been vacuum evaporated.   These sandwiches were irradiated in BEPO for a few minutes.   Then after removal of the coated aluminium sheets,   the surface layers of the mica which had been in contact with the aluminium were removed by cleavage.   The thin mica sheets, up to 0.01 cm in size, were examined in an electron microscope at 100 KV. Tracks of the fission fragments which escaped from the uranium during the neutron bombardment could be seen in those pieces sufficiently thin for good electron transmission (probably less than 1000 A^o thick). The tracks are generally straight, less than 300 A^o diameter, and range from those which pass normally through the sheet and appear as dark dots, to those travelling almost in the plane of the thin sheet and greater than four microns long.   The number of long tracks is greatest in the surface layers, but even here the number of full range tracks

would only represent about 1/100 of the total, due to the extreme
thinness of the mica sheet.

Since then, numerous investigators have reported electron-
microscope observations of heavy-charged-particle tracks in thin
films of various materials. The appearance of these tracks depends
critically on the structure and thickness of the film, and although
thin-film detectors may prove to be useful in certain high-resolution
applications, they are not in the field of solid-state track recorders
and will not be discussed here.

In 1961, P.B. Price and R.M. Walker[24] of the General Electric
Research and Development Centre, Schenectady, New York, carried forward
from the stage where Silk and Barnes had left off, trying to stabilize
the tracks in mica and to develop other techniques for observing tracks.
In 1963, R.L. Fleischer[25] joined the team of Price and Walker, and
for several years almost all the work in this field was carried out
by this trio team. They anticipated the potential generality and
importance of phenomenon and initiated activity in a variety of fields,
some of which is discussed in their 1965 article in the Annual Review
of Nuclear Science[26]. Although they have reported in this article
that they first found that tracks in mica could be "developed" and
"fixed" by immersing the crystal in hydrofluoric acid, it was D.A. Young[28]
who first observed some shallow etched pits in lithium fluoride using
the etching treatmeant. Fleischer, Price and Walker not only developed
and put the technique on firm footing, but also applied it very
successfully to neutron dosimetry, fission studies, cosmology, geophysics,
etc., and suggested the term of "trackology" for this branch

of science. A comprehensive list of their publications may be found elsewhere[26, 27]. Very recently, the field has become quite popular in other laboratories as well, and extensive use of the detectors is being made. Armani[29], Becker[30], Benton[31], Gold[29] Khan[32], Somogyi[33], Varnagy[34], etc., are among other notable names in this connection. The numbers of their publications are too many to be mentioned in all, and the References are only the latest ones.

In March 1973, R.V. Griffith[35] published the results of the 1972 survey on track registration. In this survey, questionnaires were sent to more than 550 researchers at approximately 220 laboratories where work in track registration had been reported. These laboratories represented 29 countries. The results showed a survey of 118 laboratory groups in 20 countries. The national distribution of survey replies is shown in Table 1.2, and it certainly reflects widespread geographical interest in track registration.

In the past three years there has been a dramatical increase in the number of laboratories using the techniques for registration of nuclear particles in dialectric materials. In this period, the author has found some published work on Solid-State Track Recorders (SSTR) from the countries other than those in the Table 1.2, including Brazil[36], Republic of China[37], Czechoslovakia[38], German Democratic Republic[39], Pakistan[32] and USSR[40]. It is felt that at present, probably more than 300 laboratories throughout the world are using these techniques. The more recent and comprehensive bibliography on SSTR literature can be found in Reference[41].

TABLE 1.2

The national distribution of laboratories using
solid-state track recorders (35)

Country	Number of laboratories
United States	53
West Germany	18
France	8
Japan	6
England	5
Australia	3
Belgium	3
Canada	3
Italy	3
Switzerland	3
Hungary	2
Ireland	2
Netherland	2
Austria	1
India	1
Israel	1
Poland	1
Romania	1
Sweden	1
Trinidad	1

The elements that can be determined by the SSTR technique are shown in Table 1.3[42]. The application is based on the fact that the number of tracks produced per unit area is proportional to the concentration of the element producing tracks. With the proper choice of detector and etching, it is possible to make chemical analyses in a variety of matrices.

As Table 1.4 makes evident, a variety of particles and radiation can readily be counted by their property of inducing fission; high energy charged particles including protons, electrons of a few hundred MeV, and photons of more than ~20 MeV can be detected. Such dosimetry is particularly useful around high energy accelerators and is also applicable to recording doses of the lightly ionizing nucleonic portion of the cosmic rays that are encountered at high altitudes or in space. Often detector pairs with different fissioning nuclides will be needed if neutron effects are to be separated from those of the charged particles of interest[43].

Solid-state track recorders have been used not only as detectors but spectrometers. Blok et al[44] have made a fission fragment spectroscopy of the fission of silver induced by 80 MeV alpha particles by measuring the track length distributions in mica and track diameter distribution in glass detectors. Other investigators have made use of SSTR as neutron[45] and proton[46] spectrometer. This new detector has also been used for mass discrimination of ^{3}He and ^{4}He of about the same energy[47].

TABLE   1.3

Elements that can be determined by SSTR[42]

Legend:
- ▨ (n,α) Reaction
- ▤ (n,p) Reaction
- ▧ (γ,f) Reaction
- ▦ (n,f) Reaction (thermal and fast)

H																	He
6Li	Be											10B	C	14N	17O	F	Ne
Na	Mg											Al	Si	P	S	Cl	Ar
K	Ca	Sc	Ti	V	Cr	Mn	Fe	Co	Ni	Ca	Zn	Ga	Ge	As	Se	Br	Kr
Rb	Sr	Y	Zr	Nb	Mo	Tc	Ru	Rh	Pd	Ag	Cd	In	Sn	Sb	Te	I	Xe
Cs	Ba	La*	Hf	Ta	W	Re	Os	Ir	Pt	Au	Hg	Tl	Pb	Bi	Po	At	Rn
Fr	Ra	Ac**															

*	Ce	Pr	Nd	Pm	Sm	Eu	Gd	Tb	Dy	Ho	Er	Tm	Yb	Lu
**	Th	Pa	U	Np	Pu	Am	Cm	Bk	Cf	Es	Fm	Md	No	Lw

TABLE 1.4

Particle track detectors (43)

Type of radiation	Mode of observation	Detector material	Sensitivity (tracks/cm² per particle/cm²)	Notes
Fission fragments	Direct	Any dielectric solid	1.0	
Heavy cosmic rays; Heavy ions from accelerator	Direct	Most plastic detectors	1.0	For ions at sufficiently low energies
Alpha particles	Direct	Cellulose plastic or U.V. irradiated Lexan	0.1 - 1.0	Most efficient at energies below 4 MeV
Protons	Direct	Cellulose nitrate or acetate	0.1 - 1.0	Only at very low energy (< .55 MeV)
Protons	Induced fission	Any dielectric solid	$\sim 10^{-5}$	High energy; depends on fission cross section of fissioned nuclide
Fast neutrons	Induced fission	"	$\sim 10^{-5}$	"

TABLE 1.4 (continued)

Particle track detectors (43)

Type of radiation	Mode of observation	Detector material	Sensitivity (tracks/cm^2 per particle/cm^2)	Notes
Thermal neutrons	Induced fission	Any dielectric solid	$\sim 5 \times 10^{-3}$	For ^{235}U fission plates
Thermal neutrons	(n,alpha) reaction	Cellulose nitrate or acetate	$\sim 2 \times 10^{-2}$	^{10}B reaction plates
Electrons	Induced fission	Any dielectric solid	10^{-8} to 10^{-7}	Energy 200-500MeV
Photons	Induced fission	"	$\sim 2-3 \times 10^{-6}$	Energy > 20 MeV

2. REVIEW OF THEORETICAL MODELS

Individual massive charged particles, produce linear trails of radiation damage in many solids. These damage trails or tracks may be formed in almost any sort of insulating materials - crystalline, glassy, or polymeric - but have not been seen in good conductors (Table 2.1)[48]. A large class of materials of a resistivity of more than 2000 Ω cm are known to be capable of recording and storing tracks; materials of less resistivity apparently do not have this capability. Although the resistivity by itself is not a unique criterion, Table 2.1 is used because resistivity is a simple, easily measurable quantity which seems to separate most materials into track-forming or non-track-forming groups.

2.1 Energy loss processes

When a heavy charged particle moves through a medium composed of atomic nuclei and electrons, it can lose energy by three main processes. The principal mode of energy loss is that due to interaction with the atomic electrons by Coulomb excitation or ionization. It may also lose energy by direct collisions with nuclei of the stopping medium, though such events are rare until the particle nears the end of its path. The third energy loss process, that of emission "bremsstrahlung" and "Čerenkov" radiation, is small compared to the first two processes. For every energy E, therefore, the total rate of energy loss (the absolute stopping power), is a combination of the rates of energy loss

TABLE 2.1

Relation of track-storing properties of materials
to electrical resistivity (48)

Properties	Materials	Resistivity range (Ω - cm)
Track forming		
Insulators	Silicate minerals Alkali halides Insulating glasses Polymers	$10^6 - 10^{20}$
Poor insulators	Molybdenum disulfide	3000 - 25000
Semiconductors	V_2O_5 glass	2000 - 20000
Non-track-forming		
Semiconductors	Silicon Germanium	10 - 2000
Metals	Tungsten Zinc Copper Platinum Aluminium Gold	$10^{-6} - 10^{-4}$

due to each of the three processes, and may be written in the form[49]

$$(-\frac{dE}{dx})_{total} = (-\frac{dE}{dx})_{electronic} + (-\frac{dE}{dx})_{nuclear} + (-\frac{dE}{dx})_{radiation}$$

(2.1)

2.1.1 Energy losses by radiation

"Bremsstrahlung" or braking radiation is emitted when a

charged particle is rapidly accelerated or retarded in the field of

a nucleus atom. The intensity of the radiation is, according to the

classical electrodynamics, inversely proportional to the square of

the mass of the incident particle, and consequently the phenomenon

is of much less importance in the case of heavy ions than it would

be for lighter particles such as electrons. Cerenkov radiation

arises from the polarization of a dielectric along the path of a

charged particle when the velocity of the latter exceeds the phase

velocity of light in the medium. This polarization is time dependent

owing to the moving electric field of the particle and can produce

a radiation field. This effect is, of course, vanishingly small,

in the case of a fission fragment, since the particle velocity is

very much less than the velocity of   light in any dielectric.

Therefore, the energy loss due to radiation can be neglected.

2.1.2 Nuclear collision losses

Retardation of a heavy charged particle by collisions with

atoms in the material only takes precedence near the end of the particle

range, where electronic excitation becomes small. Such two-body nuclear

collision may be described classically (Bohr, 1948) provided that

the collision diameter b, the distance of the nearest approach in

a head-on collision, is very much greater than de Broglie wavelength, λ.

For scattering of a charged particle by a Coulomb field of force,

this condition may be written

$$K = b/\lambda = (Z_1 Z_2 e^2/hv) \gg 1 \qquad (2.2)$$

where Z_1 and Z_2 are the atomic number of the moving and struck

particles respectively and v is the velocity.

It has been shown[49] that the specific rate of nuclear energy

losses for collision between two particles specified by (M_1, Z_1, E) and

$(M_2, Z_2, 0)$ is given by:

$$(-\frac{dE}{dx})_{nuclear} = (\frac{\pi Z_1^2 Z_2^2 e^4}{E}) (\frac{M_1}{M_2}) n_o \ln \left[\frac{2aE}{Z_1 Z_2 e^2} \cdot \frac{M_2}{M_1 + M_2} \right] \qquad (2.3)$$

where

n_o = spatial density of the nuclei in the medium

a = the screening parameter which takes into consideration

the screening effect of bound electrons on each nucleus.

2.1.3 Electronic energy losses

If it is assumed, in a first approximation, that the energy

loss collisions which the moving particle makes with atomic electrons

are also to be considered within the framework of classical mechanics,

then using the differential scattering cross section given by the

Rutherford law, the energy loss rate to electrons can be written as

$$(- \frac{dE}{dx})_{elecrtonic} = \frac{2 \, z_1^{2/3} \, z_2^{1/3} \, h^3 \, n_o}{\pi^2 \, e^2 \, m} (\frac{2E}{M_1})^{1/2} \qquad (2.4)$$

In the above expression the symbols Z_1, Z_2, E, M and n_o having the

same meaning as given for equation 2.3, and the symbols e, m and h

the usual meaning óf the electronic charge, electronic rest mass,

and Planck's constant, respectively.

2.2   Track formation criteria

The major properties of tracks - their high chemical reactivity,

their fading kinetics during heat treatment, their diameters, and the

damage threshold for their formation - have led to the following

physical description :   Tracks in crystals and in   glasses

consist primarily of narrow, roughly cylindrical regions, with a

high concentration of displaced atoms and vacant sites.   The case of

tracks in high polymers is more complicated, primarily because of

the greater multiplicity of chemically active defects that can occur

displaced atoms, broken molecular chains, free radicals, etc.

It has been well established[26,27] that a registration threshold

exists for each solid-state track recorder such   that for damage

densities below this threshold value, a track cannot be developed.

The track must intersect the surface and be above threshold, but this

does not necessarily lead to an observable etch pit upon development.

If V_G is the bulk etching rate and

V_T the etching rate along the track, then no tracks making an angle

less than $\theta = \sin^{-1} (V_G/V_T)$ with respect to the surface will

develop into etch pits[50,51]; that is, the surface dissolves away

faster than the etch pit develops. For this reason, registration

thresholds are experimentally determined for the given

bombarding particle.

2.2.1   Total energy loss criterion

The precise mechanisms by which chemically reactive defects

are produced are less clear than is the nature of the resulting

defects, and no completely satisfactory theory of track formation

exists.   Fleischer, Price and Walker developed a model of track

formation in which the rate of chemical dissolution of the material

along the track can be related to some parameter J that is a

function of the atomic number Z and velocity β of the particle.

This initial approach which became clearly inadequate as soon as

extensive calibration data with heavy ion beams became available,

was to equate J with dE/dx the rate of energy loss of the particle[26].

The curves of dE/dx given in Ref. (26) are now quite out of date and

do not correlate as well with subsequent observations as do curves

relating to radiation close to the trajectory.

2.2.2   Primary ionization criterion

In 1967, Fleischer et al[52] themselves reported that the

total energy loss criterion is not consistent with some of the

experimental results. In some materials the tracks were registered at the lower threshold than predicted by the total energy loss criterion and also the prediction on the basis that relativistic ions can make etchable tracks in cellulose nitrate was found to be incorrect.

The new criterion, guided by an "ion explosion spike" model of track formation (Section 2.3.3), was to associate the parameter J with the density of ionized atoms plus excited atoms within a few atom diameters of the trajectory. Fleischer et al. concluded that a quantity somewhat different from the total energy loss rate should determine the presence or absence of the tracks. It is the primary ionization rate (i.e. the number of primary electrons formed per unit length of track) and not the total energy loss rate which governs the registration of tracks. Fig. 2.1 gives a set of ionization curves for various bombarding nuclei. Approximate threshold ionization levels for several solids are indicated by dashed lines to give an idea of relative sensitivities[27]. These registration thresholds are the most significant identifying characteristic of dielectric detectors. Fig. 2.2 illustrates the track registration as a function of energy for a number of ions in muscovite mica; (a) shows the relationship between dE/dx and the energy E, and (b) illustrates a set of corresponding curves of primary ionization. Regions of (i) complete tracks, (ii) partial tracks, and (iii) no tracks, based on the total energy loss rate and primary ionization rate are also shown[52].
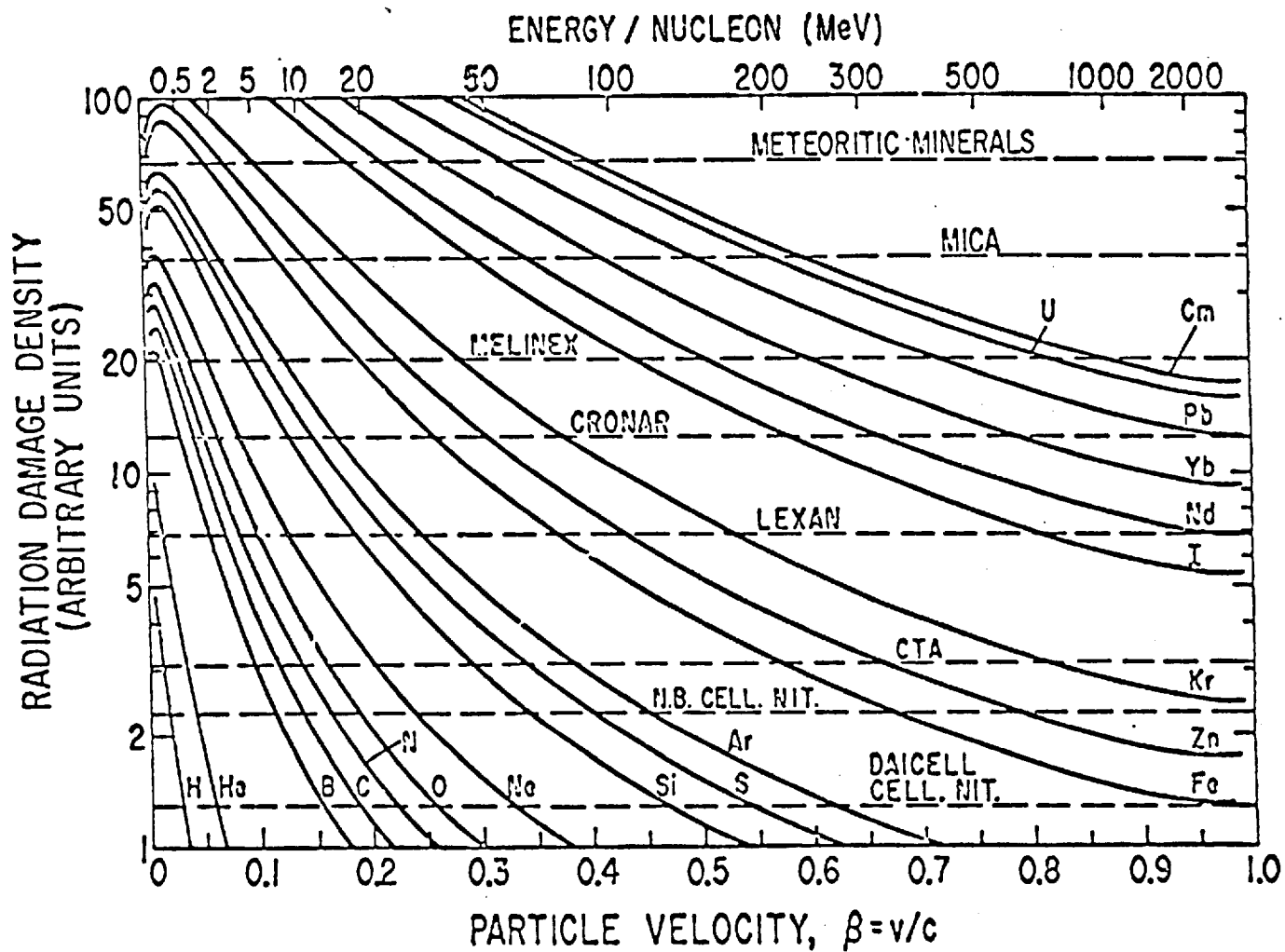
Fig. 2.1   The threshold damage density for a variety of dielectric

materials (Reproduced from Ref. 27)
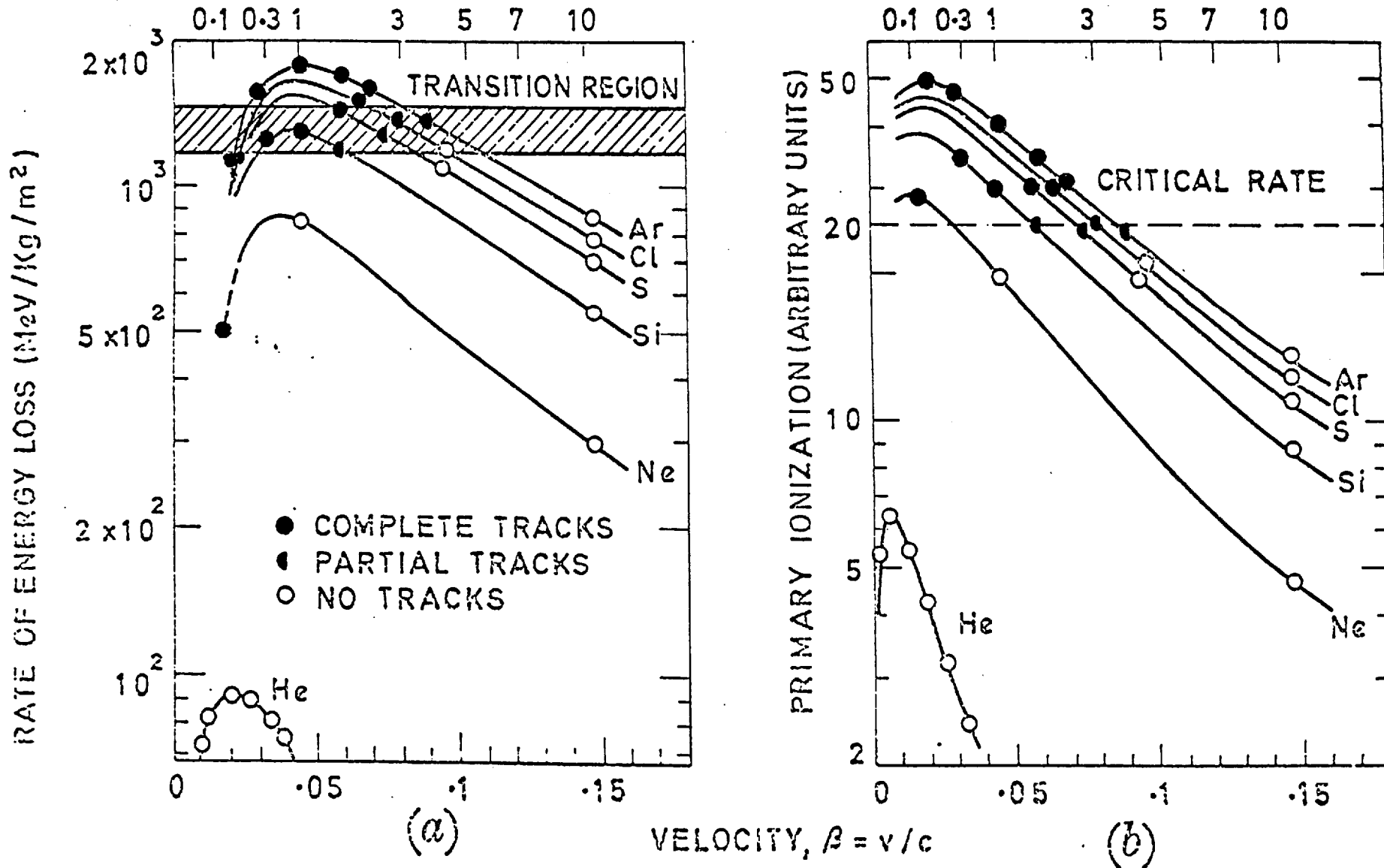
Fig. 2.2 (a) Total energy loss rate and (b) primary ionization rate in muscovite mica of various charged particles of varying energy (Reproduced from Ref. 55).

2.3   Mechanisms of track formation

In order to choose the right material for different particle registration, it is necessary to know the relation between the characteristics of the material and the particles to be registered. So far, no coherent, comprehensive theory of the latent track-formation mechanism and preferential etching kinetics in insulators is available. Various models of these mechanisms were reviewed by Fleischer et al[48] including the thermal spike, the displacement spike, and the ion explosion spike.   In addition to this, Benton[53] has proposed a restricted energy loss (REL) model, and Katz and Kobetich[54] have introduced a radiation dose or delta-rays model.

2.3.1   Thermal spike model

This model considers that the energy which is lost to the electrons eventually reappears in a relatively short time as heat in the lattice, whereupon it diffuses away by normal thermal conductivity. If this energy is initially passed to the lattice within a small cylindrical region surrounding the ion's path, a region of extremely high localized temperature is created.   Such a region is known as a "thermal spike".   For example, if a fission fragment loses 30 MeV/μm and this energy is passed to the lattice over a cylinder of radius 10 nm, a temperature rise of the order of 24000°K is predicted[55].   It is quite evident that if such a high temperature is maintained for appreciable times, the processes such as melting and recrystallization, surface evaporation, or point defect creation and migration would be highly probable.

According to Morgan and Vliet[55] there are two possible

conditions under which an intense spike of this nature will NOT

form.

(1)   If the initial energy is more rapidly spread via the free

electron collisions, then passed to the lattice via electron-photon

collisions, the eventual spike is considerably wider and correspondingly

much less intense.   This is the situation envisaged for metals, where

one has both a large number of free electrons, plus rapid electron-

electron coupling to dissipate the energy.

(2)   Or, one might envisage a situation where an intense thermal

spike is created, but due to very efficient heat conduction it lasts

for such a short time that no appreciable rearrangement of the lattice

results.

According to the thermal spike model, there are two essential

conditions for track formation.   Firstly, the state of high temperature

should exist for appreciable times, which precludes that electron-photon

coupling should be stronger than the electron-electron coupling in the

material.   Secondly, the normal heat conductivity in the material

should be low.   While Morgan and Vliet believe that the spike model

has indeed correctly demonstrated that the damage resulting from thermal

spikes is greatest in insulators, intermediate in semiconductors, and

negligible in metals, Fleischer, Price and Walker[48] discarded the

thermal spike model "as not leading to fruitful predictions".   The

failures of this theory are as follows:

(1)   No insulators have shown any sign of a high temperature

phase even in a heavily irradiated condition.

(2)   The calculation of the widths of the tracks correlated with

the relative thermal stability of different materials, is in disagreement

with Fleischer et al. and other observations.

(3)   Sensitivities of different track forming materials are not

related to their known melting, softening or transformation temperature.

2.3.2   Displacement spike model

Although a major conclusion of the analysis of energy loss was

that direct collisions with nuclei are of minor importance, it must not

be assumed that the atomic displacement is negligible.   There is high

probability that an atom as a complete entity will receive kinetic

energy in that region of high thermal and electronic excitation which

lies in the wake of a charged particle.   Therefore, a number of atoms

will be displaced by secondary processes arising from the electronic

part of the energy loss of the particle.   Secondary displacement

processes are also important in the history of a primary knocked-on

atom deriving from a nuclear collision.   Such an atom will undergo

elastic, and if energy is sufficient, inelastic collision with its

neighbours, initiating further secondary and higher order displacement.

A cascade of displaced atoms will build up until the maximum energy of

any atom falls below the appropriate "displacement threshold", E_d.

The value of E_d depends on the binding and the crystallographic

characteristics of the material and is normally about 25 eV, though it

is directionally dependent in crystalline matter, and can be much higher

in certain unfavourable directions[49].

In a very simple case where an atom in an element receives energy in excess of its displacement threshold, but insufficient for it to displace another, one can postulate with reasonable accuracy that it will eventually return to its lattice site or come to rest in an interstitial positon of metastable equilibrium. In a real situation, however, the displacement cascade is a very complicated, many body process. In particular, many neighbouring atomic displacements will be created in many small volumes adjacent to the trajectory of the particle. This multiple displacement idea lead naturally to the concept of the "displacement spike", first suggested and developed by Brinkman[49]. It is hypothesised that a multiple vacancy can be created at the end of the path of an incident charged particle or an energetic primary knock-on ($\sim$1000 eV); the configuration immediately following each event being a shell of interstitial atoms surrounding a vacancy core. A schematic representation of the application of this model to the passage of a fission fragment in a crystalline solid is given in Ref. (49).

2.3.3 Ion explosion spike model

The ion explosion model predicts that a charged particle should cause damage by formation of ion pairs along its path[52] as it passes through dielectric material. The number of ion pairs formed per unit path length is given by Bethe's primary ionization rate equation (Bethe, 1930). A narrow cylindrical region of positively ionized atoms is produced behind the ion trajectory. These positive ions mutually repel each other so that some are ejected outwards

into interstitial positions, leaving behind a vacancy-rich cylindrical core. Thus a cylinder of 40-80 A^o diameter and a few microns long is formed, which can either be directly seen under a high magnification of a transmission electron microscope or an opitcal microscope can be employed, if they are chemically enlarged.

According to the ion explositon spike mode, in order for tracks to be formed four conditions must necessarily be satisfied:

(i)   The electrostatic stress must be greater than the mechanical strength or bonding strength of the crystal which indicates that tracks are more easily formed in materials of low mechanical strength, low dielectric constant, and close interatomic spacing.

(ii)   A second criterion that in some materials tracks must be continuous, requires at least one ionization per atom plane crossed by the incident charged particle. Therefore, n > 1 (no. of ionization per atom) is a second criterion for track formation in such materials. In other materials it is likely that n will be $\sim$ unity. Using such a criterion is limited to tracks which can be identified by the etching technique. For other methods of revealing tracks (Chapter 3) different criteria will no doubt apply.

(iii)   The free electron density should be low, otherwise the electrons removed by the energetic ion are replaced by the free electrons in a short time and no tracks will result. This means that for track formation there is a maximum permissible of free electrons, which in turn relates the track-storing property of a solid to the electrical conductivity. This condition illustrates why the insulators register the tracks of the charged particles and metals do not.

(iv)   Tracks are not formed in the materials with high hole

mobility.   This is because the rapid outward diffusion of the holes

neutralizes the core atoms and thereby inhibits the formation of

defects.   It follows that metals and many semiconductors, including

silicon and germanium are normally not track storing materials.

On the other hand, in many other semiconductors, including the

vanadium glass, it is thought that the thermal activation occurs

as a result of the intermittent overlap of ions due to thermal

vibrations.   For any such material the direct ejection of ions

should be possible.

For plastics, the ion explositon spike model predicts that

3 MeV alpha particles should not register, though in fact, they are

recorded in certain plastics up to 5 MeV.   Since it is known that as

little as 2 eV is sufficient to break bonds (as a result of excited

electrons) in polymers, whereas the minimum energy for primary ion-

izations is $\sim$10 eV, it is reasonable to assume that additional energy

loss processes should be included in the track formation mechanism.

This argument is frequently used against primary ionization rate

as the correct expression for the damage density in plastics, although

an empirical form of the expression has been successfully applied

to plastics and to other dielectric materials[52].   Fig. (2.3)

shows schematic view of ion displacements[56] as a result of the

extensive ionization along the path of a massive energetic charged

particle in (a) plastics (b) crystals.

The ion explositon spike model agrees reasonably well with experiment.

It predicts correctly the conductivity dependence of track formation.

(a)

(b)
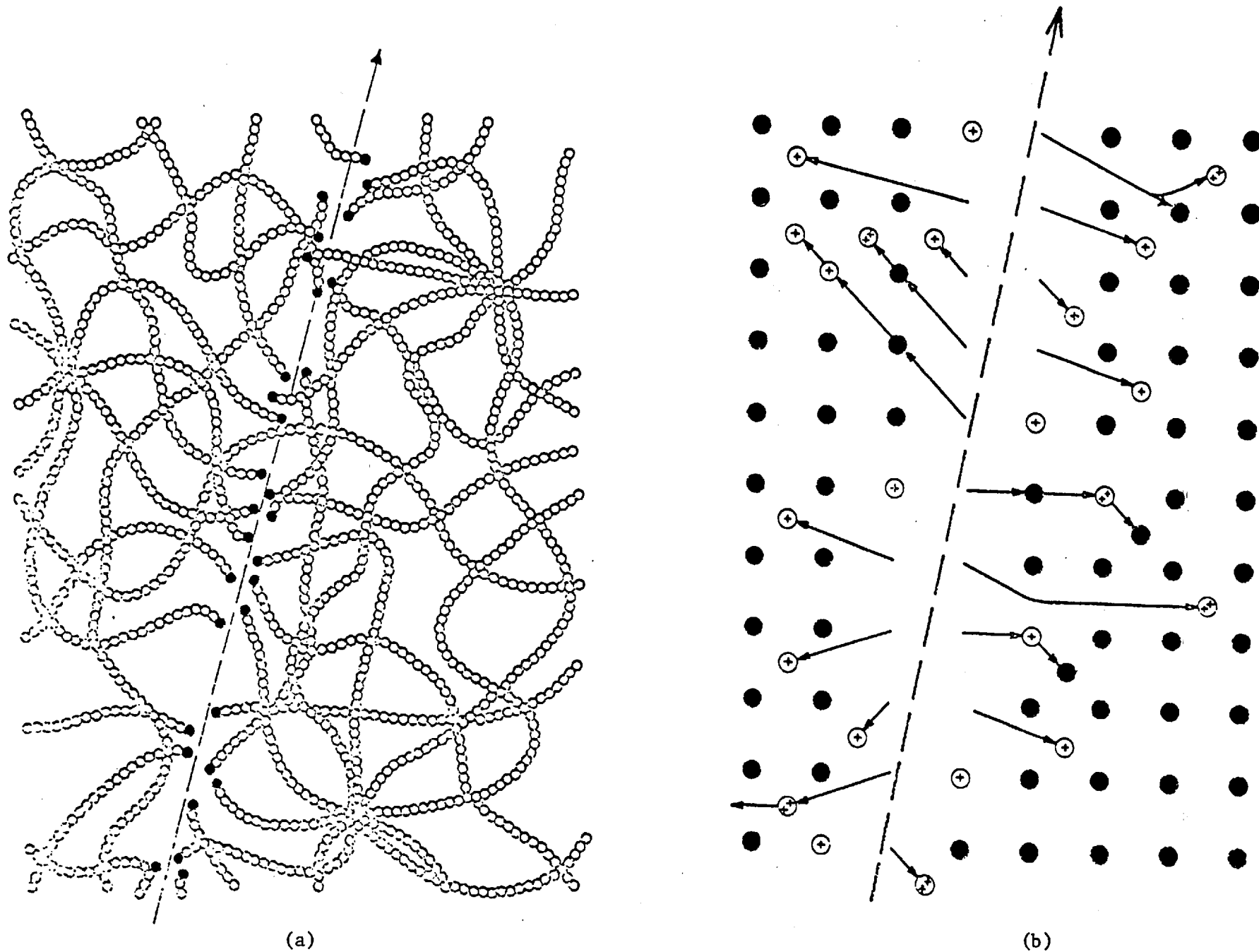
Fig. 2.3   Models showing the formation of latent trails in (a) plastics, (b) crystals (Reproduced from Ref. 56).

Further, in contrast to the thermal spike it asserts that the

primary ionization rate, not the rate of energy loss, is the

important parameter, in agreement with the experimental observations

of Fliescher et al[48].

2.3.4 Restricted energy loss model

In 1968, Benton[53] put forward a new model for the registration

of charged particle tracks in plastics. According to Benton, the

restricted energy loss (REL) model essentially considers all secondary

electrons with energies below a certain energy as important in the

formation of a track, whereas the higher energy electrons are not

important. The energy loss of a charged particle in matter, due

primarily to inelastic collisions with electrons, can be divided

into two regions according to close and distant collisions with the

electrons. REL is defined as "the rate of energy loss of the

bombarding particle in such collisions (distant collisions) with

the electrons of stopping material which result in the ejection of

electrons of energy W, less than some predetermined value W_o".

Benton used the expression for the energy loss due to distant collision

to calculate damage density, which then applied to cellulose nitrate

and Lexan (General Electric Company, U.S.A.) polycarbonate plastic

detectors gave registration thresholds that agreed with the experimental

results. Figures (2.4) and (2.5) show the restricted energy loss

(REL) rate values for a number of heavy ions in cellulose nitrate

and Lexan respectively[53].
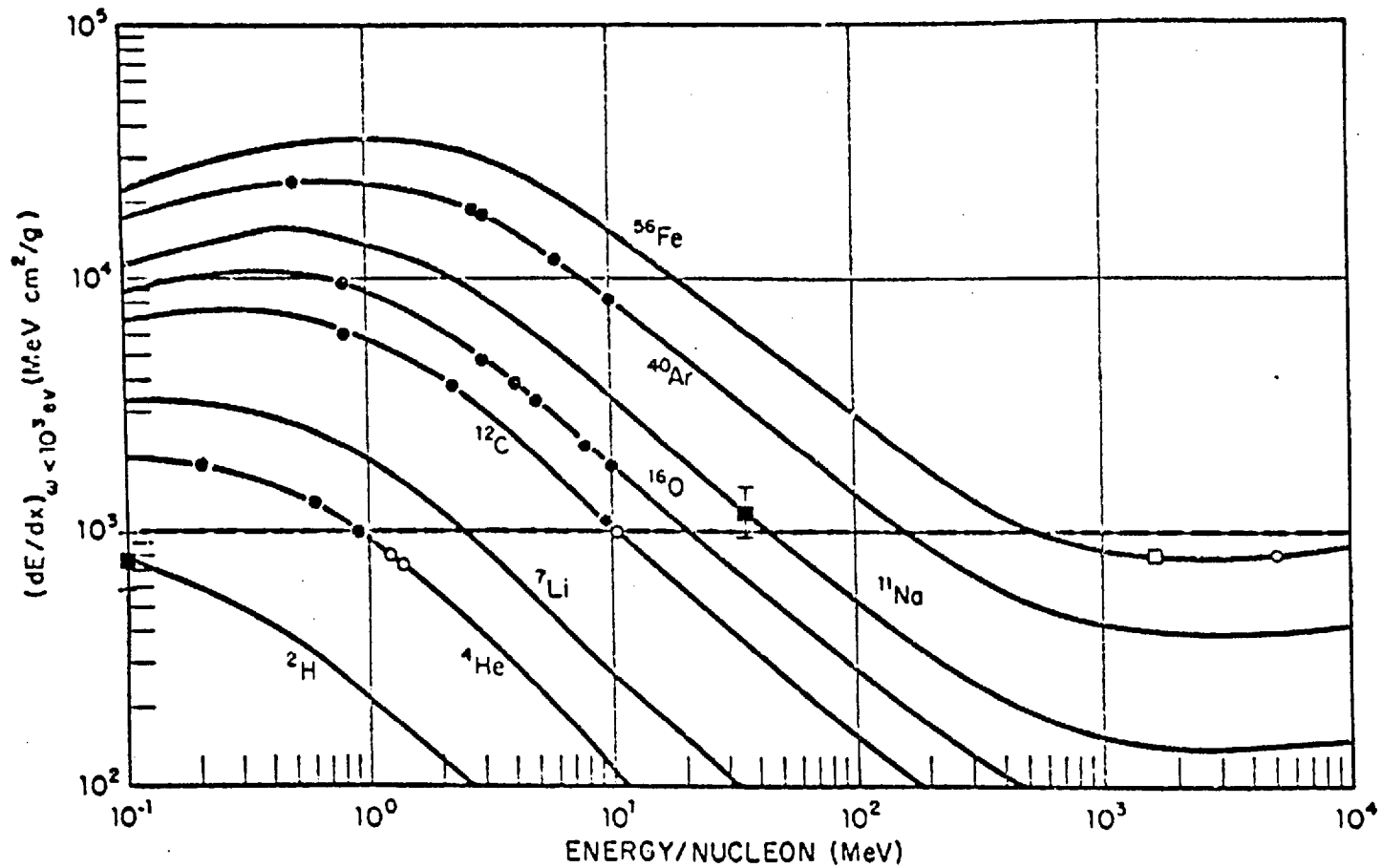
Fig. 2.4   Restricted energy loss rate, $(dE/dx)_\omega < 10^3$ eV, as a function of energy
per nucleon for a number of heavy ions in cellulose nitrate. The
experimental data on track registration is superimposed on the theoretical
curves in the form of closed and open points, indicating track registration
and lack of track registration, respectively (Reproduced from Ref. 53).
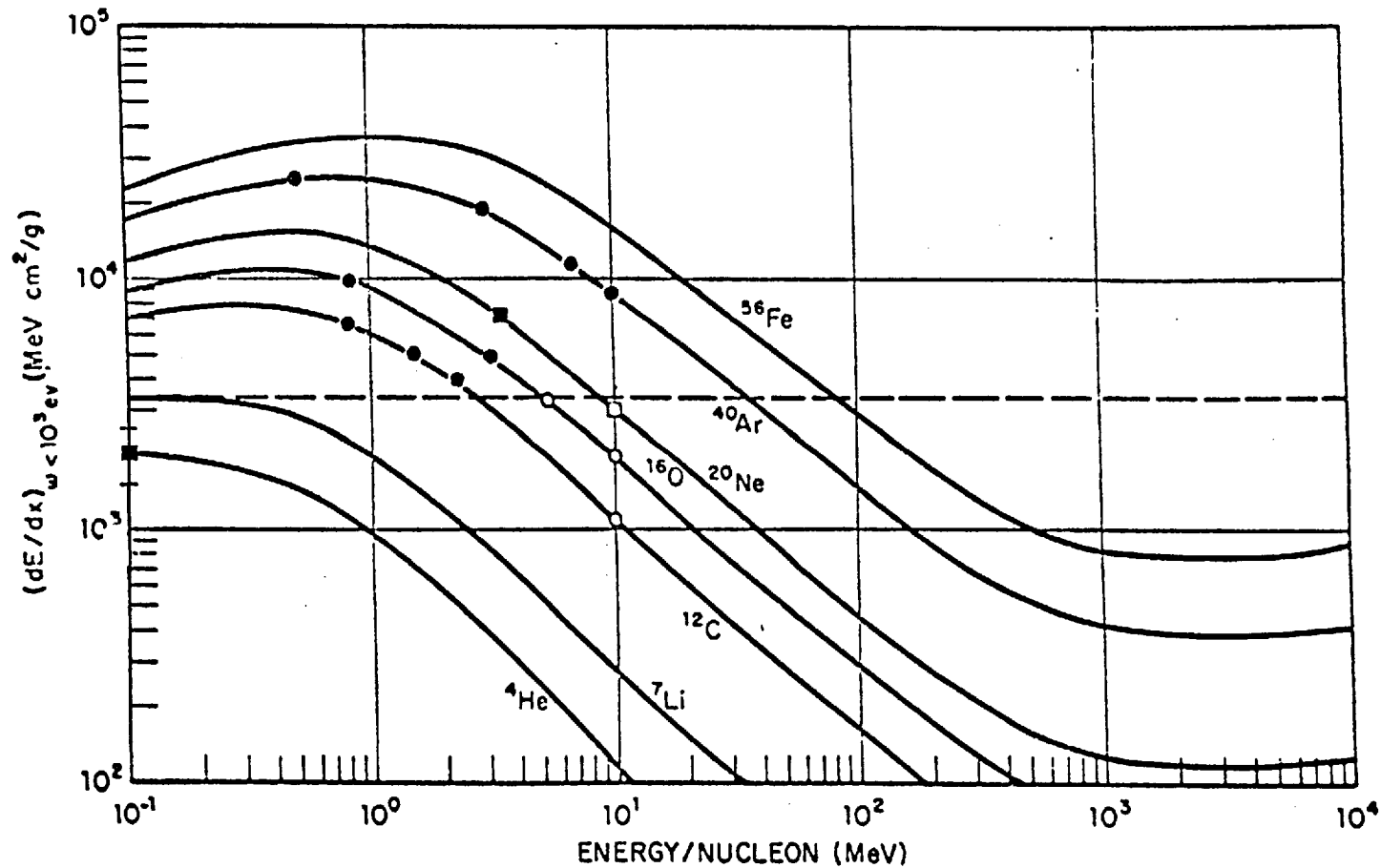
Fig. 2.5 Restricted energy loss rate, $(dE/dx)_\omega < 10^3$ eV, as a function of energy per nucleon for a number of heavy ions in Lexan polycarbonate resin. The experimental data on track registration is superimposed on theoretical curves in the form of closed and open points, indicating track registration and lack of track registration, respectively (Reproduced from Ref. 53).

2.3.5   Delta-rays model

Katz and Kobetich [54] have made an entirely new approach

to the mechanism of track formation.   According to them, the

significant part in track formation is not played by 'positive ions'

but by the 'secondary electrons'.   Their model relates the 'dose'

produced by secondary electrons at a particular radius from the

path of the particle to the charge and velocity of the particle.

They have calculated the registration thresholds for charged

particles in cellulose nitrate and Lexan and they are in agreement

with experimental results.

2.4   Critical angle of etching

The SSTR sensitivity depends, among a number of factors,

on the energy and angular distribution of the particles emitted

from the source.   It has been shown that only those particle

tracks can be revealed by chemical etching whose angles to the

surface exceed a critical angle.   The concept of "critical angle

of etching" was first introduced by Fleischer and Price [50] and

later by Somogyi et al [51], and then experimentally investigated

by Khan and Durrani [12].

The reason that tracks become visible at all is that the

damage trails are etched preferentially by the etchant;   in other

words they velocity V_t of the etchant along the track is greater

than the general or bulk velocity V_g along any other direction in

the medium.   Take a particular track entering the surface of the

detector at angle θ.   In time t, the etchant penetrates a distance

of $V_t.g$ and $V_g.t$ along the track and normal to the detector surface, respectively. So a layer of $V_g.t$ thick is etched away from the SSTR surface and that of $V_t.t$ from the damaged region. If, under the applied etching conditions, $V_t.t$ is less than $V_g.t$ then the track will fail to leave an etch pit on the final layer. This happens at all angles lower than θ_c, the critical angle of etching. Table 2.9 shows the critical angle of etching of various SSTR for ^{252}Cf fission fragments[12]. So for the value of the critical angle has been defined by the formula

$$\theta_c = arc\ sin\ \frac{V_g}{V_t} \qquad (2.5)$$

The above relation, however, represents only an ideal case. In actual practice only those tracks can be regarded as observable with the optical microscope where the projected length of Z of the tracks to the normal of the detector surface is more than a minimum value Z_{min} where Z_{min} is about 0.5 to 1μm.[51] Then, for the critical registration angle we have

$$\theta_c = arc\ sin\ (\frac{V_g}{V_t} + \frac{Z_{min}}{R_m}) \qquad (2.6)$$

where,

$$R_m = R(E) \qquad if \qquad R(E) < R(E_c)$$

TABLE 2.2

The critical angle of etching of various S S T R
for ^{252}Cf fission fragments (12)

Detecting material	Critical angle	
Soda-lime glass	35°	30
Reference glass (U-2)	31°	45
Obsidian glass	26°	00
Tektite glass	25°	45
Quartz	7°	15
Mica	4°	30
Makrofol (Bayer)	3°	00
Lexan (G.E.C.)	2°	30

and,

$$R_m = R(E_c) \quad \text{if} \quad R(E) > R(E_c)$$

where R_m is the maximum etchable track length and $R(E)$ is the
real range of the particle of energy E entering the detector;

while $R(E_c)$ is the range of the particle having the critical
registration energy. Relation (2.6) shows that if we investigate

particle tracks for which the value of V_t is comparable to that of
V_g, no observable tracks are revealed even for particle having

considerably higher angles to the detector surface than expected

from Eq.(2.5).

3. REVIEW OF TRACK DETECTION TECHNIQUES

The passage of charged particles, as described earlier,

appear as narrow trails of radiation damage in insulating materials

such as crystals, glass, mica and plastics. This narrow damaged

region has been termed "latent damage trail" or simply "track".

The dimensions of these damaged regions are only about $100\overset{o}{A}$

diameter by $\simeq 10$ microns depending on the material.

There are several ways for revealing tracks in solid-state

track recorders:

3.1   Electron microscopy

In several materials regions damaged by the charged particles

cause electron diffraction and, consequently, they can be observed

by an electron microscope, as first employed by Silk and Barnes[23],

without any previous procedure. The techniques employed so far

are transmitted and scanning electron microscopy.

3.1.1   Transmitted electron microscopy (TEM)

Transmitted electron microscopy is suitable for measurements

of track density greater than 10^9 tracks/cm^2, but requires the

preparation of extremely thin samples.

Plastic films, for TEM, must be very thin (less than 1 micron

thick)[57] so that they can remain stable in the electron beam.

Even with films with 1 micron and less, electron scattering in some

plastics will result in a charge build-up which can lead to a

temperature rise sufficient to cause melting and a break down of

the film. Thin specimens are normally supported on fine copper

wire grids and this helps to reduce charging in the film. The

difficulties can also be reduced by the use of a very high beam

energy (e.g. 1MV).

Since the transmission electron microscope provides

information about the internal structure of a transparent specimen,

this technique does not allow for the direct investigation of

surfaces of solids such as lunar samples. The alternative is

the application of the replica technique[58]. The direct

observation of a surface by means of a replica permits a resolving

power up to 5 nm[59].

3.1.2 Scanning electron microscopy (SEM)

Scanning electron microscopy is much more straighforward

than TEM, and is suitable for track density less than 10^9 tracks/cm^2[60].

The samples must first be etched (see Section 3.4) to produce

surface details and then coated with a conducting layer, usually

gold.

In a scanning electron microscope a primary electron beam,

emitted from a heated tungsten filament, is focused into a fine

electron probe on the specimen and made to scan and raster – similar

to television techniques – on the surface by a detection system.

Electrons liberated from the specimen by the focused primary beam

are detected by a photomultiplier tube with a scintillator mounted

on top.

The photomultiplier output signal is used to modulate the brightness of the electron beam in a cathode-ray tube, which is scanned in synchronism with the electron probe. The resolution depends upon the diameter of the electron probe, the accelerating voltage, the detector system and the type of specimen.

The electron microscopy techniques for track observation seem to be complicated and from the point of view of the majority of practical applications, cannot be taken into account. This is because the procedure is tedious, requiring the preparation of extremely thin samples, ꜰᴏʀ ᴛᴇᴍ and can be used only with great difficulty for most solids. Even with suitable solids the high magnification needed to see the tracks, requires that the track densities be high in order for studies to be possible. Finally only a small portion of the total range of most heavy particles of interest can be examined at one time in the electron microscope. This technique is, however, unique from the point of view of the investigation of the track's structure and early stage of track revealing.

3.2   The decoration method

Another possibility of revealing tracks can be provided by the so-called decoration, i.e. the formation of a new phase layer of material along the damaged region which is distinguishable in an optical manner from the surrounding material. This is, of course, the classical method of track development in photographic emulsions. So far this has been achieved in the case of silver chloride single crystals[61] and a kind of glass doped with silver[26].

The crystal of a volume of about 1 cm^3 is exposed after irradiation, to a pulsed electric field of 4kV/cm usually and - at one surface ÷ to a simultaneous pulse of ultraviolet light with 10^9 photons per pulse at a repetition rate of about 1000/sec. The conductivity electrons (and holes) produced by absorption of the photons in a surface layer of some microns, are swept through the crystal by the electric field. Electrons trapped at defects, for instance along the path of the particle, initiate the migration of Ag^+ ions, thus producing the decoration of the track as a chain of silverspots and of other disturbed structure of the crystals, such as dislocation lines for instance.

3.3   The dyeing method

This technique is an attempt to detect unetched tracks using optical microscope. The method is based on the use of cross linkage copolymerisation of irradiation-damaged polytetra-fluoroethylene, Teflon, with acrylic acid monomer followed by dyeing with the basic dye Rhodamine B which phosphoresces in orange under exposure to blue light.

Maybury and Libby[62] irradiated Teflon plastic films with fission fragments from a 50µCi ^{252}Cf source for 1-2 min. at room temperature. The samples were then inserted into glass tubes containing acrylic acid solution and degassed by freezing and pumping the system several times. After degassing, a grafting reaction with the free radicals in the tracks was allowed to continue in the absence of air at controlled temperatures (23 - 40°C), for varying times (5-30h).

After the grafting, the Teflon samples were washed thoroughly in

deionised water and dyed with a boiling 3% solution of Rhodamine B

for several hours and then washed in a 2% acid soap solution to

remove any unfixed dye. This procedure was apparently successful :

the basic dye fixed itself to the acidic polymer that was attached

to the damaged area of the Teflon. Finally, the samples were

examined with a microscope fitted with an ultraviolet lamp.

Rhodamine B phosphoresces with an orange colour when illuminated

with light at the wavelength of 400 nm. A cut-off filter eliminated

the excess blue light which produced a dark field, and the fission

tracks then appeared as bright lines.

3.4   Chemical etching

A more general method of making visible tracks intersecting

the surface is by selective chemical etching in a suitable reagent;

which is applicable to many solids and permits study of tracks in

the optical microscope, where low densities of tracks and total

ranges can be easily measured.

Although the simple discovery of track etching is widely

attributed to Fleischer, Price and Walker[63], it was Young[28] who

had first introduced chemical etching in the studies of radiation

damage in solids. While the most general applied procedure is

etching in aqueous solutions, in nickle chloride, for example,

exposure to atmosphere is sufficient to cause the track to be etched[55].

The chemical etching effect was first discovered in synthetic

fluor-phlogopite mica. When a pre-thinned mica flake containing

fission fragment tracks was immersed in a suitable reagent, the

volume of material composing the tracks was very selectively attacked.

The reagent etched fine hollow channels along the paths taken by the

fission fragments and left the rest of the mica essentially untouched.

With increasing immersion time the etchant enlarged the channels by

dissolving the surrounding mica at a rate which varied with the type

and temperature of the reagent.

In some minerals, such as muscovite mica, zircon, and diopside,

the rate at which the holes widen is much less rapid than the rate at

which the damaged material is attacked, with the result that the etched

tracks are of constant diameter.   In other materials (glass is a good

example) the rate of attack along the radiation-damaged regions is

greater than, but comparable to, the overall attack rate, so that the

etched tracks are tapered rather than cylindrical.   In extreme cases,

as in the etching of calcite or lithium fluoride, only shallow etch

pits result[64].

The geometry of the etched tracks varies with the substance

being examined, the solvants used, and the time and temperature of

attack.   There are only general guide lines to aid the experimenter

in choosing the proper etching conditions for track development, and

any new substance must still be approached empirically.   The important

thing to realize, however, is that the preferential revelation of tracks

is a very general phenomenon.   In most insulating materials - minerals,

glasses, or polymers - it has been possible to reveal charged-particle

tracks.   Thus almost any insulator can be used as a charged-particle

track detector.

3.5   Track-etch detection techniques

Detection of etched tracks may be achieved either by eye using an optical microscope or automatically by means of automatic counters. Some techniques, however, were developed to enlarge the etched tracks to be visible and counted by the unaided eye. These "semi-automatic" counting techniques which have been replaced by the complicated electronic circuits and digital computers, are the earliest simple and fast methods for detecting tracks in SSTR.

A major inconvenience of the SSTR method, is the necessity of visual counting of tracks, a task which is expensive, tedious and time consuming. This drawback is clearly found in precise measurements where inherent statistical limitations require the observation of large numbers of tracks for adequate precision. Moreover, in precise measurements, elimination of the human element is highly desirable, since it would permit the introduction of quantitative standards for track recognition. Such standards would obviate problems of personal bias in manual track counting, which can otherwise influence experimental data and therefore must be constantly guarded against. Consequently, considerable interest exists in the automation of this task.

Many groups have attacked this problem with varying degrees of success. Ozalid method[65] and light scattering[66] are two of the earliest attempts in semi-automatic track counting. A spark counting method[30, 67-69] applicable with plastic SSTR such as Makrofol or Lexan has been successfully demonstrated but possesses severe

limitations for precision work. Recent investigations take advantage of digital computers in automatic scanners[70-74]. Three commercially available instruments, the Quantimet[20-22, 73] (Inanco, England), the Classimat[70] (Leitz, Germany), and the Leitz-Texture-Analyzing-System (Leitz-T.A.S.)[74] have been used in automatic fission track counting. Some of the most commonly track-etch detection techniques are briefly discussed in the following paragraphs.

3.5.1 Ozalid method

A simple and fast method for detecting holes in polymer films and plastic track detectors has been described by Blok et al[65] of the General Electric Research Centre. It consists of placing the polymer to be examined with a sheet of Ozalid paper and passing the pair through the second (ammonia) stage of a conventional Ozalid machine. The ammonia vapour passes through the holes and darkens the Ozalid paper, clearly revealing the location of etched holes. For example, a particle track that has been etched to form a 50μm diameter hole through a 0.25 mm sheet of plastic will produce as its Ozalid image a dark spot approximately 1 mm in diameter.

3.5.2 Light scattering

Fission track densities in glass and in Lexan polycarbonate resin have been measured using light scattered from the tracks as a measure of the track density[66]. Scattered light was found to be proportional to track density up to the point where tracks begin to

overlap. For the two track detector materials tested, a scattering angle was found at which optimum signal-to-background ratios are obtained.

3.5.3 Spark scanning

There have been several attempts to count the tracks by spark scanning technique.

(a)   Lark[67] has described a technique for detecting fission fragment tracks in thin films of polycarbonate plastic (Makrofol). Very thin films are used so that the chemical etching of radiation damage produces microscopic holes through the film. The films were irradiated with ^{252}Cf fission fragments and etched in NaOH. The etched film was then placed as insulation between the two electrodes, namely copper, of a spark gap. It is convenient to use a smooth flat metal plate in a horizontal position as the grounded electrode, and either a single point or a straight blade edge as the positive electrode. As the film is moved past the gap the occurence of sparks indicates the presence and position of a hole in the film, and the sparks will enlarge the holes from ≃1 μm to 20 μm, a size visible to the unaided eye. The sparks are easily heard as well as seen and the film serves as its own recording device, as the sparks produce a dark deposit around the edge of the hole.

Since the length of fission fragment track in Makrofol is about 20 μm, films up to 15 μm can be easily used provided all the fragments enter normal to the surface. In situations where fission fragements may enter the film at any angle, the detection efficiency

decreases with increasing film thickness. They have obtained

reliable results from films 3.5 μm thick, but because of difficulties

of handling the thinnest films, they have chosen 8 μm films for routine

use as a fission detector.

It was found that the gap should be 15-20 μm and the potential

1500-200 V. These conditions give spark rates of 10-100 per second

in air, depending also upon humidity. When a fairly sharp tip is used,

the effective field is localized to less than 1 mm² and track densities

up to ≈50 per cm² can be measured reliably.

(b)   A spark counting system has been developed by Congel et al[68]
for counting etched holes in thin dielectric plastics. They exposed

Kimfol 10 μm thick to fission fragments resulting from slow neutrons

capture by ^{235}U. The etched film is placed between two metalic conductors.

One of the conductors must consist of an insulating material with a thin

metalic coating on one side. For this study, aluminium coated myler

was chosen. When a voltage is placed between the two conductors spark

discharges will occur at the site of the etched holes. Heat from the

spark will cause the aluminium to be evaporated at the point of discharge,

thus exposing the insulator and preventing additional discharges through

the same hole. Discharges continue until all holes are counted at

which time no more discharges can take place. The number of sparks

which corresponds to the number of etched holes is determined by an

electronic network and a single channel analyzer.

The efficiency of the system is about 80% and it is useful in

investigations such as environmental studies where the track densities

less than 100 tracks/cm² are encountered and accuracies of 10% are acceptable.

(c)   An improved method for locating charged particle tracks in thin plastic sheets was developed by Geisler and Phillips[69] in Washington University.   They employed short high voltage pulses rather than the steady voltages used previously.   This method is applicable to plastic sheets of larger area and of thickness down to 3.5 μm.   The background is low and the efficiency greater than 85%.

(d)   Becker and Razek[30] have shown that not only fission-fragment and alpha-particle tracks, but also heavy-recoil-particle tracks which are produced by direct fast-neutron interaction with organic foil (or foil cover) constituents can be counted automatically with the spark-counting technique.   They used a commercially available thin cellulose-nitrate foils, the strippable red-dyed LR115, 8 μm thick, supplied by Kodak-Pathe Vincennes, France.   They tested numerous radiator cover materials for the foils, including beryllium oxide, graphite, aluminium, polyethylene and Teflon, in order to establish maximum intensity.   The highest sensitivity was consistently observed with Teflon covers for various polymers and neutron energies.   This indicates that it is not the recoil proton tracks that are sparked, but the tracks of heavier recoil particles.   They reported the reproducibility of such studies is limited, more than in fission-fragment or alpha particle detection, by small fluctuations in foil thickness and/or sensitivity, the excretion of red dyestuff particles on etched LR115 foils, and variations of etching conditions.   Day-to-day reproducibilities of about ±10% have been obtained under

carefully controlled conditions.

3.5.4 Automatic scanners

Several efforts to build automatic scanners have been reported so far. Most of these were specially built for nuclear track counting in emulsions.

An automatic scanning system for solid-state fission-track recorders was developed by Oosterkamp and Schaar[71] at Karlsruhe. They used a television camera as a scanning device and a PDP-124 computer to analyze the data.

Gold and Cohn[72] developed an optical microscope having computer control of specimen motion in three dimensions, via stepping motors, and used for automatic scanning of solid-state nuclear track recorders.   This computer-controlled microscope, which is called the automatic track scanner (ATS), affords the capability of full on-line computer control, thereby lending to improved precision, reliability and accuracy.   The ATS system is the first to possess automatic focusing capability.

Image analysing computers make automatic assessments of selected features in photographs or in electron, X-ray or optical images, by recognising and isolating such features and then counting, measuring and classifying them.   They do this much more quickly, accurately and reproducibly, than human operators and they have made valuable but previously impossible tasks in research and quality control both feasible and economic.   Imanco[73] pioneered the development of image analysing computers with introduction of the

Quantimet A in 1963. The Quantimet B followed two years later.

In 1970, the Quantimet 720 series was introduced. The Quantimet 720

is an advanced series of image analysis systems, each built on a

modular design allowing the easy addition of many extra modules to

an entirely compatible basic system. The 720 offers a choice

between radically new, low noise, high uniformity image scanners

designed specifically for precision image analysis. It divides an

image into the maximum number of discrete picture points so giving

optimal sampling and statistical accuracy. Fig. 3.1 is a simplified

block diagram of the 720.

The Leitz-Texture-Analysing-System (Leitz-T.A.S.)[74] is the

latest product of the extraordinary fast improvements and developments

of the instruments for quantitative image analysis during the last

few years. When the first electronic image analyzers appeared on

the market, all the classical procedures of the linear analysis were

used, and only automatically controlled. With the Leitz-Texture-

Analysing-System (Leitz-T.A.S.) a new generation of image analyzers

has been created, that make it possible to analyse images with two

dimensional scanning elements. The basis is an analysing concept

which takes into account the practical wotk as well as the theoretical

logical foundations and delivers new analytical procedures (for

instance the generalization of the size concept.)
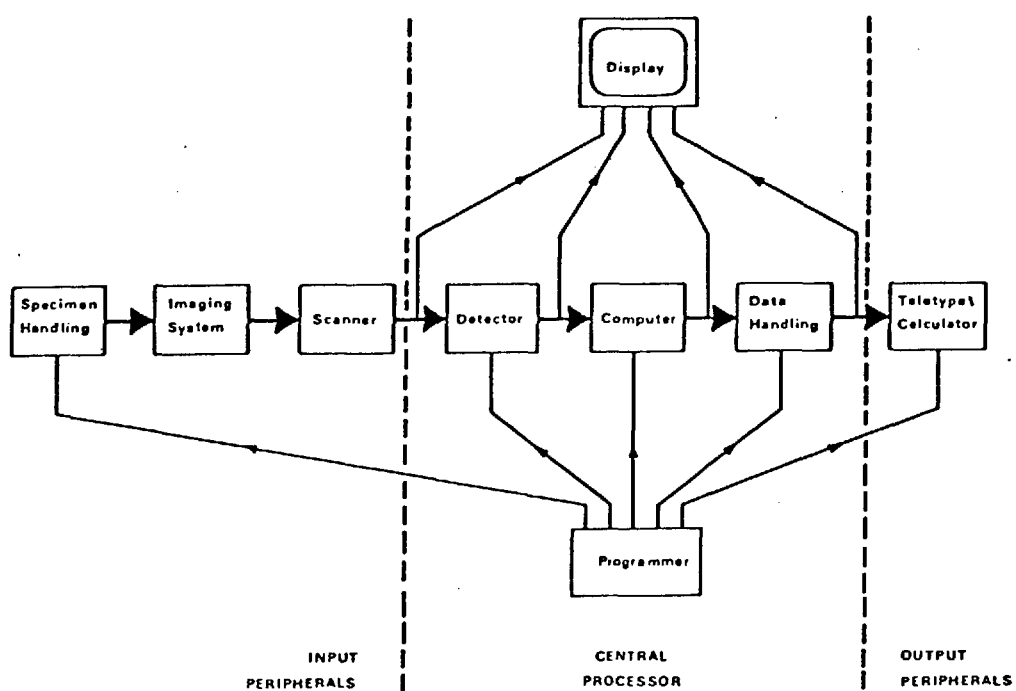
Fig. 3.1   Block diagram of Quantimet 720

4. EXPERIMENTAL RESULTS OF TRACK DETECTION

In order to obtain track recorders to meet all requirements for track counting, and to establish an accurate and reproducible fission track counting technique, a set of experiments was carried out on the NISUS facility. The aim of the measurements was to provide SSTR with satisfactory track density, low background, high contrast, and uniform features. In these experiments the track recorders were irradiated in intimate contact with the fissile materials for different irradiation times and reactor powers to give the track densities from about 1.3×10^3 track/cm^2 to about 6.6×10^4 track/cm^2. The lower limit arises since the track density becomes too low for accurate measurements, while the upper limit comes from the practical limit of the overlapping problem. This wide range of track densities was chosen to permit the study of the performance and accuracy of the Quantimet 720 in comparison with eye counting, as well as to choose the right irradiation and etching conditions to get reproducible results.

4.1 Description of the NISUS facility

The original NISUS assembly (Ref. No. NISUS 1) consists of two concentric spherical shells, the outer driver shell of natural uranium and the inner shell of boron carbide (B_4C). The shells are supported in the centre of a spherical cavity of 50 cm hollowed out of a 60 cm cube of graphite. The shells' support is manufactured from aluminium and its height can be adjusted using aluminium spacers.

The graphite block is mounted in an extension of a thermal column of the reactor. The assembly can be effectively shut off from the reactor by a remote controlled cadmium within a closed/open operation time of 46 seconds. The shutter, of total area 122 x 122 cm, has two parts moveable apart horizontally. Each part is constructed of 1 mm thick cadmium sheet sandwiched between two 3 mm sheets of aluminium. The neutron detectors are mounted on a graphite plug and can be loaded into the central cavity via an access hole of diameter 85.5 mm on the central axis of the thermal column extension. The composite plug consists of a removable piece of boron carbide shell 17 mm thick, connected to a uranium part of 80 mm long. The diameter of the boron carbide and the uranium parts is 45.75 mm matching the diameter of a hole in the shells to within ± .05 mm, so that when the plug is fully loaded, the NISUS sphere is complete. The uranium part of the plug is connected to a 990 mm long graphite plug by an aluminium stem. Figure 4.1A shows the cross-sectional side of the NISUS facility with the graphite plug in the full "in" position and the SSTR foil holder secured to its extremity.

The construction of the NISUS assembly allows the installation of concentric spherical shells of different thicknesses so that it is possible to generate spectra with a different degree of hardness. There are available in total eight natural uranium, two boron carbide, and one iron shell which can be accommodated in the assembly in different combinations. The details of these shells are given in Table 4.1. The measurements reported here all carried out in the so-called NISUS 1b assembly (Table 4.2).

Key

1. Movable Graphite Plug
2. Graphite Stack
3. Spherical Cavity Block
4. Outer Cavity
5. Inner Cavity
6. Specimen Holder for
   Solid-State Track Recorder
7. Aluminium Support
8. Natural Uranium Shell
9. Boron Carbide Shell
10. Cadmium Shutter
11. Graphite Thermal Column
    Extension

Scale: ~ 1/19
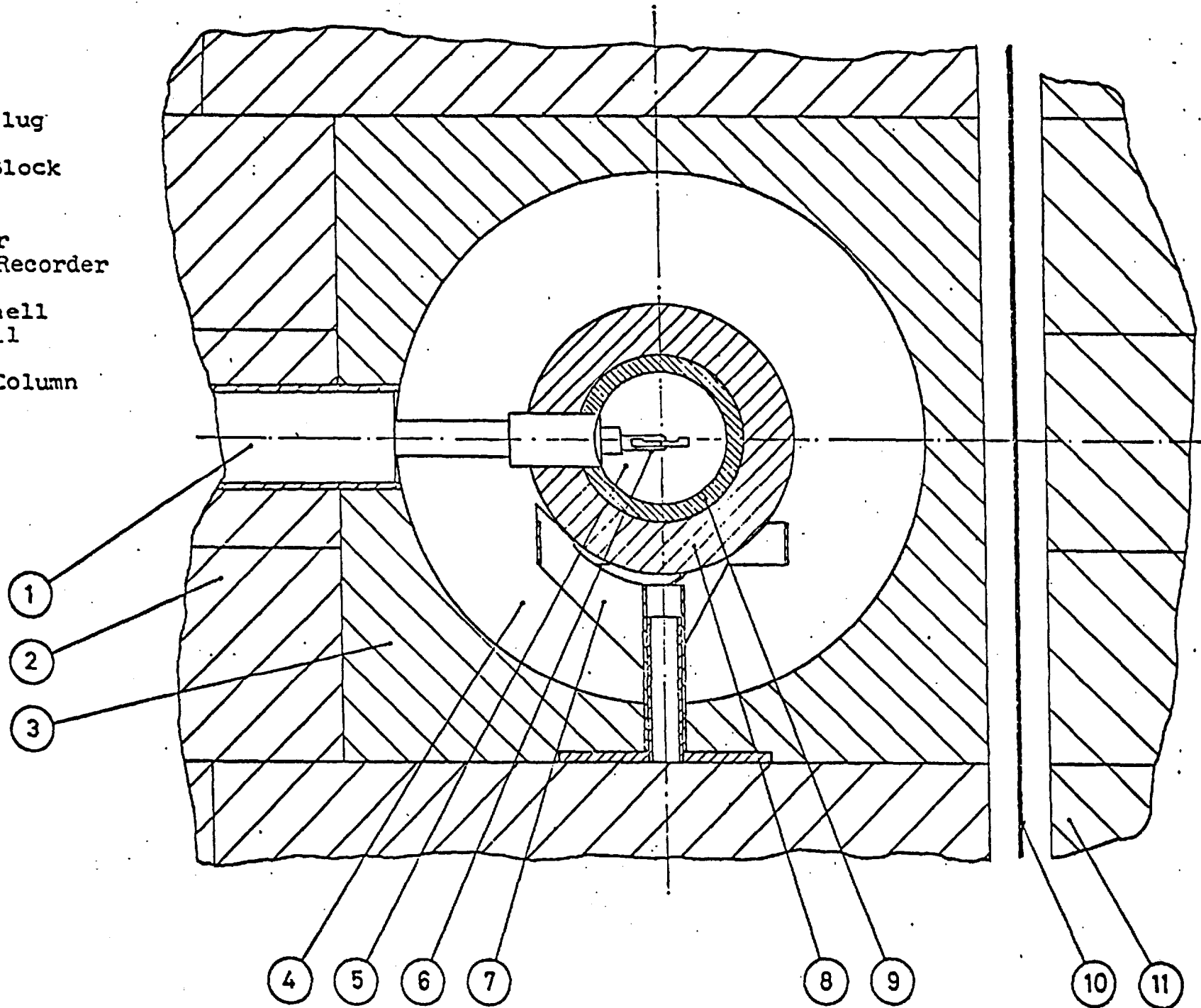
Fig. 4.1 A Cross sectional side of the NISUS facility.

TABLE 4.1

Details of the NISUS shells

Material	Ref. No.	I.D. (mm)	O.D. (mm)	Hole diameter (mm)	Comment
Nat. U	1	116.84	157.48	45.75	AWRE shell
"	2	157.48	198.12		"
"	3	198.12	238.76		"
"	4	238.76	254.0		"
"	5	254.0	269.24		"
"	6	269.24	284.48		"
"	7	284.48	299.72		"
"	8	299.72	314.96		"
B_4C *	B_4C1	110±0.1 (Nom.)	144±0.1 (Nom.)	17 (Nom.)	Belgian shell $\rho = 1.499$ gm/cm^3
B_4C *	B_4C2	123.4±0.1 (Nom.)	157.4±0.1 (Nom.)	45.75±0.05 straight hole or 55.0 ±0.05 stepped hole	American shell $\rho = 1.58$ gm/cm^3
Fe	Fe1	127.0	228.6	45.65	AWRE shell

Note: *Dimensions given for 1 mm Al cladding

TABLE 4.2

NISUS assemblies

Ref. No.	Natural uranium shells	Natural uranium thickness mm	B$_4$C shells	Fe shells
NISUS 1	2,3,4	48.26	B$_4$C1	-
NISUS 1a	2,3,4	48.26	-	-
NISUS 1b	2,3,4	48.26	B$_4$C2	-
NISUS 2a	5,6	15.24	-	-
NISUS 3a	5,6	15.24	-	Fe1

4.2   Description of the fissionable sources

In the present experiments two types of fissionable sources were used: the NISUS natural uranium shells (thick source) or uranium deposits (thin source).

(a)   The NISUS uranium shells are in the centre of the graphite cavity on the CONSORT thermal column extension.   The access to the shells is only possible by removing the heavy biological concrete sheilds and the top half of the graphite cavity block.   This necessitates the reactor to be shut down for almost a whole day and consequently preventing other experiments from being carried out on the reactor.   The alternative was found to make use of the uranium part of the NISUS compositeplug.   As   was mentioned earlier, the length of the uranium part is 80 mm, which is 32 mm longer than the uranium shell thickness in the NISUS 1b configuration.   The extended part of the uranium plug enabled the SSTR to be irradiated in contact with a thick natural uranium source, the same as the NISUS shells, without any dismantling.   However, for the fission-rate distribution measurements in the shells, the assembly had to be dismantled.

(b)   The thin fissionable sources were electro-deposits of natural and depleted uranium supplied by AERE, Harwell.   The deposits (23 to 1300 $\mu g/cm^2$ thick) were on   0.1 mm thick aluminium or platinum backings of 42 mm diameter.   The uranium deposits were about 20 mm in diameter and were concentric with the aluminium discs.

4.3   Description of the track recorders

The present work is concerned with the use of SSTR as fission

track recorders. The investigations have been confined to the

use of mica (Polaron, England) and a polycarbonate resin known as

Makrofol (Bayer, Germany). Makrofol (composition $G_6H_{14}O_3$, density

1.2 gm/cc) has been found[12] to have one of the highest efficiencies

among the fission track recorders, and mica (composition $KA\ell_3Si_3O_{10}$

$(OH,F)_2$, density ~ 2.8 gm/cc) has also a high efficiency[12]. Two

types of Makrofol were available : Makrofol E and Makrofol KG with

the thicknesses of 0.40 mm and 0.025 mm respectively. Because of

the flexibility and small thicknesses which are of great importance

in measurements made in contact with the source, Makrofol KG was

chosen in the routine experiments.

4.4   Etching technique

The work on SSTR can be divided into two categories : track

identification studies and count-rate studies. Although quite a lot

of information about the mass, energy or range of the charged particles

can be obtained by measuring the length and diameter of the tracks,

the present work was confined to the use of the count rate studies.

This was because the aim of the project was to use the SSTR as a

tool in fission rate measurements.

Following the second alternative, the simple and more general

method of chemical etching was chosen for track revealing technique.

However, the electron microscopy observation, though a cumbersome

technique, is the only method in track structure studies using particles

of less than 1 MeV/ nucleon.

The chemical etching is based on the principle that the rate

of attack of a chemical reagent to the damaged region (track) of a

track recorder is much greater than that of the bulk material, resulting

in the tracks becoming visible under the optical microscope.   There

are several parameters involving the etching mechanism, and they will

be discussed in the following paragraphs.

4.5   Etching parameters

It is now evident that the registration sensitivity of Solid-

State Track Recorders depends not only on the type of the detector but

also on the etching conditions applied.   For the characterization of

registration sensitivity several parameters should be taken into account.

The criteria of which particles leave revealable tracks by chemical

etching were described in detail in Chapter 2.   The etching parameters

which have important roles in the geometry of the etched tracks are:

the type of etchant, concentration, etching time and temperature, and

agitation during etching process.

4.5.1   Etching solutions

The type of the solvent being used as etchant depends on the

type of the track recorder being examined.   Even with one make of

SSTR different etching solutions result in appreciable different etching

rates for a given etching time and temperature.   The alkaline solutions

(e.g. NaOH) and acids (e.g. HF) are normally used as etchants for minerals

and glasses.   While for plastics, alcoholic alkaline solutions (e.g.

NaOH + C_2H_5OH), oxydyzing agents (e.g. $KMnO_4$), alkaline solutions, and

sometimes a mixture of all is recommended. A comprehensive list of

etching conditions is given in Appendix B.

In our experiments, the alcoholic alkaline solution was used.

It was found that the ethylic alcohol has a favourable effect upon

etching, which is probably due to modification of the parameters of

the crystal-lattice and the polymer radicals. The etching solution

was a mixture of 15% KOH and 40% C_2H_5OH diluted with 45% distilled[33]

water. The investigations showed that here the etching times are

much shorter than the etching in an aqueous alkaline solution. On

the other hand the tracks are more uniform and in better contrast than

those etched in a KOH solution. This is particularly desirable for

automatic track counting by the Quantimet 720, where several problems

arise from non-uniformity and poor contrast (see Section 4.10). In

agreement with Pretre[75] et al., it was found that the etching rate of

the potassium hydroxide is greater than that of the sodium hydroxide.

4.5.2   Etchant concentrations

The etching rate is a function of the solution concentration

and it has been shown[76] that it tends to an asymptotic value. In

the case of potassium hydroxide the etching rate is almost constant

above the concentration of about 30%. In some of our experiments which

were carried out with alkaline solutions, the concentration of 6.25 N KOH

(35%) was chosen. The concentration of the alkaline solutions was

determined using titration method. First a solution of potassium

hydroxide with a concentration greater than the desired one was made.

Then a given volume V_1 of this solution with unknown concentration N_1

was coloured by a few drops of a chemical indicator, e.g. Methyl

Orange. The contents of a standard hydrochloric acid ampoule diluted

to 0.5 litre with distilled water yielded the solutiong with exact

concentration of 2 normal, i.e. $N_2 = 2$. Then a 50 ml burette was

filled with this solution. The diluted hydrochloric acid was added

drop by drop to the KOH solution to turn its colour. If the volume

of the added acid is V_2, then the concentration of the KOH solution,

N_1, can be determined from the expression:

$$V_1 N_1 = V_2 N_2 \qquad\qquad (4.1)$$

Having obtained N_1, the volume of the distilled water V, which should

be added to the initial KOH solution V', to get the concentration in

question can be calculated from:

$$V'N_1 = N(V' + V) \qquad\qquad (4.2)$$

This is found to be one of the most accurate mthods of making solution

with certain concentration.

4.5.3 Saturated etchant effect

Although the details of etching mechanism are not fully known,

the effect of saturated etchant was studied in the etching rate for

given etching time and temperature. Some dummy SSTR were etched to

get an etched products saturated solutions. In agreement with Jowitt [77]

it was found that the effect of saturated etchant for alkaline solutions is to speed up the etching rate. Although this is contradictory with the explanation that the removing of the etched products layer makes the attack of the chemical reagent to the SSTR easier and consequently speeds up the etching rate (Section 4.6). The author observed that in the case of alcoholic alkaline solutions, the etching rate slows down by using saturated etchant. No satisfactory explanation was found for this effect which is obviously due to the behaviour of the alcohol in the etching solution.

4.5.4   Etching time and temperature

The etching time depends strongly on temperature, varying from about 20 minutes at $80^{o}C$ to about 24 hours at $20^{o}C$. Although at high temperature the surface of the Makrofol SSTR is likely to be damaged, it was found that at $60^{o}C$ no serious surface damage occurs. The temperature of the etching solution was controlled to $\pm 1^{o}C$. After several experiments, etching time of 30 minutes was found to produce satisfactory results, where the tracks were clearly visible, but not large enough to cause overlap problems.

4.6   Agitation effect

It is quite clear that in the developing of the ordinary photography films, agitation speeds up the appearance of the features by keeping all the time a fresh layer of the developer in contact with the film surface. This effect is also seen in chemical etching. During the etching process an etched products layer is formed on the

surface of the detector, reducing the attack effect of the etchant, and thus decreasing the etching rate. So far several types of agitations have been investigated which may be classified in the four broad modes : mechanical, interruption, ultrasonic and electrochemical.

4.6.1 Mechanical agitation

In this mode a mechanical stirrer was used to keep the solution in continuous motion. A small beaker containing the SSTR and etching solution was placed on the hot plate of a magnetic stirrer, and the temperature was fixed at $50 \pm 1^{\circ}C$ using a thermometer. Then, a magnetic follower encased in PTFE immersed in the beaker and the speed adjusted about 400 rev/min. (There are 10 speeds to 1325 rev/min.) Although the effect of this type of agitation was found to be very great, the procedure was not satisfactory because the plastic films were damaged due to striking either to the beaker wall or to the magnetic rod. The procedure was improved by using a test tube instead of the beaker and floating it in a conical flask of water. The magnetic follower was placed inside the flask so that its rotation could rotate the water and consequently the test tube in a continuous motion. This motion was more uniform with less damage to the SSTR than the previous procedure.

It was found that the track diameter being etched by this type of agitation are about twice those using no agitation for a given etching time and temperature. This mode of agitation was not adopted in the routine etching process due to inconsistency in the speed and fluctuation in the temperature.

A method of mechanical agitation is being used by Jowitt[77] at Winfrith. In this method the SSTR films are held vertically between two parallel and horizontal discs. The discs are connected to a vertical rod, and the whole system is immersed in the etching solution. The rod is attached to the shaft of a motor. The motor provides a motion in the vertical direction so that the rod can go up and come down with a given frequency. The discs and the rod are made of PTFE to be resistant to attack by the etchant. The etching solution and conditions are : 6N KOH at 25°C for 18 hours. It is thought that this mode of agitation is more consistent and reproducible over several sets of samples, particularly that 9 films can be etched simultaneously.

Khan[76] has reported a continuous mechanical brushing of the detector during the etching process with the absolutely "etched-product-layer-free" results. This method is not only cumbersome for long etching processes, but somehow impracticle if the etching process needed to be carried out at above room temperature. At high temperatures it is necessary to use a lid for the container of the etching solution to keep the concentration invaried during the process due to evaporation.

4.6.2   Interrupted mode

In this method a number of small interruptions are carried out during the etching process[76]. During one small interruption, the detector is taken out, washed, cleaned and then again immersed in the etchant. It is felt that this method may not be applied for the experiments in which the data should be obtained from a set of samples.

This is because this type of interruption cannot be exactly identical over a wide range of samples.

4.6.3 Ultrasonic

It is thought that the best consistent method may be achieved by using an ultrasonic agitation which provides rapid and efficient cleaning of the surfaces by means of cavitation caused by bombardment with ultrasonically agitated solvent molecules. On the other hand the effect of agitation frequency in etching process can be examined and a threshold frequency which makes it possible the "etch-product-layer" to be removed may be determined.

A commercially available ultrasonic cleaning tank (Dawe Type No. 625-4126/12) was used to investigate the ultrasonic agitation effect. The most obvious advantage of the ultrasonic agitation is to increase the etching rate by removing the etched-product-layer from the surface of the film and thus reducing the etching time. It was estimated that the etching rate is increased by a factor of about 2 both for Makrofol at 60°C and Mica at $\simeq 40^{\circ}$C. Both SSTR were dissolved in the etchant for 15 min. etching time. The following disadvantages of this type of the ultrasonic cleaner were observed:

(1)   The tank was too big (capacity $\simeq$ 24 litres) thus it would take a long time to reach a preset constant temperature (about 3 hours for 60°C).

(2)   Fluctuations in temperature were large, $\simeq \pm 3^{\circ}$C.

(3)   When the tank heating system was OFF, i.e. the liquid at room temperature, ultrasonic vibrations increased the temperature, probably

due to the strong friction and kinetics of the molecules, from 18.5°C

(room temperature) to 43°C in about 3 hours, making the term of the

"room temperature" meaningless.   Some typical variations are:

Time (min.)	Temperature ($^{\circ}$C)
0	18.3
50	25.9
102	34.0
158	43.0

(4)   Fixed frequency, 24.5 KHz, did not allow more investigations

at lower power.

4.6.4   Electrochemical etching

Tommasio[78], in 1970, proposed an elegant "electrochemical"

etching method for the amplification of fission fragment and alpha

particle tracks.   This technique has been used by Sohrabi[79] in the

study of polymers as fast neutron personnel dosimetry is more efficient

than conventional etching techniques.   By applying H.V. square of

sinusoidal wave forms through the irradiated insulator, the current

and treeing phenomena produced in the conductive paths increase the

preferential chemical etching of the tracks.   This type of etching

makes it possible to enlarge the damage tracks at will and in some

cases to increase the sensitivity of damage track registration.   By

this etching technique, charged particle tracks are enlarged to such

a size that they can be observed by the unaided eye.

4.6.5 Conclusion

In our experiments, because of the described inconsistencies in the agitation modes, the detectors were not interrupted in any respect, i.e. neither the detector nor the etchant was disturbed during the etching process.

4.7   Etching procedure

The etching apparatus was a 50 ml pyrex beaker containing the etching solution with a polythene lid.   The pyrex was chosen because it is resistant to attack by the solution and it is readily available. There was a small hole in the lid for the thermometer, and it was necessary to lift it off every time a film was put or taken out.   The use of the lid was necessary because of the heat conduction and keeping the concentration of the solution invaried during the process due to evaporation.

The beaker was suspended in a water bath with dimensions 26 x 34 x 49 cm.   The water was flowing through the bath in order to keep the water level at the same height.   The bath water was heated by an electric coil.   The current of the coil and the subsequent heat could be adjusted by means of a variac.   The scale of the variac was graduated in degrees centigrade, but since it was not accurate a thermometer was used inside the beaker solution to record the temperature. The temperature was controlled by means of a thermostat.   The accuracy of the regulator was so good that the temperature recorded did not very more than $\pm 1^{\circ}C$.   A perspex lid of 34 x 41 cm with six holes was made for the water bath.   The holes of 5 cm diameter each were to hold the

beakers, so that six SSTR could be etched simultaneously under the exact identical conditions, in six different beakers.

Before starting the etching procedure the bath water was running for four hours to reach the constant temperature $60^{\circ}C$ and the stabilized conditions. The temperature was checked and the variac re-adjusted if necessary from time to time. After placing the beaker of the etchant solution in the water bath, it was also necessary to wait about half an hour to reach the temperature of the solution to $60^{\circ}C$. When the etching solution was potassium hydroxide, the concentration was checked periodically by the titration method and it was found that the change in concentration is within the errors.

Since only half of the 50 ml capacity of the pyrex beaker was filled up with the etchant, it was quite convenient to renew the solution after each etching process. This meant that the solution was considerably clean, and also that the concentration of the solution did not vary from time to time due to evaporation.

When the films had been etched they were removed from the etching bath and placed in a stop bath of diluted acetic acid 1% for a few minutes to prevent further etching. Afterwards the films were washed in distilled water and then dried in a dessicator, and then mounted on glass slides under cover slips with sellotape. Table 4.3 shows the summary of the etching parameters used in the etching process.

TABLE 4.3

Summary of the etching parameters

Etching parameter	Description
Etchant	A = Alcoholic alkaline solution B = Potassium hydroxide
Concentration	A = 15% KOH + 40% C_2H_5OH + 45% H_2O B = KOH 6.25N
Time	30 minutes
Temperature	$60^{\circ}C$
Saturation	Nil
Agitation	Nil

4.8   Optical techniques for track observation

The chemical etch development of the particle damage trails

produces permanent, three dimensional cavities or tracks.   The

dimensions of tracks may vary from a fraction of micron to several

hundred microns depending upon the etching conditions as well as the

track recorder material.   The simplest and most convenient method for

observation and measurement of tracks requires the use of an optical

microscope.   The precision with which track parameters of interest,

such as track lengths, or surface openings, may be measured depends

upon the optical resolution attainable as well as the ability to perform

the actual measurements.

The microscopy of etched tracks has a number of unusual aspects

that are generally not encountered in ordinary microscopy.   The problem

centres on the fact that usually the etched tracks are in the form of

transparent cavities rather than opaque objects such as silver grains

in the processed nuclear emulsions[51].   Some of the major difficulties

encountered are as follows:

(1)   The difference in the index of refraction of the track cavity

and the bulk material is small.

(2)   Inhomogenities and inclusions present in most SSTR cause a

variation in the index of refraction of the bulk material.

(3)   The heavily pitted surfaces of the etched SSTR degrade the image.

(4)   Track specimens may require objectives and condensers with larger

working distances than available.

(5)   Track cavities tend to fill up with liquids when immersion

objectives are used, thus reducing track image contrast.

(6)   Track dimensions may be small, requiring the use of high numerical aperture (N.A.) objective condenser combinations.
Most of these difficulties, in general, can be overcome by the use of either one or a combination of optical techniques these are described below.

4.8.1   Bright-field, transmitted light illumination

(a)   Dry objectives:

For many measurements, track observations, and rapid scanning of the specimens at low magnifications, dry objectives are easy and convenient to use.   Dry lenses, even at moderate magnifying power, usually have long working distances.   This permits the observation of steeply dipping, long tracks if tilting of the specimen is required. The photomicrographs of tracks shown in Figure 4.1 were obtained using the Leitz NPL x 40, N.A. 0.65 objective having a working distance of 0.15 mm.   The photomicrographs shown in Figure 4.2 A and B were also taken using this lens.   In Figure 4.2A is shown the usual appearance of a dry track;   Figure 4.2B shows the same track when the specimen is covered with a thin layer of ethyle alcohol.   This technique can be used for reviewing and photomicrography of tracks in specimens with badly pitted surfaces.

The main limitation of the dry objectives is the lack of high resolution.   While dry objectives are available with N.A.'s of up to 0.95, most of the lenses with N.A.'s over about 0.60 require the use of an exact thickness cover glass.   The requirement decreases their utility *Considerably*.

(b)   Immersion objectives:

There are in general two types of immersion objectives, oil or water.   The immersion objectives are characteristically of higher N.A. (up to about 1.40) than the dry lenses.   Consequently, they are capable of higher resolution.   The use of these objectives requires procedures that are considerably more exacting than those necessary with the dry lenses.   To achieve the full resolution of the objectives with N.A.'s of over 1.00 requires the use of an oil immersion condenser. However, the use of an oil immersion objective, without oiling the condenser, will still give greater resolution than that possible with the dry lenses.   It is possible to overcome the problem of oil seepage into track cavities by covering the specimen with a transparent film such as cover-slip or a thin plastic film.   However, it is essential to eliminate the air gap between the cover-slip and the specimen. Otherwise a numerical aperture greater than 1.00 cannot be achieved.

A decided advantage of these objectives over the dry lenses with high magnification is the generally longer working distance.   In fact, one 100X objective (Leitz), developed for use with nuclear emulsions, has a working distance of up to 650 microns at a N.A. of 1.32.   The depth of field of the high N.A. objectives is very small.   This feature makes the oil immersion objectives less desirable for general scanning than the dry objectives.   However, the immersion objectives are extremely valuable for precise measurements, particularly the measurements of the vertical (Z) dimensions.   In Figure 4.3 is shown a photomicrograph of fission fragment tracks.   The photograph was made using Leitz NPL Plano 100X N.A. 1.30 oil immersion objective in combination with an oiled condenser.
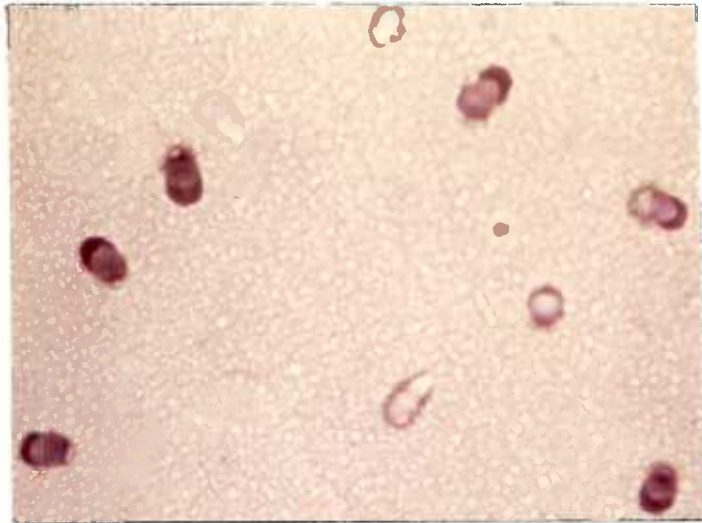
Fig. 4.1   Bright field, transmitted light
            illumination;   400 X

Fig. 4.3   Oil immersion objective in combination
            with an oiled condenser;   1000 X

(A)

(B)
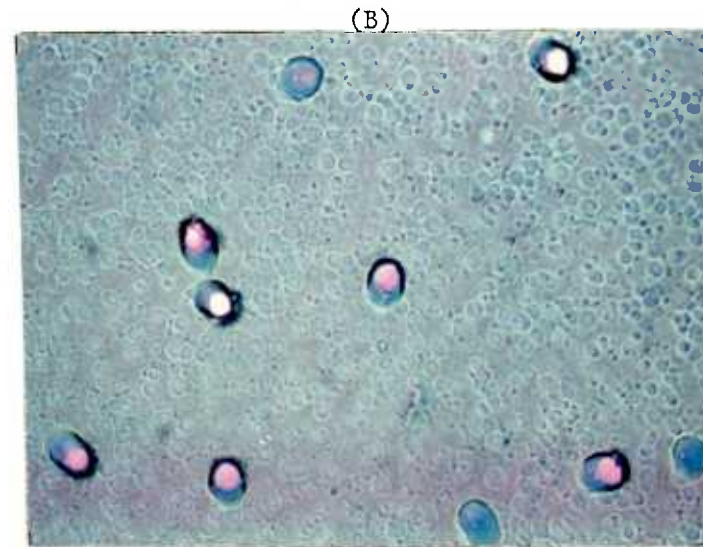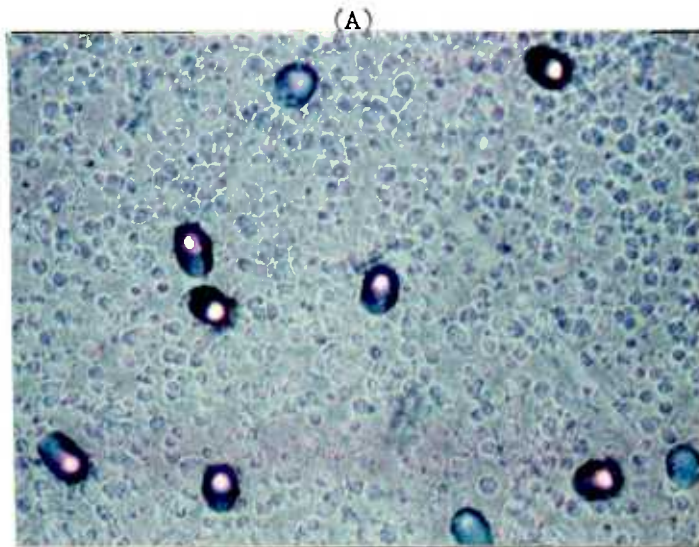
Fig. 4.2   In (A) is shown a specimen with a moderately pitted surface. In (B) is shown the same
            frame when the specimen is covered with a layer of ethyl alcohol.

4.8.2   Phase contrast imcroscopy

For observation of small, low contrast tracks, such as shallow etch pits and recoil particle tracks, phase contrast microscopy can be effectively utilized (see Figures 4.4 A and B).   It is particularly useful for the observation of long narrow tracks where the terminal ends of tracks are invisible under bright field illumination.   However, if the track contrast is adequate for the standard bright field optics, the phase contrast image is less satisfactory.   For the larger tracks with appreciable dip angles, a "halo" surrounds the image (see Figure 4.4B).

4.8.3.   Interference contrast microscopy

The use of an interference contrast equipment has improved the contrast of the transparent structures in comparison to the conventional black-and-white image obtained in the bright-field microscopy.
This new technique shows several advantages for nuclear track counting :
a brilliant relif image of etch pits, a good discrimination of the etch pits to the background, the possibility to improve the contrast by changing the colour of the image.   The kind of colour and the contrast between the etch pits and the surface of the detector may be changed individually and adapted favourably to the corresponding detector surface.   Therefore the interference contrast equipment facilitates direct counting of etch pits in the microscopy and is even advantageous for automatic track counting.

The interference contrast device used in the ORTHOPLAN Leitz[80] microscope is based on the principle of two beam interference.   In contrast to the two beam interference arrangements according to Mach/Zehnder
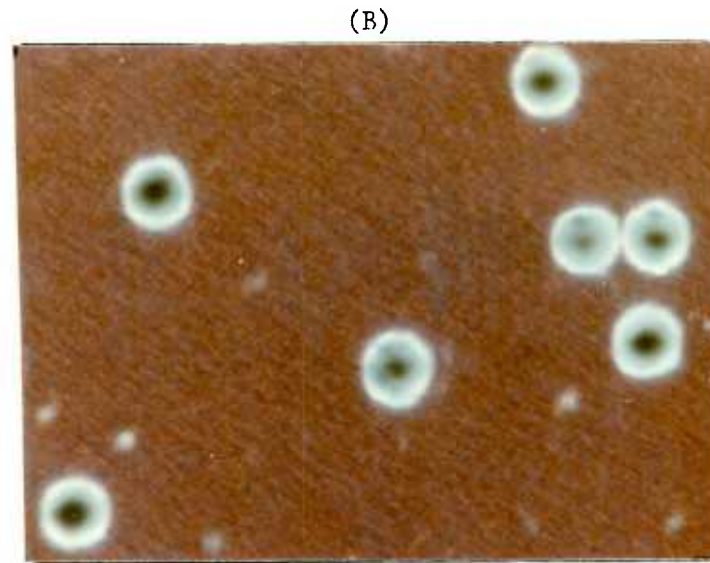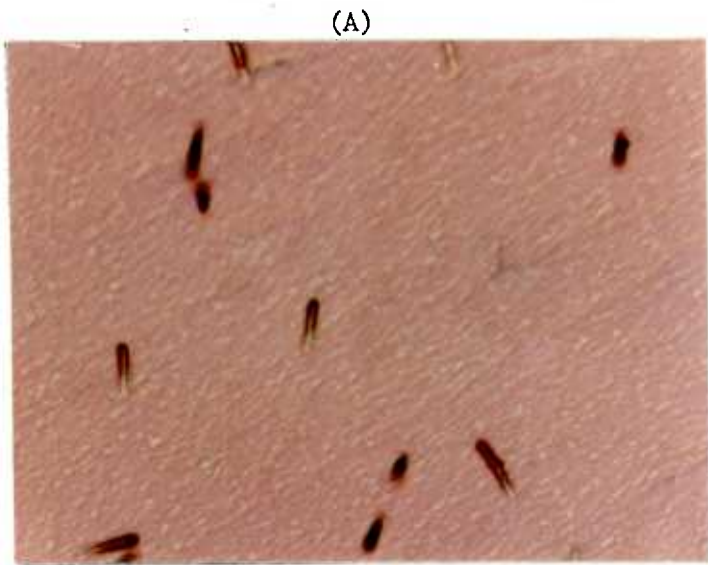
Fig. 4.4   Photomicrographs of fission fragment tracks in Makrofol KG with a phase contrast
objective;   400 X.   (A) small tracks   (B) large tracks with "halo"

and Jamin/Lebedeff, where the lateral separation between sample and

interference beam is larger than or at least the same as the object

size (total image separation), in the present device the beam separation

has been chosen a little smaller than the resolving power of the objectives

used in the microscope (differential image separation).

The spilling and recombination of the beams is carried out with

optical crystal aids, according to the arrangement of Wollaston prisms

in the front and rear focal plane of condenser and object.   Figure 4.5

is a diagrammatic. representation of the optical design of the interference

contrast device.   Here   a linear polarized beam is split by means of

a birefringent quartz prism ("Wollaston" prism, auxiliary prism) in the

focal plane of the condenser into two mutually prependicular polarized

light wave components.   After passing through the transparent object,

both the light wave components are combined in a second prism (main

prism) in the focal plane of the objective and are tuned parallel in an

analyzer so that the light can now interfere.

The $\lambda/4$ plate situated below the Wollaston prism W_1 acts as a

phase - changing compensator in conjunction with the rotating polarizer P.

By means of the λ-plate,which can also be inserted in the beam path, the

brightness and colour differences between the background and the object

can be varied.   The interference contrast depends on the interference

of two mutually perpendicular polarized light waves which suffered a

phase shift in the object as well as in the birefringent quartz prism.

Path differences arise between the ordinary and extraordinary waves in

the following way :

(1)   Light waves undergo path differences by a local variation of the
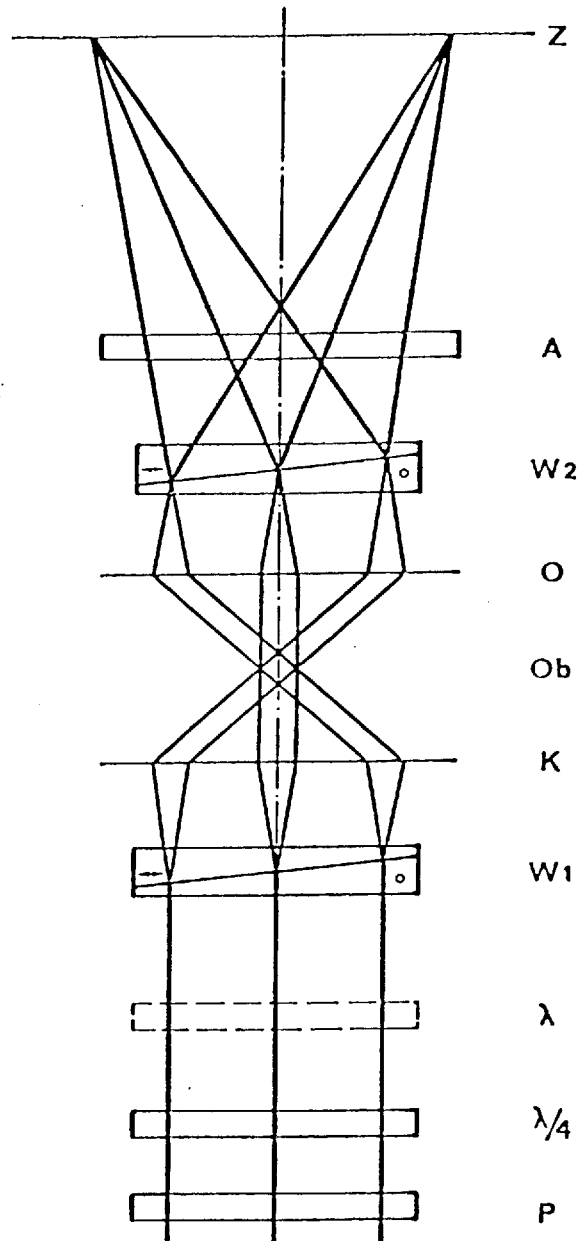
Z	= intermediate image plane	K	= condenser
A	= analyser	W_1	= Wollaston prism
W_2	= Wollaston prism	λ	= λ plate
O	= objective	$\lambda/4$	= $\lambda/4$ plate
Ob	= object plane	P	= polarizer

Fig. 4.5   Optical diagram of the interference contrast device.

thickness or by variations of the optical refraction index at the

profiles and structures of the object.

(2)   Shifting of the main prism from the centre perpendicular

to the direction of the incident light, a path difference arises

from small differences in the refraction index of both the waves

in case that there are optical path differences in front or behind

the central areas of the prism.   Using monochromatic light, this

fact leads to a contrast image of the object (brightness interference),

using white light it leads to a coloured illumination of the object

and the image background (colour interference).   Fig. 4.6 shows the

photomicrographs of fission fragment tracks in Makrofol taken with

colour interference.

4.8.4   Incident light illumination

For track observation in specimens that are very thick ($^>$ 2mm)

or specimens containing inhomogenics or inclusions, the use of the

incident light optics was found to be useful.   Usually the resolution

is somewhat inferior to the transmitted light systems.   Because of

image degradation, observations are restricted to the depth of less

than about 50 microns into the volume of the specimen.   With long

working distances and dip cones available incident light techniques

can be used for observation of tracks in specimens that are still

immersed in the etching solution contained in opaque etching tanks.

Fig. 4.7 shows fission tracks in mica obtained by incident light

illumination.
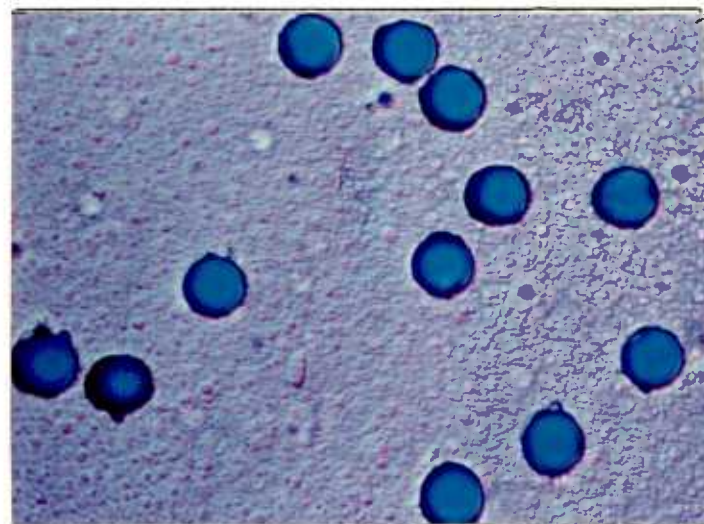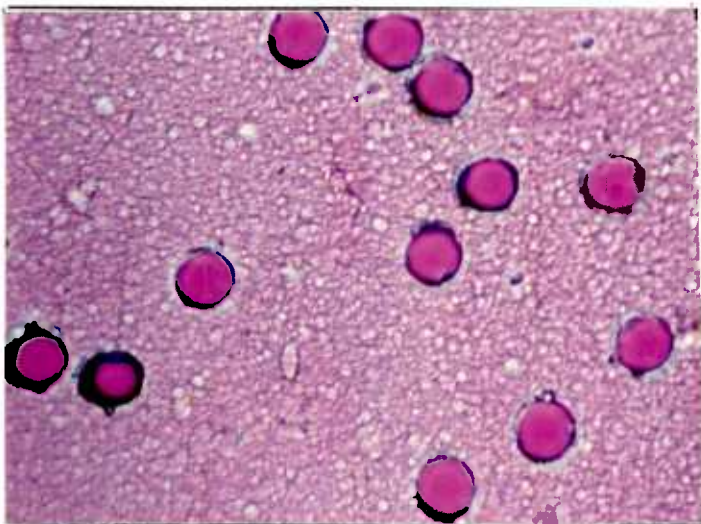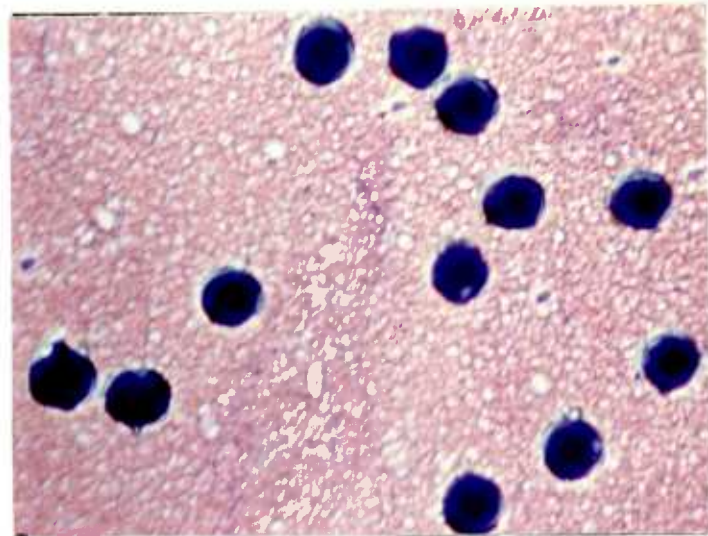
Fig. 4.6   Photomicrographs of fission fragment tracks in Makrofol KG taken with an interference contrast objective;   400 X
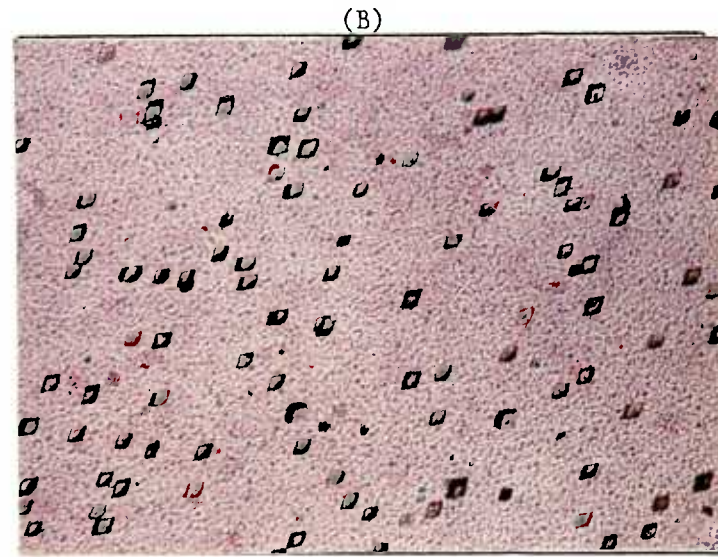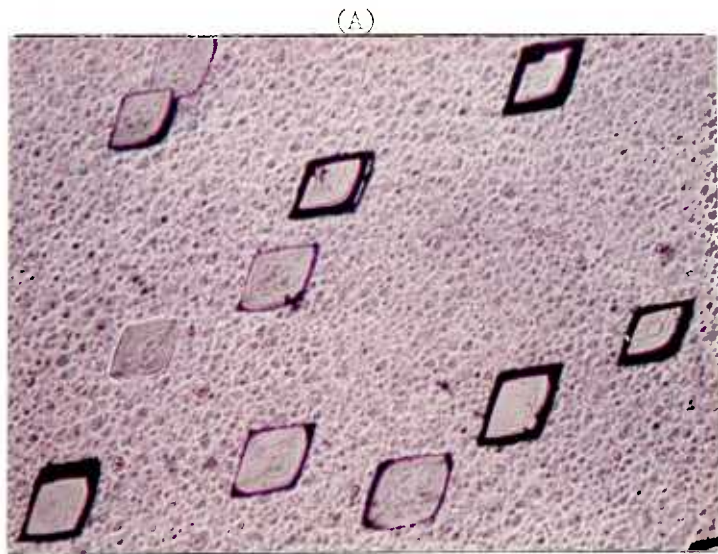
Fig. 4.7   Photomicrographs of fission fragment tracks in mica taken with incident light
illumination;   (A)   200 X   (B)   50 X

4.9   Track counting by eye

In the present work, for track counting by eye, a standard microscopy technique was used. The equipment was a binocular Leitz (Ortholux) microscope with phase and interference contrast and also oil immersion objectives. The system was arranged for use with normal incident and transmitted light. Most of the measurements were made with an overall magnification of 400X (40X objective and 10X ocular) and mainly interference contrast. It was found that track counting under this magnification is more convenient than any other ones, i.e. 100X, 250X and 1000X. Although choosing the right magnification depends on the track size and track density of the specimen, it may be a quite arbitrary factor for the observer. It was found that with magnification 100X, alpha tracks are barely seen while fission tracks, though visible, are too difficult to be counted because of the large number of tracks per field of view. Using magnification 1000X is impractical, not only because of a very low number of tracks per field of view which is obviously time consuming to get good statistics, but because the 100X objective was an oil immersion one which is not a desirable feature for general scanning of the samples.

A graticule consisting of a square divided into 25 smaller squares was incorporated into eyepiece. The calibration was made under the overall magnification of 400X using the Leitz stage micrometer with graduation 1 mm = 100 intervals. The length of the graticule was found to be 0.292 mm by one observer and 0.294 mm by another. This means that a systematic error of $\pm$ 2% is

attributable to the calibration of the graticule area.

The microscope mechanical stage was designed so that the measurement could be made over slides measuring 80 mm x 60 mm. The stage had motions at right angles to one another, each being provided by a micrometer screw with a vernier of 0.1 mm.

In the method of the counting the tracks the frame of the graticule consisting of 25 squares was chosen. Then the microscope stage was moved across a number of parallel chords of the S S T R films in discrete steps and at each position all the tracks bounded by the frame were counted from the top of frame to bottom. Tracks crossing the frame line at the tope and to the left were counted while those to the right and at the bottom were ignored. Thus if the stage is moved a distance at least equal to the width of the frame then no double counting of track will occur and a proper statistical estimate of the track density can be made. Therefore, the whole area of the S S T R was nearly scanned by moving the stage in 0.50 mm steps. The scanning of the whole area exactly may be achieved by moving the stage such that a spot or track on one boundary of the frame in the field of view was moved to the opposite boundary. The effect of any radial variations in the source thickness can be nullified using this method. The focus of the microscope and the colour of the interference contrast, if applicable, were checked and re-adjusted after every field of view. This was necessary because the high magnification entailed a very small depth of focus. Approximately between 1000 and 10000 tracks were counted on each film (depending on track density), in order to obtain good statistical accuracy. When

counting by eye, the background was negligible as one could easily differentiate between tracks and some of the extraneous marks on the film.

4.10   The Quantimet 720

The automatic image analysis has been a subject of much interest for the past 20 years and a number of different systems and instruments have appeared.   Early instruments were applied to biological problems of cell counting and discrimination, but the methods and techniques were soon extended and applied to particle measuring.   The technology advanced rapidly and a number of special instruments were developed.

Image analysis is defined as the science of extracting quantitative data - numerical, geometrical and densitometric - from images.   The images can be of microscopic or macroscopic objects, or photographs, as produced by optical or electron microscopes, or by any other imaging system.   The parameters most frequently required from a sample in materials testing applications are the area of various phases or inclusions expressed as a percentage of total area, the number of preselected type of features per unit area and the size distributions of features.   Image analysing computers can now perform these measurements, and many others with higher accuracy and at far greater speed than a human operator.   Fig. 4. 8 illustrates some of the direct measurements image analysing computers can make, and their results when applied to various shapes.   Manual extraction of these data from microscopic and other images has hitherto been   difficult, and results are prone to
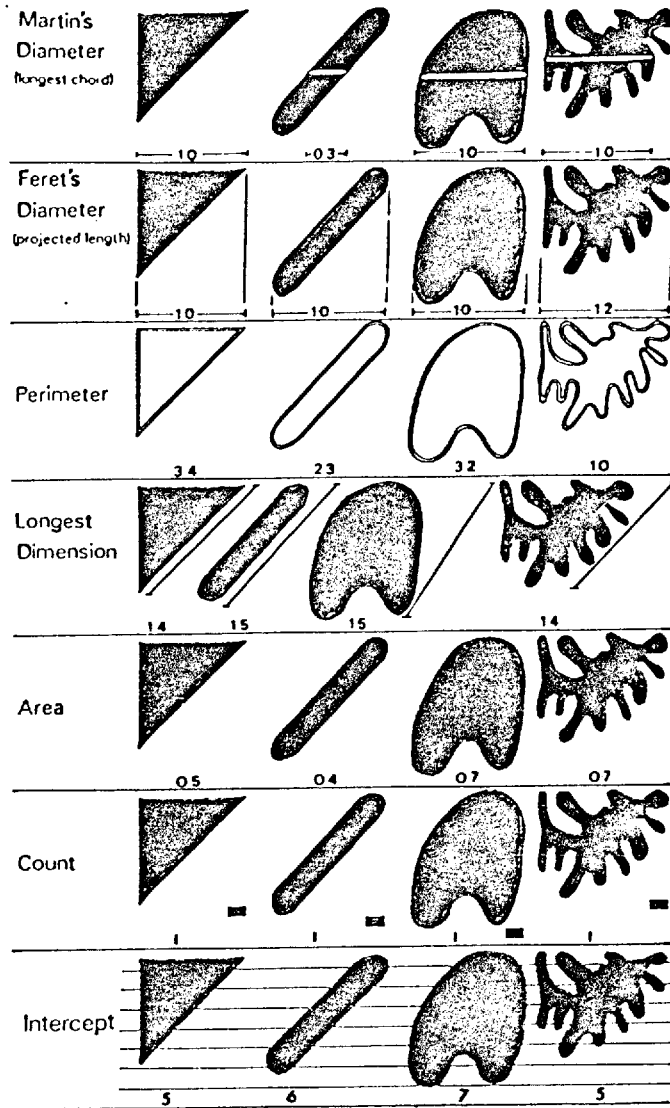
Fig 4.8   Measurement of features.

subjective error, even with trained operators.

There are three main performance criteria for image analysis :

speed in picture points surveyed per second, resolution expressed in

terms of number of picture points measured in the field of view and

discrimination expressed as the number of detectable grey levels.

All the image analyzer instruments produce and process an electrical

analog representation of the image, i.e. a voltage or current which

varies with time, in synchronism with the scanning of the sample and

with a magnitude which is determined by the optical density or

reflectivity of the features in the sample.

The first commercially available television based instrument

was the Quantimet A manufactured by Metals Research Limited[73] in

1963.   It was superseded by the Quantimet B in 1965.   These instruments

were designed with a specific application in mind, the measurement of

non-metalic inclusions and grain size in steel.   The Quantimet B

achieved the first commercial success for an image analysing instrument,

many of them for applications other than those its original design

specification called for, in both materials science and the life sciences.

The recently introduced Quantimet 720 incorporates a number of very

significant technical advances.   It divides the image into a matrix

of 6.5×10^5 discrete picture points and uses a special purpose high

speed digital computer to process the image.   This digitisation, in

addition to providing much greater accuracy than that attainable on

the earlier analog instruments, allows a considerable increase in the

scope of the computation which the instrument can perform, so opening

up applications which were logically too difficult for the earlier

analog technology. Signals from the required features are isolated

from the rest of the image by a process called "detection" which

relies on the application of various grey level criteria. The

simplest criteria are: all parts lighter or darker than a preset

threshold, or that part between two selected grey levels. The

detected signal is then fed into a computer module which makes the

required measurement, for example the number of detected features, their

area or the number above or below a certain size. Fig. 4.9 shows

the block diagram of the Quantimet 720 system.

4.10.1 Performance

The Quantimet 720 was used in conjunction with an optical

microscope with an automatic specimen handling. The X Y traverse

stage of the microscope can be operated manually or automatically,

by means of the Stage X Y control module. The automatic traverse

is not continuous as in a conventional microscope stage, but moves

in discrete steps corresponding to the stepping motor drive increments.

Over the traversed area of 50 x 50 mm the flatness is better than

± 6 microns. The Stage X Y Control Module gives seven different

sizes of step (0.08, 0.16, 0.31, 0.62, 1.2 and 5.0 mm) in the X and

Y directions. The values in X and Y can be set independently. They

are very repeatable and there are no lost steps. Built-in protection

against over travel is provided. A maximum number of 999 X steps may

be called up; the number of Y steps is controlled by the total number

of fields required to be measured. The important disadvantage of the

control module is that the stage, after scanning several fields of view,

a specimen

is imaged by

a Microscope (with optional automatic specimen handling)

or an Epidiascope

or a 35mm Film Projector which projects the image on to

the 720 Vidicon or Plumbicon Image Scanner whose output — or that from a self scan system — is passed to

a 720 Detector which selects the features to be measured and passes pulses from these to

a 720 Amender which allows modification or 'amendment' of detected signals before they are passed on to

a 720 Computer which measures the number, area, and length of the features selected and classifies them by area, length and shape

a 720 Display shows the features being measured. provides special computer displays and presents accumulating digital displays of measured parameters

alternatively or additionally results can be passed to one of the several 720 Data Processing Systems (e.g. teletype, desk top computer, etc). or to a 720 Supervisor module

the entire process can be automatically controlled by a 720 Programmer or can be manually controlled by switches.
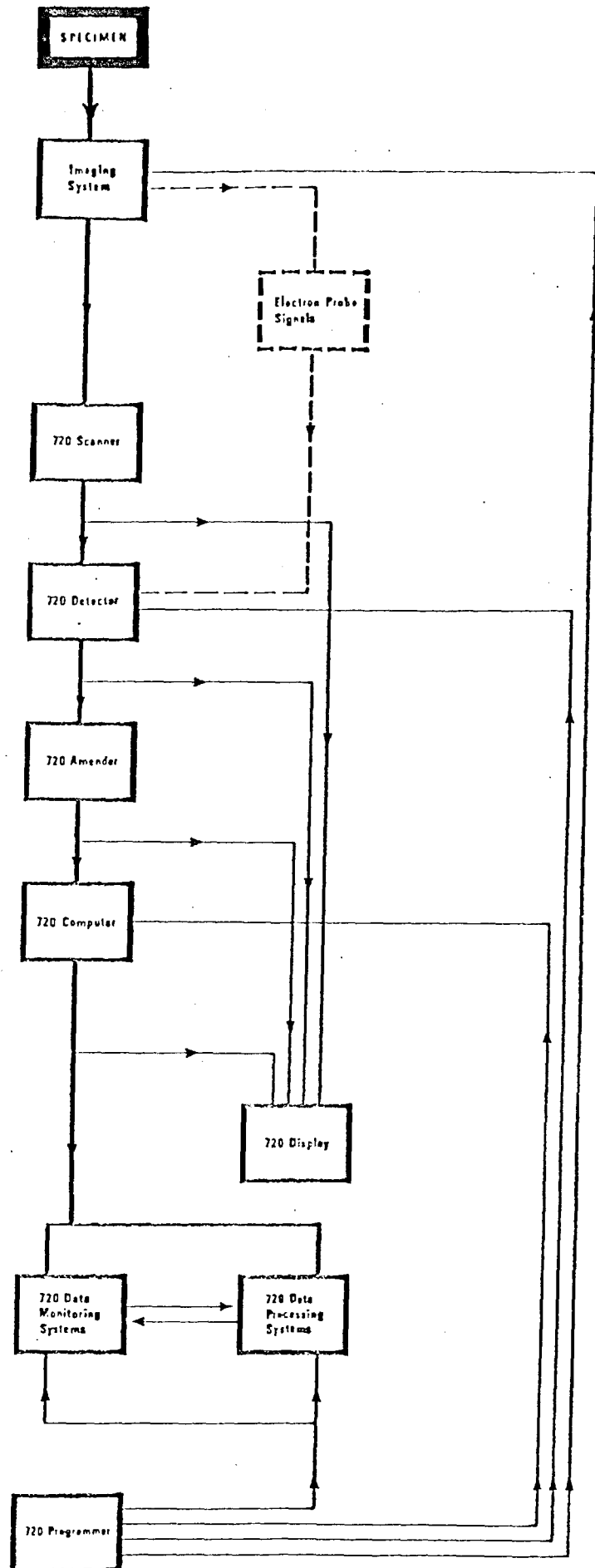
Fig. 4.9   The Quantimet 720 system.

cannot be returned to the origin, thus making impossible the scanning

reproducibility over exactly the same area of the specimen. This is

particularly desirable in the study of the variation of the detected

features (e.g. number of tracks) with the detection parameters (e.g.

detection threshold), where the inherent statistical limitations

require the observation of large numbers of tracks for adequate

precision. It is, however, possible to repeat scanning in X direction

only by setting the Y value to zero. This mode, of course, is

restricted to a few tens of fields of view which may not be sufficient

for the samples with low track density due to poor statistics.

Automatic stepping may be performed either by means of the Step Button

(or Foot Switch in parallel) on the Stage X Y Control Module, or, fully

automated under the control of the Programmer.

The factors affecting the performance of the Quantimet 720

in track counting can be divided into three groups, optical, electronic

and statistical.

(a) Optics

The optical performance depends mainly on the focusing system

and the flatness of specimen. The use of high quality lenses on the

microscope will allow smaller features to be viewed reliably at high

magnification, but this introduces two more limitations. Firstly

the higher the magnification the smaller the depth of focus and there-

fore the more difficult it is to mount the specimen so that it does

not move out of focus as the stage traverses. Frequent re-focusing

slows down the work rate severely. The more important objection to

the use of high magnification is the severely restricted field of view

which means that much more time has to be spent to cover a given area of sample.

The automatic Focus module, which will operate with incident or transmitted light specimens, provides a self focusing facility for use with the Automatic Stage. Although the precision stage is flat to within ± 6 microns over a traverse of 50 mm, it may not always be possible for the operator to level his samples to this accuracy. There may be inherent difficulties with particular samples which may be accentuated when operating with a high magnification. The Automatic Focus takes a few seconds to go through its routine, and the operator can set the module to operate on every field or on every 3rd, 7th or 15th field of view, whichever is most appropriate. It was found that using Automatic Focus does not speed up the scanning rate very much, when the automatic stage movement is controlled by Foot Switch. This semi-automatic operation was necessary because some of the fields of view had to be rejected due to track pileup, or imperfections on the film. So, it was decided to use the manual focus operation instead, although to check every field of view considerably slows down the 720.

(b)   Electronic

The electronic performance depends on the uniformity, sensitivity, noise, and resolution of the scanner. The Quantimet B - the 720's precursor - used a television camera but experience demonstrated that better performance could be achieved by using special purpose scanners[81].

The 720 scan is digitally controlled so that every scan line and even

every picture point is identical in length and precisely positioned.
The scan standard of 720 lines scanned sequentially 10.5 times/sec
has been chosen to give equal resolution in both directions, along
and across, and the best possible compromise between noise, resolution
and speed.

The scanner must have the same sensitivity at all points of
the scan so that a uniformly illuminated image produces a uniform
video output. The new 720 scanners have been specially designed
with this requirement in mind and can achieve as little as six per
cent sensitivity variation over an image containing one half million
picture points - almost the whole image. Unfortunately, the scanner
is not the only source of non-uniformity; it can also arise from the
imaging system, the illumination system, and even the specimen. It
has been reported[81] that the 720 fully automatic correction system
can compensate for all sensitivity and illumination variations,
possibly down to as little as one per cent.

All video systems generate electrical noise in the form of
small random variations in the output signal. To overcome this, one
uses an averaging arrangement designed so that the 720 can be required
to average the results over 16 scans to reduce the random noise
components. Of course, this facility slows the instrument by a factor
of 16, so it is only used when the operator needs all possible accuracy
and repeatability.

The Quantimet 720 has a resolution of 720 vertical lines each
containing 910 resolvable picture elements to give a total resolution
of 655200 picture points. It is important to realise that the term

resolution does not mean absolute resolving power, but simply the number of resolvable picture elements in the scanned image. The absolute resolving power can be altered by changing the magnification up to the limits of light or electron microscopy, but the number of resolvable elements per image is of fundamental importance and a major limit to the applications of any image analysing computer. The scanner resolution should be equal in horizontal and vertical directions, so that if an anisotropic image is presented to the scanner at different orientations, it will be examined with a consistent resolving power so as to detect identically in the different directions, and therefore 720 scanners have been designed to give equal resolution in both directions.

(c)   Statistics

The statistical accuracy is determined by the number of tracks per field of view, which depends on the overall magnification, which in turn depends on the physical size of the specimen. Scanning a large area of the specimen is not only time consuming, but in some cases impractical. It was found that with the objective 10X and the specimen 15 mm diameter the max. possible number of frames that can be scanned is about 550. It is, of course, obvious that some of the fields of view must be rejected because of background contributions due to scratches and other surface imperfections which vary from sample to sample. It was found that for typical samples as many as 100 fields of view may have to be rejected. Track pile-up or overlap determines the maximum track density which can be used and therefore the statistics. In order

to get statistical accuracy better than 2.5%, the average number

of tracks per field of view with objective 10X and the overall

magnification of 423, should not be less than 4, i.e. about 1600

tracks/cm^2, and to avoid excessive overlap not more than 125, i.e.

5 x 10^4 tracks/cm^2.

4.10.2 Calibration

An important new concept introduced in the 720 is the use of

two separate image limiting frames. The first and the largest is

called the "Blank Frame" and the detection process is disabled outside this

rectangle so as to avoid detecting over the edge of the picture. If

(Picture Point)

necessary, it can be set to any size in 1 p.p. digital increment so

as to limit the field of operation to gain better uniformity or perhaps

to fit in with matrix parameters of the specimen. Inside this is the

second smaller frame, the "Live Frame", inside which measurements are

made. This too is fully variable in 1 p.p. increments. The region

between the two frames is called the guard region. Tracks crossing

the guard frame line at the top and to the left are counted while

those to the right and at the bottom are ignored.

According to the figures supplied by the manufacturer (Table 4.4)

and eyepiece 8X.

the field of view is 0.54 x 0.42 mm with objective 10X   To check

this figure, a calibration was made using the Leitz 10 μm stage

micrometer, and it was found that there are 142 picture points per

100 μm, resulting in 0.563 x 0.440 mm field of view which is 9% greater

in area than the manufacturer's figure, probably due to drifting over

a year of operation.

TABLE 4.4

Quantimet microscope calibration transmitted light

Eye-piece Objective	X5		X6.3		X8	
	p.p/100 μ	μ/100 p.p	p.p/100 μ	μ/100 p.p	p.p/100 μ	μ/100 p.p
1	9.87	1013	12.4	806.5	15.9	628.9
2.5	24.5	408.2	30.9	323.6	39	256.4
4	39	256.4	50	200.0	63	158.7
10	92	108.7	116	86.21	148	67.57
25	226	44.25	285	35.09	362	27.62
40	360	27.78	453	22.08	575	17.39

TABLE 4.4 (continued)

Quantimet microscope calibration transmitted light

Field of view (mm)

1	8.11 x 6.33	6.45 x 5.04	5.03 x 3.93
2.5	3.27 x 2.55	2.59 x 2.02	2.06 x 1.62
4	2.06 x 1.62	1.60 x 1.26	1.27 x 1.00
10	0.87 x 0.68	0.69 x 0.54	0.54 x 0.42
25	0.35 x 0.28	0.28 x 0.22	0.22 x 0.17
40	0.22 x 0.17	0.18 x 0.14	0.16 x 0.11

Magnification

1	28	35	45
2.5	70	88	111
4	111	143	180
10	262	330	423
25	645	810	1030
40	1030	1290	1640

4.10.3 Gray level threshold setting

The most convenient and straightforward way to set the threshold is by direct detection. The threshold is turned up until the desired features appear to be fully detected but the background remained undetected. This method is attractive because of the simplicity, but the results have been found to be unreliable. Since there is no obvious criterion, different operators will set different thresholds for one field of view, and it is not possible for one person to be consistent over a period of time. It has been found that there is an appreciable variation in track counting for the same field detected at different threshold settings. It is sometimes difficult to say which one is correct.

Another method put forward for accurate threshold setting is the "flicker" method. Instead of viewing the meter output (the detection) super-imposed on the image and trying to match them in this condition they can be viewed separately and alternately by switching the display control to and fro from "image" to "meter". If the polarity switch is turned to "white" the super-imposed meter image appears black on a white ground instead of the normal white on black, and this avoids the optically difficult task of comparing a white image with a black one. While switching to and fro the threshold control is adjusted until the tracks appear identical in the two fields.

The most accurate and reproducible threshold setting is illustrated by plotting the threshold setting against some parameter measured by the Quantimet, say number of tracks. It is more accurate to consider the total number of tracks in several successive fields

corresponding to one value for threshold setting, and counting the
same fields for another value *of threshold,* and so on. The ideal curve would

show that as the threshold setting is increased, no feature is

detected. Beyond a certain value all feature are detected and the

number of tracks remains constant as the threshold setting increases

until the background is detected at higher threshold. This behaviour

is not obtained in practice because the features are not uniform,

due to diffraction effects, internal structure, uneven illumination

and scanner sensitivity. Thus the ideal step shape is rounded off

into a curve, the best setting being at the middle of the plateau.

Table 4.5 shows the results of the two S S T R irradiated

in contact with the NISUS uranium shell (thick source) and 0.5 mg/cm^2

depleted uranium deposit (thin source) at 10 kW for 2 min and 100 kW

for 150 min, respectively. The threshold detection curves for these

two films are shown in Fig. 4.10.

4.10.4 Size setting

The size setting, a new concept introduced in the Quantimet 720,

discriminates against features with a longest chord less than a value

chosen in discrete steps in picture points (p.p.). This capability

has improved precision, reliability and accuracy of the results

compared with those of its predecessor - Quanitmet B. The effect

of size setting - the longest chord of the features - is much more

important than the threshold setting in detection operation. However,

the threshold variation is continuous, in the form of a selector,

whereas that of the size is in 1 p.p. digital increment. The ideal

TABLE 4.5

Threshold setting for two films with different fissile sources and irradiation conditions

Film No. = 198
Source   = Natural Uranium Shell
Position = NISUS Uranium Plug
Condition = 10 kW 2 min

Film No. = 514
Source   = 0.5 mg/cm^2 Depleted Uranium Deposit
Position = NISUS Thermal Column
Condition = 100 kW 150 min

Threshold setting*	Total count of 20 frames	Threshold setting*	Total count of 20 frames	Threshold setting*	Total count of 19 frames	Threshold setting*	Total count of 19 frames
4.0	464	7.4	1292	5.0	708	6.7	1093
4.2	581	7.6	1290	5.1	779	6.8	1082
4.4	751	7.8	1299	5.2	807	6.9	1094
4.6	838	8.0	1316	5.3	810	7.0	1098
4.8	990	8.2	1303	5.4	886	7.1	1104
5.0	1118	8.4	1315	5.5	889	7.2	1112
5.2	1198	8.6	1345	5.6	941	7.3	1107
5.4	1188	8.8	1455	5.7	963	7.4	1109
5.6	1213	9.0	2138	5.8	971	7.5	1103
5.8	1200			5.9	986	7.6	1134
6.0	1237			6.0	1016	7.7	1127
6.2	1241			6.1	1027	7.8	1105
6.4	1244			6.2	1049	7.9	1132
6.6	1252			6.3	1070	8.0	1134
6.8	1257			6.4	1057	8.2	1108
7.0	1258			6.5	1064	8.4	1177
7.2	1281			6.6	1057	8.6	1475

Note: *Size setting = 8
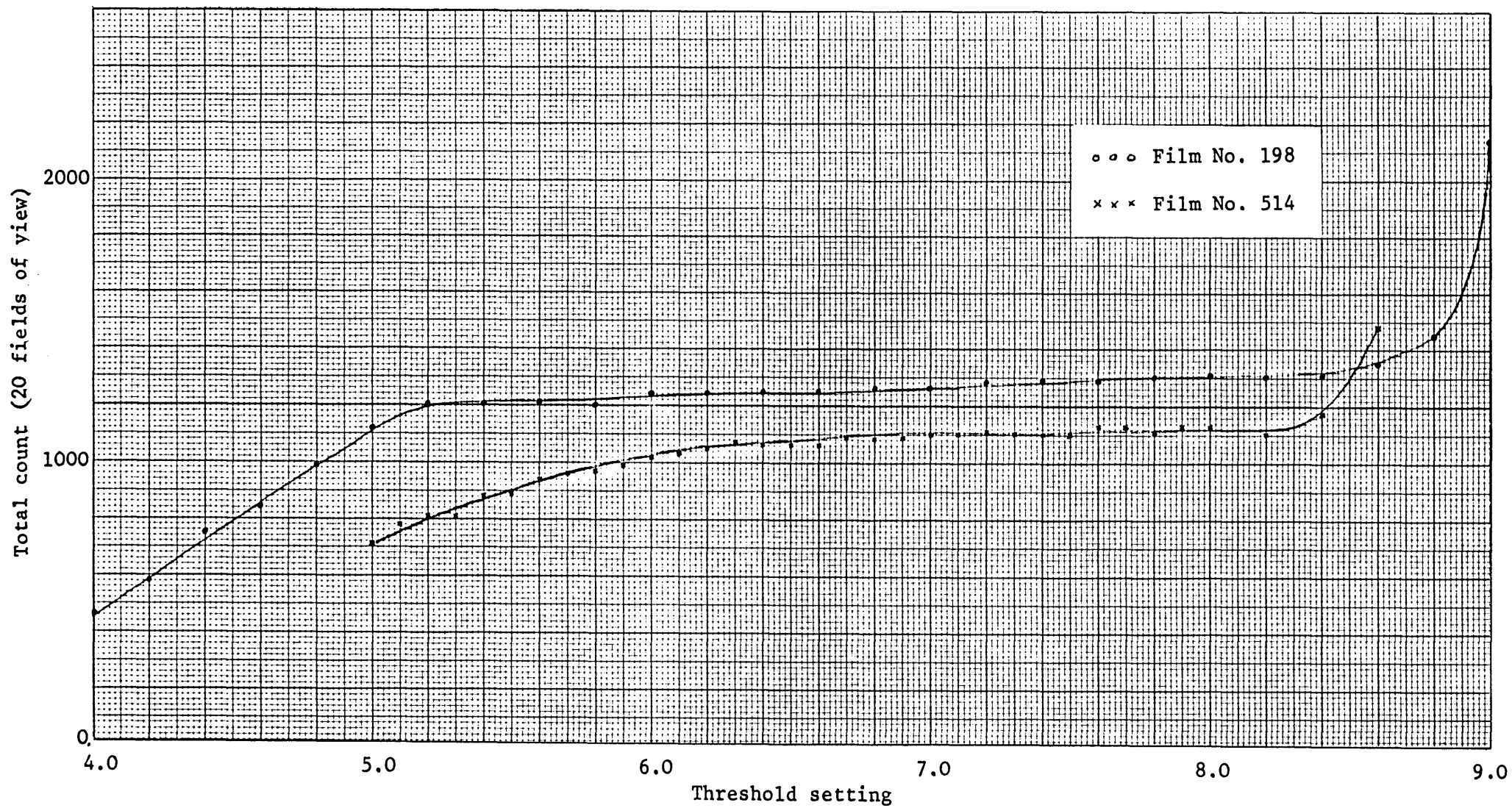
Fig. 4.10   Threshold setting curves for two different films.

detection conditions depend on the right settings both for the size

and the threshold and varies from sample to sample. Perhaps the

most significant sample-to-sample variations are (a) etching procedure,

(b) background, and (c) track overlap or pile-up. The etch rate

cannot be an exact constant, and changes in etching solution concentration

as well as bath temperature introduce fluctuations in the etching

process.

In order to find the size setting, as with the threshold setting,

the total number of tracks should be plotted against the size when

the threshold is kept constant at the right setting. The integral

curve shows up a rough plateau, Fig. 4.11, but a more informative graph

is the differential histogram which illustrates a sharp decrease in the

total number of tracks and then a peak. The background component

dominates in the low size region near the origin, but falls very

rapidly with increasing size. As size further increases, the

experimental data first rise, then attain a maximum and finally decrease

monotonically. A similar and more isotropic one-dimensional frequency

histogram is obtained when the number of tracks $N(X)$ is observed as a

function of track area X expressed in picture points. Analysis of

these data can be formulated in terms of a differential track area

distribution, denoted by $P(X)$. Hence $P(X)dX$ represents the probability

that an observed track possesses an area between X and $X+dX$. In order

to ensure correct settings of the discriminators, measurements of

differential track area probability distributions and experimental

estimates of $P(X)$ are an essential aspect of automatic fission track

counting.

The variations of total count for several fields of view with size and area, for two different samples are shown in Tables 4.6 and 4.7, respectively. Typical frequency histograms of the number of tracks as a function of track size (longest chord) and track area, for two different samples, are given in Figs. 4.12 to 4.15. One of the samples (Film No. 175) was irradiated with normal incidence in an evacuated small cylinder in the CONSORT vertical thermal column at 100 kW for 7 hours. The fissile source was 1.30 mg/cm^2 natural uranium deposit, and the source and S S T R were 10 cm apart.

Since the fission tracks are randomly orientated with different sizes, and the size setting indicates the longest chord of the features, it is expected to get better differential histogram for the samples with normal incidence, in which the track sizes are more uniform. The results shown in Figs. 4.12 and 4.14 are not as good as those of the samples irradiated in contact with uranium deposit (Film No. 206). One factor which may explain the apparently worse background in the case of Film 175 is the lower geometrical efficiency for detection in this case. Because of this a much higher neutron fluence was needed to provide adequate statistics, and therefore the likelihood of background effects due to processes other than fission was increased. These processes are not fully understood at the present time. The other two factors affecting the results of the normal incident film are the contrast and the statistics. It was found that the larger the tracks the worse the contrast, and the more difficult it is to have the right threshold setting. At low threshold,

TABLE 4.6

Size setting for two films with different fissile sources
and irradiation conditions

Film No.   =   175
Source   =   Natural Uranium Deposit (Normal Incident)
Position   =   CONSORT Vertical Thermal Column
Condition   =   100 kW 7 hours

Size setting* (P.P.)	Total count of 13 frames	Δ C	Size setting* (P.P.)	Total count of 13 frames	Δ C
0	3360	–	16	460	42
1	2758	602	17	406	54
2	2459	299	18	345	61
3	2226	233	19	295	50
4	1777	449	20	217	78
5	1311	466	21	157	60
6	1054	257	22	119	38
7	817	237	23	92	27
8	673	144	24	63	29
9	623	50	25	47	16
10	599	24	26	36	11
11	583	16	27	29	7
12	571	12	28	21	8
13	562	9	29	21	0
14	534	28	30	15	6
15	502	32			

Note: *Threshold setting = 8.4

TABLE 4.6 (continued)

Size setting for two films with different fissile sources
and irradiation conditions

Film No.   =   206
Source   =   Natural Uranium Shell
Position   =   NISUS Uranium Plug
Condition =   10 kW 5 min

Size setting* (P.P.)	Total count of 22 frames	Δ C	Size setting* (P.P.)	Total count of 22 frames	Δ C
0	3833	–	16	1070	352
1	3571	262	17	865	206
2	3573	2	18	697	168
3	3516	57	19	585	112
4	3441	75	20	475	110
5	3411	30	21	390	85
6	3360	51	22	313	77
7	3303	57	23	257	56
8	3227	76	24	200	57
9	3110	117	25	170	30
10	2940	170	26	138	32
11	2814	126	27	106	32
12	2614	200	28	90	16
13	2367	247	29	72	18
14	1890	477	30	57	15
15	1422	468			

Note: *Threshold setting = 7.1

TABLE 4.7

Area distribution for two films with different fissile
sources and irradiation conditions

Film No. = 175

Source = Natural Uranium Deposit (Normal Incident)

Position = CONSORT Vertical Thermal Column

Condition = 100 kW 7 hours

Area* (P.P.)	Total count of 20 frames	Area* (P.P.)	Total count of 20 frames
20	3241	300	56
40	600	320	64
60	178	340	45
80	72	360	56
100	52	380	39
120	48	400	32
140	36	420	18
160	37	440	16
180	40	460	14
200	37	480	12
220	53	500	14
240	57	520	4
260	58	540	6
280	48	560	3

Note: *Threshold setting = 7.5

TABLE 4.7 (continued)

Area distribution for two films with different fissile
sources and irradiation conditions

Film No.   = 206

Source   = Natural Uranium Shell

Position   = NISUS Uranium Plug

Condition = 10 kW 5 min

Area* (P.P.)	Total count of 20 frames	Area* (P.P.)	Total count of 20 frames
10	903	220	110
20	339	230	94
30	167	240	94
40	90	250	91
50	69	260	80
60	63	270	74
70	70	280	47
80	69	290	39
90	60	300	47
100	65	310	37
110	79	320	38
120	89	330	38
130	103	340	29
140	129	350	27
150	149	360	29
160	145	370	17
170	125	380	15
180	147	390	13
190	143	400	12
200	110	410	11
210	120	420	13

Note: *Threshold setting = 7.5
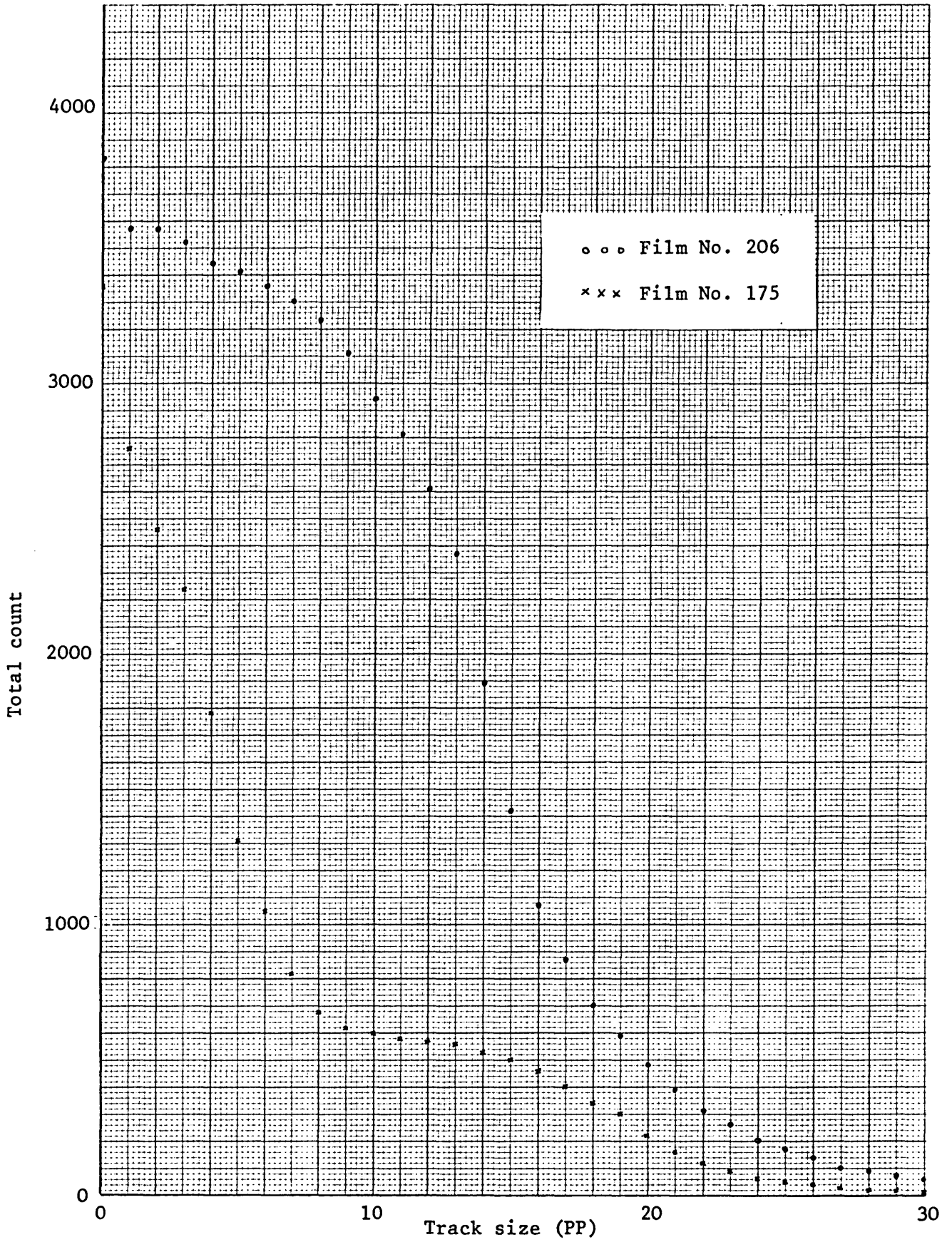
Fig. 4.11   Integral size distribution curves for two films.
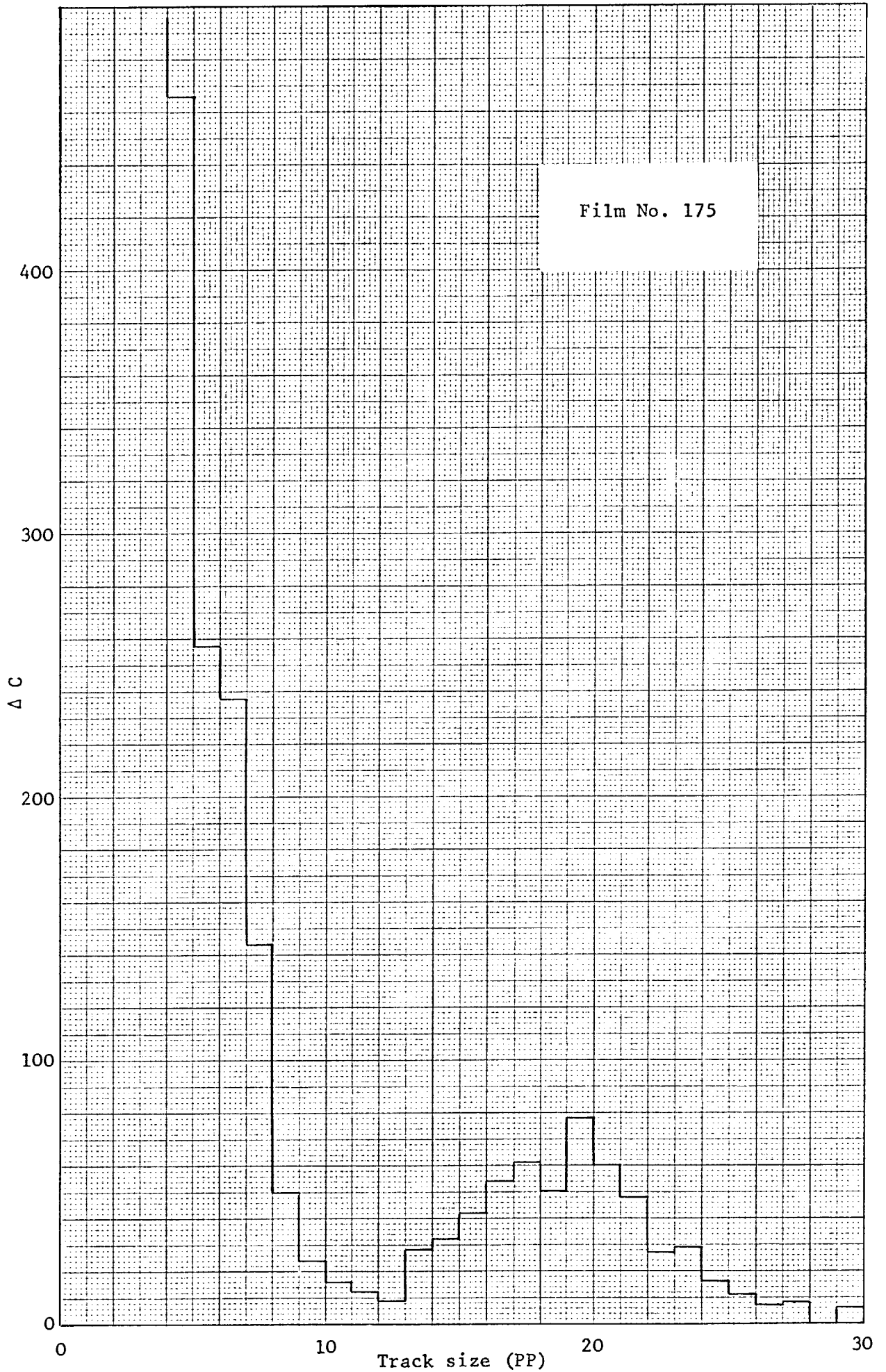
Fig. 4.12 Typical frequency histogram of the number of tracks as a

function of track size (longest chord).
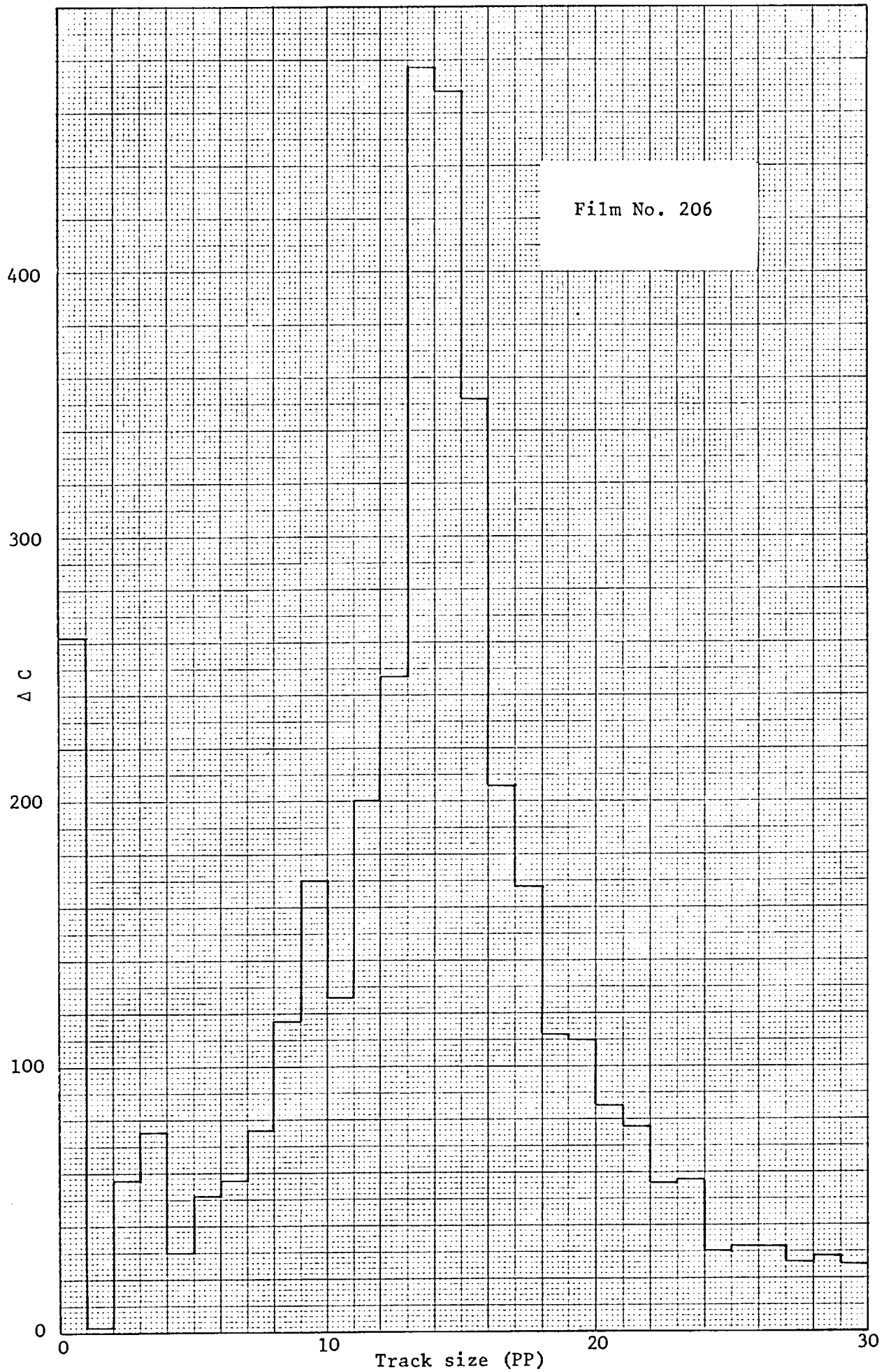
Fig. 4.13   Typical frequency histogram of the number of tracks
as a function of track size.
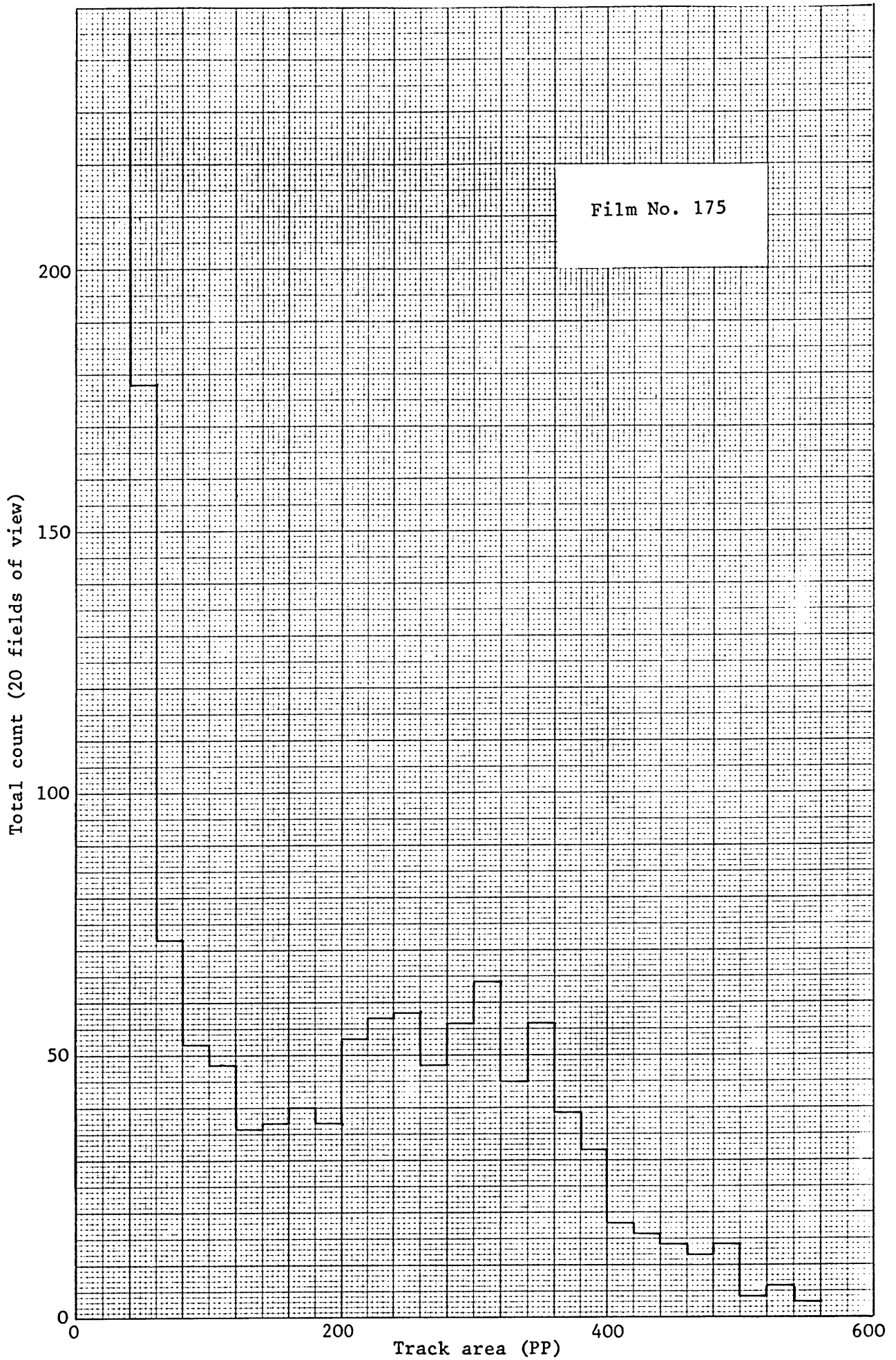
Fig. 4.14   Typical frequency histogram of the number of tracks as a function of track area.
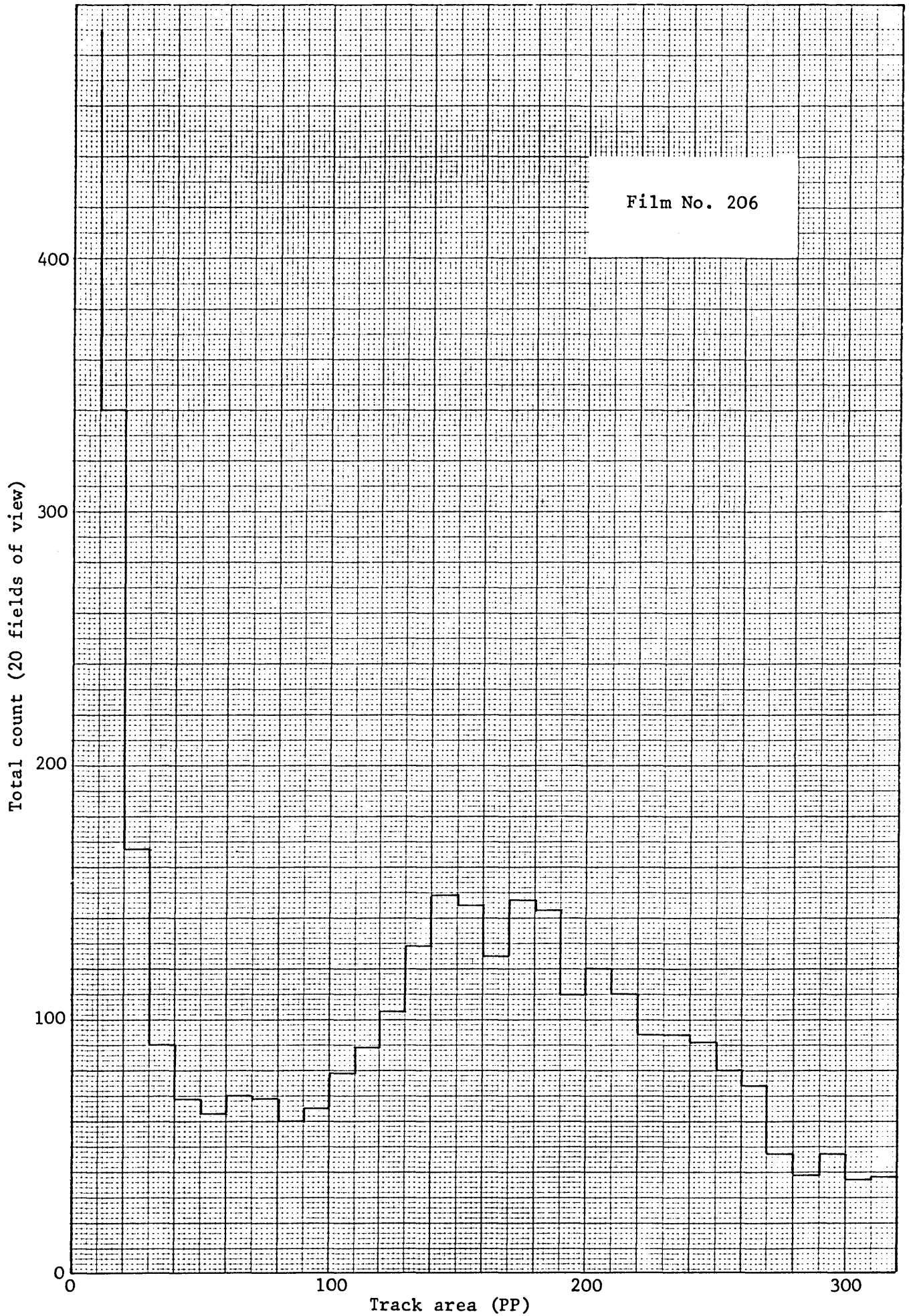
Fig. 4.15   Typical frequency histogram of the number of tracks as a

function of track area.

the breaking up and the partial detection are the problems, and at the higher threshold the background detection. Partial detection of a feature is a serious and sometimes unavoidable problem in size or area distribution measurements, but, of course, not in track counting provided tracks do not break up into several parts. The average number of tracks per field of view is about 140 for the Film No. 206, and that of the Film No. 175 is about 42, resulting in the poor statistics for the latter.

4.10.5 Overlap correction

If two tracks overlap, the Quantimet counts them as one feature. Thus at high track densities, when the probability of overlap is high it is necessary to make a correction. Richmond and Rüegger[82] have found that an accurate correction can be made using the following equation:

$$N = N_o \exp (-AN_o) \qquad (4.3) \quad *$$

where N_o is the actual track density,

       N is the observed track density,

       A is the average track area.

This does not, however, allow one to work with tracks of unlimited densities, for one quickly reaches a stage where there is a large uncertainty in the correction factor. The limitation is governed by A, the single track area, depending on the irradiation and etching conditions.

* This formula has been consistently applied in the present work. There is however some doubt about its validity, depending on the way in which the parameter A is defined.

The overlap correction was made for the Film Nos. 175 and
206. Fig. 4.14 shows that the average track area is about 320 pp
for the Film No. 175.   Converting picture points into micron
(Section 4.10.2) and assuming that the tracks are round, which they
really are (Fig. 4.6), the average track area 1.59×10^{-6} cm^2 is
obtained.   The actual track density can be calculated using
Equ. 4.3 where N = 17014 tracks/cm^2, the number of tracks counted
by the Quantimet.   The results show the actual track density of
N_o = 17494 tracks/cm^2 comparedwith 17557 tracks/cm^2 counted by eye,
with a discrepancy of less than 0.4% which is fortuitously small.

A separate measurement was made to measure the average track
area of the same specimen (Film No. 175) by selecting 342 random tracks
in 342 fields of view, using the Light Pen module of the Quantimet.
By this module the region or features of interest in the sample are
detected in the usual way, irrespective of the detection of the other
features, when the Light Pen is pointed at the feature of interest.
The results showed that the average track area is about 350 picture
points, i.e. 1.74×10^{-6} cm^2, resulting in the actual track density
17541 tracks/cm^2.

Fig. 4.15 shows that the average track area is about 180 picture
points for the Film No. 206.   Assuming the tracks are round (Fig. 4.1),
which is not a true assumption in this case,

$$A = 8.93 \times 10^{-7} \ cm^2$$

The actual number density obtained using Equ. 4.3 where N = 56502
tracks/cm^2.   Therefore, N_o = 59590 tracks/cm^2 which is about 2% less

than 60724, the eye counted number of tracks/cm^2, perhaps because of
the errors in converting the units of picture points into micron.
The correction factor derived from Equ. 4.3 is plotted in Fig. 4.16
as a function of track density for an asymptotically thick source
(NISUS uranium shell) and a very thin deposit ($\simeq$ 23 μg/cm^2). The
average track area for these two cases were taken as 180 pp and 280 pp
(see Section 7.11) respectively.   Table 4.8 shows a comparison between
eye and Quantimet counting for Film Nos. 175 and 206, and the effect of
overlap correction.

4.11   Data analysis and results

Experiments were made in order to test the reproducibility
of the experiments and to make comparison between eye and Quantimet
counting.   Several sets of samples were irradiated with identical
irradiation positions and etching conditions, but for different neutron
fluences.   In each set pairs of Makrofol S S T R were irradiated in
contact with the NISUS natural uranium plug (Fig. 4.17).   The pairs
of films were placed one on the outer surface of the plug and the other
on the inner surface, between the boron carbide and uranium shells.
The etched films were counted by the Quantimet 720 and by eye using a
Leitz microscope.   The results are shown in Tables 4.9 to 4.12.   The
overlap corrected values of the Quantimet counts were calculated
assuming an average track area of 180 picture points, the value measured
for Film 206.

The quantities of interest in these comparisons are the
reproducibility of each method of counting, reflected in the ratios of
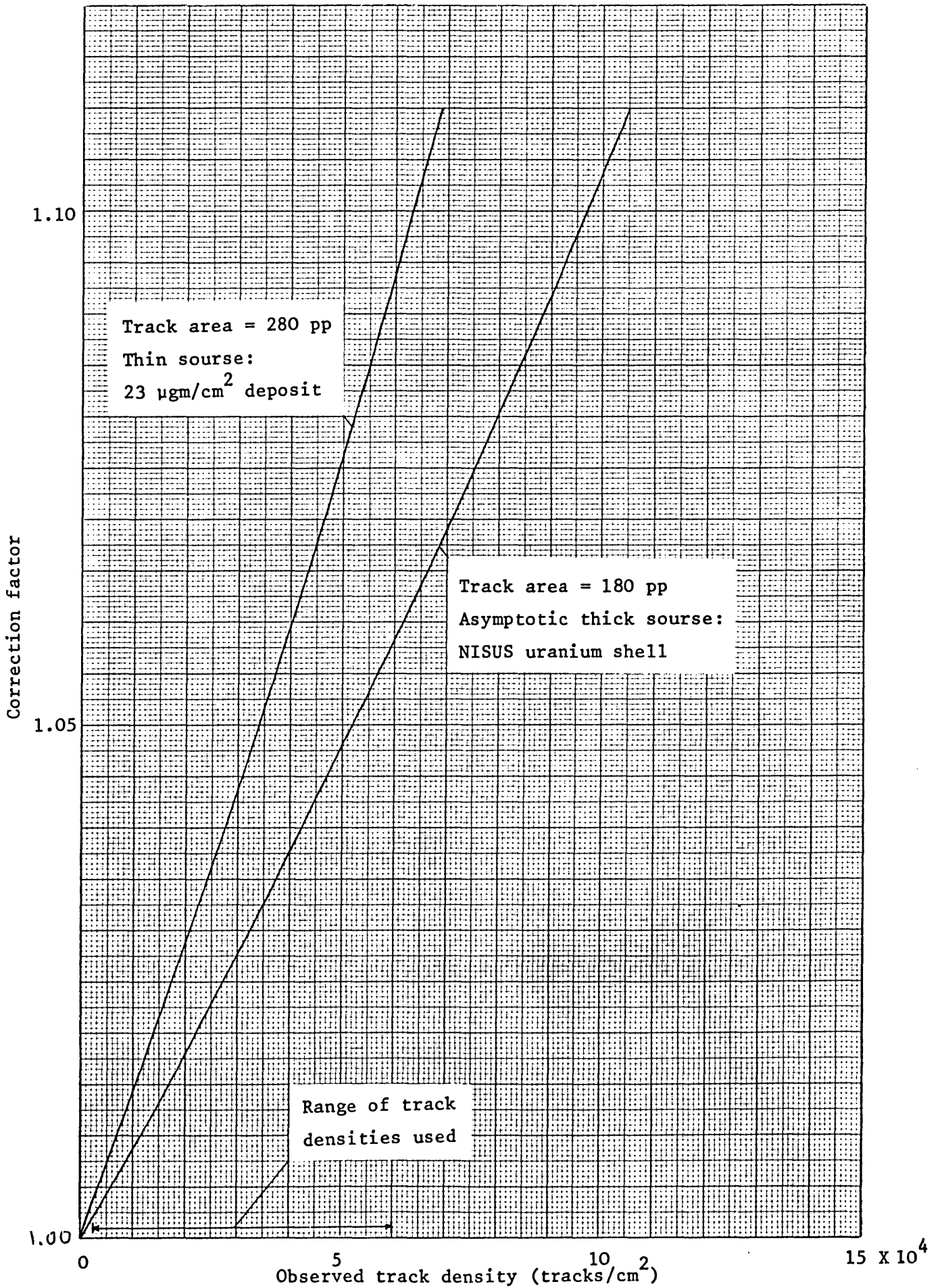
Fig. 4.16 Correction factor for overlap.

TABLE 4.8

Overlap correction for two different films

Film No. = 175
Source = Natural Uranium Deposit (Normal Incident)
Position = CONSORT Vertical Thermal Column
Condition = 100 kW 7 hours

Eye			QTM			
No. of	Total	Tracks/cm^2	No. of	Total	Tracks/cm^2	
					Observed	Overlap
frames	count		frames	count		corrected
490	7235	17557 ± 1.2%*	215	9062	17014	17494 ± 1.1%*

Film No. = 206
Source = Natural Uranium Shell
Position = NISUS Uranium Shell
Condition = 10 kW 5 min

Eye			QTM			
No. of	Total	Tracks/cm^2	No. of	Total	Tracks/cm^2	
					Observed	Overlap
frames	count		frames	count		corrected
532	4347	60724 ± 1.5%*	250	34992	56502	59590 ± 0.5%*

Note: *Statistical error only
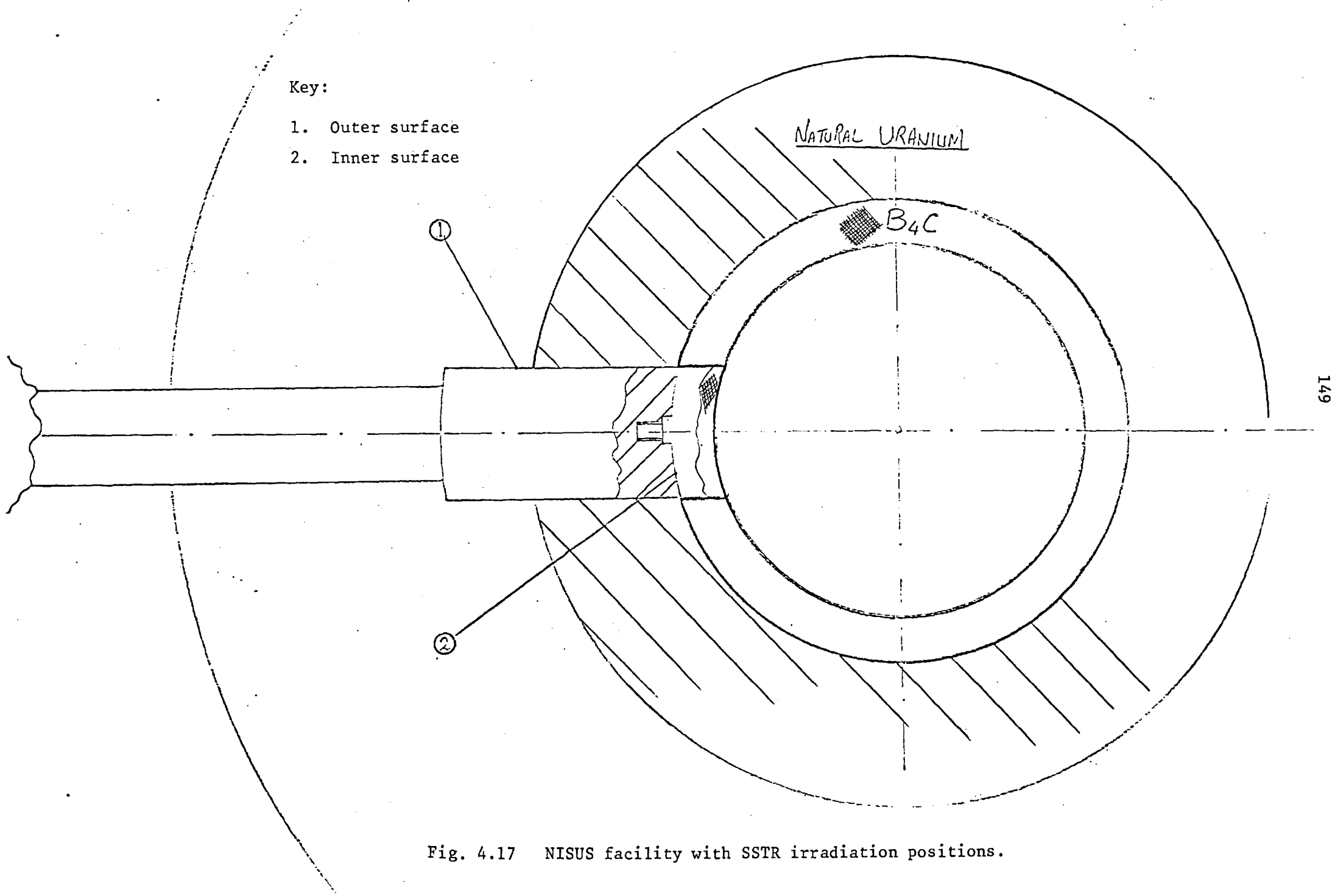
Key:

1. Outer surface
2. Inner surface

NATURAL URANIUM

B₄C

Fig. 4.17   NISUS facility with SSTR irradiation positions.

TABLE 4.9

Comparison of track counting by eye and Quantimet 720

Reactor Power   = 1 kW

Irradiation Time = 10 min.

Film No.	Position	Eye			QTM				Ratios[*]	
		No. of frames	Total count	Tracks/cm^2	No. of frames	Total count	Tracks/cm^2		Eye	QTM
							Observed	Overlap corrected		
235	Outer	595	6906	13807	250	8187	13220	13380	7.54	10.61
236	Inner	334	514	1830	152	474	1259	1261	±4.6%	±5.0%
253	Outer	514	5750	13302	250	7923	12793	12941	7.34	10.81
254	Inner	240	366	1813	248	735	1196	1197	±5.4%	±4.0%
255	Outer	514	5865	13568	250	8142	13147	13304	7.44	10.60
256	Inner	311	477	1824	281	873	1254	1255	±4.8%	±3.5%

Note: * Errors shown are statistical sampling errors only (1σ).

150

TABLE 4.10

Comparison of track counting by eye and Quantimet 720

Reactor Power   =   1 kW

Irradiation Time   =   20 min.

Film No.	Position	Eye			QTM				Ratios*	
		No. of frames	Total count	Tracks/cm^2	No. of frames	Total count	Tracks/cm^2 Observed	Overlap corrected	Eye	QTM
237	Outer	450	9751	25766	250	15618	25219	25805	10.22	10.74
238	Inner	355	753	2522	171	1016	2398	2403	±3.8%	±3.0%
225	Outer	448	9752	25883	300	18842	25354	25947	10.19	10.75
226	Inner	430	919	2541	259	1545	2408	2413	±3.5%	±2.6%
257	Outer	459	10148	26289	250	15681	25321	25912	10.52	10.08
258	Inner	379	797	2500	250	1465	2565	2571	±3.7%	±2.7%

Note: * Errors shown are statistical sampling errors only (1σ).

TABLE 4.11

Comparison of track counting by eye and Quantimet 720

Reactor Power   =   10 kW

Irradiation Time   =   2 min.

Film No.	Position	Eye			QTM				Ratios*	
		No. of frames	Total count	Tracks/cm^2	No. of frames	Total count	Tracks/cm^2 Observed	Overlap corrected	Eye	QTM
195	Outer	323	7227	26605	196	12137	24997	25573	10.34	10.47
201	Inner	275	595	2573	183	1105	2437	2442	±4.3%	±3.0%
198	Outer	414	9137	26243	196	12117	24956	25530	10.45	10.59
203	Inner	365	771	2512	179	1067	2406	2411	±3.8%	±3.0%
229	Outer	387	8704	26743	250	15991	25821	26436	10.16	10.57
230	Inner	444	983	2633	250	1546	2496	2502	±3.4%	±2.6%

Note: * Errors shown are statistical sampling errors only (1σ).

152

TABLE 4.12

Comparison of track counting by eye and Quantimet 720

Reactor Power   =   10 kW

Irradiation Time   =   5 min.

| Film No. | Position | Eye | | | QTM | | | | Ratios[*] | |
		No. of frames	Total count	Tracks/cm^2	No. of frames	Total count	Tracks/cm^2 Observed	Tracks/cm^2 Overlap corrected	Eye	QTM
206	Outer	532	4347	60724	250	34992	56502	59582	9.90	10.05
209	Inner	374	1930	6136	175	2558	5901	5931	±2.7%	±2.0%
261	Outer	430	3273	56567	250	32335	52212	54825	9.82	9.15
262	Inner	430	2084	5763	250	3692	5962	5994	±2.8%	±1.7%
263	Outer	430	3532	61043	250	33676	54377	57220	9.92	9.79
264	Inner	430	2224	6150	250	3601	5815	5845	±2.7%	±1.7%

Note: [*] Errors shown are statistical sampling errors only (1σ).

counts in two films simultaneously irradiated in different positions, and the relative efficiency of the two methods of counting, reflected in the ratio of count of a single film by the two methods.

4.11.1 Reproducibility

The ratio of fission rates in the two positions calculated by the neutron transport theory code ANISN[83] is 10.86. The experiment thus tests the reproducibility of the two counting techniques for measurements of fission rates differing by one order of magnitude. Since the techniques have a limited dynamic range in track density one can expect that the ratio is only correctly measured when the neutron fluence during the irradiation is within rather narrow limits.

The ratios are plotted against the larger track density in Fig. 4.18. It can be seen that the Quantimet 720 results are superior to the eye counts in this test. In particular the eye count results are widely discrepant at the lowest track densities. This was later found to be due to miscounting the samples at very low track density. In fact at this order of track density several frames can be found with no tracks at all, and they should be counted as zero number of tracks per field of view. Both the eye and Quantimet counted ratios seem to be systematically low for the experiment in which the track density of one of the films was greater than 5×10^4 tracks/cm^2. This is probably attributable to track overlap errors.

For the nine pairs of films satisfactorily counted with the Quantimet the mean ratio was 10.55 with a standard deviation of 0.22, or 2.1%.
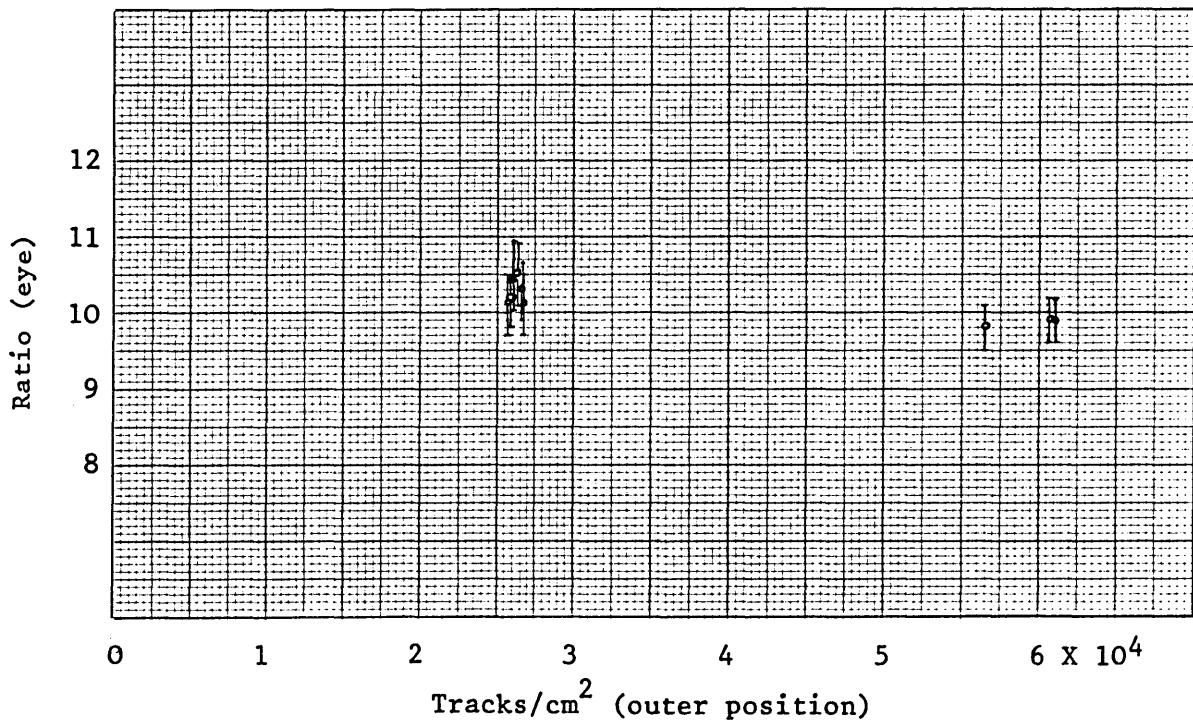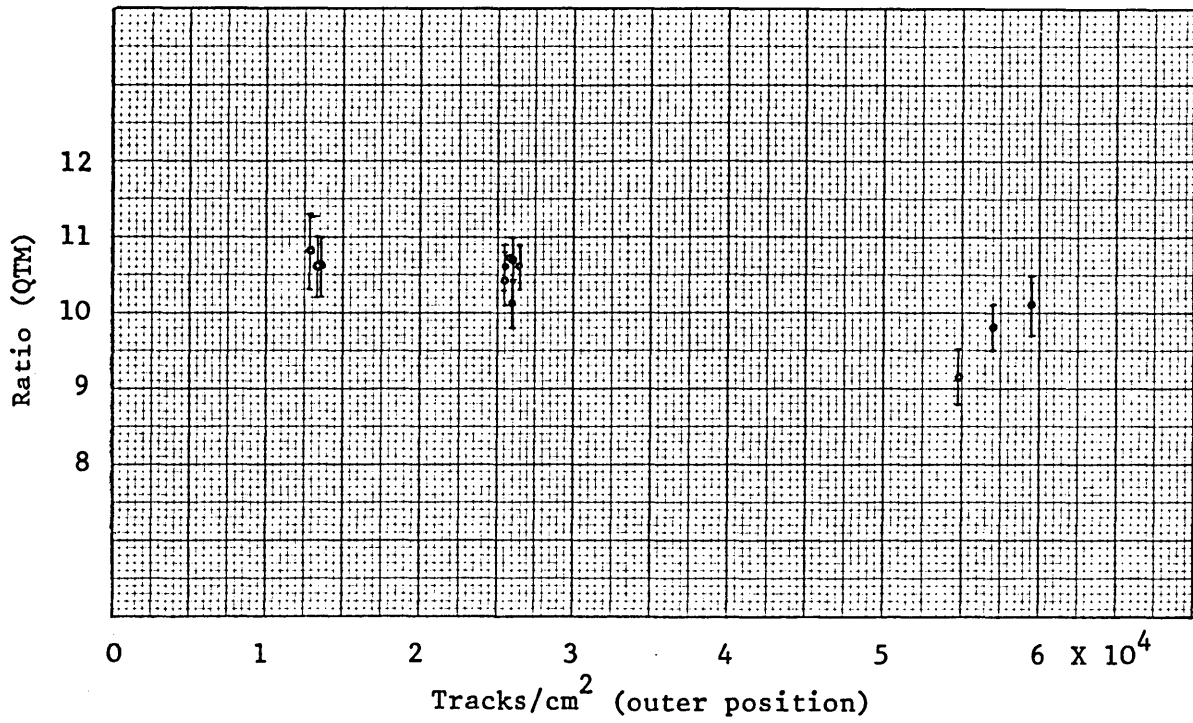
Fig. 4.18   Ratio of track density for the films irradiated on the
outer position of the uranium plug to the inner ones
for the two counting methods.

For the six pairs of films satisfactorily counted by eye the
mean ratio was 10.31 with a standard [deviation] of 0.15, or 1.4%.

The above values for the standard [deviation] are actually less than one
would expect from the number of tracks counted. This may reflect the
selection implied in choosing films "satisfactorily" counted.

4.11.2 Relative counting efficiency

The ratios of Quantimet counted track density to eye counted
track density for the 24 films are shown in Table 4.13 and Fig. 4.19.
The three very low ratios for films 236, 254 and 256 are attributed to
incorrect eye counting. The remaining ratios are consistent with a
constant value of relative counting efficiency at all track densities
up to the highest value used in the experiment of 6×10^4 tracks/cm^2.
This seems surprising in view of the expected overlap errors at such
high densities.

For the 21 films satisfactorily counted by both methods the
mean ratio of Quantimet to eye counts was 0.974 with a standard [deviation] of
0.026. The expected standard [deviation] for this sample was 0.028.

For the 12 ratios counted with an expected standard deviation
of less than 2% the mean ratio was 0.975 with a standard [deviation] of 0.018.
The expected standard [deviation] for this sample was 0.015.

From the above one can deduce that the ratio of the track
densities by the two methods differs significantly from 1 and is
0.974 ± 0.006 or 0.975 ± 0.005.

There are two plausible explanations for the difference of
the ratio from unity. The more likely of the two is that the measurements

TABLE 4.13

The ratios of the Quantimet counted track

density to eye counted track density

Film No.	Eye[a] Tracks/cm^2	QTM[a] Tracks/cm^2 [b]	Ratio[a] QTM/Eye
235	13807 ± 1.2%	13380 ± 1.2%	0.969 ± 0.016
236	1830 ± 4.4%	1261 ± 4.6%	0.689 ± 0.044
253	13302 ± 1.3%	12941 ± 1.1%	0.973 ± 0.017
254	1813 ± 5.2%	1197 ± 3.7%	0.660 ± 0.042
255	13568 ± 1.3%	13304 ± 1.1%	0.981 ± 0.017
256	1824 ± 4.6%	1255 ± 2.8%	0.688 ± 0.037
237	25766 ± 1.0%	25805 ± 0.8%	1.002 ± 0.013
238	2522 ± 3.6%	2403 ± 3.1%	0.953 ± 0.046
225	25883 ± 1.0%	25947 ± 0.7%	1.002 ± 0.013
226	2541 ± 3.3%	2413 ± 2.5%	0.950 ± 0.040
257	26289 ± 1.0%	25321 ± 0.8%	0.963 ± 0.012
258	2500 ± 3.5%	2571 ± 2.6%	1.028 ± 0.045
195	26605 ± 1.2%	25573 ± 0.9%	0.961 ± 0.014
201	2573 ± 4.1%	2442 ± 3.0%	0.949 ± 0.048
198	26243 ± 1.0%	25530 ± 0.9%	0.973 ± 0.013
203	2513 ± 3.6%	2411 ± 3.1%	0.960 ± 0.045
229	26743 ± 1.1%	26436 ± 0.8%	0.989 ± 0.013
230	2633 ± 3.2%	2502 ± 2.5%	0.950 ± 0.039
206	60724 ± 1.5%	59582 ± 0.5%	0.981 ± 0.016
209	6136 ± 2.3%	5931 ± 2.0%	0.967 ± 0.029
261	56567 ± 1.7%	54825 ± 0.6%	0.969 ± 0.018
262	5763 ± 2.2%	5994 ± 1.6%	1.040 ± 0.028
263	61043 ± 1.7%	57220 ± 0.5%	0.937 ± 0.017
264	6150 ± 2.1%	5845 ± 1.7%	0.950 ± 0.026

N	Mean ratio	standard deviation (External consistency) of ratio S	Internal consistency σ	Standard error of mean $S/\sqrt{N}$
21[c]	0.974	0.026	0.028	0.006
12[d]	0.975	0.018	0.015	0.005

(a)　Errors are statistical sampling errors only (1 s.d.)

(b)　Overlap corrected

(c)　Excluding films 236, 254 and 256

(d)　Excluding ratios with standard deviation greater than 2.0%
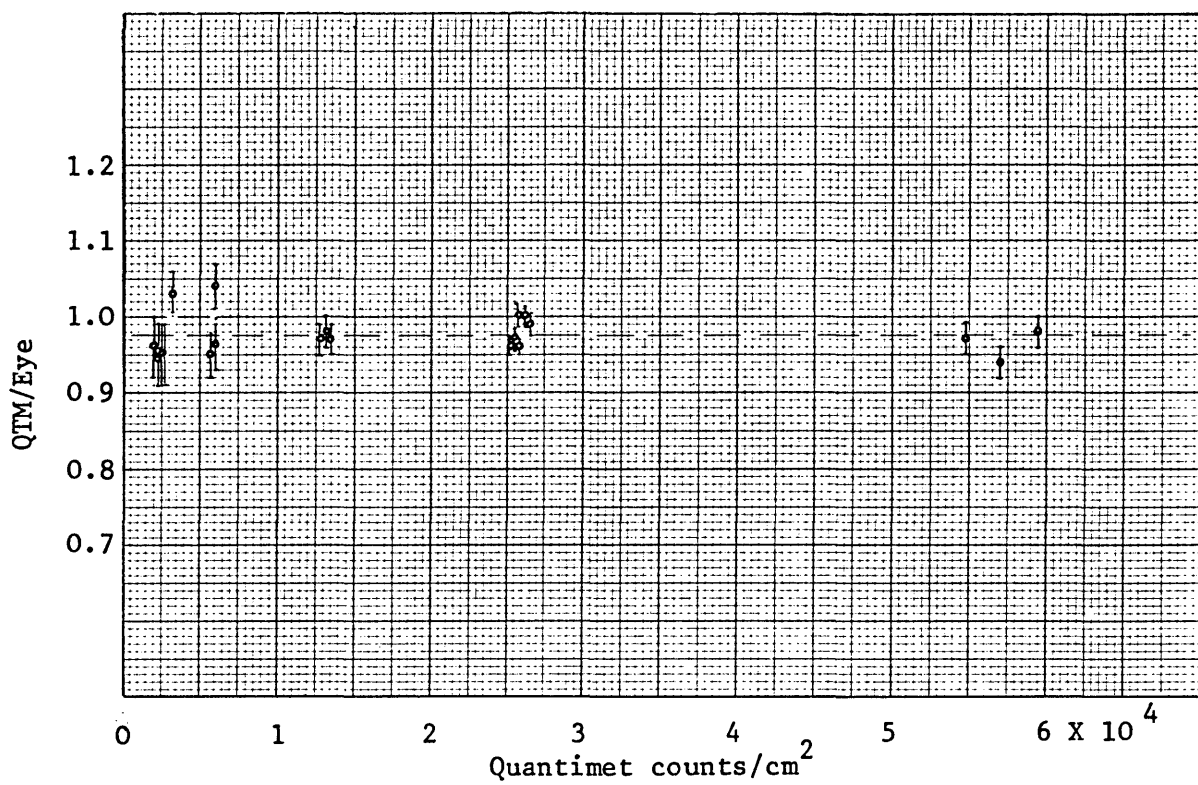
Fig. 4.19   Ratio of track densities by the two methods.

of the areas of the fields of view of the two instruments used were in error. The same stage micrometer with 10 μm divisions was used to measure both fields of view. An error of less than 2 μm on each of the four linear dimensions measured could result in the observed discrepancy of 2.5%. Also the size of the field of view of the Quantimet depends to some extent on electronic stability and therefor requires frequent measurement. The other probable cause of discrepancy between the two methods is a systematic difference in the detection criteria of the human observer and the Quantimet.

4.11.3 Poisson distribution

One crucial assumption employed in these experiments has been the applicability of Poisson statistics. It is not immediately evident, however, that this assumption holds for human track counting observations. The validity of this assumption was tested with the data obtained from the experiments. In a typical measurement (Film No. 206), the Makrofol S S T R was scanned in 532 frames and a total of 4347 tracks were observed, corresponding to a mean value of 8.171 tracks per frame. The frequency histogram for these data is displayed in Fig. 4.20 in comparison with the Poisson distribution

$$P_x = 532 \frac{m^x e^{-m}}{x!} \qquad (4.4)$$

Here the normalization constant 532 is simply the total number of frames and m is the mean value of the distribution. As can be seen from this figure, the Poisson distribution obtained with m = 8.171 is

4347 Events

532 Frames

m = 8.171

$$P_x = 532 \, \frac{m^x \, e^{-m}}{x!}$$

Number of tracks per frame
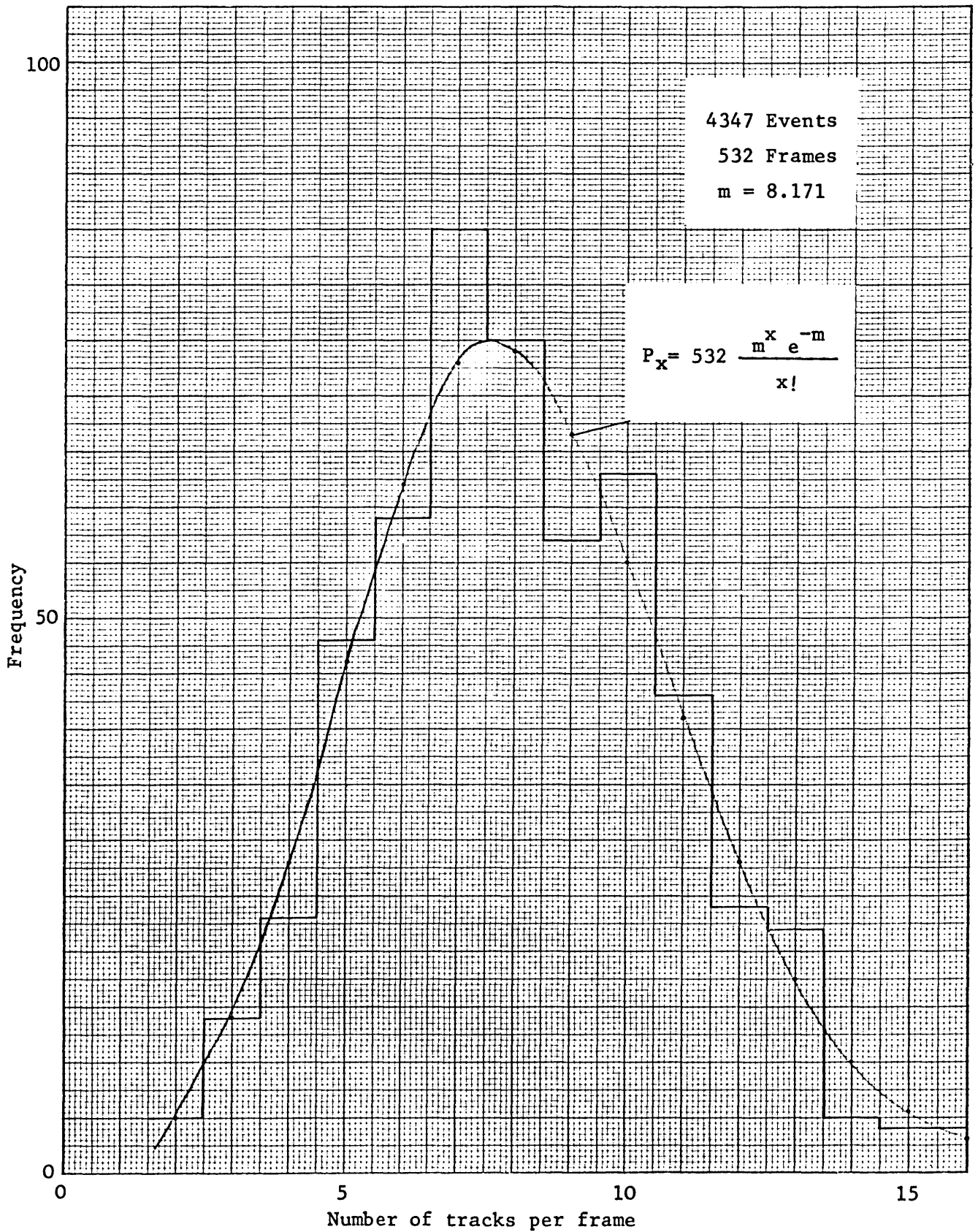
Fig. 4.20   Comparison of the frequency histogram of observed number of tracks per frame with the Poisson distributuion.

in agreement with the frequency histogram. Moreover, the standard deviation obtained directly from the histogram is 2.760 whereas the value found from Poisson statistics is $(m)^{\frac{1}{2}} = (8.171)^{\frac{1}{2}} = 2.858$. To conclude whether Poisson distribution can be employed, the chi-square test was used. This test is used to determine how well theoretical distributions, such as Poisson, fit empirical distributions, i.e. those obtained from sample data.

4.11.4 The chi-square test

According to the rules of probability, results obtained in samples do not agree exactly with theoretical results[84]. Suppose in a particular sample a set of possible events E_1, E_2, E_3, ..., E_k (Table 4.14) are observed to occur with frequencies o_1, o_2, o_3, ..., o_k, called "observed frequencies", and according to probability rules they are expected to occur with frequencies e_1, e_2, e_3, ..., e_k, called "expected" or "theoretical frequencies". Often we wish to know whether observed frequencies differ significantly from expected frequencies.

A measure of the discrepancy existing between observed and expected frequencies is supplied by the statistic χ^2 given by

$$\chi^2 = \frac{(o_1 - e_1)^2}{e_1} + \frac{(o_2 - e_2)^2}{e_2} + \ldots + \frac{(o_k - e_k)^2}{e_k}$$

$$= \sum_{j=1}^{j} \frac{(o_j - e_j)^2}{e_j} \qquad (4.5)$$

where if the total frequency is N,

$$\Sigma\, o_j \;=\; \Sigma\, e_j \;=\; N \qquad\qquad (4.6)$$

If $\chi^2 = o$, observed and theoretical frequencies agree exactly, while $\chi^2 > o$, they do not agree exactly. The larger the value of χ^2, the greater is the discrepancy between observed and expected frquencies. The sampling distribution of χ^2 is approximated very closely by the chi-square distribution.

$$Y = Y_o \; (\chi^2)^{\frac{1}{2}(\nu-2)} e^{-\frac{1}{2}\chi^2} = Y_o \; \chi^{\nu-2} \; e^{-\frac{1}{2}\chi^2} \qquad\qquad (4.7)$$

TABLE 4.14

Event	E_1	E_2	E_3	$\ldots$	E_k
Observed frequency	o_1	o_2	o_3	$\ldots$	o_k
Expected frequency	e_1	e_2	e_3	$\ldots$	e_k

where ν is the number of degrees of freedom and Y_o is a constant

depending on ν such that the total area under the curve is one.

The number of degrees of freedom ν is given by

(a) $\nu = k-1$ if expected frequencies can be computed without

having to estimate population parameters from sample statistics.

(b) $\nu = k-1-m$ if expected frequencies can be computed only by

estimating m population parameters from sample statistics.   In the

present case, Poisson distribution, m = 1.

In practice expected frequencies are computed on the basis

of a hypothesis H_o.   If under this hypothesis the computed value of

χ^2 given by Equ. 4.5 is greater than some critical value such as

$\chi^2_{0.95}$ or $\chi^2_{0.99}$, which are the critical values at the 0.05 and 0.01

significance levels respectively, we would conclude that the observed

frequencies differ significantly from expected frequencies and would

reject H_o at the corresponding level of significance.   Otherwise we

would accept it or at least not reject it.   This procedure is called

the chi-square test of hypothesis or significance.

The chi-square test was applied to the data obtained from all

the measurements by writing the POIS computer program.   The program

calculates the Poisson distribution, observed and expected frequencies,

the probability of having a certain number of tracks per frame and

finally the corresponding value of χ^2.   The results showed that the

"Goodness of Fit" is valid, i.e. the Poisson statistics can be employed

in the present counting experiments.

4.11.5 Conclusions

Apart from the overlap problem which can easily be overcome by choosing the right irradiation time and etching conditions, the main disadvantage of the Quantimet 720 is the detection of "unwanted features". This includes background, partial detection and breaking up. It was found that this performance depends strongly on the focus, so that it is sometimes necessary to defocus a given field of view to get the right detection. Since the tracks are normally darker than the background, slight defocusing has no effect on the number of tracks per field of view. As it was described earlier in order to get the best results, threshold and, in particular, size setting (or differential track area distribution) should be determined for any given sample. In practice, when dealing with tens of samples, this procedure is time consuming and expensive and virtually impossible. So, it is assumed that the determination of the threshold and size setting for one or two specimens of a given set can be chosen as a typical setting for the rest of the samples.

The most important advantages of the Quantimet 720 are the speed and reproducibility. The eye counting speed, even with no overlapping problem, depends on the number of tracks per field of view. The greater the number of tracks per frame, the longer the counting time. It was found that for a film with track density of the order of 2×10^4 tracks/cm^2, it takes about 3 hours to count 400 fields of view for a typical 20 tracks per frame. Although the

slight focus adjustment for almost every field of view, and rejection

of some frames slows down the Quantimet counting speed, it is still

possible to count some 12 samples with track density of about

2×10^4 tracks/cm^2 in a normal working day. Since eye counting is

not possible continuously for about three hours, counting by the

Quantimet is about 8-10 times faster than that by eye.

Either method of counting is capable of a precision of ±2%

or better in fission rate ratio. At this level of statistical

accuracy no evidence has been found that the variance of the measure-

ment exceeds that expected from random sampling errors provided that

track densities are not greater than 5×10^4 tracks/cm^2 for eye or

Quantimet counting or less than 2×10^3 tracks/cm^2 for eye counting.

The relative efficiency of the Quantimet to eye counting was

found to be 0.975 ± 0.005 (random). This value is subject to a

systematic error of ±2% attributable to the calibration of field

areas.

The data reported were obtained during a period of about

one month, so the values obtained for the variances reflect the

stability of the counting method over this period.

5.   TRANSPORT THEORY CALCULATIONS

The design of the NISUS facility involved choosing a

configuration which would generate a fast reactor simulation

spectrum.   This standard neutron field is designed in a $\overset{such}{a}$ way

as to allow optimal neutron spectrum characterization by

measurements, but also by computations.   The choice of the

spherical shell geometry enabled a simple and more economic

one-dimensional code to be used.

It is assumed that the fast neutron flux generated in

NISUS is nearly spherically symmetrical.   The departures from

the symmetry are caused by the flux gradient in the thermal

column extension.   A traverse measurement has been made[17]

using threshold detectors across the diamter of the NISUS cavity

along the graphite plug axis, and a gradient of up to 5% in 8 cm

has been found.   Nevertheless, the use of one-dimensional solution

of the transport equation is justified since the fission rate

distribution in the driver shell, as it will be shown in Chapter 7,

can be separated in the form $F(r,\psi,\theta) = R(r)\psi(\psi)\theta(\theta)$. This

means that the scalar neutron flux at the centre of NISUS does

not depend on the thermal neutron source distribution.

5.1   The ANISN code

ANISN[83] solves the one dimensional Boltzmann transport

equation for neutrons or gamma rays in slab, sphere or cylinder

geometry.   The source may be fixed, fission or a sub-critical

combination of the two. Criticality search may be performed on any one of the several parameters. Cross sections may be weighted using the space and energy dependent flux generated in solving the transport equation. The solution technique is an advanced discrete ordinates method which has been developed and extended to curvilinear geometry at Los Alamos Scientific Laboratory.

ANISN was designed to solve deep-penetration problems in which angle-dependent spectra are calculated in detail. The principal feature that makes ANISN suitable for such problems is the use of a programming technique with optional data-storage configuration which allows execution of small, intermediate, and extremely large problems. ANISN also includes a technique for handling general isotropic scattering, pointwise convergence criteria, and alternate step function difference equations that effectively remove the oscillating flux distributions sometimes found in discrete ordinates solutions.

In the solution by the discrete ordinates (S_N) method, the so-called "diamond" difference scheme, wherein flux is assumed to be linear between adjacent mesh points, is employed. The solution in the code will approach the exact solution of the Boltzmann equation with increasing orders of approximation as the space, angle and energy mesh approaches differential size.

In the present work, the ANISN code was used with a 37 group data set derived from the UKAEA Nuclear Data Library by the GALAXY processing code[85]. The data file numbers (DFN) of the elements used in the central NISUS spectrum and reaction rate calculations are as follows:

Al : 35, ^{10}B : 90, ^{11}B : 49, C : 21, ^{235}U : 66, and ^{238}U : 401.

5.2   Problem specification

The ANISN code utilizes variable dimensioning to facilitate efficient core data storage allocation. Because of the variable dimensioning technique, on any given data array, no size restriction is imposed; only a size restriction on the length of the sum of all arrays is imposed. The amount of core data storage for a given problem may be exactly computed as indicated in the documentaion.

The input data for the ANISN code are divided into the following seven data:

(A)   Overall problem data storage allocation

(B)   Overall problem title and CPU time estimate

(C)   Overall problem parameters

(D)   Cross section data

(E)   Fixed source data

(F)   Flux or fission guess data

(G)   Remainder of data

The first data set is entered on a single, formatted card which is the first physical card of each problem deck. The second data set consists of a single card containing a problem descriptive title and Central Processor Unit (CPU) time estimate. All remaining input data sets (C through G) of an ANISN problem are written in the ANISN standard format. Besides specifications which are associated with the nature of the physical problem to be solved, radial mesh spacing may be rather a troublesome matter. An ill-specified mesh

spacing creates a great number of inner iterations which require a

considerable amount of computer time, oscillation of flux values may

occur in regions with large flux attenuation, and questionable

results as a whole may be obtained. The main input data used for

ANISN may be summarized as follows:

(a)   The maximum order of scatter in any zone assumed to be zero,

i.e. the P_o isotropic scattering was used because the higher P_1 moment

is not needed for sensitivity studies.

(b)   The order of angular quadrature was chosen as 4 and 8

depending on the degree of approximation in S_N calculation.

(c)   The left boundary condition was specified as reflection

$d\phi/dx = o$. The white boundary with the albedo by group was

specified for the outer boundary (some fraction returns isotropically).

(d)   The number of zones or regions in the problem geometry was

made equal to the different layers of construction materials. For

instance, in the case of NISUS 1b eight zones were defined in the

following order : air, Al, B_4C, Al, air, natural uranium, air and

graphite. The gap between the aluminium cladding and uranium shell

is less than 0.1 mm and may be ignored. In the case of reaction

rate calculation a detector was assumed in the centre of the system,

forming the first zone.

(e)   The number of mesh intervals was estimated from the

investigations of the effect of the mesh number on the predicted

spectrum. It was found that 51 mesh intervals are adequate for

the problem in question and larger mesh number offered no significant

advantages.

(f)   The spherical shell fixed source was specified at the outer
edge of the graphite reflector 50 cm thick (the rightmost mesh
interval in the last zone).   The thickness 50 cm of the reflector
resulted from Emmett's studies;   it has been shown[86] that the
inner spectrum has been insensitive to a change in thickness of
the reflector over the range between 35 and 50 cm.

(g)   The group cross section averaged in GALAXY with weighting
function $1/\Sigma_t$, where Σ_t is the macroscopic total cross section for
each isotope.   The nuclear data of the following elements were
used: Al, ^{10}B, ^{11}B, C, ^{235}U and ^{238}U.   The number densities
(10^{24} atoms/gm) in the cross section mixing table were calculated
using atomic mass, specific density in gm/cm^3 , and percentage of
the natural abundance of the isotopes.

(h)   The value for EPS, epsilon for lambda and upscatter convergence
(accuracy desired) was chosen as 0.0001.   If small perturbations
are under analysis, tighter convergence is required.

(i)   The angular quadrature constants (direction cosines and weights)
for the specified order of S_N approximation were taken from ANISN
manual.

5.3   Fission neutron spectrum

The energy distribution of neutrons produced in the fission
process is known as the fission spectrum and has been measured for
all the common fissile elements.   Although rarely encountered in
reactor experiments, the fission spectrum is a convenient reference
and has been used extensively in developing conventions for reporting

data. Several semi-empirical representations of the fission spectrum have been proposed and fitted to the experimental results within the accuracy of the measurements and are in common usage. Three of these, the formulae of Watt, Cranberg, and Grundl will be discussed for illustration purposes[87].

The Watt fission spectrum is represented by the equation

$$\phi(E) = C \exp(-E) \sinh(2E)^{\frac{1}{2}} \qquad (5.1)$$

where E is in units of MeV. For a normalized distribution C is equal to $(2/\pi e)^{\frac{1}{2}} = 0.484$

The Cranberg equation is:

$$\phi(E) = C \exp(-E/0.965) \sinh(2.29E)^{\frac{1}{2}} \qquad (5.2)$$

$$C = 0.45270$$

This expression differs only slightly from that due to Watt. In the method of Grundl the fission spectrum is represented by the equation

$$\phi(E) = C E^{\frac{1}{2}} \exp(-BE) \qquad (5.3)$$

with

$$B = 0.776$$

and

$$C = 2B^{3/2} / \pi^{1/2} = 0.77$$

The computer program CHI was used to calculate the $\phi(E)$ fission spectrum from these three relations for the 37 group GALAXY energy boundaries. The program calculates the probability distribution of the function $\phi(E)$ so that the area under the curve is one. The representations of these fission spectra are illustrated in Fig. 5.1. Except for minor departures in the high energy range (E > 5 MeV), the Watt and Cranberg forms are very nearly the same, while the Grundl form differs significantly in the lower energies. Throughout the present calculation the Cranberg fission spectrum was used. This choice is arbitrary and based primarily on its more widespread usage. The illustrated differences in fission spectrum forms may lead to differences in spectrum calculations. For this reason, it is important to specify the form being used.

5.4 Degrees of approximation

In the present calculations, a comparison of the two S_N approximations were made only with isotropic scattering. However, a comparison based on Emmett's calculations made with S_4P_0 and S_8P_6 approximations show that on average the discrepancy between these two approximations was sufficiently small to justify the use of S_4P_0 approximation. The ratio S_8P_6/S_4P_0 varied from 1.062 to 1.017 over the energy range 40 keV to 2 MeV, respectively. Therefore, for sensitivity calculation, it is thought that the use of the S_4P_0 approximation calculations is adequate with a reasonably good confidence in results.
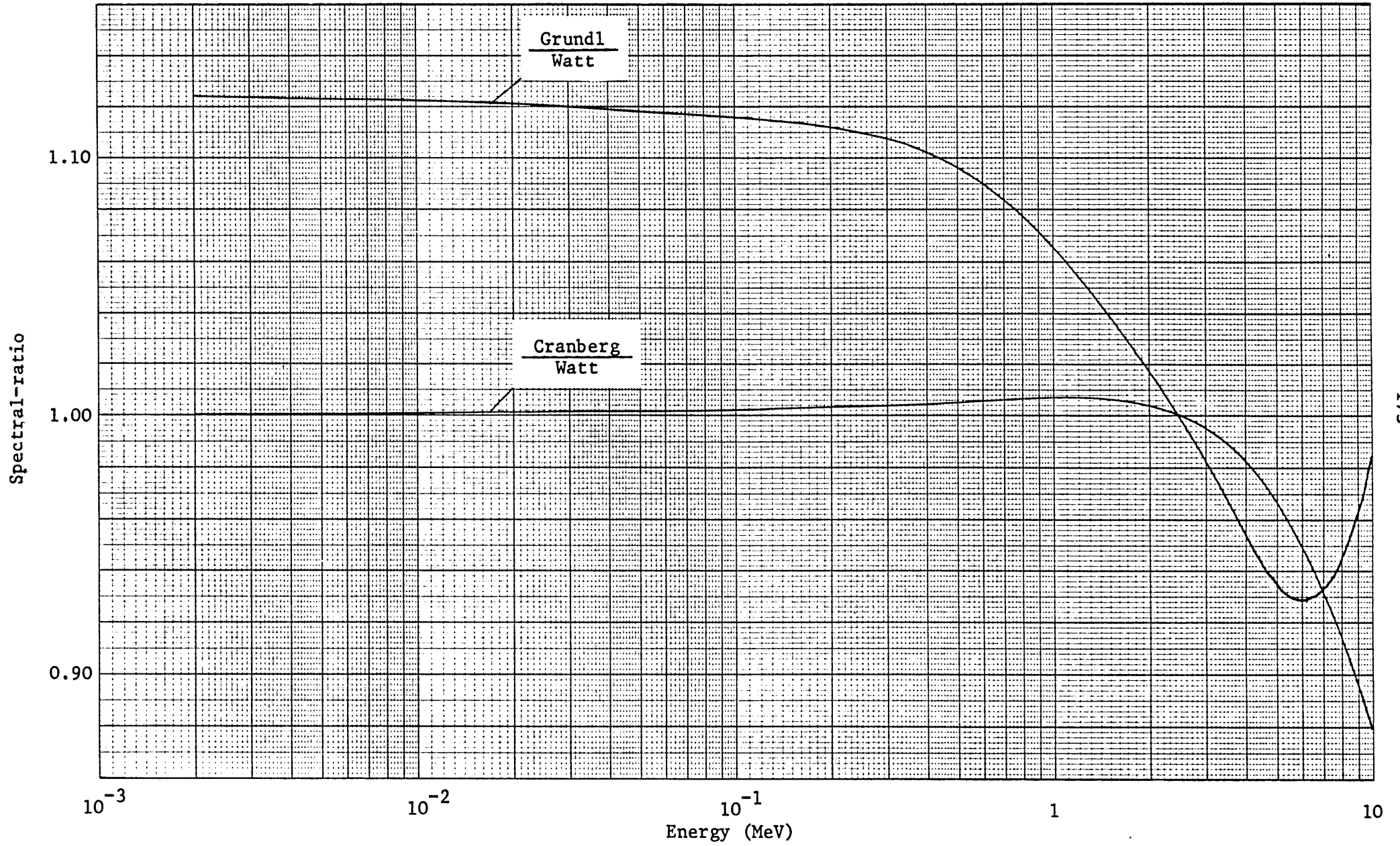
Fig. 5.1 Variation of the Cranberg/Watt and Grundl/Watt spectral-ratios with energy.

The CDC 6600 computer CP (Central Processing) time and the usage of the units depend on the individual problem, but on average the S_4P_o approximation calculation requires about 450 seconds and uses approximately 20 units.

5.5 Methods of calculation

The central NISUS spectrum and reaction rate ratios are the major concern of the standard neutron field measurements. The uncertainties which could have an effect on the shape of the spectrum and the reaction rates may be considered in two broad categories: macroscopic parameters and cross sections. The first includes density, impurity, abundance, and tolerance; the last includes nuclear data file. The effect of these uncertainties in NISUS components on the central spectrum and reaction rate ratios were calculated using ANISN one-dimensional discrete code. In these calculations the UKNDL/GALAXY 37 group structure was used and 20 reaction rates were calculated. The total flux in the NISUS central spectrum was expressed in units of flux per unit lethargy. The 37 group structure and lethargy width are shown in Table 5.1.

The reaction rate ratios were found relative to the most fundamental reaction rate, $^{235}U(n,f)$. The computer program LETHAR with subroutine RATIO was written to calculate flux per unit lethargy and reaction rate ratios. The program also calculates the percent difference between two spectra in 37 groups and that of the reaction rate ratios. The data input for this program were the NISUS central total flux $(n.cm^{-2}.sec^{-1})$ by group and activities (reactions $cm^{-3}.sec^{-1}$)

TABLE 5.1

The GALAXY 37 group structure and lethargy width

Group	Energy interval (MeV)		Lethargy
1	14.60E+00	13.50E+00	78.33184E-03
2	13.50E+00	12.50E+00	76.96104E-03
3	12.50E+00	11.25E+00	10.53605E-02
4	11.25E+00	10.00E+00	11.77830E-02
5	10.00E+00	85.00E-01	16.25189E-02
6	85.00E-01	70.00E-01	19.41560E-02
7	70.00E-01	60.70E-01	14.25515E-02
8	60.70E-01	47.20E-01	25.15498E-02
9	47.20E-01	36.80E-01	24.88960E-02
10	36.80E-01	28.70E-01	24.86007E-02
11	28.70E-01	17.40E-01	50.04269E-02
12	17.40E-01	11.50E-01	41.41232E-02
13	11.50E-01	82.10E-02	33.63941E-02
14	82.10E-02	63.90E-02	25.06187E-02
15	63.90E-02	38.80E-02	49.88991E-02
16	38.80E-02	23.50E-02	50.14198E-02
17	23.50E-02	14.30E-02	49.67409E-02
18	14.30E-02	11.10E-02	25.33144E-02
19	11.10E-02	86.50E-03	24.93858E-02
20	86.50E-03	67.40E-03	24.94994E-02
21	67.40E-03	40.90E-03	49.95150E-02
22	40.90E-03	24.80E-03	50.02864E-02
23	24.80E-03	15.00E-03	50.27935E-02
24	15.00E-03	91.20E-04	49.75804E-02
25	91.20E-04	43.10E-04	74.95319E-02
26	43.10E-04	20.40E-04	74.79881E-02
27	20.40E-04	96.10E-05	75.27307E-02
28	96.10E-05	58.30E-05	49.97872E-02
29	58.30E-05	27.50E-05	75.14161E-02
30	27.50E-05	16.60E-05	50.47833E-02
31	16.60E-05	75.50E-06	76.78551E-02
32	75.50E-06	27.70E-06	10.02700E-01
33	27.70E-06	16.00E-06	54.88437E-02
34	16.00E-06	50.00E-08	34.65736E-01
35	50.00E-08	18.00E-08	10.21651E-01
36	18.00E-08	70.00E-09	94.44616E-02
37	70.00E-09	10.00E-10	42.43495E-01

of the ANISN outputs. Table (5.2) shows the 20 data files used for reactions cross sections and their origins[86]. The last reaction with unity cross section reflects the average total flux in the NISUS centre. The cross sections for these reactions were produced by Emmett in the same group structure as obtained from GALAXY program.

5.6 Nuclear data file

The 37 group GALAXY cross section data file was used for ANISN and one-dimensional discrete code. It was found that in some energy groups the corresponding cross section values for the two different weighting functions, i.e. $1/E$ and $1/\Sigma_t$, are not the same. ANISN calculation showed that the fission ratio in the NISUS uranium shell with $1/E$ data file is ~ 6 times greater than that with $1/\Sigma$ cross section set. The experimental results obtained by S S T R (see Chapter 7) agree with $1/\Sigma$ data file. A careful study of the two data sets which have been used by some research workers for several years showed that there are some significant errors in both cross section lists. Comparing $1/\Sigma_t$ list with the $1/E$ data set shows the following differences for different materials:

5.6.1 Aluminium

(a) The values of the downscatters to group one in the first three groups in the $1/\Sigma$ list are too large by a factor of 10.

(b) Absorption cross sections in some groups are considerably smaller compared with those of the $1/E$ list, e.g. in groups 22 and 37 with the factors of ~ 3 and ~ 5 respectively.

TABLE 5.2

The reactions cross sections data file and their origins

No	Reaction	Origins[86]
1	^{58}Ni (n,p) ^{58}Co	Grundl 50 group set
2	^{56}Fe (n,p) ^{56}Mn	Grundl 50 group set
3	^{115}In (n,n')^{115m}In	Grundl 50 group set
4	^{238}U (n,f)	Grundl 50 group set
5	^{56}Fe (n,p) ^{56}Mn	Howey 50 group set
6	^{32}S (n,p) ^{32}P	Howey 50 group set
7	^{103}Rh (n,n') ^{103m}Rh	Howey 50 group set
8	^{56}Mn (n,γ) ^{56}Mn	Howey 50 group set*
9	^{115}In (n,γ)^{116}In	Combined Grundl and Howey
10	^{197}Au (n,γ)^{198}Au	Combined Grundl and Howey
11	^{115}In (n,γ)^{116}In(Cd)	Howey 50 group set
12	^{197}Au (n,γ)^{198}Au(Cd)	Howey 50 group set
13	^{56}Mn (n,γ) ^{56}Mn(Cd)	Howey 50 group set*
14	^{197}Au (n,γ)^{198}Au	Howey 50 group set
15	^{56}Mn (n,γ) ^{56}Mn	Howey 50 group set
16	^{56}Mn (n,γ) ^{56}Mn(Cd)	Howey 50 group set
17	^{238}U (n,f)	UKNDL/GALAXY
18	^{238}U (n,γ)	UKNDL/GALAXY
19	^{235}U (n,f)	UKNDL/GALAXY
20	1.0	

*Resonances suppressed

(c)   Selfscatter in group 22 is about 7 times smaller than, and

that of the group 20 is nearly half of the corresponding values in

the 1/E data.

(d)   In groups 20, 22 and 23 downscatters from preceeding groups

are nearly half of those in the 1/E weighting function list.

(e)   Total cross sections in groups 22 and 37 are smaller than

the corresponding values in the 1/E list with the factors of ∿6 and

∿ 2 respectively.

5.6.2   Boron 11

(a)   In the $1/\Sigma$ data list, absorption cross section in groups 23

and 37 are smaller by factors of ∿ 4 and ∿ 5 respectively.

(b)   Selfscatter cross section in group 11 is about 10% smaller

than that in the 1/E list.   Downscatter in group 13 from the preceeding

group is small with a factor of 1.2 in the $1/\Sigma$ data set.

5.6.3   Boron 10

There is no appreciable difference between the two ^{10}B cross

section sets.

5.6.4   Carbon

(a)   In the $1/\Sigma$ weighting function list, in group 9, downscatters

from groups 2-6 are zero, and that from group one is large by a factor

of 10.

(b)   In the first five groups, downscatters from groups 1-5 are at

the order of few hundreds mb in the 1/E cross section data, but they

were given as zero in the 1/Σ list.

(c)   In the 1/Σ weighting function data, from group 10 onwards, downscatters less than 10 mb were given as zero, and in group 10 downscatter from group 5 is at the order of a hundred mb in the 1/E list, but it was also given as zero in the 1/Σ list.

5.6.5   Uranium 235

Absorption and fission cross sections in the 1/E list in groups 32 and 34 are twice those in the 1/Σ data set, and in group 33 is large by a factor of $\sim$ 3. The difference between the two sets is about 20% in groups 29 and 30 and at the order of 5 magnitude in thermal region (group 37). The above-mentioned difference in groups 29 to 34 are due to the resonances which are suppressed in the 1/Σ set.

5.6.6   Uranium 238

Absorption cross section in the list with 1/E weighting function is drastically higher by factors of 2 to 59 in groups 26 - 34, while the maximum discrepancy in the total and self-scattering cross sections in the same range is a factor of about 15 in group 33, and about 8 in group 32, respectively. These differences are again due to the suppression of resonances in the 1/Σ data.

5.6.7   Conclusions

The conclusion is that neither of the two data sets is reliable, but a cross-check with the Neutron Cross-Sections BNL-325[88]

and Azad's[17] results showed that the cross section list with $1/\Sigma_t$

weighting function is rather more acceptable than the other one, in

particular in the case of important reaction ^{235}U(n,f) below 580 eV .

The differences which are expected to produce the largest effect

on central NISUS spectrum are those due to resonance effects below

$\sim$ 1 keV. Neither set can be expected to perform well in this region,

but the $1/\Sigma_t$ data provides the more acceptable fission rate distribution

across the shells. The latter is important, for it determines the

fast spectrum in NISUS. Thus $1/\Sigma_t$ cross section list was chosen as

data file for ANISN calculations.

5.7   Density variations

The values given for aluminium density are consistent to better

than $\pm$ 0.05% in the literature. So, the effect of variation in density

for graphite, boron carbide, and uranium shell was studied.

5.7.1   Graphite density

The density of graphite depends on the quality or grade and

impurities[89], and different values are reported in the publications

(Table 5.3).

A measurement was made to determine the graphite density used

in NISUS configuration. A specimen of NISUS graphite thermal column

was chosen and cut in cylindrical form with 74.40 $\pm$ 0.02 mm diamter and

95.40 $\pm$ 0.02 mm length. The weight of the sample was measured

714.21 $\pm$ 0.01 gm and the density was determined as 1.722 $\pm$ 0.001 gm/cm^3.

The calculation showed that the total flux in all groups for the graphite density of 1.722 gm/cm^3 is less than that with the density of 1.60 gm/cm^3. This variation is about 12% in the top group down to 6.7% in thermal region (Table 5.4). It was also found that the effect of this variation in graphite density in the reaction rate ratios is less than 1% in the case of threshold detectors and ^{238}U (n,f) and ^{238}U (n,γ) reactions, but it is of the order of 2.0% and 2.5% for Mn (n,γ) reaction for suppressed and not suppressed resonances, respectively. The difference for the rest of the reaction rate ratios is of the order of 1%, except In (n,γ) bare reaction, which is about 0.5% (Table 5.5).

TABLE 5.3

Variation of graphite density in the literature

Graphite density gm/cm^3	References
1.60	(90)
1.62	(91)
2.27 – 2.28	(92)
2.3	(93)
2.30 – 2.72	(94)

TABLE 5.4

Flux per unit lethargy

Group	Graphite density (gm/cm^3)		Difference, %
	1.722	1.60	
1	13.78363E-08	15.43125E-08	11.95
2	30.93926E-08	34.63632E-08	11.95
3	73.26672E-08	82.02051E-08	11.95
4	18.14043E-07	20.30772E-07	11.95
5	48.00922E-07	53.74450E-07	11.95
6	13.00417E-06	14.55506E-06	11.93
7	26.41921E-06	29.56711E-06	11.92
8	50.54689E-06	56.56478E-06	11.91
9	89.00382E-06	99.59214E-06	11.90
10	12.60001E-05	14.09831E-05	11.89
11	16.02705E-05	17.92504E-05	11.84
12	20.02337E-05	22.38371E-05	11.79
13	31.61776E-05	35.33554E-05	11.76
14	40.24365E-05	44.96676E-05	11.74
15	44.35159E-05	49.52747E-05	11.67
16	39.08868E-05	43.61770E-05	11.59
17	30.01688E-05	33.46123E-05	11.47
18	25.40237E-05	28.29517E-05	11.39
19	21.72384E-05	24.17700E-05	11.29
20	19.59158E-05	21.77998E-05	11.17
21	13.62379E-05	15.11216E-05	10.92
22	82.13377E-06	90.82134E-06	10.58
23	48.22919E-06	53.10610E-06	10.11
24	29.80495E-06	32.65480E-06	9.56
25	16.43515E-06	17.89286E-06	8.87
26	12.84809E-06	13.89675E-06	8.16
27	10.40363E-06	11.21047E-06	7.76
28	78.11490E-07	84.03388E-07	7.58
29	52.70123E-07	56.59791E-07	7.39
30	34.65372E-07	37.17948E-07	7.29
31	20.16741E-07	21.61043E-07	7.16
32	69.82185E-08	74.73600E-08	7.04
33	19.79194E-08	21.17399E-08	6.98
34	33.62189E-10	35.91529E-10	6.82
35	33.06880E-12	35.31043E-12	6.78
36	46.49336E-14	49.62938E-14	6.75
37	26.37590E-15	29.57329E-15	12.12

TABLE 5.5

Reaction rate ratios

Reaction	Graphite density (gm/cm³)		Difference %
	1.722	1.60	
^{58}Ni(n,p) ^{58}Co	18.09645E-03	18.21899E-03	.68
^{56}Fe(n,p) ^{56}Mn	16.09527E-05	16.20956E-05	.71
^{115}In(n,n') ^{115m}In	33.99325E-03	34.20946E-03	.64
^{238}U (n,f)	53.52106E-03	53.86549E-03	.64
^{56}Fe(n,p) ^{56}Mn	93.29380E-06	93.96208E-06	.72
^{32}S (n,p) ^{32}P	11.03743E-03	11.11185E-03	.67
^{103}Rh(n,n') ^{103m}Rh	22.65384E-02	22.78633E-02	.58
^{56}Mn(n,γ) ^{56}Mn	16.91677E-03	16.59669E-03	-1.89
^{115}In(n,γ) ^{116}In	19.07686E-02	18.98585E-02	-.48
^{197}Au(n,γ) ^{198}Au	28.95133E-02	28.61936E-02	-1.15
^{115}In(n,γ) ^{116}In (Cd)	83.19246E-03	81.87383E-03	-1.58
^{197}Au(n,γ) ^{198}Au (Cd)	28.91213E-02	28.57990E-02	-1.15
^{56}Mn(n,γ) ^{56}Mn (Cd)	16.91589E-03	16.59584E-03	-1.89
^{197}Au(n,γ) ^{198}Au	28.91270E-02	28.53045E-02	-1.15
^{56}Mn(n,γ) ^{56}Mn	26.65988E-03	26.00999E-03	-2.44
^{56}Mn(n,γ) ^{56}Mn (Cd)	26.65899E-03	26.00915E-03	-2.44
^{238}U (n,f)	52.74289E-03	53.08527E-03	.65
^{238}U (n,γ)	14.25027E-02	14.16568E-02	-.59
^{235}U (n,f)	10.00000E-01	10.00000E-01	0.00
1.0	66.86772E-02	67.02887E-02	.24

5.7.2 Boron carbide density

There are two boron carbide shells available for NISUS :
Belgian and American shells with densities of 1.49 and 1.58 gm/cm^3,
respectively. The physical dimensions of these shells are given
in Table 5.6.

The calculation showed (Table 5.7) that the effect of about 6%
increment in boron carbide density is less than 2% in the total flux
above 10 keV, but it becomes significant in the lower tail of the
spectrum where the boron absorption cross section is high. . It is
seen that in the energy range 40.9 - 9.12 keV the difference between
the two spectra is about -1%. This seems surprising in the view of
the expected higher absorption by the denser boron carbide shell. A
similar effect is observed in the case of 1 mm tolerance in the B_4C
shell (Table 5.18).

The effect of variation in boron carbide density is negligible
in the reaction rate ratios for the threshold detectors (Table 5.8).
It was found that the increase of 6% in boron carbide density results
in 2.8% and 4.0% decrease in the reaction rate ratios of Mn (n,γ) for
suppressed and not suppressed resonances, respectively. This decrement
is about 1.5% for Au (n,γ) (bare and cadmium cover) and In (n,γ)
(cadmium cover) reactions. In the case of bare In (n,γ) reaction the
difference is 0.6%.

5.7.3 Uranium density

The NISUS central spectrum and reaction rates were calculated
for uranium densities of 18.84[94] and 18.92[6] gm/cm^3 respectively.

It was found that the difference between the two spectra is less than ± 1% over the whole 37 group, and the difference in the reaction rate ratios is less than 0.4%.for all reactions (Tables 5.9 and 5.10).

5.8   Impurities

The impurities in graphite depends on the grade[89] and may vary from batch to batch, and the actual determination is only possible by chemical analysis.   Some typical impurities are : aluminium, boron, calcium, iron, nickel, silicon etc.   Among the major impurities which could have an effect in neutron slowing down and consequently in the NISUS central spectrum is thought to be water and boron which may have a considerable effect on graphite capture cross section.

TABLE   5.6

NISUS boron carbide shells[*]

Ref.	Diameter (mm)			ρ
No.	Inner	Outer	Hole	gm/cm^3
B_4C 1	110 ±.1	144 ±.1	17	1.49
B_4C 2	123.4 ±.1	157.4 ±.1	45.75 ± .05 Straight hole OR 55.0 ± .05 Stepped hole	1.58

Note: * Dimensions given for Al cladding, t=1 mm .

TABLE 5.7

Flux per unit lethargy

| Group | Boron carbide density (gm/cm^3) | | Difference % |
	1.58	1.49	
1	13.60527E-08	13.78363E-08	1.31
2	30.54952E-08	30.93926E-08	1.28
3	72.37681E-08	73.26672E-08	1.23
4	17.92865E-07	18.14043E-07	1.18
5	47.46751E-07	48.00922E-07	1.14
6	12.85788E-06	13.00417E-06	1.14
7	26.13180E-06	26.41921E-06	1.10
8	50.00314E-06	50.54689E-06	1.09
9	88.11920E-06	89.00382E-06	1.00
10	12.48263E-05	12.60001E-05	.94
11	15.87715E-05	16.02705E-05	.94
12	19.86589E-05	20.02337E-05	.79
13	31.38343E-05	31.61776E-05	.75
14	39.76469E-05	40.24365E-05	1.20
15	43.67394E-05	44.35159E-05	1.55
16	38.60904E-05	39.08868E-05	1.24
17	29.75265E-05	30.01688E-05	.89
18	25.21511E-05	25.40237E-05	.74
19	21.59010E-05	21.72384E-05	.62
20	19.46518E-05	19.59158E-05	.65
21	13.59290E-05	13.62379E-05	.23
22	82.46426E-06	82.13377E-06	-.40
23	48.58253E-06	48.22919E-06	-.73
24	29.97335E-06	29.80495E-06	-.56
25	16.35541E-06	16.43515E-06	.49
26	12.50248E-06	12.84809E-06	2.76
27	99.68017E-07	10.40363E-06	4.37
28	74.13641E-07	78.11490E-07	5.37
29	49.40581E-07	52.70123E-07	6.67
30	31.97495E-07	34.65372E-07	8.38
31	18.21514E-07	20.16741E-07	10.72
32	60.59574E-08	69.82185E-08	15.23
33	16.29411E-08	19.79194E-08	21.47
34	21.38870E-10	33.62189E-10	57.19
35	21.96802E-12	33.06880E-12	50.53
36	29.28728E-14	46.49036E-14	58.74
37	15.73324E-15	26.37590E-15	67.64

TABLE 5.8

Reaction rate ratios

Reaction	Boron carbide density (gm/cm^3)		Difference %
	1.58	1.49	
^{58}Ni(n,p)^{58}Co	18.09796E-03	18.0³645E-03	-.01
^{56}Fe(n,p)^{56}Mn	16.07783E-05	16.09527E-05	.11
^{115}In(n,n')^{115m}In	34.01771E-03	33.99325E-03	-.07
^{238}U (n,f)	53.56196E-03	53.52106E-03	-.08
^{56}Fe(n,p)^{56}Mn	93.17571E-06	93.29380E-06	.13
^{32}S (n,p)^{32}P	11.03941E-03	11.03743E-03	-.02
^{103}Rh(n,n')^{103m}Rh	22.65973E-02	22.65344E-02	-.03
^{56}Mn(n,γ)^{56}Mn	16.45159E-03	16.91677E-03	2.83
^{115}In(n,γ)^{116}In	18.96142E-02	19.07686E-02	.61
^{197}Au(n,γ)^{198}Au	28.51303E-02	28.95133E-02	1.54
^{115}In(n,γ)^{116}In (Cd)	82.02075E-03	83.19240E-03	1.43
^{197}Au(n,γ)^{198}Au (Cd)	28.47201E-02	28.91213E-02	1.55
^{56}Mn(n,γ)^{56}Mn (Cd)	16.45102E-03	16.91589E-03	2.83
^{197}Au(n,γ)^{198}Au	28.47238E-02	28.91270E-02	1.55
^{56}Mn(n,γ)^{56}Mn	25.64156E-03	26.65988E-03	3.97
^{56}Mn(n,γ)^{56}Mn (Cd)	25.64099E-03	26.65899E-03	3.97
^{238}U (n,f)	52.77810E-03	52.74289E-03	-.07
^{238}U (n,γ)	14.17249E-02	14.25027E-02	.55
^{235}U (n,f)	10.00000E-01	10.00000E-01	0.00
1.0	66.87405E-02	66.85772E-02	-.01

TABLE   5.9

Flux per unit lethargy

Group	Uranium density (gm/cm^3)		Difference %
	18.84	18.92	
1	13.60527E-08	13.57554E-08	-.22
2	30.54952E-08	30.48481E-08	-.21
3	72.37681E-08	72.22673E-08	-.21
4	17.92865E-07	17.89119E-07	-.21
5	47.46751E-07	47.36354E-07	-.22
6	12.85788E-06	12.82651E-06	-.24
7	26.13180E-06	26.06175E-06	-.27
8	50.00314E-06	49.85804E-06	-.29
9	88.11920E-06	87.84752E-06	-.31
10	12.48263E-05	12.44364E-05	-.31
11	15.87715E-05	15.82829E-05	-.31
12	19.86589E-05	19.81685E-05	-.25
13	31.38343E-05	31.35669E-05	-.09
14	39.76469E-05	39.77925E-05	.04
15	43.67394E-05	43.73896E-05	.15
16	38.60904E-05	38.69261E-05	.22
17	29.75265E-05	29.83135E-05	.26
18	25.21511E-05	25.29040E-05	.30
19	21.59010E-05	21.66196E-05	.33
20	19.46518E-05	19.53737E-05	.37
21	13.59290E-05	13.64427E-05	.38
22	82.46426E-06	82.72951E-06	.32
23	48.58253E-06	48.68520E-06	.21
24	29.97335E-06	29.99248E-06	.06
25	16.35541E-06	16.33031E-06	-.15
26	12.50248E-06	12.47187E-06	-.24
27	99.68017E-07	99.43453E-07	-.25
28	74.13641E-07	73.93140E-07	-.28
29	49.40581E-07	49.25372E-07	-.31
30	31.97495E-07	31.86250E-07	-.35
31	18.21514E-07	18.14301E-07	-.40
32	60.59574E-08	60.28469E-08	-.51
33	16.29411E-08	16.19006E-08	-.64
34	21.38870E-10	21.27775E-10	-.52
35	21.96802E-12	21.83813E-12	-.59
36	29.28728E-14	29.06279E-14	-.77
37	15.73324E-15	15.57677E-15	-.99

TABLE   5.10

Reaction rate ratios

Reaction	Uranium density (gm/cm^3)		Difference %
	18.84	18.92	
^{58}Ni(n,p)^{58}Co	18.09796E-03	18.02597E-03	-.40
^{56}Fe(n,p)^{56}Mn	16.07783E-05	16.02053E-05	-.36
^{115}In(n,n')^{115m}In	34.01771E-03	33.89273E-03	-.37
^{238}U (n,f)	53.56196E-03	53.35641E-03	-.38
^{56}Fe(n,p)^{56}Mn	93.17571E-06	92.85640E-06	-.34
^{32}S (n,p)^{32}P	11.03941E-03	10.99535E-03	-.40
^{103}Rh(n,n')^{103m}Rh	22.65973E-02	22.60273E-02	-.25
^{56}Mn(n,γ)^{56}Mn	16.45159E-03	16.42460E-03	-.16
^{115}In(n,γ)^{116}In	18.96142E-02	18.96075E-02	-.00
^{197}Au(n,γ)^{198}Au	28.51303E-02	28.49488E-02	-.06
^{115}In(n,γ)^{116}In (Cd)	82.02075E-03	81.97727E-03	-.05
^{197}Au(n,γ)^{198}Au (Cd)	28.47201E-02	28.45591E-02	-.06
^{56}Mn(n,γ)^{56}Mn (Cd)	16.45102E-03	16.42403E-03	-.16
^{197}Au (n,γ)^{198}Au	28.47238E-02	28.45628E-02	-.06
^{56}Mn(n,γ)^{56}Mn	25.64156E-03	25.57593E-03	-.26
^{56}Mn(n,γ)^{56}Mn (Cd)	25.64099E-03	25.57537E-03	-.26
^{238}U (n,f)	52.77810E-03	52.57151E-03	-.39
^{238}U (n,γ)	14.17249E-02	14.17062E-02	-.01
^{235}U (n,f)	10.00000E-01	10.00000E-01	0.00
1.0	66.87405E-02	66.87076E-02	-.00

5.8.1 Moisture in graphite

It was found[97] that the NISUS extension thermal column and the cavity have been made of graphite blocks supplied by the manufacturer more than 20 years ago. This long term storage could have resulted in absorption of an appreciable moisture in graphite. A measurement was made to determine the amount of water in graphite. The procedure was based on drying a sample in an oven and measuring the weight of the sample before and after drying. A sample of graphite extension thermal column was chosen and cut in eight discs each 7.5 cm diameter and 1.0 cm thick. The weights of the discs were measured to accuracy of $\pm$ 0.1 mg, and then dried in an oven at $100^{\circ}C$ for different drying times to find out the time in which all moisture is nearly dried out. It was found that at the end of drying time, when a sample is taken out of the oven it starts to absorb moisture in air immediately so that there is a sharp increase in weight followed by an approach to an asymptotic value. At the time of taking out the sample a stop watch was started and the weight was recorded as a function of elapsed time in one minute intervals for 90 min, after which the weight of the sample reached a value about 40 ppm less than the initial weight before drying. The weight of the sample at the end of the drying time can be determined by extrapolating to zero time. Fig. 5.2 shows a typical increase in weight as a function of time for a sample dried for 31 hours. The results of a set of experiments showed that the minimum time of 15 hours is required for graphite sample to be dried at $100^{\circ}C$. The average weight loss of several samples dried from 15 hours to about 4 days was found to be 0.0185 gm, resulting in the amount of 248 $\pm$ 2 ppm
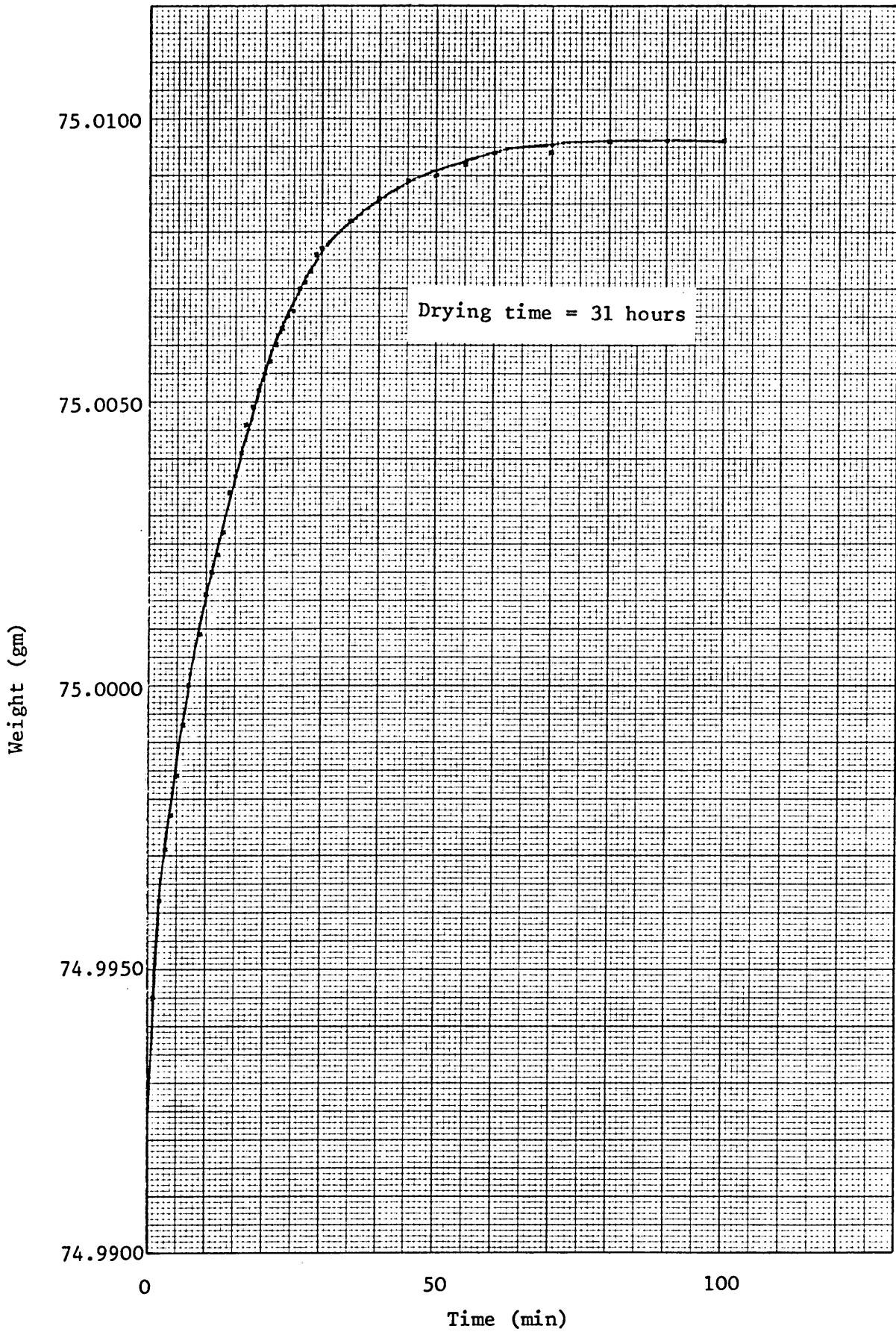
Fig. 5.2 Variation of the weight of the graphite sample as a function of time after taking out of the oven.

moisture in graphite. Taking this value into consideration and assuming that water and graphite are homogeneous mixture with the mean density factor of that graphite, ANISN code was used to calculate the NISUS central spectrum. The number densities of hydrogen and oxygen were taken as 16.71644 E - 06 and 83.58220 E - 07 respectively.

The effect of the moisture in graphite in the central NISUS spectrum is shown in Fig. 5.3 in comparison with the case assuming dry graphite. It is seen that the shape of the spectrum is unchanged, but when there is a moisture of 250 ppm the flux is about 13% lower than the case of dry graphite (Table 5.11). This is because of the high capture cross section of hydrogen and some contribution of oxygen. The ratio of the flux in the two spectra in all groups in constant within $<\pm$ 1%. Calculation of the reaction rates showed that the effect of moisture in graphite is negligible as far as reaction rate ratio is concerned. That is the difference in the reaction rate ratios is less than 0.2% for all reactions (Table 5.12).

5.8.2   Boron in graphite

Graphite capture cross section is an important factor in spectrum calculation and it was reported to be 3.4 mb for highest purity in graphite[88] and varies from 4.3 mb up to 6.0 mb for different grades[98]. Calculation showed that adding of 0.4 ppm ^{10}B in graphite results in a typical average capture cross section of 5 mb. Taking this value into account, NISUS central spectrum and reaction rate ratios were calculated and it was found that the effect of 0.4 ppm ^{10}B in graphite is to reduce the total flux in all

TABLE 5.11

Flux per unit lethargy

| Group | Moisture in graphite | | Difference |
	Dry	250 ppm	%
1	13.77560E-08	11.99851E-08	-12.90
2	30.92317E-08	26.93359E-08	-12.90
3	73.23283E-08	63.78432E-08	-12.90
4	18.13276E-07	15.79327E-07	-12.90
5	47.98943E-07	41.79775E-07	-12.90
6	12.99806E-06	11.32097E-06	-12.90
7	26.40601E-06	22.99866E-06	-12.90
8	50.52053E-06	44.00158E-06	-12.90
9	88.96091E-06	77.48146E-06	-12.90
10	12.59481E-05	10.96952E-05	-12.90
11	16.02177E-05	13.95412E-05	-12.91
12	20.02159E-05	17.43730E-05	-12.91
13	31.62313E-05	27.54091E-05	-12.91
14	40.24150E-05	35.04644E-05	-12.91
15	44.34712E-05	38.61979E-05	-12.91
16	39.09457E-05	34.04301E-05	-12.92
17	30.02418E-05	26.14166E-05	-12.93
18	25.41197E-05	22.12400E-05	-12.94
19	21.72860E-05	18.91603E-05	-12.94
20	19.59793E-05	17.06002E-05	-12.95
21	13.62932E-05	11.86097E-05	-12.97
22	82.17931E-06	71.48647E-06	-13.01
23	48.24977E-06	41.94862E-06	-13.06
24	29.80560E-06	25.89881E-06	-13.11
25	16.42808E-06	14.26573E-06	-13.16
26	12.82886E-06	11.13619E-06	-13.19
27	10.38029E-06	90.11147E-07	-13.19
28	77.89439E-07	67.62786E-07	-13.18
29	52.50211E-07	45.59511E-07	-13.16
30	34.48634E-07	29.95604E-07	-13.14
31	20.03368E-07	17.40739E-07	-13.11
32	69.19014E-08	60.14569E-08	-13.07
33	19.56215E-08	17.00791E-08	-13.06
34	32.94019E-10	28.65961E-10	-12.99
35	32.39861E-12	28.17080E-12	-13.05
36	45.22645E-14	39.25079E-14	-13.21
37	24.88707E-15	21.07742E-15	-12.90
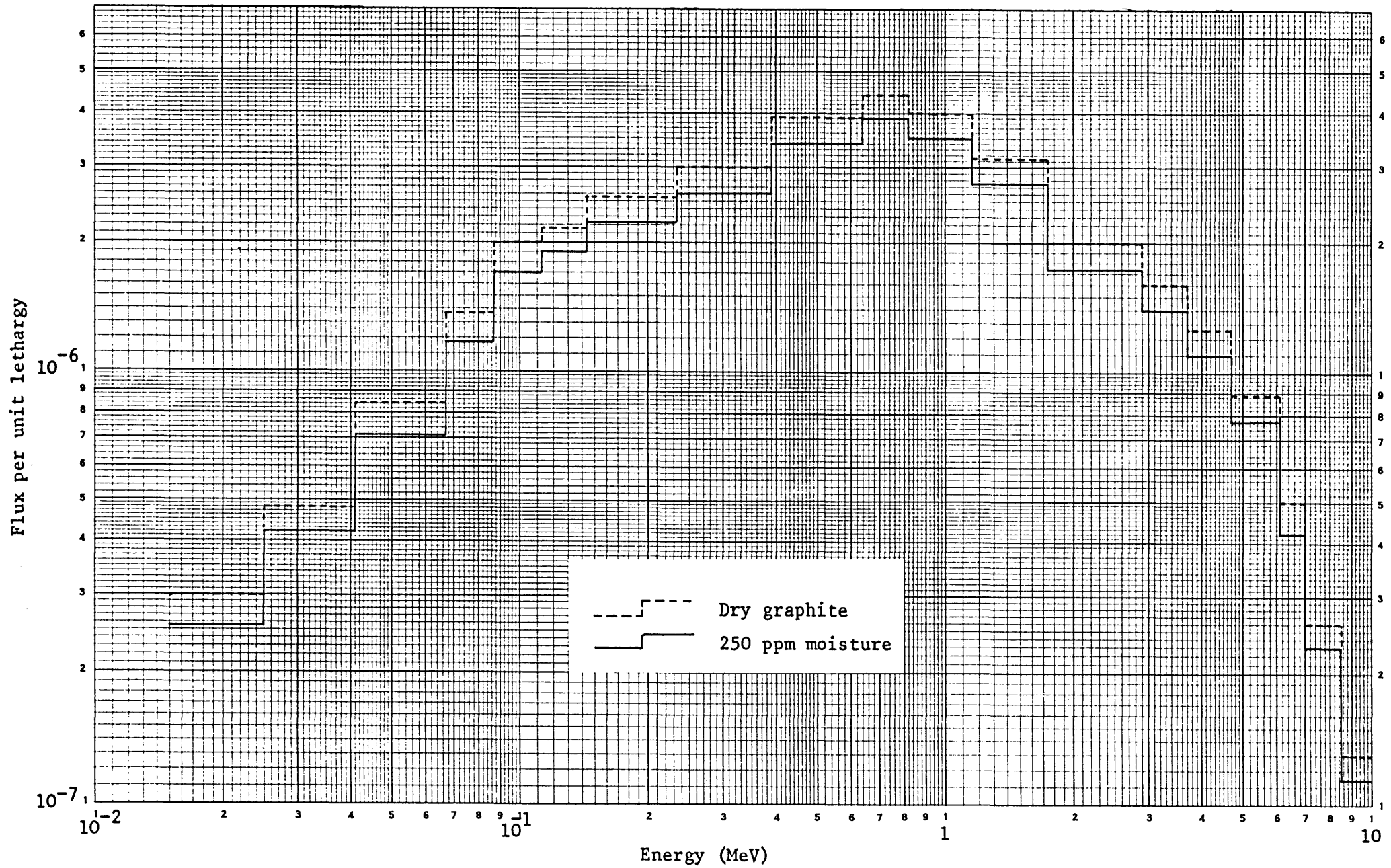
Fig. 5.3   Effect of moisture in graphite in the NISUS central spectrum.

TABLE 5.12

Reaction rate ratios

Reaction	Moisture in graphite		Difference %
	Dry	250 ppm	
^{58}Ni(n,p)^{58}Co	18.09796E-03	18.10870E-03	.06
^{56}Fe(n,p)^{56}Mn	16.07783E-05	16.08752E-05	.06
^{115}In(n,n')^{115m}In	34.01771E-03	34.03736E-03	.06
^{238}U (n,f)	53.56196E-03	53.59313E-03	.06
^{56}Fe(n,p)^{56}Mn	93.17571E-06	93.23202E-06	.06
^{32}S (n,p)^{32}P	11.03941E-03	11.04596E-03	.06
^{103}Rh(n,n')^{103m}Rh	22.65973E-02	22.67212E-02	.05
^{56}Mn(n,γ)^{56}Mn	16.45159E-03	16.43119E-03	-.12
^{115}In(n,γ)^{116}In	18.96142E-02	18.95496E-02	-.03
^{197}Au(n,γ)^{198}Au	28.51303E-02	28.48890E-02	-.08
^{115}In(n,γ)^{116}In (Cd)	82.02075E-03	81.91593E-03	-.13
^{197}Au(n,γ)^{198}Au (Cd)	28.47201E-02	28.44961E-02	-.08
^{56}Mn(n,γ)^{56}Mn (Cd)	16.45102E-03	16.43063E-03	-.12
^{197}Au(n,γ)^{198}Au	28.47238E-02	28.44998E-02	-.08
^{56}Mn(n,γ)^{56}Mn	25.64156E-03	25.60211E-03	-.15
^{56}Mn(n,γ)^{56}Mn (Cd)	25.64099E-03	25.60154E-03	-.15
^{238}U (n,f)	52.77810E-03	52.80894E-03	.06
^{238}U (n,γ)	14.17249E-02	14.16607E-02	-.05
^{235}U (n,f)	10.00000E-01	10.00000E-01	0.00
1.0	66.87405E-02	66.88966E-02	.02

groups by 38% (Table 5.13). However, no effect is observed at all in the reaction rate ratios (Table 5.14).

5.9   Abundance variations

The percent of abundance of some isotopes given on "atom percent" basis is different in the publications. This variation is negligible for ^{238}U and less than 1.3%[93-96] for ^{235}U. Because of this nominal discrepancy, the variation only in ^{10}B isotopic abundance was considered.

5.9.1 ^{10}B abundance

Some of the light elements have variations in compositions outside the accuracy of determinations, and significant differences in the abundance values have been observed in some samples. Table 5.15 shows the different isotopic abundance of ^{10}B in the literature.

The NISUS central flux and the reaction rates were calculated for abundances of 18.37% and 19.78% respectively. The results show the greater the ^{10}B abundance the lower the total flux at different energy groups, because of ^{10}B high absorption cross section. It was found as far as spectrum measurement concerned this effect is that   are
negligible (< 1%) above 70 keV, but it is significant in thermal region. In the case of reaction rate ratios the difference in ^{10}B abundance would have an effect of about 2.2% and 4.0% in the Au (n,γ) and Mn (n,γ) reactions, respectively. Other relevant reactions are less sensitive ($\sim \pm$ 1%) than these (Tables 5.16 and 5.17).

TABLE 5.13

Flux per unit lethargy

Group	^{10}B in graphite		Difference %
	Pure	.4 ppm	
1	13.60527E-08	84.35793E-09	-38.00
2	30.54952E-08	18.94070E-08	-38.00
3	72.37681E-08	44.87281E-08	-38.00
4	17.92365E-07	11.11556E-07	-38.00
5	47.46751E-07	29.42917E-07	-38.00
6	12.85788E-06	79.71682E-07	-38.00
7	26.13180E-06	16.20133E-06	-38.00
8	50.00314E-06	31.00117E-06	-38.00
9	88.11920E-06	54.63249E-06	-38.00
10	12.43263E-05	77.39024E-06	-38.00
11	15.87715E-05	98.43615E-06	-38.00
12	19.86589E-05	12.31658E-05	-38.00
13	31.38343E-05	19.45728E-05	-38.00
14	39.76469E-05	24.65328E-05	-38.00
15	43.67394E-05	27.07714E-05	-38.00
16	38.60904E-05	23.93675E-05	-38.00
17	29.75265E-05	18.44586E-05	-38.00
18	25.21511E-05	15.63263E-05	-38.00
19	21.59010E-05	13.38527E-05	-38.00
20	19.45518E-05	12.06796E-05	-38.00
21	13.59290E-05	84.26589E-06	-38.01
22	82.46426E-06	51.12871E-06	-38.00
23	48.58253E-06	30.12124E-06	-38.00
24	29.97335E-06	18.58410E-06	-38.00
25	16.35541E-06	10.14033E-06	-38.00
26	12.50248E-06	77.51773E-07	-38.00
27	99.68017E-07	61.80217E-07	-38.00
28	74.13641E-07	45.96428E-07	-38.00
29	49.40581E-07	30.63074E-07	-38.00
30	31.97495E-07	19.82300E-07	-38.00
31	18.21514E-07	11.29289E-07	-38.00
32	60.59574E-08	37.56552E-08	-38.01
33	16.29411E-08	10.10112E-08	-38.01
34	21.38870E-10	13.25432E-10	-38.03
35	21.96802E-12	13.60726E-12	-38.06
36	29.28728E-14	18.12439E-14	-38.12
37	15.73324E-15	97.55122E-16	-38.00

TABLE 5.14

Reaction rate ratios

Reaction	^{10}B in graphite		Difference %
	Pure	.4 ppm	
$^{58}Ni(n,p)\,^{58}Co$	18.09796E-03	18.09792E-03	-.00
$^{56}Fe(n,p)\,^{56}Mn$	16.07783E-05	16.07782E-05	-.00
$^{115}In(n,n')\,^{115m}In$	34.01771E-03	34.01767E-03	-.00
$^{238}U(n,f)$	53.56196E-03	53.56193E-03	-.00
$^{56}Fe(n,p)\,^{56}Mn$	93.17571E-06	93.17572E-06	.00
$^{32}S(n,p)\,^{32}P$	11.03941E-03	11.03939E-03	-.00
$^{103}Rh(n,n')\,^{103m}Rh$	22.65973E-02	22.65967E-02	-.00
$^{56}Mn(n,\gamma)\,^{56}Mn$	16.45159E-03	16.45163E-03	.00
$^{115}In(n,\gamma)\,^{116}In$	18.95142E-02	18.96145E-02	.00
$^{197}Au(n,\gamma)\,^{198}Au$	28.51303E-02	28.51138E-02	-.01
$^{115}In(n,\gamma)\,^{116}In$ (Cd)	82.02075E-03	82.02195E-03	.00
$^{197}Au(n,\gamma)\,^{198}Au$ (Cd)	28.47201E-02	28.47211E-02	.00
$^{56}Mn(n,\gamma)\,^{56}Mn$ (Cd)	16.45102E-03	16.45106E-03	.00
$^{197}Au(n,\gamma)\,^{198}Au$	28.47238E-02	28.47247E-02	.00
$^{56}Mn(n,\gamma)\,^{56}Mn$	25.64156E-03	25.64151E-03	-.00
$^{56}Mn(n,\gamma)\,^{56}Mn$ (Cd)	25.64099E-03	25.64094E-03	-.00
$^{238}U(n,f)$	52.77810E-03	52.77806E-03	-.00
$^{238}U(n,\gamma)$	14.17249E-02	14.17256E-02	.00
$^{235}U(n,f)$	10.00000E-01	10.00000E-01	0.00
1.0	66.87405E-02	66.87379E-02	-.00

5.10 Tolerances

The only parts of NISUS arrangements which might be subject
to uncertainty in tolerance are the boron carbide shell and its
aluminium canning. The thickness of the uranium shell is well known
within ± 0.1 mm and the tolerance in cavity diameter is 1 part in
500. These two nominal tolerances are negligible as far as the accuracy
of calculations is concerned.

5.10.1 Tolerance in B_4C shell

A tolerance of 1 mm was assumed for boron carbide shell and
the NISUS central spectrum and the reaction rate ratios were calculated
for a 14 mm boron carbide shell. It was found that the thinner the
shell the higher the flux, much more noticably below 4.3 keV where the
variation is from about 3% up to 81% in the thermal region (Table 5.18).

TABLE 5.15

Isotopic abundance of ^{10}B

Atom %	Atomic mass	References
18.37 ± .04	10.8118	(6)
18.45	-	(95)
18.7	10.811	(93)
19.78	10.811	(94)
19.8	10.81	(96)
19.8 ± .2	-	(99)

TABLE 5.16

Flux per unit lethargy

Group	^{10}B abundance		Difference %
	19.78%	18.37%	
1	13.60527E-08	13.63763E-08	.24
2	30.54952E-08	30.62213E-08	.24
3	72.37681E-08	72.55612E-08	.25
4	17.92865E-07	17.97463E-07	.26
5	47.46751E-07	47.59365E-07	.27
6	12.85788E-06	12.89257E-06	.27
7	26.13180E-06	26.20218E-06	.27
8	50.00314E-06	50.14081E-06	.28
9	88.11920E-06	88.40912E-06	.33
10	12.43263E-05	12.52340E-05	.33
11	15.87715E-05	15.92177E-05	.28
12	19.86589E-05	19.92591E-05	.30
13	31.38343E-05	31.53684E-05	.49
14	39.76469E-05	39.96865E-05	.51
15	43.67394E-05	43.90469E-05	.53
16	38.60904E-05	38.86711E-05	.67
17	29.75265E-05	30.00083E-05	.83
18	25.21511E-05	25.47040E-05	1.01
19	21.59010E-05	21.84801E-05	1.19
20	19.46518E-05	19.74216E-05	1.42
21	13.59290E-05	13.85029E-05	1.89
22	82.46426E-06	84.58105E-06	2.57
23	48.58253E-06	50.18202E-06	3.29
24	29.97335E-06	31.16829E-06	3.99
25	16.35541E-06	17.09815E-06	4.54
26	12.50248E-06	13.07437E-06	4.57
27	99.68017E-07	10.47377E-06	5.07
28	74.13641E-07	78.58884E-07	6.01
29	49.40581E-07	52.93196E-07	7.14
30	31.97495E-07	34.83578E-07	8.95
31	18.21514E-07	20.25165E-07	11.18
32	60.59574E-08	70.58067E-08	16.48
33	16.29411E-08	20.28541E-08	24.50
34	21.38876E-10	36.62708E-10	71.25
35	21.96802E-12	37.10036E-12	68.88
36	29.28728E-14	52.54281E-14	79.40
37	15.73324E-15	30.00321E-15	90.70

TABLE   5.17

Reaction rate ratios

Reaction	^{10}B abundance		Difference %
	19.78%	18.37%	
^{58}Ni(n,p) ^{58}Co	18.09796E-03	17.90746E-03	-1.05
^{56}Fe(n,p) ^{56}Mn	16.07783E-05	15.90366E-05	-1.08
^{115}In(n,n') ^{115m}In	34.01771E-03	33.66499E-03	-1.04
^{238}U (n,f)	53.56196E-03	52.99941E-03	-1.05
^{56}Fe(n,p) ^{56}Mn	93.17571E-06	92.16320E-06	-1.09
^{32}S (n,p) ^{32}P	11.03941E-03	10.92329E-03	-1.05
^{103}Rh(n,n') ^{103m}Rh	22.65973E-02	22.44358E-02	-.95
^{56}Mn(n,γ) ^{56}Mn	16.45159E-03	16.99125E-03	3.28
^{115}In(n,γ) ^{116}In	18.96142E-02	19.15581E-02	1.03
^{197}Au(n,γ) ^{198}Au	23.51303E-02	29.13682E-02	2.19
^{115}In(n,γ) ^{116}In (Cd)	82.02075E-03	84.61963E-03	3.17
^{197}Au(n,γ) ^{198}Au (Cd)	28.47201E-02	29.09778E-02	2.20
^{56}Mn(n,γ) ^{56}Mn (Cd)	16.45102E-03	16.99029E-03	3.28
^{197}Au(n,γ) ^{198}Au	28.47238E-02	29.09840E-02	2.20
^{56}Mn(n,γ) ^{56}Mn	25.64156E-03	26.74542E-03	4.30
^{56}Mn(n,γ) ^{56}Mn (Cd)	25.64099E-03	26.74446E-03	4.30
^{238}U (n,f)	52.77810E-03	52.22173E-03	-1.05
^{238}U (n,γ)	14.17249E-02	14.31961E-02	1.04
^{235}U (n,f)	10.00000E-01	10.00000E-01	0.00
1.0	66.87405E-02	66.62489E-02	-.37

Above 4.30 keV the total flux is about 1% higher in all groups

except in groups 22, 23 and 24 in the energy range 40.9 - 9.12 keV,

where the flux is reduced by about 1%. This seems surprising in

the view of the expected less absorption by the thinner boron carbide

shell. Similar effect was observed for variation in the B_4C density

(see Table 5.7).

In the reaction rate calculations (Table 5.19) the differences

in the reaction rate ratios are less than 0.2% for the threshold

detectors, and those of the Mn (n,γ) reactions are 3.2% and 4.5% for

suppressed and not suppressed reactions respectively. The difference

is about 1.8% for Au (n,γ) and In (n,γ) (cadmium covered) reactions

but less than 1% for bare In (n,γ) reaction.

5.10.2 Tolerance in Al canning

The effect of 0.5 mm tolerance in both sides of the boron

carbide aluminium canning was studied in the central spectrum and

reaction rate ratios. The effect is less than ± 1% in the total

flux in all groups except for the aluminium resonances at 35, 89

and 143 keV, where the differences are just over - 1% (Table 5.20).

In the reaction rate ratios the difference is about 1% for

the threshold detectors and negligible for the rest of the reaction

rates (Table 5.21).

5.11 Cross sections

In the spectrum and reaction rate calculations the largest

uncertainties are due to cross sections, mainly in uranium.

TABLE 5.18

Flux per unit lethargy

Group	Tolerance in B_4C shell		Difference %
	15 mm	14 mm	
1	13.60527E-08	13.79735E-08	1.41
2	30.54952E-08	30.96777E-08	1.37
3	72.37681E-08	73.32904E-08	1.32
4	17.92865E-07	18.15448E-07	1.26
5	47.46751E-07	48.04218E-07	1.21
6	12.85788E-06	13.01169E-06	1.20
7	26.13180E-06	26.43158E-06	1.15
8	50.00314E-06	50.56629F-06	1.13
9	88.11920E-06	89.02456E-06	1.03
10	12.48263E-05	12.60171E-05	.95
11	15.87715E-05	16.02825E-05	.95
12	19.86589E-05	20.02082E-05	.78
13	31.38343E-05	31.61254E-05	.73
14	39.76469E-05	40.25040E-05	1.22
15	43.67394E-05	44.35494E-05	1.56
16	38.60904E-05	39.07486E-05	1.21
17	29.75265E-05	30.00069E-05	.83
18	25.21511E-05	25.39058E-05	.70
19	21.59010E-05	21.71471E-05	.58
20	19.46518E-05	19.58642E-05	.62
21	13.59290E-05	13.61862E-05	.19
22	82.46426E-06	82.09933E-06	-.44
23	48.58253E-06	48.22264E-06	-.74
24	29.97335E-06	29.80986E-06	-.55
25	16.35541E-06	16.44444E-06	.54
26	12.50248E-06	12.87028E-06	2.94
27	99.68017E-07	10.43313E-06	4.67
28	74.13641E-07	78.42425E-07	5.78
29	49.40581E-07	53.08618E-07	7.45
30	31.97495E-07	34.97015E-07	9.37
31	18.21514E-07	20.43249E-07	12.17
32	60.59574E-08	71.26002E-08	17.60
33	16.29411E-08	20.38453E-08	25.10
34	21.38870E-10	36.19754E-10	69.24
35	21.96802E-12	35.06723E-12	59.63
36	29.28728E-14	49.73317E-14	69.81
37	15.73224E-15	28.47425E-15	80.98

TABLE 5.19

Reaction rate ratios

Reaction	Tolerance in B_4C shell		Difference %
	15 mm	14 mm	
$^{58}Ni(n,p)$ ^{58}Co	18.09796E-03	18.09975E-03	.01
$^{56}Fe(n,p)$ ^{56}Mn	16.07783E-05	16.10303E-05	.16
$^{115}In(n,n)$ ^{115m}In	34.01771E-03	33.99416E-03	-.07
$^{238}U(n,f)$	53.56196E-03	53.52335E-03	-.07
$^{56}Fe(n,p)$ ^{56}Mn	93.17571E-06	93.34491E-06	.18
$^{32}S(n,p)$ ^{32}P	11.03941E-03	11.03923E-03	-.00
$^{103}Rh(n,n)$ ^{103m}Rh	22.65973E-02	22.65267E-02	-.03
$^{56}Mn(n,\gamma)$ ^{56}Mn	16.45159E-03	16.97989E-03	3.21
$^{115}In(n,\gamma)$ ^{116}In	18.96142E-02	19.09700E-02	.72
$^{197}Au(n,\gamma)$ ^{198}Au	28.51303E-02	29.01769E-02	1.77
$^{115}In(n,\gamma)$ ^{116}In (Cd)	82.02075E-03	83.42314E-03	1.71
$^{197}Au(n,\gamma)$ ^{198}Au (Cd)	28.47201E-02	28.97846E-02	1.78
$^{56}Mn(n,\gamma)$ ^{56}Mn (Cd)	16.45102E-03	16.97894E-03	3.21
$^{197}Au(n,\gamma)$ ^{198}Au	28.47238E-02	28.97908E-02	1.78
$^{56}Mn(n,\gamma)$ ^{56}Mn	25.64156E-03	26.79768E-03	4.51
$^{56}Mn(n,\gamma)$ ^{56}Mn (Cd)	25.64099E-03	26.79674E-03	4.51
$^{238}U(n,f)$	52.77810E-03	52.74608E-03	-.06
$^{238}U(n,\gamma)$	14.17249E-02	14.26276E-02	.64
$^{235}U(n,f)$	10.00000E-01	10.00000E-01	0.00
1.0	66.87405E-02	66.85993E-02	-.02

TABLE 5.20

Flux per unit lethargy

Group	Tolerance in Al cladding		Difference %
	1 mm	.5 mm	
1	13.60527E-08	13.71606E-08	.81
2	30.54952E-08	30.79141E-08	.79
3	72.37681E-08	72.93629E-08	.77
4	17.92865E-07	18.06492E-07	.76
5	47.46751E-07	47.81983E-07	.74
6	12.85788E-06	12.95550E-06	.76
7	26.13180E-06	26.34171E-06	.80
8	50.00314E-06	50.37467E-06	.74
9	88.11920E-06	88.75038E-06	.72
10	12.48263E-05	12.55374E-05	.57
11	15.87715E-05	15.90831E-05	.20
12	19.86589E-05	19.99403E-05	.14
13	31.38343E-05	31.39592E-05	.04
14	39.76469E-05	39.86086E-05	.24
15	43.67394E-05	43.68094E-05	.02
16	38.60904E-05	38.49872E-05	-.29
17	29.75265E-05	29.75618E-05	.01
18	25.21511E-05	24.94277E-05	-1.06
19	21.59010E-05	21.63463E-05	.21
20	19.46518E-05	19.22377E-05	-1.24
21	13.59290E-05	13.47552E-05	-.86
22	82.46426E-06	81.60146E-06	-1.05
23	48.53253E-06	48.14987E-06	-.89
24	29.97335E-06	29.78968E-06	-.61
25	16.35541E-06	16.27807E-06	-.47
26	12.50248E-06	12.44944E-06	-.42
27	99.68017E-07	99.28203E-07	-.40
28	74.13641E-07	73.85103E-07	-.38
29	49.40581E-07	49.21553E-07	-.39
30	31.97495E-07	31.87387E-07	-.32
31	18.21514E-07	18.17934E-07	-.20
32	60.59574E-08	60.52442E-08	-.12
33	16.29411E-08	16.28145E-08	-.08
34	21.38870E-10	21.30356E-10	-.40
35	21.96802E-12	21.65159E-12	-1.44
36	29.28728E-14	29.02205E-14	-.91
37	15.73324E-15	15.71285E-15	-.13

TABLE   5.21

Reaction rate ratios

Reaction	Tolerance in Al cladding		Difference %
	1 mm	.5 mm	
^{58}Ni(n,p)^{58}Co	18.09796E-03	18.24782E-03	.83
^{56}Fe(n,p)^{56}Mn	16.07783E-05	16.24056E-05	1.01
^{115}In(n,n')^{115m}In	34.01771E-03	34.21683E-03	.59
^{238}U (n,f)	53.56196E-03	53.68661E-03	.61
^{56}Fe(n,p)^{56}Mn	93.17571E-06	94.11993E-06	1.01
^{32}S (n,p)^{32}P	11.03941E-03	11.12824E-03	.80
^{103}Rh(n,n')^{103m}Rh	22.65973E-02	22.76334E-02	.46
^{56}Mn(n,γ)^{56}Mn	16.45159E-03	16.41977E-03	-.19
^{115}In(n,γ)^{116}In	18.96142E-02	18.93830E-02	-.12
^{197}Au(n,γ)^{198}Au	28.51303E-02	28.45809E-02	-.19
^{115}In(n,γ)^{116}In (Cd)	82.02075E-03	81.69714E-03	-.39
^{197}Au(n,γ)^{198}Au (Cd)	28.47201E-02	28.41868E-02	-.19
^{56}Mn(n,γ)^{56}Mn (Cd)	16.45102E-03	16.41920E-03	-.19
^{197}Au(n,γ)^{198}Au	28.47238E-02	28.41905E-02	-.19
^{56}Mn(n,γ)^{56}Mn	25.64156E-03	25.59864E-03	-.17
^{56}Mn(n,γ)^{56}Mn (Cd)	25.64099E-03	25.59807E-03	-.17
^{238}U (n,f)	52.77810E-03	53.10817E-03	.63
^{238}U (n,γ)	14.17249E-02	14.15332E-02	-.14
^{235}U (n,f)	10.00000E-01	10.00000E-01	0.00
1.0	66.87405E-02	66.93334E-02	.09

Calculations were made to see how the central flux and the reaction rate ratios are sensitive to variations in fission cross sections. Although there might be some large uncertainties in the ^{238}U (n,n'), ^{238}U (n,γ) and ^{238}U (n,n) elastic cross sections, it is most important in the present measurements to understand the effect of errors in the fission cross sections since these can affect the measured fission rates in two ways : (i) in the generation of the fast neutron spectrum, and (ii) in the response function of the detectors themselves. In order to distinguish the calculations were made with fission cross sections of the uranium in the shells only changed.

5.11.1 Uranium 235

The calculations showed that a change of ± 2% in the fission cross section in all groups results in a decrease of about ± 4.6% in the total flux, while there is a negligible change in the reaction rate ratios for all groups (Tables 5.22 and 5.23).

5.11.2 Uranium 238

The effects of the cross section variations in the ^{238}U (n,f) reaction were studied separately for a change of ± 2% above threshold energy and ± 10% covering threshold region 1.74 - 0.639 Mev[94].

It was found that the effect of both changes in the fission cross sections is less than ± 1% and ± 0.1% in the central NISUS spectrum and reaction rate ratios, respectively (Tables 5.24 to 5.27).

TABLE 5.22

Flux per unit lethargy

Group	^{235}U(n,f) cross section*		Difference %
	No change	−2% (in 37 groups)	
1	13.60527E-08	12.97869E-08	−4.61
2	30.54952E-08	29.14254E-08	−4.61
3	72.37681E-08	69.04355E-08	−4.61
4	17.92865E-07	17.10295E-07	−4.61
5	47.46751E-07	45.28109E-07	−4.61
6	12.85788E-06	12.26549E-06	−4.61
7	26.13180E-06	24.92753E-06	−4.61
8	50.00314E-06	47.69823E-06	−4.61
9	88.11920E-06	84.05666E-06	−4.61
10	12.48263E-05	11.90712E-05	−4.61
11	15.87715E-05	15.14537E-05	−4.61
12	19.86589E-05	18.95088E-05	−4.61
13	31.38343E-05	29.93916E-05	−4.60
14	39.76469E-05	37.93523E-05	−4.60
15	43.67394E-05	41.66570E-05	−4.60
16	38.60904E-05	36.83367E-05	−4.60
17	29.75265E-05	28.38460E-05	−4.60
18	25.21511E-05	24.05660E-05	−4.59
19	21.59010E-05	20.59951E-05	−4.59
20	19.46518E-05	18.57380E-05	−4.58
21	13.59290E-05	12.97018E-05	−4.58
22	82.46426E-06	78.68459E-06	−4.58
23	48.58253E-06	46.35420E-06	−4.59
24	29.97335E-06	28.59640E-06	−4.59
25	16.35541E-06	15.60359E-06	−4.60
26	12.50248E-06	11.93003E-06	−4.58
27	99.68017E-07	95.11634E-07	−4.58
28	74.13641E-07	70.73906E-07	−4.58
29	49.40581E-07	47.14159E-07	−4.58
30	31.97495E-07	30.50947E-07	−4.58
31	18.21514E-07	17.38044E-07	−4.58
32	60.59574E-08	57.81774E-08	−4.58
33	16.29411E-08	15.54739E-08	−4.58
34	21.38870E-10	20.40859E-10	−4.58
35	21.96802E-12	20.96146E-12	−4.58
36	29.28728E-14	27.94513E-14	−4.58
37	15.73324E-15	15.33157E-15	−2.55

Note: * No change made in the ^{235}U(n,f) detector response.

TABLE 5.23

Reaction rate ratios

Reaction	$^{235}U(n,f)$ cross section*		Difference %
	No change	-2% (in 37 groups)	
$^{58}Ni(n,p)\ ^{58}Co$	18.09796E-03	18.09528E-03	-.01
$^{56}Fe(n,p)\ ^{56}Mn$	16.07783E-05	16.07573E-05	-.01
$^{115}In(n,n')\ ^{115m}In$	34.01771E-03	34.01320E-03	-.01
$^{238}U\ (n,f)$	53.56196E-03	53.55462E-03	-.01
$^{56}Fe(n,p)\ ^{56}Mn$	93.17571E-06	93.16424E-06	-.01
$^{32}S\ (n,p)\ ^{32}P$	11.03941E-03	11.03778E-03	-.01
$^{103}Rh(n,n')\ ^{103m}Rh$	22.65973E-02	22.65741E-02	-.01
$^{56}Mn(n,\gamma)\ ^{56}Mn$	16.45159E-03	16.45324E-03	.01
$^{115}In(n,\gamma)\ ^{116}In$	18.96142E-02	18.96210E-02	.00
$^{197}Au(n,\gamma)\ ^{198}Au$	28.51303E-02	28.51324E-02	.00
$^{115}In(n,\gamma)\ ^{116}In$ (Cd)	82.02075E-03	82.03019E-03	.01
$^{197}Au(n,\gamma)\ ^{198}Au$ (Cd)	28.47201E-02	28.47397E-02	.01
$^{56}Mn(n,\gamma)\ ^{56}Mn$ (Cd)	16.45102E-03	16.45267E-03	.01
$^{197}Au(n,\gamma)\ ^{198}Au$	28.47238E-02	28.47434E-02	.01
$^{56}Mn(n,\gamma)\ ^{56}Mn$	25.64156E-03	25.64441E-03	.01
$^{56}Mn(n,\gamma)\ ^{56}Mn$ (Cd)	25.64099E-03	25.64383E-03	.01
$^{238}U\ (n,f)$	52.77810E-03	52.77071E-03	-.01
$^{238}U\ (n,\gamma)$	14.17249E-02	14.17307E-02	.00
$^{235}U\ (n,f)$	10.00000E-01	10.00000E-01	0.00
1.0	66.87405E-02	66.87267E-02	-.00

Note: * No change made in the $^{235}U(n,f)$ detector response.

TABLE 5.24

Flux per unit lethargy

| Group | $^{238}U(n,f)$ cross section* | | Difference % |
	No change	+2% (above 1.74 MeV)	
1	13.60527E-08	13.72286E-08	.86
2	30.54952E-08	30.81320E-08	.86
3	72.37681E-08	73.00086E-08	.86
4	17.92865E-07	18.08333E-07	.86
5	47.46751E-07	47.87847E-07	.87
6	12.85788E-06	12.96989E-06	.87
7	26.13180E-06	26.36106E-06	.88
8	50.00314E-06	50.44472E-06	.88
9	88.11920E-06	88.90041E-06	.89
10	12.48263E-05	12.59336E-05	.89
11	15.87715E-05	16.01716E-05	.88
12	19.86589E-05	20.03803E-05	.87
13	31.38343E-05	31.64931E-05	.85
14	39.76469E-05	40.09729E-05	.84
15	43.67394E-05	44.03594E-05	.83
16	38.60904E-05	38.92734E-05	.82
17	29.75265E-05	29.99658E-05	.82
18	25.21511E-05	25.42097E-05	.82
19	21.59010E-05	21.76558E-05	.81
20	19.46518E-05	19.62256E-05	.81
21	13.59290E-05	13.70200E-05	.80
22	82.46426E-06	83.12029E-06	.80
23	48.58253E-06	48.96434E-06	.79
24	29.97335E-06	30.20577E-06	.78
25	16.35541E-06	16.47886E-06	.75
26	12.50248E-06	12.59593E-06	.75
27	99.68017E-07	10.04227E-06	.74
28	74.13641E-07	74.69028E-07	.75
29	49.40581E-07	49.77309E-07	.74
30	31.97495E-07	32.21228E-07	.74
31	18.21514E-07	18.35047E-07	.74
32	60.59574E-08	61.04459E-08	.74
33	16.29411E-08	16.41472E-08	.74
34	21.3387CE-10	21.54683E-10	.74
35	21.96802E-12	22.13034E-12	.74
36	29.28728E-14	29.50352E-14	.74
37	15.73324E-15	15.79746E-15	.41

Note: * No change made in the $^{238}(n,f)$ detector response.

TABLE 5.25

Reaction rate ratios

Reaction	^{238}U(n,f) cross section*		Difference %
	No change	+2% (above 1.74 MeV)	
^{58}Ni(n,p) ^{58}Co	18.09796E-03	18.10897E-03	.06
^{56}Fe(n,p) ^{56}Mn	16.07783E-05	16.08623E-05	.05
^{115}In(n,n') ^{115m}In	34.01771E-03	34.03613E-03	.05
^{238}U (n,f)	53.56196E-03	53.59207E-03	.06
^{56}Fe(n,p) ^{56}Mn	93.17571E-06	93.22126E-06	.05
^{32}S (n,p) ^{32}P	11.03941E-03	11.04614E-03	.06
^{103}Rh(n,n') ^{103m}Rh	22.65973E-02	22.66869E-02	.04
^{56}Mn(n,γ) ^{56}Mn	16.45159E-03	16.44387E-03	-.05
^{115}In(n,γ) ^{116}In	18.96142E-02	18.95861E-02	-.01
^{197}Au(n,γ) ^{198}Au	28.51303E-02	28.50229E-02	-.04
^{115}In(n,γ) ^{116}In (Cd)	82.02075E-03	81.98319E-03	-.05
^{197}Au(n,γ) ^{198}Au (Cd)	28.47201E-02	28.46299E-02	-.03
^{56}Mn(n,γ) ^{56}Mn (Cd)	16.45102E-03	16.44330E-03	-.05
^{197}Au(n,γ) ^{198}Au	28.47233E-02	28.46336E-02	-.03
^{56}Mn(n,γ) ^{56}Mn	25.64156E-03	25.62671E-03	-.06
^{56}Mn(n,γ) ^{56}Mn (Cd)	25.64099E-03	25.62614E-03	-.06
^{238}U (n,f)	52.77810E-03	52.80858E-03	.06
^{238}U (n,γ)	14.17249E-02	14.16991E-02	-.02
^{235}U (n,f)	10.00000E-01	10.00000E-01	0.00
1.0	66.87405E-02	66.87950E-02	.01

Note: * No change made in the ^{238}U(n,f) detector response.

TABLE 5.26

Flux per unit lethargy

| Group | $^{238}U(n,f)$ cross section[*] | | Difference |
	No change	· +10%[**]	%
1	13.60527E-08	13.71532E-08	.81
2	30.54952E-08	30.79624E-08	.81
3	72.37681E-08	72.96066E-08	.81
4	17.92865E-07	18.07338E-07	.81
5	47.46751E-07	47.85214E-07	.81
6	12.85788E-06	12.96278E-06	.82
7	26.13180E-06	26.34604E-06	.82
8	50.00314E-06	50.41717E-06	.83
9	88.11920E-06	88.85203E-06	.83
10	12.48263E-05	12.58651E-05	.83
11	15.87715E-05	16.00844E-05	.83
12	19.86589E-05	20.02705E-05	.81
13	31.38343E-05	31.63171E-05	.79
14	39.76469E-05	40.07483E-05	.78
15	43.67394E-05	44.01116E-05	.77
16	38.60904E-05	38.90542E-05	.77
17	29.75265E-05	29.97967E-05	.76
18	25.21511E-05	25.40664E-05	.76
19	21.59010E-05	21.75331E-05	.76
20	19.46518E-05	19.61150E-05	.75
21	13.59290E-05	13.69427E-05	.75
22	82.46426E-06	83.07341E-06	.74
23	48.58253E-06	48.93699E-06	.73
24	29.97335E-06	30.18893E-06	.72
25	16.35541E-06	16.47096E-06	.71
26	12.53248E-06	12.58921E-06	.69
27	99.68017E-07	10.03678E-06	.69
28	74.13641E-07	74.64539E-07	.69
29	49.40581E-07	49.74438E-07	.69
30	31.97495E-07	32.19387E-07	.68
31	18.21514E-07	18.34002E-07	.69
32	60.59574E-08	61.00992E-08	.68
33	16.29411E-08	16.40540E-08	.68
34	21.38870E-10	21.53460E-10	.68
35	21.96862E-12	22.11778E-12	.68
36	29.28728E-14	29.48678E-14	.68
37	15.73324E-15	15.79246E-15	.38

Note: * No change made in the $^{238}U(n,f)$ detector response.

   ** Energy range 1.74 - .693 MeV .

TABLE 5.27

Reaction rate ratios

Reaction	^{238}U(n,f) cross section[*]		Difference
	No change	+10%[**]	%
^{58}Ni(n,p) ^{58}Co	18.09796E-03	18.10919E-03	.06
^{56}Fe(n,p) ^{56}Mn	16.07783E-05	16.08637E-05	.05
^{115}In(n,n') ^{115m}In	34.01771E-03	34.03648E-03	.06
^{238}U (n,f)	53.56196E-03	53.59269E-03	.06
^{56}Fe(n,p) ^{56}Mn	93.17571E-06	93.22204E-06	.05
^{32}S (n,p) ^{32}P	11.03941E-03	11.04627E-03	.06
^{103}Rh(n,n') ^{103m}Rh	22.65973E-02	22.66862E-02	.04
^{56}Mn(n,γ) ^{56}Mn	16.45159E-03	16.44374E-03	-.05
^{115}In(n,γ) ^{116}In	18.96142E-02	18.95858E-02	-.01
^{197}Au(n,γ) ^{198}Au	28.51303E-02	28.50221E-02	-.04
^{115}In(n,γ) ^{116}In (Cd)	82.02075E-03	81.98324E-03	-.05
^{197}Au(n,γ) ^{198}Au (Cd)	28.47201E-02	28.46290E-02	-.03
^{56}Mn(n,γ) ^{56}Mn (Cd)	16.45102E-03	16.44317E-03	-.05
^{197}Au(n,γ) ^{198}Au	28.47238E-02	28.46327E-02	-.03
^{56}Mn(n,γ) ^{56}Mn	25.64156E-03	25.62641E-03	-.06
^{56}Mn(n,γ) ^{56}Mn (Cd)	25.64099E-03	25.62584E-03	-.06
^{238}U (n,f)	52.77810E-03	52.80919E-03	.06
^{238}U (n,γ)	14.17249E-02	14.16989E-02	-.02
^{235}U (n,f)	10.00000E-01	10.00000E-01	0.00
1.0	66.87405E-02	66.87942E-02	.01

Note: * No change made in the ^{238}U(n,f) detector response.

  ** Energy range 1.74 - .693 MeV .

5.12   Comparison between NISUS and $\Sigma\Sigma$

The Mol $\Sigma\Sigma$ central flux and reaction rates were calculated using ANISN code with 37 group cross section data file.   The results are shown in Tables 5.28 and 5.29.   Fig. 5.4 shows a comparison between NISUS and $\Sigma\Sigma$ central spectrum.   The detailed material and geometrical data of NISUS and $\Sigma\Sigma$ are compared in Table 5.30.   The ^{10}B abundance for NISUS has been taken as 19.78% which is found in most literature (see Table 5.15) and also been used by Petr[11].

The parameters which have a great effect in the $\Sigma\Sigma$ central flux compared with that of NISUS are summarized in Table 5.31.   It is seen that the 14% increase in the $\Sigma\Sigma$ total flux above group 21 (67.4 keV) is due to variations in the graphite, boron carbide and uranium densities and also uncertainties in ^{10}B abundance.   This means that the two central spectra are in agreement within about 3% above 67.4 keV.   The agreement departs sharply from group 26 onwards (below 4.31 keV) due to the high effects of boron carbide density and ^{10}B abundance in this region of the spectrum.   The reason for the difference of about − 4% (after subtracting 14%) in the energy range 40.9 − 9.12 keV is not fully understood, but it is clear that it is due to variation in boron carbide density (see Table 5.7).   Similar effect was also observed in the case of a tolerance of 1 mm in the boron carbide shell (see Table 5.18).

In the case of threshold detectors, the reaction rate ratios in $\Sigma\Sigma$ are less than 1.3% smaller than those in NISUS.   In the case of ^{56}Mn (n,γ) ^{56}Mn reaction (bare and Cd covered) the reaction rate ratios in NISUS are 1.18% smaller than those in $\Sigma\Sigma$.   The value of

TABLE 5.28

Flux per unit lethargy

Group	NISUS	ΣΣ	Difference %
1	13.60527E-08	15.73674E-08	15.67
2	30.54952E-08	35.34058E-08	15.68
3	72.37681E-08	83.72140E-08	15.67
4	17.92865E-07	20.72740E-07	15.61
5	47.46751E-07	54.81970E-07	15.49
6	12.85788E-06	14.81252E-06	15.20
7	26.13180E-06	30.03380E-06	14.93
8	50.00314E-06	57.36323E-06	14.72
9	88.11920E-06	10.08712E-05	14.47
10	12.48263E-05	14.27061E-05	14.32
11	15.87715E-05	18.11944E-05	14.12
12	19.85589E-05	22.70366E-05	14.28
13	31.38343E-05	36.27514E-05	15.59
14	39.76469E-05	46.57850E-05	17.14
15	43.67394E-05	51.62713E-05	18.21
16	38.60904E-05	45.54042E-05	17.95
17	29.75265E-05	34.91851E-05	17.36
18	25.21511E-05	29.51022E-05	17.03
19	21.59010E-05	25.24501E-05	16.93
20	19.46518E-05	22.73597E-05	16.80
21	13.59290E-05	15.72230E-05	15.67
22	82.46426E-06	93.67022E-06	13.59
23	48.58253E-06	54.15532E-06	11.47
24	29.97335E-06	32.93261E-06	9.87
25	16.35541E-06	17.82793E-06	9.00
26	12.50248E-06	13.84449E-06	10.73
27	99.68017E-07	11.28191E-06	13.18
28	74.13641E-07	85.31737E-07	15.08
29	49.40581E-07	58.10875E-07	17.62
30	31.97495E-07	38.52304E-07	20.48
31	18.21514E-07	22.69317E-07	24.58
32	60.59574E-08	80.83098E-08	33.39
33	16.29411E-08	23.95963E-08	47.04
34	21.38870E-10	54.73363E-10	155.90
35	21.96802E-12	54.46937E-12	148.04
36	29.23728E-14	79.80275E-14	172.46
37	15.73324E-15	50.66208E-15	223.28

TABLE 5.29

Reaction rate ratios

Reaction	NISUS	ΣΣ	Difference %
$^{58}Ni(n,p)\ ^{58}Co$	18.09796E-03	17.88498E-03	-1.18
$^{56}Fe(n,p)\ ^{56}Mn$	16.07783E-05	15.97122E-05	-.66
$^{115}In(n,n')\ ^{115m}In$	34.01771E-03	33.61966E-03	-1.17
$^{238}U\ (n,f)$	53.56196E-03	52.87880E-03	-1.28
$^{56}Fe(n,p)\ ^{56}Mn$	93.17571E-06	92.67942E-06	-.53
$^{32}S\ (n,p)\ ^{32}P$	11.03941E-03	10.90607E-03	-1.21
$^{103}Rh(n,n')\ ^{103m}Rh$	22.65973E-02	22.56005E-02	-.44
$^{56}Mn(n,\gamma)\ ^{56}Mn$	16.45159E-03	16.55967E-03	.66
$^{115}In(n,\gamma)\ ^{116}In$	18.96142E-02	19.02178E-02	.32
$^{197}Au(n,\gamma)\ ^{198}Au$	28.51303E-02	28.62400E-02	.39
$^{115}In(n,\gamma)\ ^{116}In$ (Cd)	82.02075E-03	81.68384E-03	-.41
$^{197}Au(n,\gamma)\ ^{198}Au$ (Cd)	28.47201E-02	28.58608E-02	.40
$^{56}Mn(n,\gamma)\ ^{56}Mn$ (Cd)	16.45102E-03	16.55842E-03	.65
$^{197}Au(n,\gamma)\ ^{198}Au$	28.47238E-02	28.58689E-02	.40
$^{56}Mn(n,\gamma)\ ^{56}Mn$	25.64156E-03	25.94367E-03	1.18
$^{56}Mn(n,\gamma)\ ^{56}Mn$ (Cd)	25.64099E-03	25.94242E-03	1.18
$^{238}U\ (n,f)$	52.77810E-03	52.09057E-03	-1.30
$^{238}U\ (n,\gamma)$	14.17249E-02	14.15275E-02	-.14
$^{235}U\ (n,f)$	10.00000E-01	10.00000E-01	0.00
1.0	66.87405E-02	67.14190E-02	.40
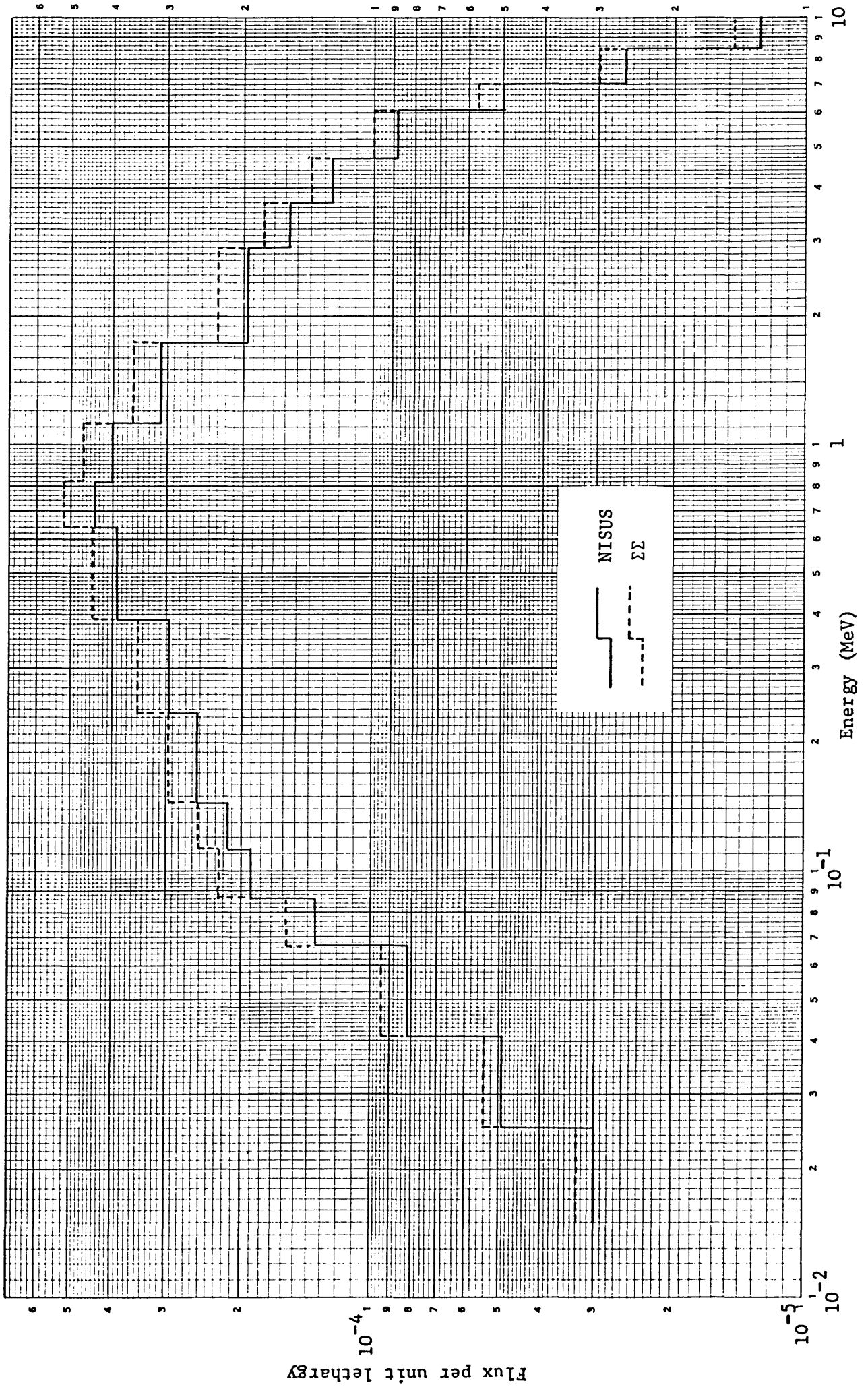
Fig. 5.4 Comparison between NISUS and ΣΣ central spectrum.

TABLE 5.30

NISUS and ΣΣ detailed material and geometrical data

Description	NISUS	ΣΣ
Uranium shell		
Outer Diameter	254.0 mm	245 ± 0.2 mm
Thickness	48.26 mm	50 ± 0.1 mm
Density	18.84 gm/cm^3	18.92 ± 0.03 gm/cm^3
Boron carbide shell		
Thickness	15 ± 0.1 mm	15 ± 0.1 mm
Density	1.58 gm/cm^3	1.499 ± 0.005 gm/cm^3
^{10}B Abundance	19.78%	18.37 ± 0.04%
Moisture	—	≃ 500 ppm
Graphite reflector		
Density	1.722 ± 0.001 gm/cm^3	1.60 ± 0.02 gm/cm^3
Moisture	≃ 250 ppm	—

TABLE   5.31

Comparison in flux per unit lethargy

Parameter	NISUS	$\Sigma\Sigma$	Difference* %	References
Graphite density (gm/cm^3)	1.722	1.60	+12	Table 5.4
B_4C density (gm/cm^3)	1.58	1.49	+1	Table 5.7
Uranium density (gm/cm^3)	18.84	18.92	< ±.5	Table 5.9
^{10}B abundance (atom %)	19.78	18.37	+1	Table 5.16

Note: * Above 67.4 keV

F_8/F_5 in $\Sigma\Sigma$ is 1.3% less than that in NISUS. For the rest of the

reactions, the difference between the reaction rate ratios is less

than 0.7%. Fig. 5.5 shows a comparison of calculated reaction rate

ratios for NISUS and $\Sigma\Sigma$ based on GALAXY and ENDF/B-III data files.

5.13   Fission rate distribution

The fission rate distributions in the natural uranium shell

are shown in the Figures 5.6 and 5.7 for 10 and 20 mesh points

respectively. It is seen that the thermal flux attenuates very

rapidly due to absorption in the driver shell and the effective

source is concentrated in the outer region; the inner region serves

mainly to degrade the spectrum shape by inelastic scattering. The

effect of boron carbide shell in the fission distribution is also

shown, and it can be seen that the relative fission rate in the inner

region with and without boron carbide shell differs by a factor of

1.5. The fission rate distribution within the uranium shell can be

measured experimentally. Measurements of the ratio of fission rates

on the inner and outer surfaces of the shells at various azimuthal

angles are reported in Chapter 7.
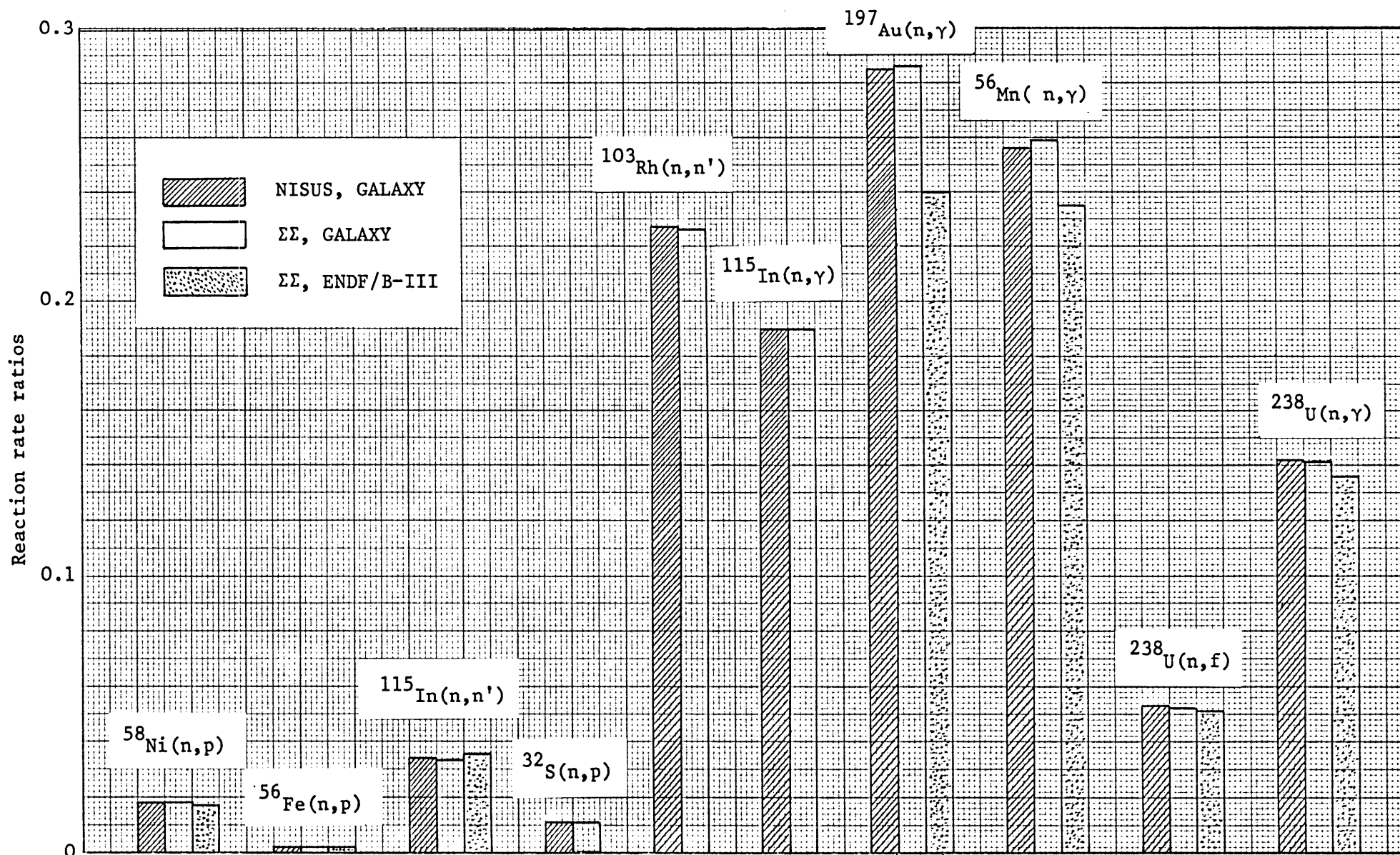
Fig. 5.5   Comparison of calculated reaction rate ratios for NISUS and ΣΣ based on different files.
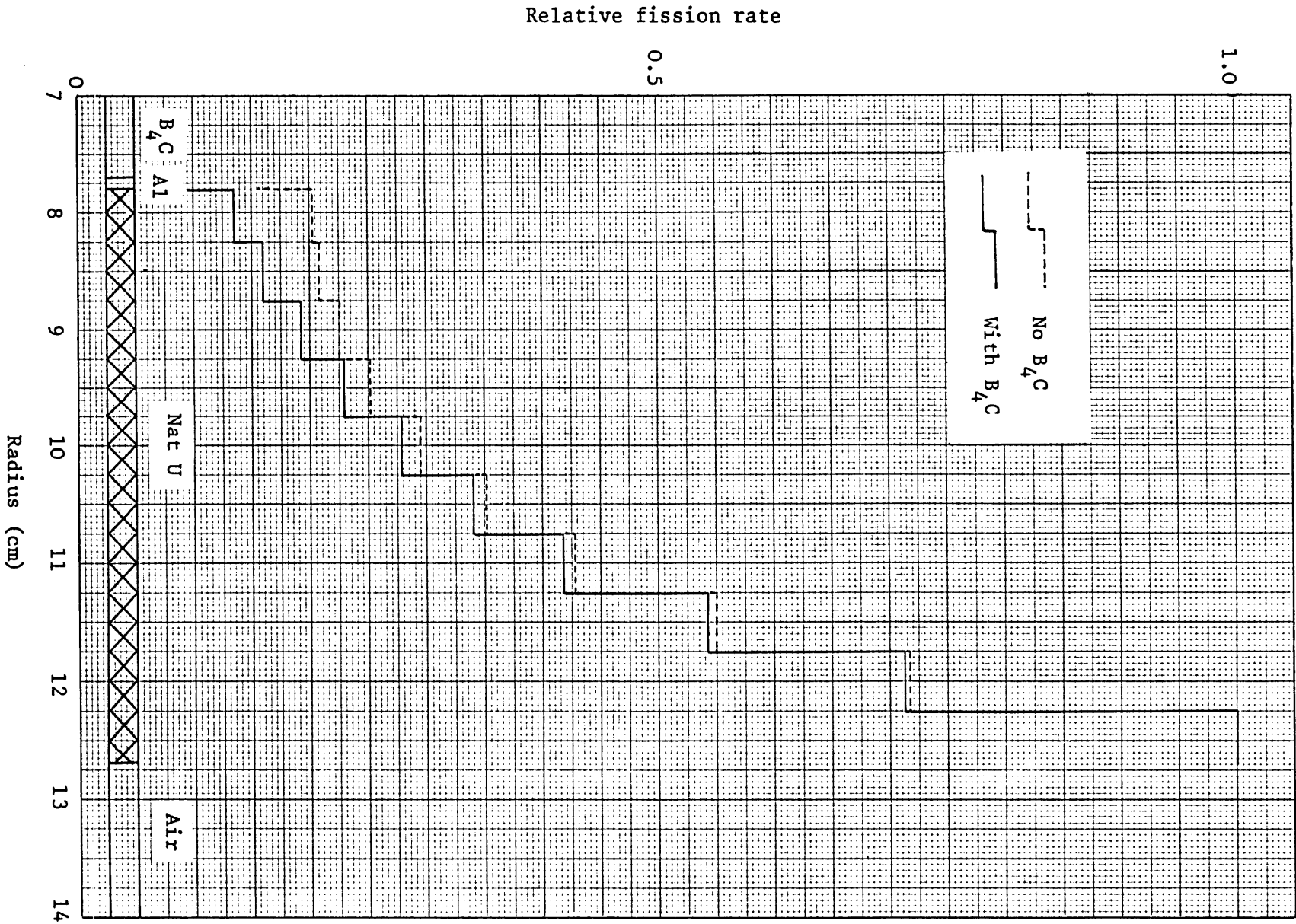
Fig. 5.6   Relative fission rate distribution within the NISUS uranium shell (10 mesh points).

Relative fission rate
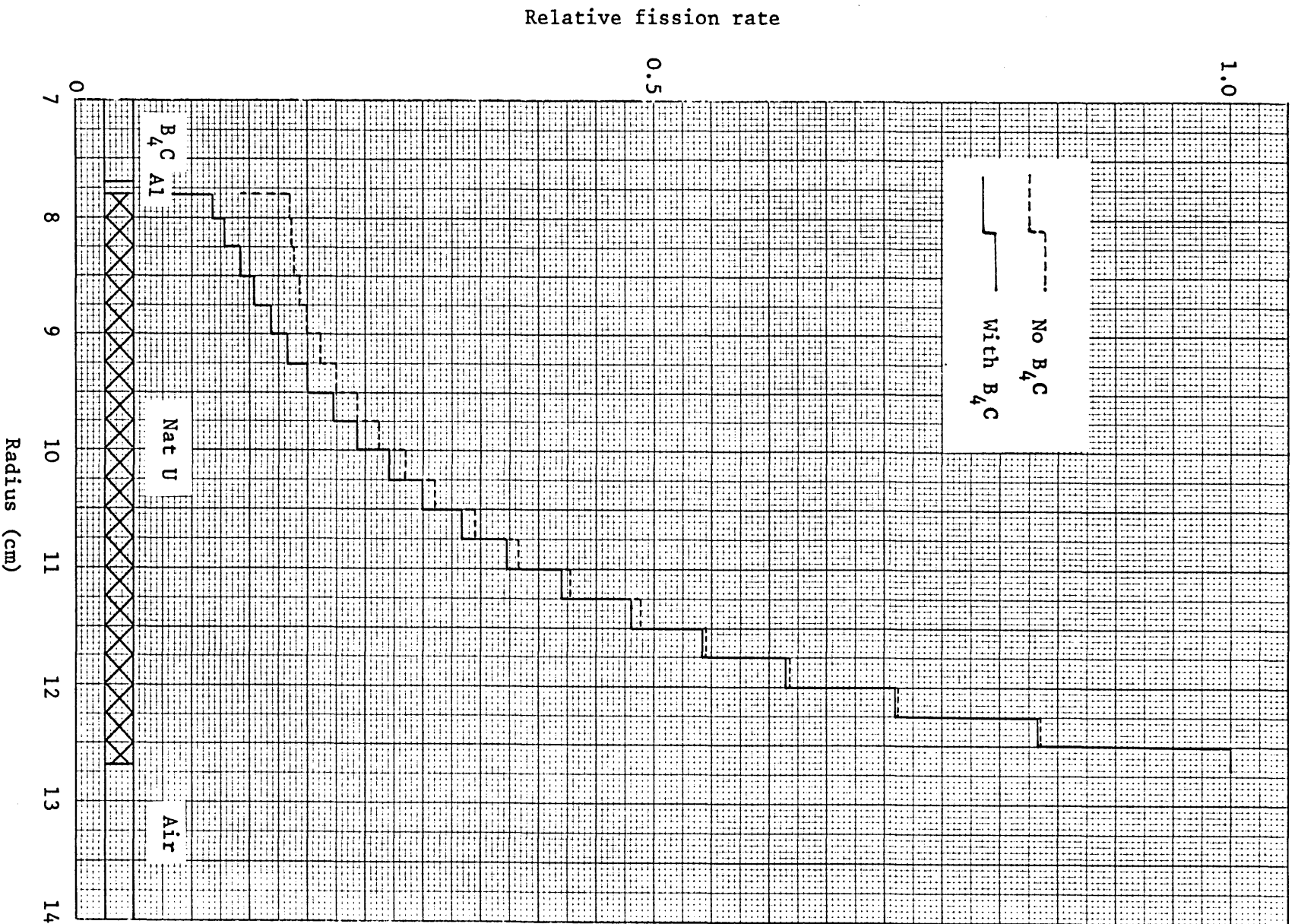
Fig. 5.7   Relative fission rate distribution within the NISUS
uranium shell (20 mesh points).

223

6. FISSION CHAMBER MEASUREMENTS IN NISUS

Measurements of the absolute fission rates have been recently performed by using the absolute fission chambers. This is because the accuracy requirements for fast reactor fuels and materials dosimetry have surpassed the existing capabilities of fission foil activation measurements. The absolute fission rates are derived from the absolute counting of the fissions occurring in a known quantity of fissile material. Several corrections have to be made to the observed number of fission fragments in order to find the absolute fission rates. These corrections include the number of fragments lost due to alpha discrimination, absorption of fission fragments in the fissile material, fission in other isotopes than the principal one, dead time loss, and perturbation introduced from the fission chamber material such as neutron scattering and absorption, and also perturbation due to the access hole for electronic cables and gas tubing.

The absolute fission rate measurement has two distinct features:

(a)   determination of the isotopic mass of the fissionable deposits, and

(b)   recording with precision a known fraction of fission fragments originating within the deposits when exposed to a flux of neutrons.

6.1   Fissionable deposits

A selection of 13 deposits were exposed at the centre of the NISUS standard neutron field. Five of these deposits came from the set of reference and working deposits belonging to the National Bureau of Standards (NBS), Washington. These deposits were mainly used in

the small, lightly constructed NBS double fission chamber[14].

The deposits were 12.7 mm diameter fissionable oxides prepared by vacuum evaporation. Deposit backings were 19.0 mm diameter polished platinum 0.13 mm thick disks.

Two of the deposits with diameter of 28.0 mm of fissile material on the platinum backing of 39.0 mm diameter came from AWRE, Aldermaston. These deposits are being extensively used for delayed neutron yield measurements. The remaining six deposits were specifically prepared for the University of London Reactor Centre (ULRC) at AERE, Harwell. These deposits were 20 mm diameter vacuum evaporated or painted in the case of the two thickest fissionable oxides on the backings of 42.0 mm diameter polished platinum.

6.2   Description of the ULRC fission chamber

A special double fission ionization chamber was designed and constructed at the University of London Reactor Centre. The chamber consists of two independent fast ionization chambers with easily demountable deposits (Fig. 6.1). The deposits are positioned back-to-back between two square aluminium plates each with holes larger than the area of the fissile material. The deposits are kept tight in position by four tiny screws at the corners of the aluminium plates. This sandwich of the aluminium holder and deposits is slid into the groove between the two anodes of the chamber. This arrangement makes exchanging of the deposits quite simple and quick with no need of special tools. When it is necessary, the holder of the deposits can be replaced by another one. This is particularly attractive when

SCALE ∿ 2/1

DIMS. IN CM
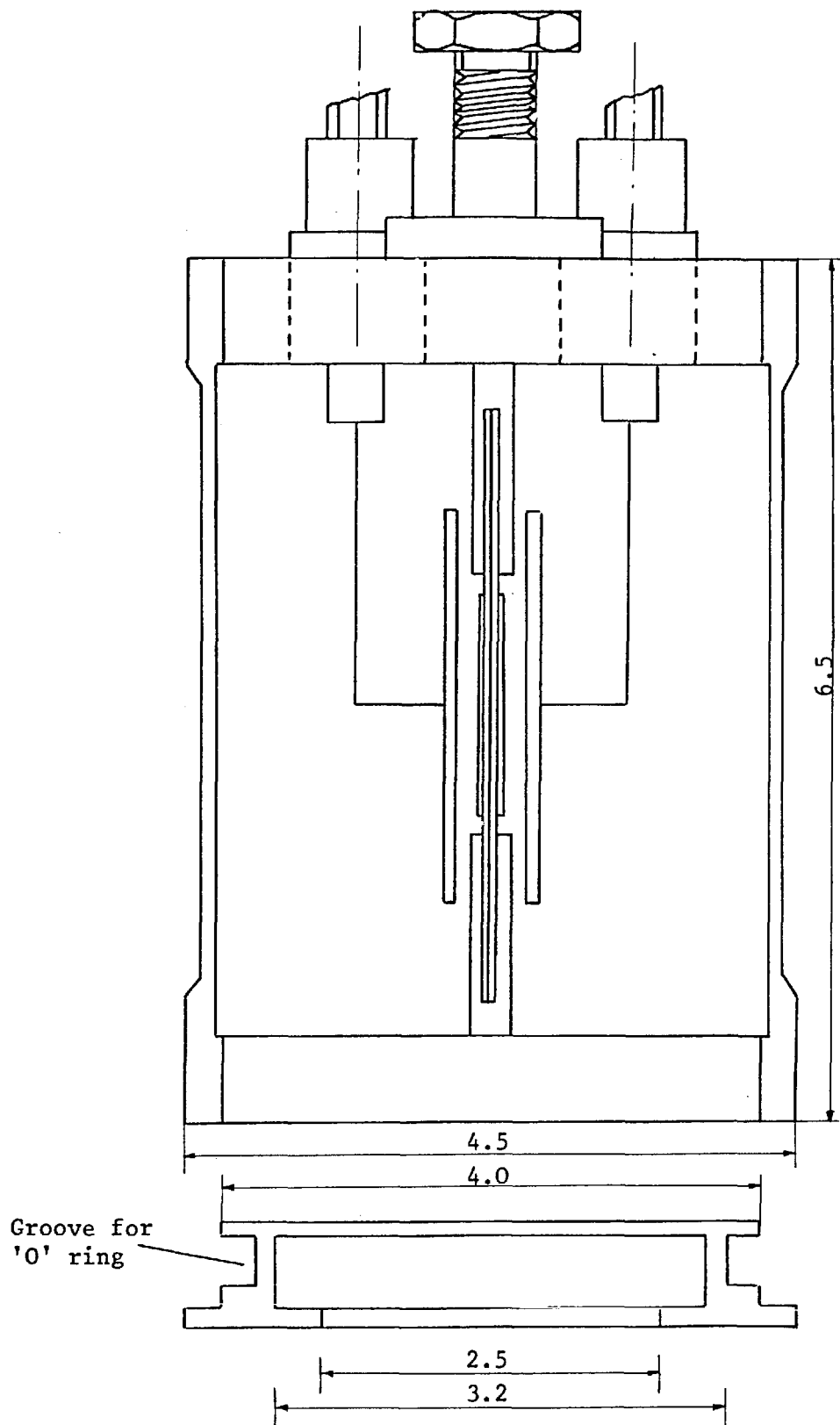
Fig. 6.1   The enlarged cross-sectional view of the ULRC double
            fission chamber.

several reactor runs are planned in a normal working day. The

backings of the fissionable deposits serve as the common grounded

electrode between the chambers. The anode disks parallel to the

fissionable deposits are 32 mm in diameter and since they are 12 mm

larger than the deposit diameter, the loss of fission fragments at

the edges of the active volume is prevented. To reduce neutron

absorption and scattering effects, the electrodes and structural

elements are made of aluminium, and the insulators are made of a

hydrogen-free polymer.

6.3   Chamber performance and operation

The ULRC chamber is operated with sealed gas, so tight

seals are necessary and "O" rings are used in the top and bottom

lids. The chamber was evacuated down to 0.01 torr ($\simeq 10^{-5}$ atm)

and filled up with 1 atm P-10 gas (90% argon, 10% methane). In

order to keep the air impurity to minimum, the chamber was filled

up and evacuated several times before the final filling.

The chamber filling up and pumping down were performed through

a nitrogen trap (Fig. 6.2) to condense any oil vapour coming from

the pump which otherwise could migrate to the chamber and spoil the

deposits. At very low pressure the probability of oil molecules

travelling in either way is about equal. The nitrogen trap arrange-

ment was proved to be necessary as after several runs, an appreciable

amount of oil was observed in the trap.

6.4 Mass calibration of ULRC deposits

The first task of the present fission chamber measurements was to make a mass comparison between the NBS, AWRE and ULRC deposits. In this comparison the masses of AWRE and ULRC deposits were calibrated against those of the NBS deposits. The mass assay of the NBS fissionable deposits originally used in the Coupled Fast Reactivity Measurement Facility (CFRMF) has been made by absolute alpha emission rates measurements complemented by fission comparison counting in thermal-neutron beams[14] and also at the centre of the $\Sigma\Sigma$ standard neutron field[100].
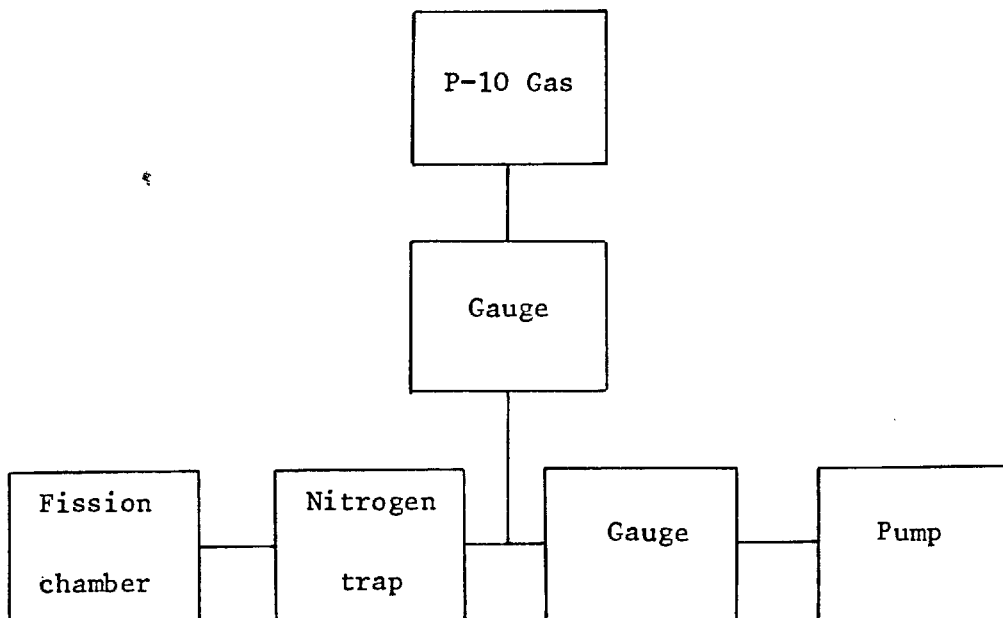
Fig. 6.2   Block diagram of the fission chamber filling system.

Several experiments were carried out in the NISUS central flux with the NBS and ULRC double fission chambers and the mass of the AWRE and ULRC fissionable deposits determined. In one experiment the AWRE and NBS (25 S-2-3) ^{235}U deposits were exposed in the ULRC chamber at the centr of NISUS. In another experiment the ULRC (No. 3) and NBS (28 HD-5-1) ^{238}U deposits were used in the ULRC chamber. In these two measurements the masses of the AWRE ^{235}U and ULRC-3 ^{238}U deposits were calibrated against the NBS deposits and in the subsequent measurements the mass assay of the other AWRE and ULRC fissionable deposits was made on the basis of these two measurements. Table 6.1 shows the isotopic concentrations and mass assay of the fissionable deposits exposed at the NISUS centre.

6.5   Corrections of pulse rates

The pulse height distribution of the deposits has three principal features (Fig. 6.3):

(1)   a very sharp peak near zero pulse height due to alpha activity, electronic noise, and energetic electrons.

(2)   the valley in which the integral discriminator is set.

(3)   a very broad peak that rises sharply on the low pulse height side.

In order to find the true number of fissions occurring in the deposit when a chamber is exposed to a flux of neutrons, several corrections should be applied to the recorded number of fissions. These corrections include the fraction of fission pulses below alpha discriminator level, absorption of fission fragments in the deposits,

TABLE 6.1

The fissionable deposits exposed at the centre of NISUS standard neutron field

Foil identification and principal isotope	Deposit diameter (mm)	Isotopic concentration (atom percent)	Mass of principal isotope	
			μgm	μgm/cm^2
NBS 49 I-1-1 ^{239}Pu	12.7	^{239}Pu: 99.11; ^{240}Pu: 0.0880; ^{241}Pu: 0.010; ^{242}Pu: 0.005	105.1 ± 1.3%	83.0
NBS 28 N-5-2 ^{238}U (natural)	12.7	^{238}U: 99.275; ^{235}U: 0.72	686 ± 1.4%	541.5
NBS 25 S-2-3 ^{235}U	12.7	^{235}U: 99.748; ^{238}U: 0.1261; ^{234}U: 0.0608; ^{236}U: 0.0652	222 ± 1.2%	175.2
NBS 37 S-5-2 ^{237}Np	12.7	^{237}Np: 99.3; ^{239}Pu: 0.68	630 ± 1.8%	497.3
NBS 28 HD-5-1 ^{238}U (depleted)	12.7	^{238}U: 99.999; ^{235}U: $\sim$ 0.0001	651 ± 1.5%	513.9
AWRE ^{235}U (enriched)	28.0	^{235}U: 93.0; ^{238}U: 7.0	127.7 ± 1.3%[a]	20.7
AWRE ^{238}U (depleted)	28.0	^{238}U: 99.965; ^{235}U: 0.035	1284.6 ± 1.9%[b]	208.6

TABLE   6.1   (continued)

The fissionable deposits exposed at the centre of NISUS standard neutron field

Foil identification and principal isotope	Deposit diameter (mm)	Isotopic concentration (atom percent)	Mass of principal isotope	
			μgm	μgm/cm^2
ULRC-1 ^{238}U	20.5 ± .3	^{238}U: 99.965; ^{235}U: 0.035	3114.3 ± 2.5%	943.5
ULRC-2 ^{238}U	20.6 ± .3	^{238}U: 99.965; ^{235}U: 0.035	3164.4 ± 2.5%	949.4
ULRC-3 ^{238}U	20.3 ± .2	^{238}U: 99.965; ^{235}U: 0.035	780.6 ± 1.9%	241.2
ULRC-4 ^{235}U	20.0 ± .1	^{235}U: 93.0; ^{238}U: 7.0	73.2 ± 1.4%[c]	23.3
ULRC-5 ^{235}U	20.0 ± .1	^{235}U: 93.0; ^{238}U: 7.0	319.4 ± 1.3%[d]	101.7
ULRC-6 ^{235}U	20.0 ± .1	^{235}U: 93.0; ^{238}U: 7.0	326.3 ± 1.3%[e]	102.8

Note: (a)   Figure supplied by AWRE: 129 μgm

(b)   Figure supplied by AWRE: 1270 μgm

(c)   Mass from 2π geometry alpha counting, AERE, Harwell: 72.8 μgm

(d)   Mass from 2π geometry alpha counting, AERE, Harwell: 310.1 μgm

(e)   Mass from 2π geometry alpha counting, AERE, Harwell: 316.1 μgm
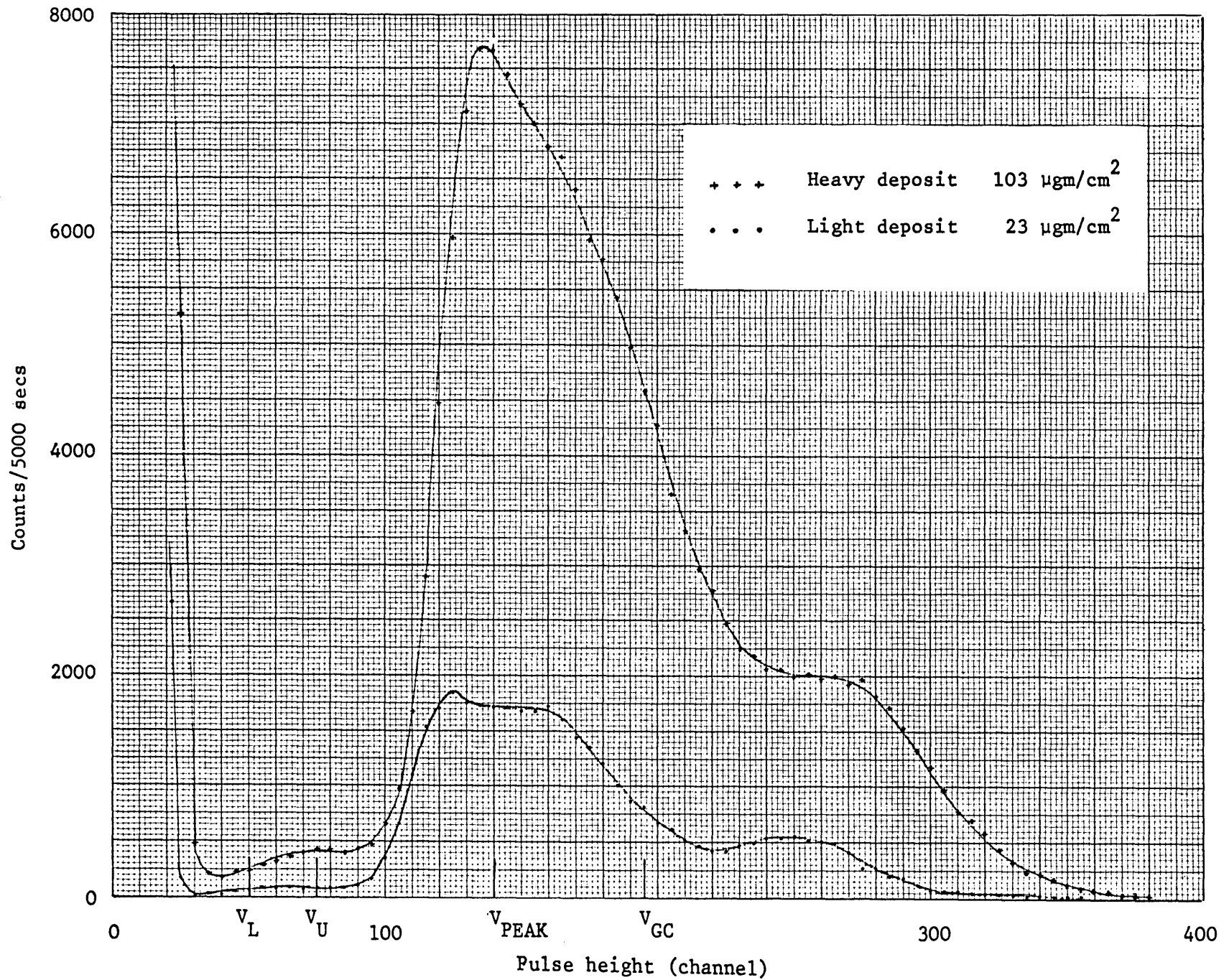
Fig. 6.3   Typical pulse height distribution for uranium.

fission in other isotopes, neutron scattering and absorption, access hole perturbation, and dead time loss of the chamber.

6.5.1 Extrapolation-to-zero (ETZ)

The most important correction is to determine the undetected number of fissions below discriminator level. The estimated fraction of fission pulses that lie in the range of discriminator to zero is termed the extrapolation-to-zero (ETZ) correction. There are three methods to find out the extrapolation-to-zero correction:

(1)   Using only one discriminator and setting just above the alpha peak, the undetected number of fission is simply the area of the pulse height distribution below the discriminator level, assuming a flat distribution between the discriminator level and zero.

(2)   White[101] has suggested extrapolating of the lower tail of the fission peak to zero with no pulse-height flatness assumption. This method leads to a smaller value for ETZ than the first one, particularly for thick deposits.

(3)   Each side of the dual fission chamber is monitored independently by a triple-scaler counting system. A charge-sensitive preamplifier, three integral discriminators, and three scalers constitute the main pulse-processing system. The relative positions of the discriminator levels to the peak of the pulse height distribution are established with the aid of the multichannel analyzer and a pulser.

The dual triple-scaler counting system originally developed at NBS[14] and modified at MOL[100] was reproduced for the present fission chamber measurements. There are several advantages to the chosen

arrangements of the dual triple-scaler counting systems (Fig. 6.4).

The count rate above the lower discriminator level, V_L, is called S_L, and the count rate above the upper discriminator level, V_U, is called S_U. The positions (in volts) of these two disciminators relative to the peak of the pulse height distribution V_{PEAK} were always fixed carefully in such a way that $V_U = 0.54\ V_{PEAK}$ and $V_L = 0.36\ V_{PEAK}$. The gain check discriminator level, V_{GC}, was set so that $V_{GC} = 1.4\ V_{PEAK}$ to get a sensitive monitor of the amplifier gain stability. The count S_{GC} serves as a gain check and also allows one to detect if eventual flashes of noise exceeed V_U, so that the corresponding counting result can be rejected: this has sometimes happened, and could essentially be attributed to the switching of reactor control instruments, and in particular, the operation of In-Core Irradiation System (ICIS); in such cases, the ratio S_L/S_U of count rates above V_L and V_U respectively was also perturbed in a characteristic way.

The difference in the counts S_L and S_U is used to infer the number of valid fission counts between V_L and zero on the basis of the assumption that the pulse height distribution is flat between zero and V_U. The extrapolation-to-zero (ETZ) correction is the fraction of fission pulses in the range $0 < V < V_L$. According to Grundl[14] V_L is set at $(1/2)V_U$ and therefore the ETZ is $(S_L - S_U)/S_L$ or $(1 - S_U/S_L)$. While Fabry[102] takes S_U as primary counting data and sets V_L at $(2/3)V_U$ and thus the ETZ is $3(S_L - S_U)/S_U$ or $3(S_L/S_U - 1)$. The actual extrapolation-to-zero, which is slightly adjusted, may be obtained from the following recipe:
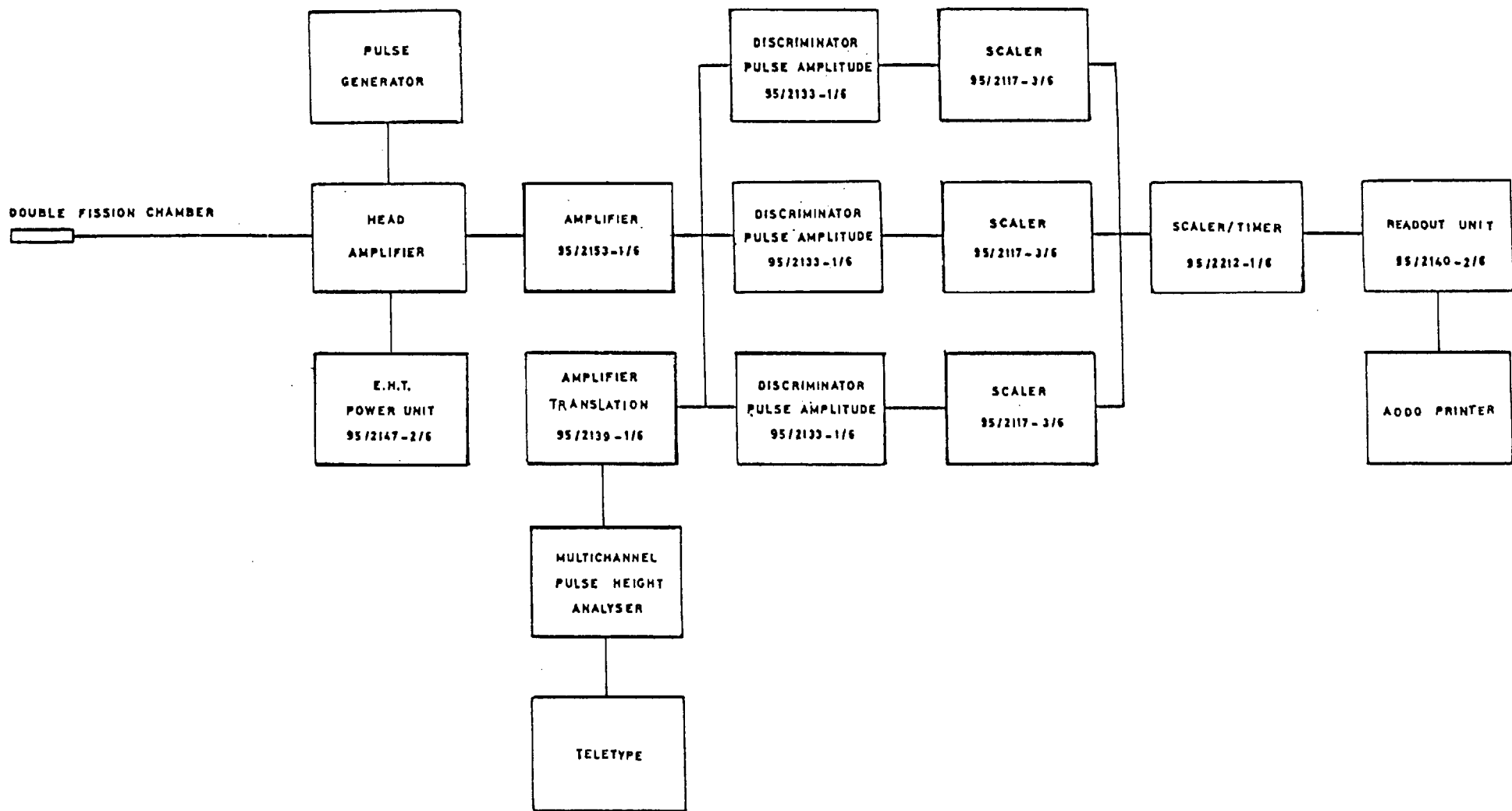
Fig. 6.4   Block diagram of one side of the dual triple-scaler counting system.

$$(ETZ)_{applied} = (ETZ)_{nominal} + \tfrac{1}{2}(3(S_L/S_U - 1) - (ETZ)_{nominal}) \qquad (6.1)$$

The nominal ETZ values are either inferred from Grundl's data or from measurements under ideal count rate and signal-to-noise conditions. In the present work the method equivalent to Fabry's was followed and the ETZ values were taken as $2(S_L/S_U - 1)$, when applied to S_L as primary counting data. The peak-to-valley ratios of the pulse-height distribution (Fig. 6.3) vary from about 75 for a 23 $\mu g/cm^2$ deposit to 38 for a 103 $\mu g/cm^2$ deposit. Correspondingly, the correction for extrapolation of the pulse height distribution to zero varies from 1.98% for a 23 $\mu g/cm^2$ deposit to 2.24% for a 103 $\mu g/cm^2$ deposit. The extrapolation-to-zero correction for the NBS, AWRE and ULRC deposits exposed at the NISUS centre in the NBS and ULRC chambers are shown in Table 6.2. Fig. 6.5 shows a plot of the ETZ correction versus deposit thickness. The quantity plotted is $2(S_L/S_U - 1)$ in units of percent. The data show that the performance of the ULRC chamber is inferior to NBS chamber in two respects: (i) the slope of the upper line in Fig. 6.5 is much greater, (ii) the intercept for zero deposit thickness (ULRC curve) shows an intercept of $\sim$ 1%. Because of the latter value the chamber may not be regarded as a truly absolute chamber. A possible reason may be in the method of holding the deposits, since an AWRE chamber which was similar in all other respects performed better.

6.5.2 Fission fragment absorption

A small fraction of the fission fragments generated inside a deposit are emitted at angles close to the plane of the deposit and

TABLE 6.2

Typical ETZ corrections for the deposits exposed at the centre of NISUS

Fission chamber	Foil identification and principal isotope	Mass $\mu gm/cm^2$	Extrapolation-to-zero
NBS	NBS 49 I-1-1 ^{239}Pu	83.0	1.00776 ± .00074
	NBS 28 N-5-2 ^{238}U (natural)	541.5	1.05140 ± .00390
	NBS 25 S-2-3 ^{235}U	175.2	1.01102 ± .00074
	NBS 37 S-5-2 ^{237}Np	497.3	1.02404 ± .00142
	NBS 28 HD-5-1 ^{238}U (depleted)	513.9	1.03026 ± .00316
ULRC	NBS 25 S-2-3 ^{235}U	175.2	1.01996 ± .00102
	NBS 28 HD-5-1 ^{238}U (depleted)	513.9	1.04576 ± .00390
	AWRE ^{235}U (enriched)	20.7	1.01256 ± .00092
	AWRE ^{238}U (depleted)	208.6	1.02072 ± .00174
	ULRC-1 ^{238}U	943.5	1.09204 ± .00706
	ULRC-2 ^{238}U	949.4	1.14702 ± .00352
	ULRC-3 ^{238}U	241.2	1.03184 ± .00230
	ULRC-4 ^{235}U	23.3	1.01980 ± .00192
	ULRC-5 ^{235}U	101.7	1.02014 ± .00236
	ULRC-6 ^{235}U	102.8	1.02238 ± .00322
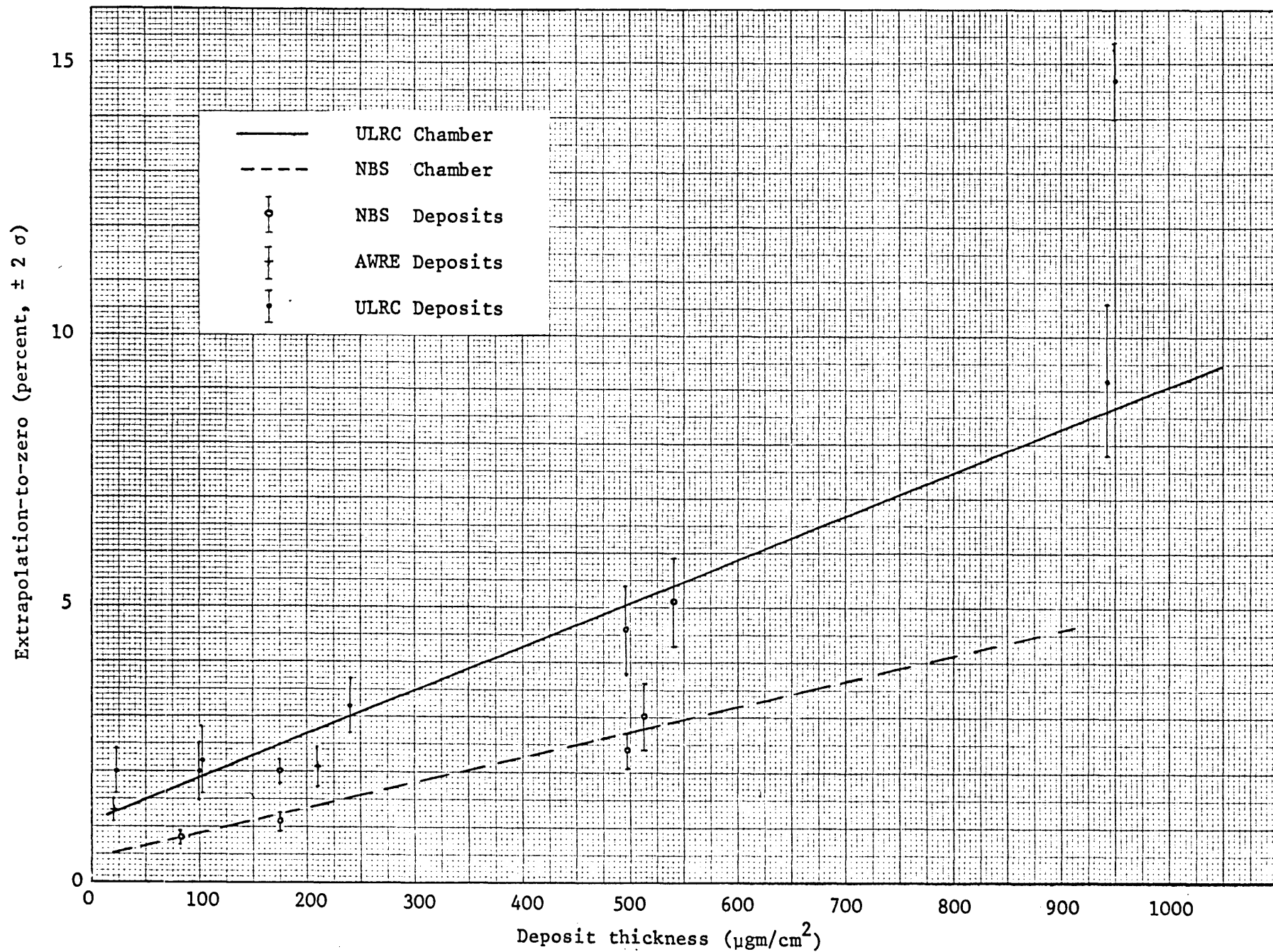
Fig. 6.5   The ETZ correction to zero pulse height.   The lines are the linear least-squares fit.

238

may not escape before dissipating all their energy. In 2π geometry, the fraction F lost due to absorption is $t/2R$, where t is the thickness of the deposit and R is the average fission fragment range in the deposit material (usually a dioxide). White[101] has shown that if the deposit thickness is not uniform the fraction F becomes $(t^2 + \sigma^2)^{\frac{1}{2}}/2R$ where t is the mean thickness and σ the standard deviation on the variation of the thickness.

White[101] has calculated the mean range of fission fragment in U_3O_8 as 7.5 ± 0.5 mg/cm^2 and Grundl et al[14] have taken the value of 7.74 ± 0.90 mg U_3O_8/cm^2. They corrected this value for the difference in oxygen content in UO_2 by assuming that the range (in mg/cm^2) is proportional to $\sqrt{A}$, where A is the effective atomic mass evaluated according to the recipe $(A)^{\frac{1}{2}} = \sum_j n_j A_j / \sum_j n_j (A_j)^{\frac{1}{2}}$, and n_j are atom fractions. The resulting correction is 0.69% per 100 μgm U/cm^2 in UO_2. In the present work the fission fragment absorption correction was calculated on the basis of the Grundl's value. The estimated uncertainty in the absorption correction was taken to be 25% of the correction or 0.35%, whichever is larger.

6.5.3 Fission in other isotopes

No direct measurement has been made to estimate the correction for fission in isotopes other than the principal one. The corrections for NBS deposits were taken from Ref. (100). The corrections for AWRE and ULRC deposits were, however, based on the values of 93% ^{235}U and 350 ppm ^{235}U in the ^{235}U and ^{238}U deposits respectively, supplied by AWRE, Aldermaston and AERE, Harwell.

6.5.4 Neutron scattering and absorption

The effect of neutron scattering and absorption has been measured by irradiating an In foil at the centre of NISUS using the conventional aluminium foil holder[103]. The results of the ^{115}In (n,n') and ^{115}In (n,γ) reaction rates were compared with those of the similar measurement with the fission chamber where an In foil was sandwiched between the two back-to-back deposits (Table 6.3). These measurements were first carried out with uranium foils but due to high statistical error of about 10%, In foils were used instead. The choice of In was because the ^{115}In (n,n') reaction has a threshold energy of about 1.4 MeV, almost the same as ^{238}U (n,f) reaction, and ^{115}In (n,γ) reaction is a thermal reaction similar to the ^{235}U(n,f) reaction. It was found that the neutron scattering and absorption due to fission chamber body is negligible for ^{235}U fission rates, and that for the ^{238}U is less than 1%.

6.5.5 Access hole perturbation

Fabry et al[100] have shown that in $\Sigma\Sigma$ the epicadmium hole corrections for non-threshold fission reactions do not exceed 1% and are negligible for threshold reactions, in the usual conditions of NBS fission chamber exposures, e.g. hole axis parallel to reactor thermal column axis and looking outward from reactor core. They have taken the value of .995 ± .005 for the $\Sigma\Sigma$ access hole perturbation correction. This value applies to data taken under the condition of no thermal streaming.

In the early NBS fission chamber measurements carried out

in NISUS, the thermal streaming effect of $\approx$ 1% was observed (see

Section 6.7). The same streaming effect exists for the ULRC fission

chamber measurements before the modification to the access hole (see

Section 6.8). The access hole perturbation correction was found to

be negligible after the modification, since the ^{115}In (n,γ) reaction

rate measurement showed that the thermal neutron streaming effect is

within the error of about $\pm$ 2% (Table 6.3). Since no NBS fission

TABLE 6.3

Effect of flux depression by fission chamber and thermal
neutron streaming through the access hole*

Reaction	Reaction rate/^{197}Au(n,γ)		Difference
	Without fission chamber	With fission chamber	
In(n,γ)	2.78658 E-02 $\pm$ 2.00%	2.82876 E-02 $\pm$ 1.70%	+1.5%
In(n,n')	6.79736 E-03 $\pm$ .29%	6.74395 E-03 $\pm$ .29%	-0.8%

Note: * All errors shown are statistical errors only.

chamber measurements were made in NISUS after modification to the

access hole only cadmium box data used for NBS chamber measurements.

6.5.6 Dead-time loss correction

No correction has been applied for the dead time loss. This

correction was estimated to be negligible since the count rate would

never exceed 165 couns/sec. The dead time loss correction has been

found to be less than 0.1% for a typical NBS 25 S-2-3 deposit for

$\simeq$ 200 counts/sec $^{(100)}$.

6.5.7 Summary of the corrections

Table 6.4 shows the summary of the corrections applied to the

recorded counting rates, in order to obtain the true isotopic fission

rates. In Table 6.4 the ETZ corrections for the NBS deposits are

those obtained in the exposure of the NBS fission chamber, and those

for the rest of the deposits in the ULRC chamber.

6.6 Reactor power monitoring

Two mutually independent monitor systems have been used for

reactor power monitoring:

1.   two pulse fission chambers type FC4A/100/235 with sensitivity

of 3 x 10^{-3} cps/unit flux

2.   two Au foils in the graphite thermal column extension with

the aim of checking the chambers' performance.

TABLE 6.4

Corrections of the pulse rates to isotopic unperturbed fission rates of the NBS and ULRC fission chambers.

Foil identification and principal isotope	Etrapolation-to-zero*	Absorption in deposit	Fission in other isotpoes	Neutron scattering and absorption	Access hole perturbation
NBS 49 I-1-1 ^{239}Pu	1.0078 ± .0007	1.0055 ± .0035	0.997	1.000	0.995 ±0.005
NBS 28 N-5-2 ^{238}U (natural)	1.0514 ± .0039	1.0375 ± .0095	0.885	1.006 ±0.003	1.000 ±0.000
NBS 25 S-2-3 ^{235}U	1.0114 ± .0009	1.0121 ± .0035	0.9995	1.000	0.995 ±0.005
NBS 37 S-5-2 ^{237}Np	1.0240 ± .0014	1.0343 ± .0080	0.980	1.006 ±0.003	1.000 ±0.000
NBS 28 HD-5-1 ^{238}U (depleted)	1.0303 ± .0032	1.0355 ± .0090	1.000	1.006 ±0.003	1.000 ±0.000
AWRE ^{235}U (enriched)	1.0126 ± .0009	1.0014 ± .0035	0.996	1.000	1.000
AWRE ^{238}U (depleted)	1.0207 ± .0017	1.0144 ± .0036	0.994	1.000	1.000

243

TABLE 6.4 (continued)

Corrections of the pulse rates to isotopic unperturbed fission rates of the NBS and ULRC fission chambers.

Foil identification and principal isotope		Etrapolation-to-zero*	Absorption in deposit	Fission in other isotpoes	Neutron scattering and absorption	Access hole perturbation
ULRC-1	^{238}U	1.0920 ± .0071	1.0651 ± .0163	0.994	1.000	1.000
ULRC-2	^{238}U	1.1470 ± .0035	1.0655 ± .0164	0.994	1.000	1.000
ULRC-3	^{238}U	1.0318 ± .0023	1.0166 ± .0042	0.994	1.000	1.000
ULRC-4	^{235}U	1.0198 ± .0019	1.0016 ± .0035	0.996	1.000	1.000
ULRC-5	^{235}U	1.0201 ± .0024	1.0070 ± .0035	0.996	1.000	1.000
ULRC-6	^{235}U	1.0224 ± .0032	1.0071 ± .0035	0.996	1.000	1.000

Note: *The NBS deposits exposed in the NBS chamber and the AWRE and ULRC deposits in the ULRC chamber.

6.6.1 Fission chamber monitors

The reactor power monitor chambers have been positioned in the graphite stack, with different distances with respect to the cadmium shutter. Details are shown in Fig. 6.6. These chambers were connected to two independent electronic systems so that the total number of fissions in each chamber could be accumulated over the length of irradiation. In order to check the performance of the chambers in short intervals, they also were connected to the dual triple-scaler counting system to get the monitor counts, S_M, simultaneously with the double fission chamber counts, namely S_L, S_U and S_{GC}. Fig. 6.7 shows a block diagram of one of the monitor fission chambers connected to one of the triple-scaler counting system.

It was found that the long term monitoring consistency may not be achieved with fission chambers due to drifting in the electronic system. Because of this drawback, it was necessary to adjust the gain and/or the discriminator levels or both from time to time to obtain a consistent result. Fig. 6.8 shows the electronic system that was used to get the monitor fission chamber pulse-height distribution to set up discriminator levels. A criterion was adopted for this adjustment[104]. If A,B,C,D and E are some specific points on the pulse height distribution (Fig. 6.9), then the variation of these points with channel number for different runs should essentially be a straight line. The points A,B,C,D, and E are corresponding to the discriminator level, mid-point of the first peak, the two peaks, and mid-point of the second peak,

PLAN VIEW   SIDE VIEW

REACTOR CORE

FISSION
CHAMBER

REACTOR
CORE

30

30   30

15   15

Cd SHUTTER
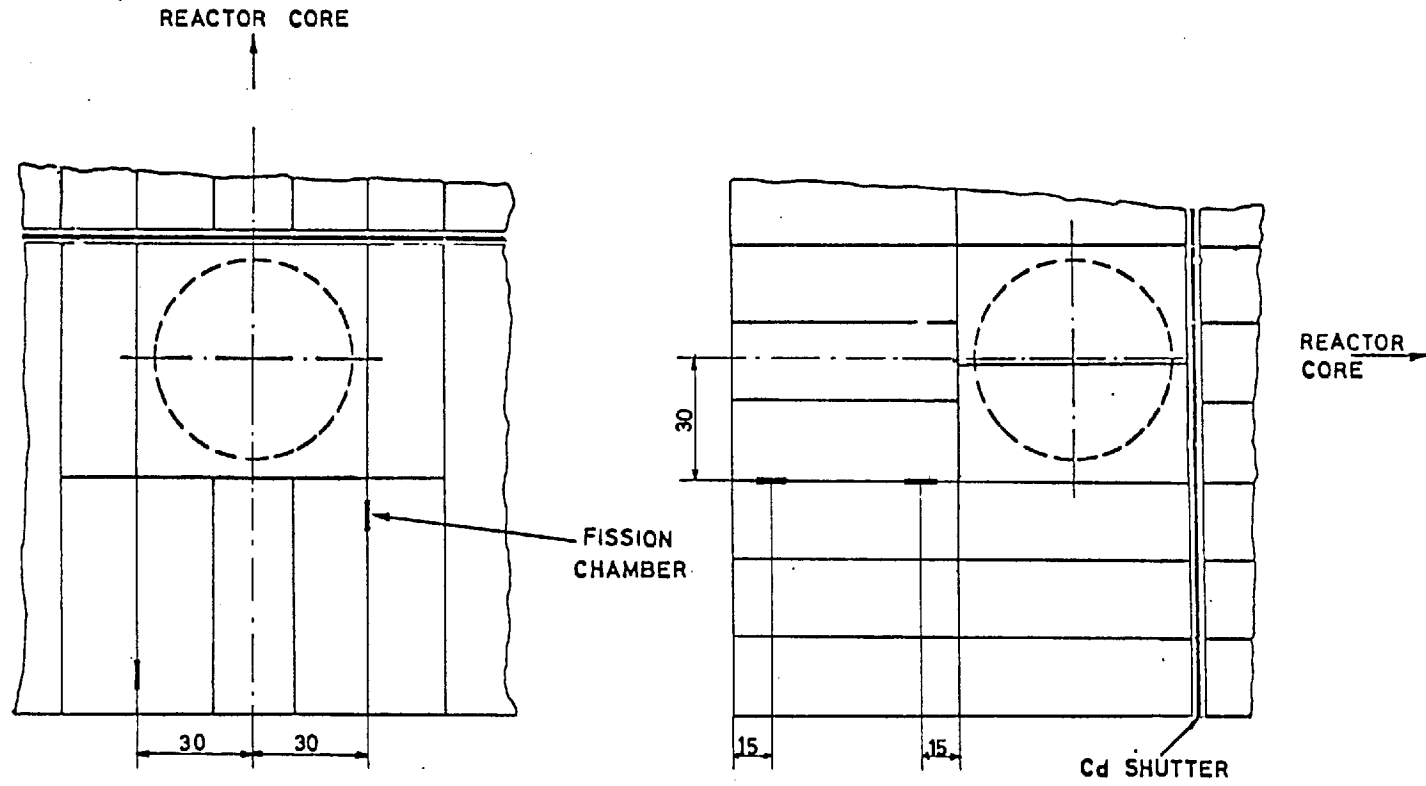
DIMS. IN CM

Fig. 6.6   Block diagram of the position details of the monitor fission chambers.
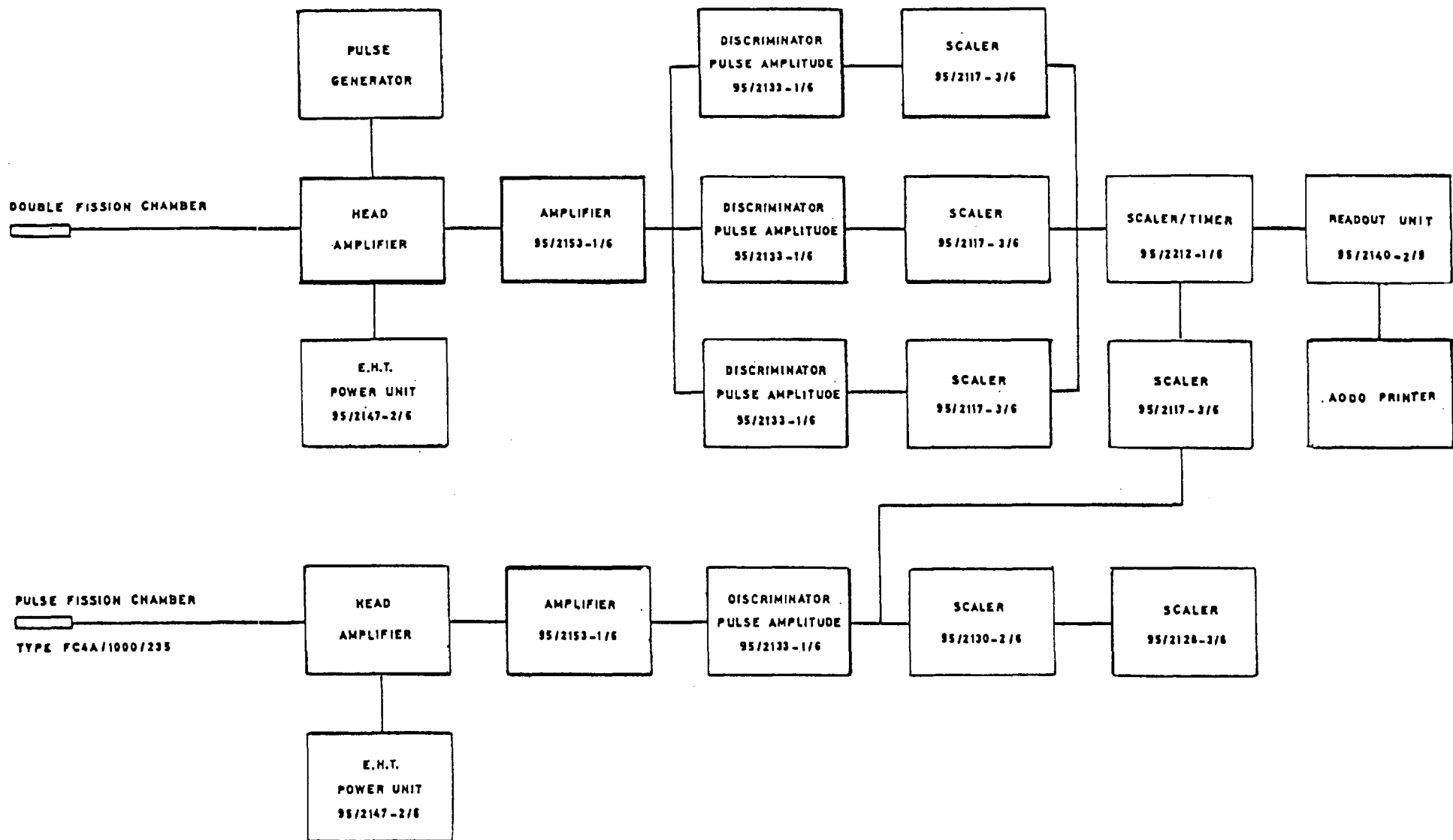
Fig. 6.7   Block diagram of the power monitor fission chamber connected to the triple-scaler counting system.

PULSE FISSION CHAMBER

TYPE FC4A/1000/235

HEAD AMPLIFIER	
AMPLIFIER 95/2153-1/6	
DISCRIMINATOR PULSE AMPLITUDE 95/2133-1/6	
SCALER 95/2130-2/6	
SCALER 95/2128-3/6	

E.H.T. POWER UNIT 95/2147-2/6

AMPLIFIER TRANSLATION 95/2139-1/6

MIXER NE 6418

LINEAR DELAY NE 4615

LINEAR GATE NE 6414

MULTICHANNEL PULSE HEIGHT ANALYSER

TELETYPE
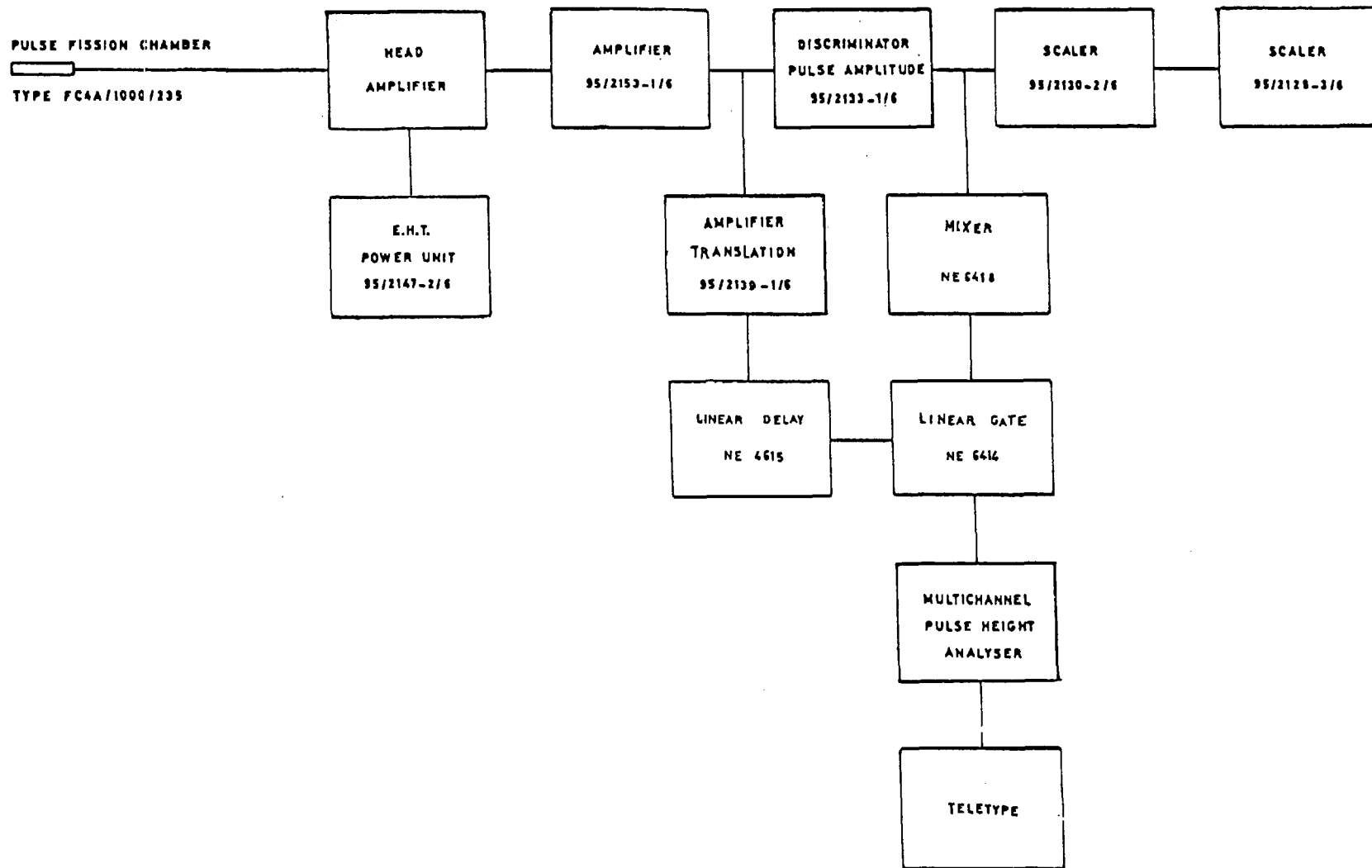
Fig. 6.8   Block diagram of the electronic system to get the monitor fission chamber pulse height distribution.
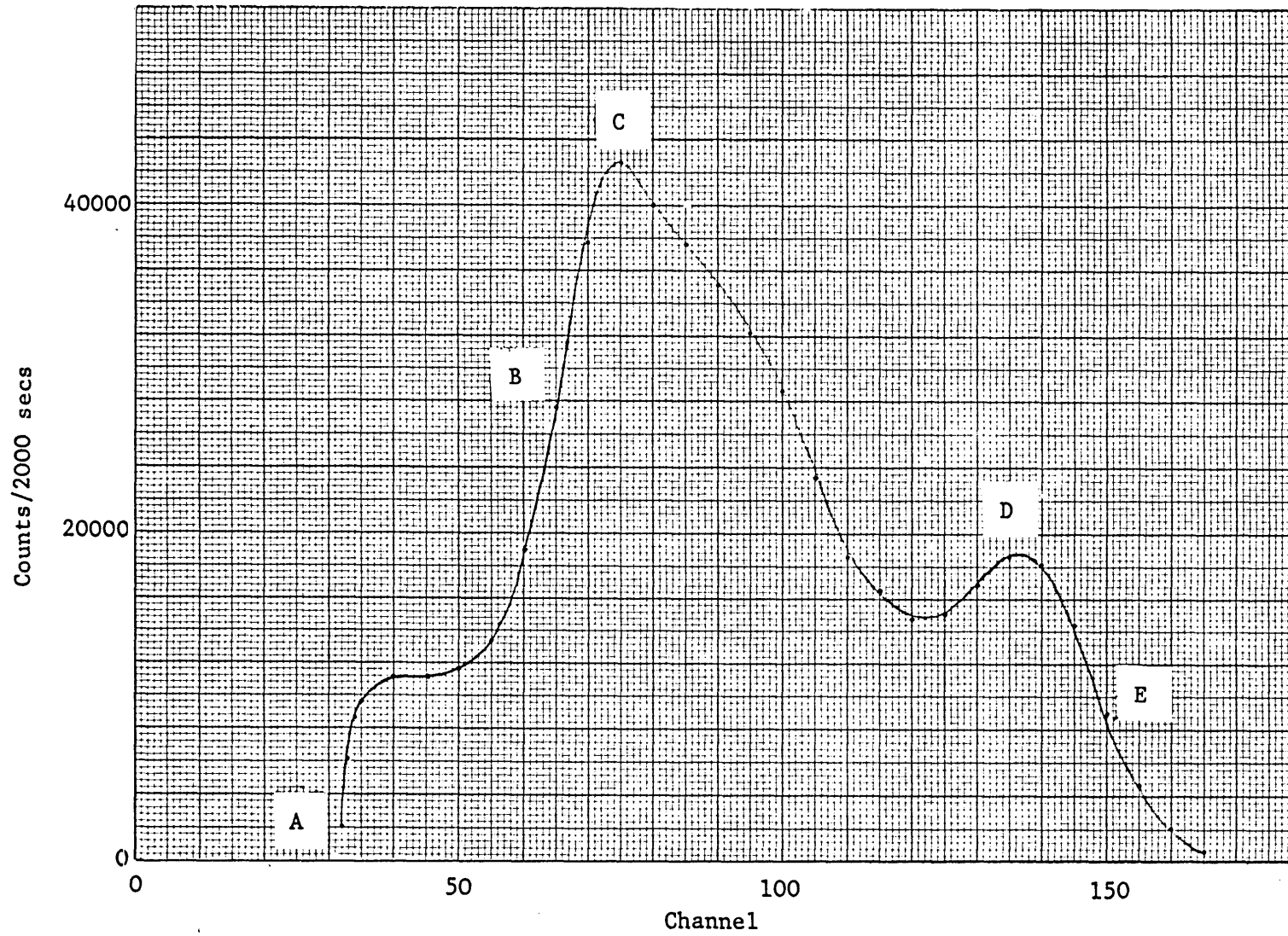
Fig. 6.9   Typical pulse height distribution from the monitor fission chamber.

respectively.   The departure of the point A from straight line

indicates the drift in discriminator level.   Fig. 6.10 shows the

variation of these four points for two different runs with channel

number.

6.6.2 Au foil monitors

All fission chamber experiments were monitored with two Au

foils irradiated in the NISUS thermal column extension.   Fig. 6.11

shows the block diagram of the position details of the foil monitors.

The foils were placed in the positions A and B of the square graphite

plug and loaded in the hole 1 of the NISUS thermal column.   Hole

No. 1 was chosen because it is far away from the NISUS assembly,

and also not close to the edge of the stack which is not suitable

due to flux gradient effect.

The Au foil monitors were counted on a Ge(Li) system and

ECON II pulse height analyzer.   The conversion gain of the multi-

channel analyzer was set in such a way that the 412 keV peak was

almost in the middle of the 1024 channels.   To analyze the data

and to find the area under the peak, the classical peak method which

simply subtracts the background from the total count was preferred

to any fitting method, e.g. SAMPO[105].   SAMPO tries to fit a

Gausian distribution with two exponential tailings to the data input,

while the upper side of the Au peak falls very sharply with no

similarity to exponential.   The computer program ACT was used[103]

to calculate the saturated activity of the Au foils.   The measured

counts, irradiation time, decay time, counting time, half life,
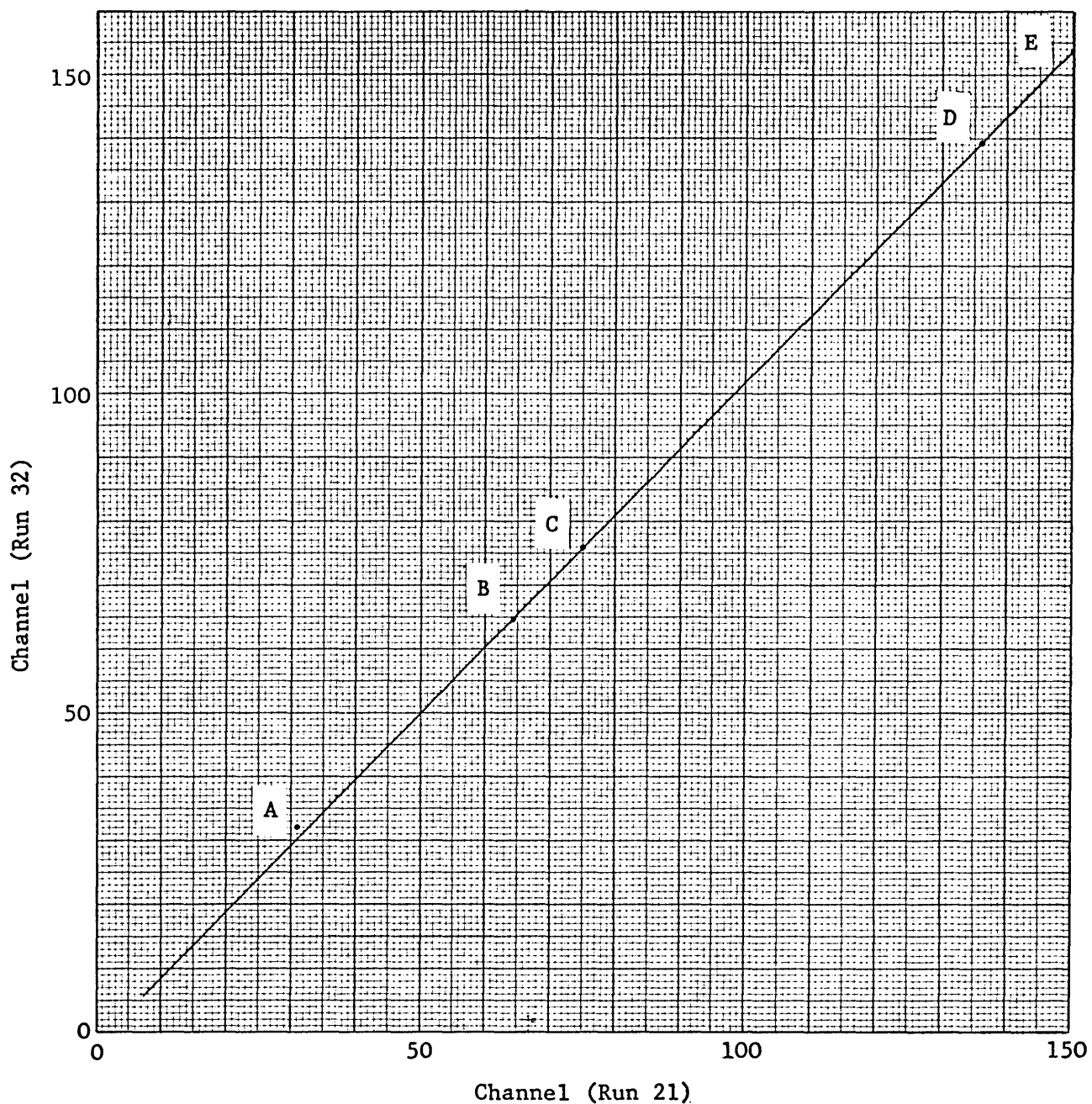
Fig. 6.10   Variation of some specific points of the monitor chamber

pulse height distribution with channel number.   Point A

shows a drift of about 3% in the discriminator level.

FRONT VIEW   ‘SIDE VIEW

180

1   2   3   4

5   6   7   8

75   60   75

73.7   73.7

SQUARE PLUG   Au FOIL MONITOR

B   A

3.2

73.7
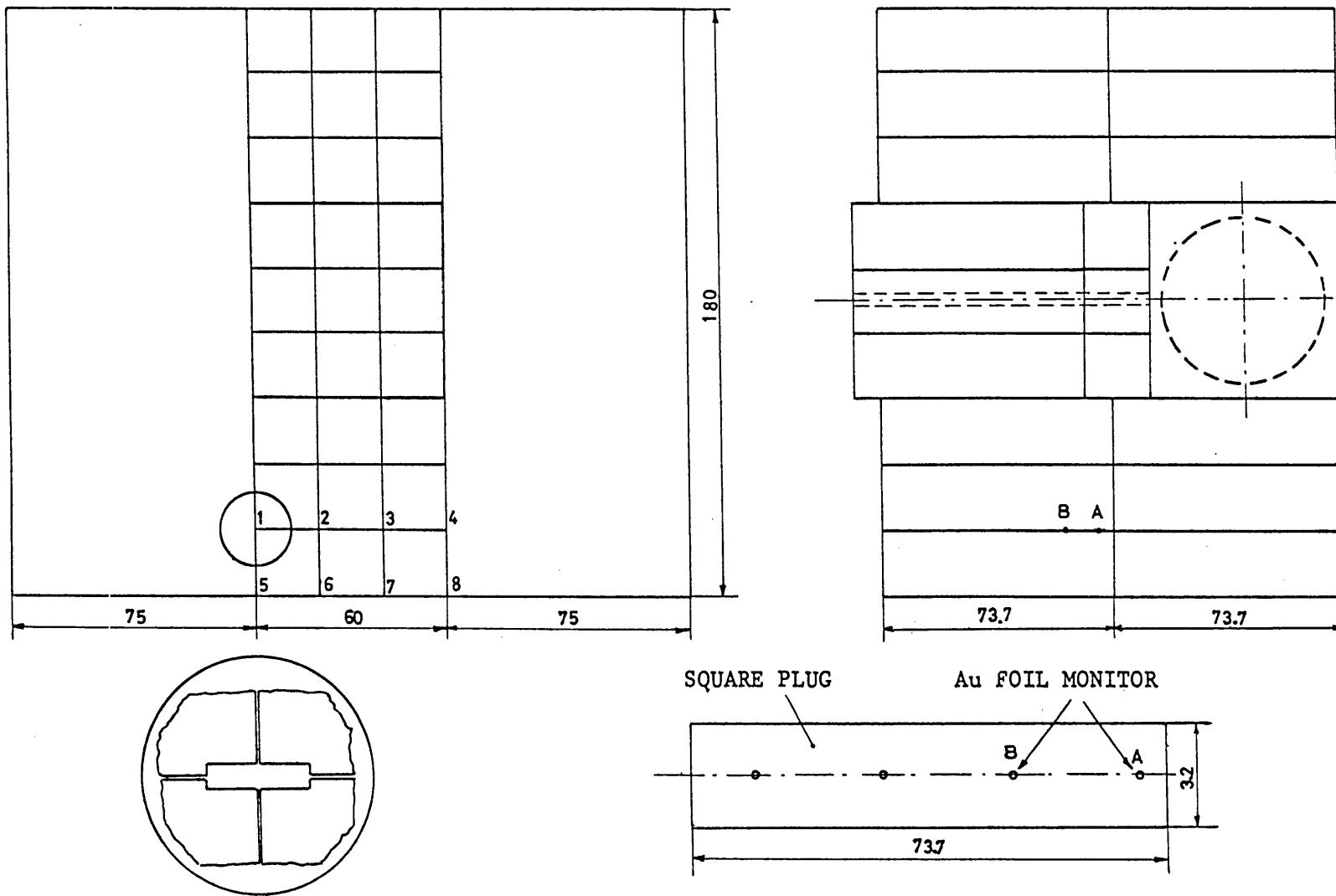
DIMS. IN CM

Fig. 6.11   Block diagram of the position details of the Au foil monitors.

branching ratio and the efficiency of the detector were data and

the reaction rate for each gold foil was calculated from the

following relationship:

$$A_s = \frac{\lambda C}{P\eta \ (1-\exp \ (-\lambda t_a)) \ \exp \ (-\lambda t_d) \ (1-\exp \ (-\lambda t_c))} \qquad (6.2)$$

where A_s is the saturation activity per atom of the foil per second,

λ is the decay constant of the foil material,

C   is the true number of counts on the foil,

P   is the branching ratio,

η is the detector efficiency,

t_a is the irradiation time

t_d is the time interval between the end of irradiation and

the start of counting,

t_c is the counting time on the foil.

The true number of counts on the foil is obtained from

$$C = \frac{(C_o - B) \ \mu t}{F_d \ F_s \ (1-\exp(-\mu t))} \qquad (6.3)$$

where C_o is the observed number of counts,

B   is the natural background,

μ is the absorption coefficient of the foil,

t   is the foil thickness,

F_d is the correction factor for the flux depression,

F_s is the correction factor for the neutron self-shielding.

The absolute activity per atom of the foil per second is equal to:

$$A = \frac{A_s \times M}{W \times N_o}$$
(6.4)

where M is the weight of the foil,

W is the atomic weight of the material,

N_o is the Avogadro's number.

In the calculation of the saturated activity of the gold foils, no correction has been applied for the foil self-absorption, flux depression, and neutron self-shielding since the ^{197}Au (n,γ) monitor reaction rates are relative. The natural background has been found to be negligible and this correction was unnecessary.

6.6.3 Conclusions

Table 6.5 shows the reproducibility and linearity of flux levels by means of the two independent monitoring systems in the course of fission rates measurements in NISUS. The results were obtained over a period of two months and hence reflect the stability of the systems. The variations in the fission chamber monitor 1 is about 0.5% (1 σ) while that of the monitor 2 is $\sim$ 2% (1 σ). In the case of the Au foil monitors the variance for the foils in position A is 1.3% and that of the foils in position B is 1.5%. In the present fission rate measurements both fission chamber 1 and Au foil A monitors were taken for reactor power monitoring.

TABLE 6.5

Reactor power monitoring by means of fission chamber
and activation foil monitors[a]

| Run No. | Reactor power KW | Fission chamber monitor Counts/sec | | | | Au foil monitor Reaction rate/atom | |
| | | Monitor 1 | | Monitor 2 | | Position A | Position B |
		Average[b]	Accumulated[c]	Average[b]	Accumulated[c]	$\times 10^{-15}$	$\times 10^{-16}$
1	100	1319.8 ± .2	–	–	–	1.01518 ± .13%	6.33411 ± .17%
2	"	1323.1 ± .6	1322.8 ± .5	548.1 ± .5	547.2 ± .3	1.06433 ± .20%	6.59360 ± .28%
3	"	1323.0 ± .8	1334.3 ± .5	548.4 ± .4	–	1.04381 ± .24%	6.43500 ± .30%
4	"	1323.9 ± .6	1332.6 ± .5	547.8 ±1.0	–	1.05964 ± .21%	6.46140 ± .44%
5	"	1325.6 ± .5	–	548.6 ± .4	–	–	–
6	"	1325.5 ± .6	1316.7 ± .5	546.9 ± .4	–	1.02427 ± .20%	6.28830 ± .25%
7	"	1316.5 ± .6	–	–	533.6 ± .3	1.00910 ± .34%	6.22220 ± .42%
8	"	1313.3 ± .7	1320.3 ± .5	546.8 ± .4	549.9 ± .3	1.03506 ± .31%	6.41212 ± .40%
9	"	1314.6 ± .8	1310.7 ± .5	547.2 ± .5	–	1.02576 ± .34%	6.30960 ± .42%
10	"	1323.9 ± .6	–	545.1 ±1.0	530.8 ± .3	1.01889 ± .30%	6.24562 ± .39%
11	"	1324.7 ± .8	1347.4 ± .7	543.6 ± .6	553.0 ± .5	1.03300 ± .52%	6.33430 ± .63%
12	"	1323.9 ± .8	–	543.9 ± .7	–	1.04534 ± .32%	6.36256 ± .40%

TABLE 6.5 (continued)

Reactor power monitoring by means of fission chamber and activation foil monitors[a]

Run No.	Reactor power KW	Fission chamber monitor Counts/sec				Au foil monitor Reaction rate/atom	
		Monitor 1		Monitor 2		Position A	Position B
		Average[b]	Accumulated[c]	Average[b]	Accumulated[c]	$\times 10^{-15}$	$\times 10^{-16}$
13	100	1324.7 ± .7	1326.6 ± .3	543.4 ± .3	544.6 ± .2	1.04862 ± .17%	6.56091 ± .20%
14	"	1319.3 ± .3	1322.5 ± .2	541.8 ± .3	543.2 ± .2	1.02018 ± .15%	6.31904 ± .18%
15	"	1330.1 ± .6	1329.5 ± .2	548.9 ± .3	549.3 ± .1	1.04828 ± .20%	6.26810 ± .25%
16	"	1343.9 ±2.4	–	550.0 ± .4	550.6 ± .2	1.03266 ± .26%	6.33448 ± .32%
17	"	1331.7 ± .7	1336.1 ± .9	550.0 ±1.1	551.6 ± .6	1.04572 ± .40%	6.40251 ± .50%
18	"	1330.3 ± .5	1331.2 ± .2	552.5 ± .3	552.1 ± .2	1.05003 ± .21%	6.48148 ± .25%
19	"	1334.5 ± .3	1333.9 ± .2	568.2 ± .2	567.9 ± .2	1.03670 ± .20%	6.35040 ± .25%
20	"	1333.3 ± .7	1331.7 ± .2	551.3 ± .3	–	1.04583 ± .30%	6.29871 ± .40%
21	"	1331.1 ±1.5	1331.9 ± .2	550.1 ± .5	550.5 ± .2	1.02996 ± .26%	6.34854 ± .33%
22	10	–	–	53.0 ± .1	53.1 ± .1	0.10514 ±1.70%	0.63256 ±2.23%
23	10	–	–	53.3 ± .3	53.6 ± .1	0.10277 ±1.72%	0.62402 ±2.12%
24	100	–	–	523.3 ± .8	524.7 ± .4	1.02745 ± .64%	6.19959 ± .85%

TABLE 6.5 (continued)

Reactor power monitoring by means of fission chamber
and activation foil monitors[a]

Run No.	Reactor power KW	Fission chamber monitor Counts/sec				Au foil monitor Reaction rate/atom	
		Monitor 1		Monitor 2		Position A	Position B
		Average[b]	Accumulated[c]	Average[b]	Accumulated[c]	X 10^{-15}	X 10^{-16}
25	100	1323.2 ± .4	–	525.1 ± .3	–	1.02032 ± .24%	6.30304 ± .30%
26	"	1325.4 ± .5	1325.9 ± .2	526.3 ± .3	526.9 ± .2	1.02924 ± .22%	6.32180 ± .30%
27	25	337.6 ± .6	338.7 ± .3	133.9 ± .4	134.6 ± .2	0.27086 ± .85%	1.63774 ±1.04%
28	100	1327.4 ±2.1	1326.2 ± .9	526.3 ± .5	525.7 ± .5	1.03439 ± .80%	6.37539 ±1.02%
29	"	1327.3 ±1.3	1333.1 ± .2	526.2 ± .8	529.7 ± .4	1.03004 ± .60%	6.33221 ± .73%
30	20	–	273.0 ± .4	–	108.8 ± .2	0.21533 ±1.10%	1.30559 ±1.33%
31	100	1336.4 ± .7	–	548.0 ±2.0	542.7 ± .2	–	–
32	"	1339.8 ± .6	1338.9 ± .2	553.1 ± .6	552.7 ± .2	1.04992 ± .16%	6.49251 ± .20%
33	"	1326.4 ± .8	1326.5 ± .2	544.7 ±1.5	545.7 ± .2	1.02977 ± .16%	6.31024 ± .20%

Note: (a)   All errors shown are statistical random errors only (1σ).

(b)   Average over several intervals, e.g. every 5 min.

(c)   Accumulated over the length of irradiation.

The linearity and normalization of the reactor power is shown in
Table 6.6.

6.7 Central NISUS fission rate measurements with an NBS chamber

The first accurate measurements of fission rates in the NISUS

facility by means of the NBS fission chamber have been performed during

the visit by A. Fabry of Mol, Belgium, to ULRC, with collaboration of

J.G. Williams and A.H.M.A. Hannan.   These measurements including

^{239}Pu, ^{237}Np, ^{235}U, and ^{238}U fissionable deposits were carried out

with the Ortec electronics specifically brought from Mol.   The ULRC

fission chamber measurements were performed with the Harwell 2000

Series electronic system which has been used at ULRC for some time.

It was found, however, that there is no significant difference between

the two systems as far as the fission rate measurement are concerned.

The NBS fission chamber measurements were performed with a

cadmium "umbrella" to shield against thermal neutron penetration

through the access hole (Fig. 6.12).   In the first experiment the

chamber was accidentally off-centred by 2.5 mm, and the fission ratio

of $^{239}Pu/^{238}U$ was found to be 21.61 with a discrepancy of about + 3.6%

compared with that of $\Sigma\Sigma$.   The corrections of 0.2% and 0.4% had

consequently to be applied to the ^{239}Pu and ^{238}U fission rates

respectively observed in this run.   These corrections were deduced

from an array of activation rate traverses through the central

exposure zones in NISUS and $\Sigma\Sigma^{(106)}$.   In the second run the $^{237}Np/^{235}U$

ratio was measured to be 0.3783 with a discrepancy of -0.98% compared

with 0.380, the value for the $\Sigma\Sigma$ F_7/F_5 ratio.   The $^{239}Pu/^{235}U$ fission

TABLE 6.6

Reactor power normalization

Reactor power KW	Fission chamber monitor				Au foil monitor			
	Monitor 1		Monitor 2		Position A		Position B	
	Counts/sec	Normalized	Counts/sec	Normalized	Reaction rate/atom $\times 10^{-15}$	Normalized	Reaction rate/atom $\times 10^{-16}$	Normalized
10	–	–	53.2	.098	.10396	.100	.62829	.099
20	273.0	.206	108.8	.200	.21533	.208	1.30559	.205
25	337.6	.255	133.9	.246	.20786	.262	1.63774	.258
100	1326.5	1.000	544.3	1.000	1.03531	1.000	6.35918	1.000

(a)

REACTOR CORE

CADMIUM SHIELD

URANIUM SHELL

BORON CARBIDE SHELL

(b)

REACTOR CORE

CADMIUM SHIELD
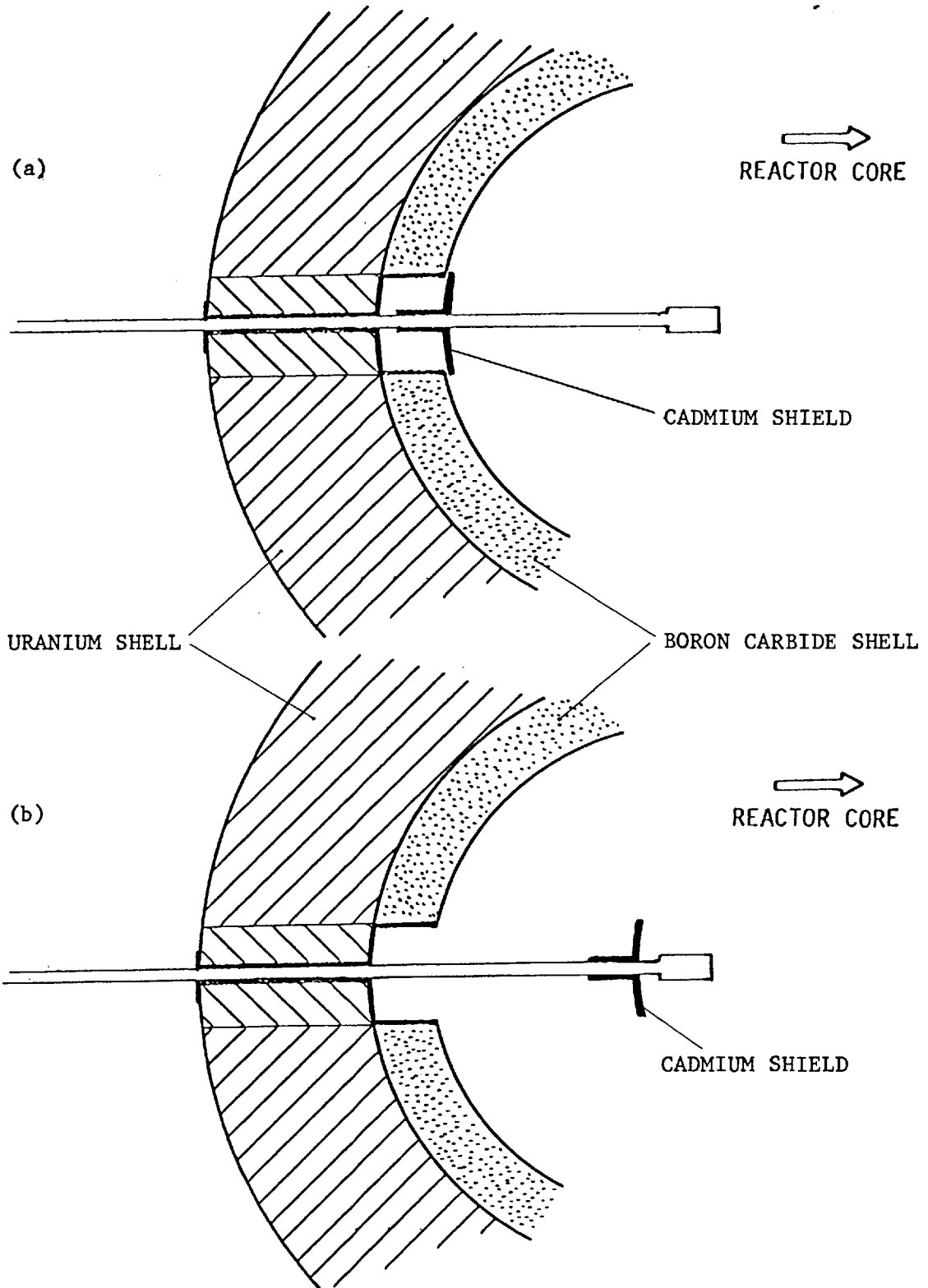
Fig. 6.12   Cross-sectional sketch of the NBS fission chamber in NISUS.

ratio implied *by* these two measurements and the value of
1.228 was found *to be* + 4.5% higher than 1.175, that of $\Sigma\Sigma$. In the
third run the $^{237}Np/^{235}U$ fission ratio was measured with the NBS
chamber under a 1 mm cadmium cover and the F_7/F_5 ratio was found
to be 0.3805 with a discrepancy of 0.1% compare with that of $\Sigma\Sigma$.
The results showed that the fission rates of ^{237}Np and ^{235}U are
about 0.4% and 1% lower than those of the bare chamber, respectively.
The 0.4% difference in the ^{237}Np fission rate which is a threshold
detector is the effect of cadmium down-scattering perturbation. In
run 4 the $^{238}U/^{235}U$ fission rate measurement was performed with a
bare chamber and the value of F_8/F_5 = 0.05669 was obtained. The
higher fission rates in ^{239}Pu and ^{235}U deposits were found to be
due to thermal neutron streaming through the access hole. The
access hole is shielded against thermal neutron perturbation by
using a uranium plug and cadmium pieces. Although the plug is
kept tight in the access hole, such is not the case neutronically,
i.e. there is a penetration through the aluminium cladding of the
boron carbide shell. There also exists the possibility of thermal
neutron streaming through central hole of the plug for electronic
cables and gas tubing. Measurements in $\Sigma\Sigma$ have shown[102] this
component to be negligible. The thermal neutron streaming was
proved by performing three more experiments (runs 7 to 9) with ^{239}Pu
and ^{238}U deposits. In runs 7 and 8 the ^{238}U fission rates were not
obtained due to chamber malfunctioning. In run 7 the $^{239}Pu/^{238}U$
fission ratio was measured by placing the bare chamber exactly at
the centre of NISUS, and the value of 21.29 was found for F_9/F_8.

The $^{239}Pu/^{235}U$ fission ratio for bare chamber deduced from runs

2 and 7 was 1.197 with a discrepancy of $\sim$ 1.9% compared with

that of $\Sigma\Sigma$.   In run 8 the same measurement was repeated with the

NBS chamber under 1 mm cadmium box.   The $^{239}Pu/^{238}U$ fission ratio

was measured to be 20.72 with a discrepancy of about 0.6% compared

with that of $\Sigma\Sigma$ (F_9/F_8 = 20.85).   The ratio of F_9/F_5 was then

deduced as 1.177 with a discrepancy of less than 0.2% compared

with 1.175, the corresponding ratio in $\Sigma\Sigma$.   In run 9 the inner

cadmium screen (umbrella) was moved inwards so that the "umbrella"

was at $\sim$ 2 cm from NISUS centre (Fig. 6.12b).   The $^{239}Pu/^{238}U$

fission ratio measurement was performed under the new conditions

and the value of 20.90 was obtained for F_9/F_8.   Agreement between

this value and the value obtained with Cd box shows that the thermal

neutrons observed with the bare chamber were indeed coming from the

direction of the access hole.   The $^{239}Pu/^{235}U$ fission ratio was

inferred from runs 3 (^{235}U) and 9 (^{239}Pu) and found to be 1.186.

The $^{238}U/^{235}U$ fission ratio from runs 3 (^{235}U) and 4 (^{238}U) was found

to be 0.05735 with a discrepancy of 1.7% compared with 0.05636, that

of $\Sigma\Sigma$.

The effect of thermal neutron streaming through the access

hole in the fission rate measurements with the NBS fission chamber

is shown in Table 6.7 in comparison with $\Sigma\Sigma$.   It is worth noting

that all the NBS fission chamber measurements were performed at the

reactor power of 100 kW but for short irradiation times, namely a

couple of hours, to make it possible to have several runs in a

normal working day.   It was found that for such short intervals

the monitor chamber was more reliable than the Au foil monitor because of the low activity of the foils and the likelihood of systematic error in timing. This error, if any, was not applicable to the fission chamber monitor where the counts were recorded every 5 minutes and the average was made over several intervals. Thus the fission ratios in Table 6.7 are those on the basis of monitor chamber.

TABLE 6.7

The effect of thermal neutron streaming through the access hole in the fission ratio measurements with the NBS fission chamber

Fission ratio	NISUS			$\Sigma\Sigma$
	Bare chamber	Cd unbrella	Cd box	
$^{239}Pu/^{238}U$	21.29	20.90	20.72	20.85
$^{239}Pu/^{235}U$	1.197	1.186	1.177	1.175
$^{237}Np/^{235}U$	.3783	–	.3805	.380
$^{238}U/^{235}U$	.05669	–	.05735	.05636

6.8   Central NISUS fission rate measurements with the ULRC chamber

Since the thermal neutron streaming through the access hole

was proved in the course of the NBS fission chamber measurements,

it was decided to modify the hole to reduce streaming effect to a

minimum.   The modification was to fix an annular piece of cadmium

around the inner edge of the access hole on the boron carbide shell

(Fig. 6.13) so that any thermal neutron streaming through the Al

cladding was shielded against.   On the other hand a cadmium cover

was fixed on the inner surface of the uranium plug with a small hole

as large as the thickness of the cables to keep the thermal neutron

streaming to a minimum.   In order to investigate the effect of

streaming after the modification two experiments were made with In

foils.   In one experiment an In foil was sandwiched between the two

deposits of the fission chamber and in another experiment the foil was

irradiated with the aluminium foil holder by using the solid uranium

plug with no hole.   The results of the ^{115}In (n,γ) reaction rate measurements

from these two experiments showed that the thermal neutron streaming

effect is within the experimental error (Table 6.3).

The central NISUS fission rate measurements in the ULRC

fission chamber were carried out with two NBS (25S-2-3 and 28 HD-5-1),

AWRE and ULRC deposits.   In the first set of these measurements the

deposits were used in different combinations for mass comparison

purposes (see Section 6.4).   Two experiments were carried out with

^{235}U and ^{238}U activation foils wrapped in an aluminium catcher and

sandwiched between the two back-to-back ^{235}U and ^{238}U deposits.

From these two measurements the average ^{238}U/^{235}U fission ratio was

REACTOR CORE

Cadmium pieces mounted
on the B_4C shell
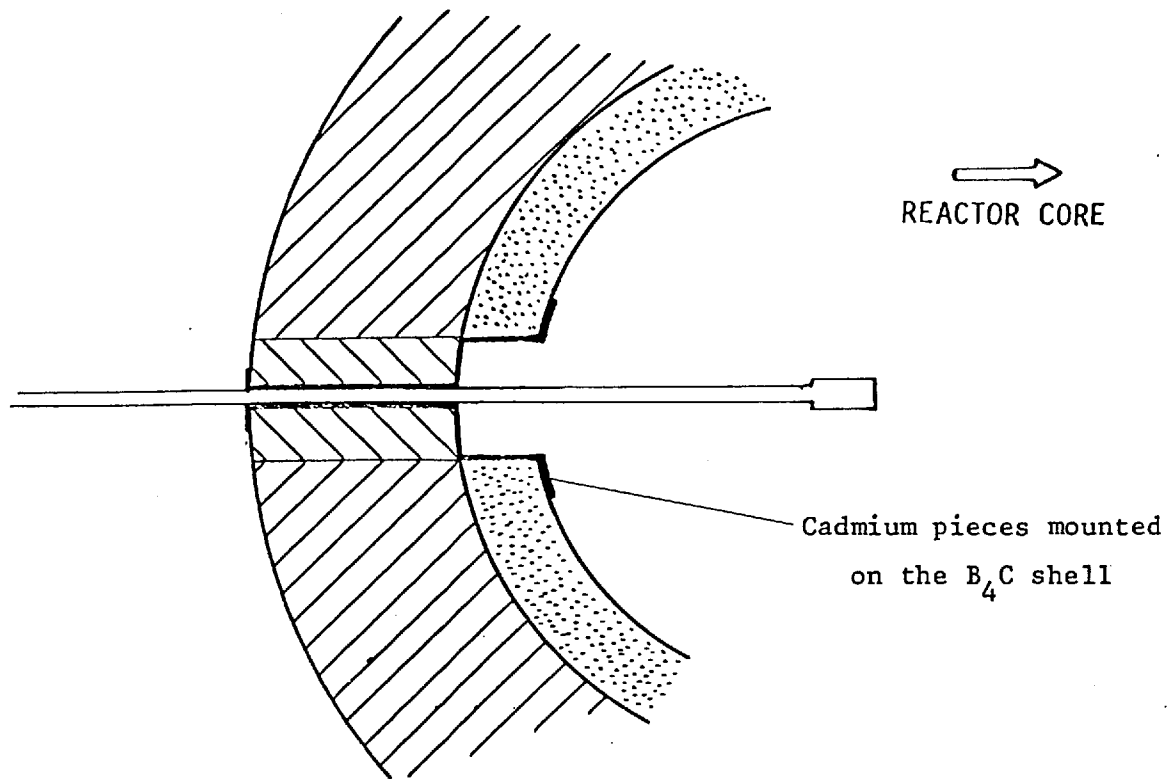
Fig. 6.13   Modification to the access hole.

found[103] to be .05781 ± 1.9% (random) for the foils compared

with 0.05533 ± .17% (random) that from the ULRC fission chamber

with the discrepancy of + 4.5%.   Some experiments were made with

track recorders to determine the optical efficiency of the SSTR and

to make a comparison between the $^{238}U/^{235}U$ fission ratios obtained

by the SSTR and fission chamber (see Chapter 7).

6.9   Summary and conclusions

The summary of the fission rates measurements in NISUS with

the NBS, AWRE and ULRC deposits in the NBS and the ULRC fission

chambers is shown in Table 6.8.   The first 9 runs (except run 6)

were performed with the NBS chamber and the rest with the ULRC

chamber.   In run Nos. 6 and 12 the ULRC chamber was used to calibrate

the AWRE and ULRC deposits against those of the NBS.

In each run the fission rate for each deposit was derived

from the S_L count rate, the number of counts above V_L discriminator,

by taking the extrapolation-to-zero as $2(S_L/S_U-1)$ and applying the

corrections listed in Table 6.4.   The maximum discrepancy for the

ETZ correction between the NBS and the ULRC chambers is 1.5% for

the same deposits.   This is because of the geometrical difference

between the two chambers and probably due to the larger distance

(5 mm) between the deposits and the anodes in the ULRC chamber than

that of the NBS chamber ($\simeq$ 4 mm).

The reproducibility of the ETZ correction for different runs

was found to be within   0.1% for the NBS fission chamber, and that

of the ULRC chamber varies from 0.5% to 1.7% for different deposits.

TABLE 6.8

Summary of the experimental components for the exposures of the

NBS and ULRC fission chambers at NISUS centre

Foil identification and principal isotope	Run No.	S_L (cps)	S_L/S_U	ETZ	Fission rate/atom[a] X 10^{-17}
NBS 49 I-1-1 ^{239}Pu	1[b]	64.17 ± .14	1.00339 ± .00042	1.00678 ± .00084	24.3304 ± .22%
	7	62.37 ± .15	1.00375 ± .00041	1.00750 ± .00082	23.6648 ± .24%
	8[c]	60.55 ± .11	1.00388 ± .00037	1.00776 ± .00074	22.9802 ± .18%
	9[d]	61.04 ± .20	1.00449 ± .00020	1.00898 ± .00040	23.1942 ± .33%
NBS 28 N-5-2 ^{238}U (natural)	1[b]	20.13 ± .07	1.02570 ± .00195	1.05140 ± .00390	1.1261 ± .35%
	9[d]	19.81 ± .08	1.02665 ± .00124	1.05330 ± .00248	1.1102 ± .40%
NBS 25 S-2-3 ^{235}U	2	111.07 ± .13	1.00557 ± .00040	1.01114 ± .00080	19.8673 ± .12%
	3[c]	110.00 ± .19	1.00551 ± .00037	1.01102 ± .00074	19.6736 ± .17%
	4	111.33 ± .12	1.00557 ± .00046	1.01114 ± .00092	19.9138 ± .11%
	6	110.68 ± .21	1.00998 ± .00051	1.01996 ± .00102	20.0706 ± .19%
NBS 37 S-5-2 ^{237}Np	2	115.24 ± .11	1.01202 ± .00071	1.02404 ± .00142	7.5160 ± .10%
	3[c]	114.79 ± .16	1.01190 ± .00080	1.02380 ± .00160	7.4849 ± .14%

TABLE 6.8 (continued)

Summary of the experimental components for the exposures of the
NBS and ULRC fission chambers at NISUS centre

Foil identification and principal isotope	Run No.	S_L (cps)	S_L/S_U	ETZ	Fission rate/atom $\times 10^{-17}$
NBS 28 HD-5-1 ^{238}U (depleted)	4	17.33 ± .06	1.01513 ± .00158	1.03026 ± .00316	1.1290 ± .35%
	12	16.79 ± .06	1.02288 ± .00195	1.04576 ± .00390	1.1036 ± .36%
AWRE ^{235}U (enriched)	6*	65.02 ± .11	1.00628 ± .00046	1.01256 ± .00092	20.0631 ± .17%
	18	64.12 ± .14	1.00813 ± .00071	1.01626 ± .00142	19.8577 ± .22%
AWRE ^{238}U (depleted)	19*	34.86 ± .06	1.01036 ± .00087	1.02072 ± .00174	1.1036 ± .17%
ULRC-1 ^{238}U	21*	75.23 ± .14	1.04602 ± .00353	1.09204 ± .00706	1.1036 ± .19%
	33	74.40 ± .07	1.04848 ± .00216	1.09696 ± .00432	1.0963 ± .09%
ULRC-2 ^{238}U	26*	72.75 ± .10	1.07351 ± .00176	1.14702 ± .00352	1.1036 ± .14%
ULRC-3 ^{238}U	12*	20.54 ± .09	1.02489 ± .00143	1.04978 ± .00286	1.1030 ± .44%
	16	20.85 ± .06	1.02295 ± .00180	1.04590 ± .00360	1.1155 ± .29%
	19	20.78 ± .09	1.02210 ± .00193	1.04420 ± .00386	1.1099 ± .43%
	21	20.80 ± .04	1.02208 ± .00143	1.04416 ± .00286	1.1110 ± .19%

TABLE 6.8 (continued)

Summary of the experimental components for the exposures of the

NBS and ULRC fission chambers at NISUS centre

Foil identification and principal isotope	Run No.	S_L (cps)	S_L/S_U	ETZ	Fission rate/atom X 10^{-17}
	25	20.77 ± .07	1.01592 ± .00115	1.03184 ± .00230	1.0963 ± .34%
	26	20.75 ± .04	1.01651 ± .00121	1.03302 ± .00242	1.0965 ± .19%
ULRC-4 ^{235}U	14*	37.12 ± .07	1.01302 ± .00099	1.02604 ± .00198	20.2521 ± .19%
	33	36.89 ± .16	1.01003 ± .00082	1.02006 ± .00164	20.0093 ± .43%
ULRC-5 ^{235}U	20*	159.03 ± .13	1.01527 ± .00043	1.03054 ± .00086	20.0795 ± .08%
	23(e)	16.05 ± .08	1.01007 ± .00118	1.02014 ± .00236	2.0061 ± .50%
ULRC-6 ^{235}U	14	164.15 ± .16	1.01195 ± .00034	1.02390 ± .00068	20.1590 ± .10%
	16	163.78 ± .14	1.01119 ± .00161	1.02238 ± .00322	20.0837 ± .09%
	17	163.32 ± .22	1.01195 ± .00053	1.02390 ± .00106	20.0570 ± .14%
	18*	163.48 ± .11	1.01182 ± .00044	1.02364 ± .00088	20.0716 ± .07%
	20	163.76 ± .17	1.01116 ± .00058	1.02232 ± .00116	20.0800 ± .10%
	22(e)	16.41 ± .09	1.01281 ± .00089	1.02562 ± .00178	2.0187 ± .55%

TABLE 6.8 (continued)

Summary of the experimental components for the exposures of the

NBS and ULRC fission chambers at NISUS centre

Foil identification and principal isotope	Run No.	S_L (cps)	S_L/S_U	ETZ	Fission rate/atom X 10^{-17}
	24	161.92 ± .27	1.01045 ± .00073	1.02090 ± .00146	19.8268 ± .17%
	25	160.98 ± .21	1.01780 ± .00042	1.03560 ± .00084	19.9956 ± .13%
	27 (f)	41.75 ± .21	1.01179 ± .00087	1.02358 ± .00174	5.1195 ± .50%
	28	163.72 ± .34	1.01077 ± .00086	1.02154 ± .00172	20.0598 ± .21%
	29	163.05 ± .33	1.01022 ± .00034	1.02044 ± .00068	19.9562 ± .20%

Note:

(a) Errors shown are statistical sampling errors only (1σ)

(b) The chamber was accidentally off-centred by 2.5 mm

(c) Cadmium box

(d) Cadmium unbrella

(e) Reactor power 10 kW

(f) Reactor power 25 kW

* Mass calibration run for this deposit. Fission rate not included in the mean.

It was found that in the ULRC chamber the positions of the two electrodes are not exactly identical with respect to the deposit holder. This means that the side with larger distance between the anode and the deposit gives higher ETZ than the other side because the number of undetected fragments is increased. The reproducibility of the ETZ correction for each side does not exceed 1.2%. It is, however, clear that the value of ETZ correction does not matter if a proper estimate of the undetected fission fragments is carried out. Table 6.8 shows that the variation of the fission rates per atom for all deposits in different runs is about 1%. In Table 6.9 the fission per monitor ratios are shown both for the monitor chamber and the ^{197}Au (n,γ) reaction. It is seen that the variation of the fission rate per atom per monitor chamber is ∿ 1% and that of the fission rate per ^{197}Au (n,γ) reaction is about 2%. Since the consistency of the monitors was of about this order of magnitude, one finds that there is a good agreement between the results of more than 25 runs.

The ^{235}U fission rates obtained with the bare ULRC chamber in run Nos. 6 and 12 are subject to ∿ 1% correction due to thermal neutron streaming effect since these runs were performed before modification to the access hole. This correction has not been applied to the relevant fission/monitor ratios shown in Table 6.9. The values of fission rates in $\Sigma\Sigma^{(100)}$ carry corrections of + 0.6% for chamber moderation on ^{237}Np and ^{238}U and − 0.5% for epicadmium streaming on ^{239}Pu and ^{235}U. To be consistent the same corrections have been made to the NBS chamber data in NISUS. The values for

TABLE 6.9

Summary of the fission/monitor ratios for the exposures of the
NBS and ULRC fission chambers at NISUS centre[a]

Foil identification and principal isotope	Run No.	Fission rate/atom $\times 10^{-17}$	Monitor		Fission rate/monitor	
			Monitor chamber (cps)	$^{197}Au(n,\gamma)$ Reaction rate/atom $\times 10^{-15}$	Monitor chamber	$^{197}Au(n,\gamma)$
NBS 49 I-1-1 ^{239}Pu	1[b]	24.3304 ± .22%	1319.8 ± .02%	1.01518 ± .13%	18.43491 ± .22%	.23966 ± .26%
	7	23.6648 ± .24%	1316.5 ± .05%	1.00910 ± .34%	17.97554 ± .25%	.23452 ± .42%
	8[c]	22.9802 ± .18%	1313.3 ± .05%	1.03506 ± .31%	17.49781 ± .19%	.22202 ± .36%
	9[d]	23.1942 ± .33%	1314.6 ± .06%	1.02576 ± .34%	17.64354 ± .34%	.22612 ± .47%
NBS 28 N-5-2 ^{238}U (natural)	1[b]	1.1261 ± .35%	1319.8 ± .02%	1.01518 ± .13%	.85324 ± .35%	.01109 ± .37%
	9[d]	1.1102 ± .40%	1314.6 ± .06%	1.02576 ± .34%	.84452 ± .40%	.01082 ± .52%
NBS 25 S-2-3 ^{235}U	2	19.8673 ± .12%	1323.1 ± .05%	1.06433 ± .20%	15.01572 ± .13%	.18666 ± .23%
	3[c]	19.6736 ± .17%	1323.0 ± .06%	1.04381 ± .24%	14.87045 ± .18%	.18848 ± .29%
	4	19.9138 ± .11%	1323.9 ± .05%	1.05964 ± .21%	15.04177 ± .12%	.18793 ± .24%
	6	20.0706 ± .19%	1325.5 ± .05%	1.02427 ± .20%	15.14191 ± .20%	.19595 ± .28%
NBS 37 S-5-2 ^{237}Np	2	7.5160 ± .10%	1323.1 ± .05%	1.06433 ± .20%	5.68060 ± .11%	.07062 ± .22%
	3[c]	7.4849 ± .14%	1323.0 ± .06%	1.04381 ± .24%	5.65752 ± .15%	.07171 ± .32%

TABLE   6.9   (continued)

Summary of the fission/monitor ratios for the exposures of the
NBS and ULRC fission chambers at NISUS centre[a]

Foil identification and principal isotope	Run No.	Fission rate/atom $\times 10^{-17}$	Monitor		Fission rate/monitor	
			Monitor chamber (cps)	^{197}Au(n,γ) Reaction rate/atom $\times 10^{-15}$	Monitor chamber	^{197}Au(n,γ)
NBS 28 HD-5-1 ^{238}U (depleted)	4	1.1290 ± .35%	1323.9 ± .05%	1.05964 ± .21%	.85278 ± .35%	.01065 ± .41%
	12	1.1036 ± .36%	1323.9 ± .06%	1.04534 ± .32%	.83360 ± .36%	.01056 ± .48%
AWRE ^{235}U (enriched)	6*	20.0631 ± .17%	1325.5 ± .05%	1.02427 ± .20%	15.13625 ± .18%	.19588 ± .26%
	18	19.8577 ± .22%	1330.3 ± .04%	1.05003 ± .21%	14.92723 ± .22%	.18912 ± .30%
AWRE ^{238}U (depleted)	19*	1.1036 ± .17%	1334.5 ± .02%	1.03670 ± .20%	.82698 ± .17%	.01065 ± .26%
ULRC-1 ^{238}U	21*	1.1036 ± .19%	1331.1 ± .11%	1.02996 ± .26%	.82909 ± .22%	.01071 ± .32%
	33	1.0963 ± .09%	1326.4 ± .06%	1.02977 ± .16%	.82652 ± .11%	.01065 ± .18%
ULRC-2 ^{238}U	26*	1.1036 ± .14%	1325.4 ± .04%	1.02924 ± .22%	.83265 ± .15%	.01072 ± .26%
ULRC-3 ^{238}U	12*	1.1030 ± .44%	1323.9 ± .06%	1.04534 ± .32%	.83314 ± .44%	.01055 ± .54%
	16	1.1155 ± .22%	1343.9 ± .18%	1.03266 ± .26%	.83005 ± .28%	.01080 ± .34%
	19	1.1099 ± .43%	1334.5 ± .02%	1.03670 ± .20%	.83170 ± .43%	.01071 ± .47%
	21	1.1110 ± .19%	1331.1 ± .11%	1.02996 ± .26%	.83465 ± .22%	.01079 ± .32%

TABLE 6.9 (continued)

Summary of the fission/monitor ratios for the exposures of the
NBS and ULRC fission chambers at NISUS centre[a]

Foil identification and principal isotope	Run No.	Fission rate/atom $\times 10^{-17}$	Monitor		Fission rate/monitor	
			Monitor chamber (cps)	^{197}Au(n,γ) Reaction rate/atom $\times 10^{-15}$	Monitor chamber	^{197}Au(n,γ)
	25	1.0963 ± .34%	1323.2 ± .03%	1.02032 ± .24%	.82852 ± .34%	.01074 ± .42%
	26	1.0965 ± .19%	1325.4 ± .04%	1.02924 ± .22%	.82730 ± .19%	.01065 ± .29%
ULRC-4 ^{235}U	14*	20.2521 ± .19%	1319.3 ± .02%	1.02018 ± .15%	15.35064 ± .19%	.19851 ± .24%
	33	20.0093 ± .43%	1326.4 ± .06%	1.02977 ± .16%	15.08542 ± .43%	.19431 ± .46%
ULRC-5 ^{235}U	20*	20.0795 ± .08%	1333.3 ± .05	1.05483 ± .30%	15.06000 ± .09%	.19199 ± .31%
	23[e]	2.0061 ± .50%	-	.10277 ±1.72%	-	.19520 ±1.79%
ULRC-6 ^{235}U	14	20.1590 ± .10%	1319.3 ± .02%	1.02018 ± .15%	15.28007 ± .10%	.19760 ± .18%
	16	20.0837 ± .09%	1343.9 ± .18%	1.03266 ± .26%	14.94434 ± .20%	.19449 ± .28%
	17	20.0570 ± .14%	1331.7 ± .05%	1.04572 ± .40%	15.06120 ± .15%	.19180 ± .42%
	18*	20.0716 ± .07%	1330.3 ± .04%	1.05003 ± .21%	15.08803 ± .08%	.19115 ± .73%
	20	20.0800 ± .10%	1333.3 ± .05%	1.04583 ± .30%	15.06038 ± .11%	.19200 ± .32%
	22[e]	2.0187 ± .55%	-	.10514 ±1.70%	-	.19200 ±1.80%

TABLE   6.9   (continued)

Summary of the fission/monitor ratios for the exposures of the

NBS and ULRC fission chambers at NISUS centre[a]

Foil identification and principal isotope	Run No.	Fission rate/atom $\times 10^{-17}$	Monitor		Fission rate/monitor	
			Monitor chamber (cps)	^{197}Au(n,γ) Reaction rate/atom $\times 10^{-15}$	Monitor chamber	^{197}Au(n,γ)
	24	19.8268 ± .17%	–	1.02745 ± .64%	–	.19279 ± .66%
	25	19.9956 ± .13%	1323.2 ± .03%	1.02032 ± .24%	15.11155 ± .13%	.19597 ± .27%
	27[f]	5.1195 ± .50%	337.6 ± .18%	.27086 ± .85%	15.16440 ± .53%	.18901 ± .99%
	28	20.0598 ± .21%	1327.4 ± .16%	1.03439 ± .80%	15.11210 ± .26%	.19393 ± .83%
	29	19.9562 ± .20%	1327.3 ± .10%	1.03004 ± .60%	15.03518 ± .22%	.19374 ± .63%

Note: (a)   Errors shown are statistical sampling errors only (1σ)

(b)   The chamber was accidentally off-centred by 2.5 mm

(c)   Cadmium box

(d)   Cadmium unbrella

(e)   Reactor power 10 kW

(f)   Reactor power 25 kW

*   Mass calibration run for this deposit. Fission rate not included in the mean.

chamber moderation and epicadmium streaming in the ULRC chamber

are not exactly known, but two independent experiments with In

activation foil (see Section 6.5.4) and SSTR (see Chapter 7) showed

that these corrections are within the errors and less than 1%.

Nevertheless, no moderation and streaming correction has been

applied to the ^{238}U and ^{235}U fission rates data obtained with the

ULRC chamber.

Table 6.10 shows the average of the fission/monitor ratios

for the NBS, AWRE and ULRC deposits exposed in the NBS and ULRC

fission chambers at the centre of NISUS. In Table 6.10 the

fission/monitor ratios of the ^{239}Pu and ^{235}U NBS deposits are

those obtained with cadmium box since these experiments were performed

before the access hole modification against the thermal neutron

streaming. The fission/monitor ratio of the ^{237}Np deposit is that

obtained with the bare NBS chamber because there is a 0.4% depression

due to cadmium downscattering. The fission/monitor ratios of the

NBS 25 S-2-3 deposit exposed in the ULRC chamber (run 6) has been

corrected for the thermal neutron streaming through the access hole.

For the rest of the deposits, the fission/monitor ratios are the means

of the different runs listed in Table 6.9.

Table 6.10 shows that the difference (1 σ) in the fission rate

per atom per monitor chamber ratios for ^{235}U isotope for both chambers

is about 0.6% and that for ^{238}U isotope is 1.2%. The difference

between 0.6% and 1.2% is probably due to uncorrected ULRC data for

chamber moderation. The variations of 1.4% and 0.8% in the fission

rates per atom per ^{197}Au (n,γ) reaction for the ^{235}U and ^{238}U isotopes

TABLE 6.10

The average fission/monitor ratios for the exposures of the

NBS and ULRC fission chambers at NISUS centre[a]

Fission chamber	Foil identification and principal isotope	Fission/monitor	
		Fission rate/atom. monitor chamber X 10^{-20}	Fission rate/ ^{197}Au(n,γ) reaction rate
NBS	NBS 49 I-1-1 ^{239}Pu	17.49781 ± .19%	.22202 ± .36%
	NBS 28 N-5-2 ^{238}U (natural)	.84452 ± .40%	.01082 ± .52%
	NBS 25 S-2-3 ^{235}U	14.87045 ± .18%	.18848 ± .29%
	NBS 37 S-5-2 ^{237}Np	5.68060 ± .11%	.07062 ± .22%
	NBS 28 HD-5-1 ^{238}U (depleted)	.85278 ± .35%	.01065 ± .41%
ULRC	NBS 25 S-2-3 ^{235}U	14.99049 ± .20%	.19399 ± .28%
	NBS 28 HD-5-1 ^{238}U (depleted)	.83360 ± .36%	.01056 ± .48%
	AWRE ^{235}U (enriched)	14.92723 ± .22%	.18912 ± .30%
	AWRE ^{238}U (depleted)	.82698 ± .17%	.01065 ± .26%
	ULRC-1 ^{238}U	.82652 ± .11%	.01065 ± .18%
	ULRC-2 ^{238}U	.83265 ± .15%	.01072 ± .26%
	ULRC-3 ^{238}U	.83044 ± .14%	.01074 ± .17%
	ULRC-4 ^{235}U	15.08542 ± .43%	.19431 ± .46%
	ULRC-5 ^{235}U	15.06000 ± .09%	.19359 ± .91%
	ULRC-6 ^{235}U	15.09615 ± .09%	.19335 ± .25%

Note: (a)   All uncertainties random at 1σ confidence level.

respectively, reflect the consistency of the gold monitors during

the course of fission rate measurements in NISUS. The summary of

the variations in the fission/monitor ratios are shown in Table 6.11.

The isotopic fission/monitor ratios for the NBS, AWRE and

ULRC deposits exposed at the centre of NISUS are shown in Table 6.12.

The ratios are the means of those in Table 6.9 excluding the mass

calibration runs. Table 6.13 shows the fission rate ratios for

TABLE 6.11

Summary of the variations (1 σ) in the fission/monitor ratios
of the NBS and ULRC fission chambers

Fission chamber	Variation, ±%			
	^{235}U		^{238}U	
	Fission rate/atom. monitor chamber	Fission rate/ $^{197}Au(n,\gamma)$ reaction rate	Fission rate/atom. monitor chamber	Fission rate/ $^{197}Au(n,\gamma)$ reaction rate
NBS	–	–	0.7	1.1
ULRC	0.5	1.1	0.4	0.7
Both	0.6	1.4	1.2	0.8

TABLE 6.12

The average isotopic fission/monitor ratios for the exposures of the

NBS and ULRC fission chambers at NISUS centre[a]

Fission chamber	Foil identification	Principal isotope	Fission/monitor	
			Fission rate/atom. monitor chamber $\times 10^{-20}$	Fission rate/ ^{197}Au(n,γ) reaction rate
NBS	NBS	^{239}Pu	17.49781 ± .19%	.22202 ± .36%
		^{237}Np	5.68060 ± .11%	.07062 ± .22%
		^{235}U	14.87045 ± .18%	.18848 ± .29%
		^{238}U N	.84452 ± .40%	.01082 ± .52%
		D	.85278 ± .35%	.01065 ± .41%
ULRC	NBS	^{235}U	14.99049 ± .20%	.19399 ± .28%
		^{238}U	.83360 ± .36%	.01056 ± .48%
	AWRE	^{235}U	14.92723 ± .22%	.18912 ± .30%
		^{238}U	.82698 ± .17%	.01065 ± .26%
	ULRC	^{235}U	15.09496 ± .09%	.19359 ± .26%
		^{238}U	.82979 ± .11%	.01072 ± .14%

Note: (a) All uncertainties random at 1σ. cofidence level.

TABLE 6.13

The fission rate ratios for the exposures of the NBS

and ULRC fission chambers at NISUS centre[a]

Fission chamber	Foil identification	Ratio	Fission rate ratio	
			Monitor chamber	^{197}Au(n,γ) reaction
NBS	NBS	^{239}Pu/^{238}U	20.72 ± .44%	20.52 ± .63%
		^{239}Pu/^{235}U	1.177 ± .26%	1.178 ± .46%
		^{237}Np/^{235}U	.3820 ± .21%	.3747 ± .36%
		^{238}U/^{235}U	.05735 ± .39%	.05650 ± .50%
ULRC	NBS	^{238}U/^{235}U	.05561 ± .41%	.05444 ± .56%
	AWRE	^{238}U/^{235}U	.05540 ± .28%	.05631 ± .40%
	ULRC	^{238}U/^{235}U	.05497 ± .14%	.05499 ± .30%

Note: (a) All uncertainties random at 1σ confidence level.

the NBS, AWRE and ULRC deposits derived from Table 6.12. Table 6.13

shows that the $^{238}U/^{235}U$ fission ratios obtained by the ULRC fission

chamber is $\sim$ 3% less than that by the NBS chamber for the same

deposits. A relevant factor is the increase in F_8/F_5 of + 1.1%

in the NBS chamber data due to corrections applied for epicadmium

streaming and chamber moderation. No comparable correction has

been made for the ULRC chamber data since no effect has been demon-

strated experimentally. Further work is needed to elucidate these

corrections for ULRC chamber measurements. The variation (1 σ) of

the $^{238}U/^{235}U$ fission ratios (Table 6.13) in the ULRC chamber is

better than 0.6% for the monitor chamber and $\sim$ 1.7% for the gold

monitor. These variations reflect the consistency of the chamber

performance for three sets of deposits.

The summary and final fission chamber data for NISUS are shown

in Table 6.14. In Table 6.15 the fission rates of the NBS chamber,

relative to the fundamental reaction ^{235}U (n,f), are compared with

those of $\Sigma\Sigma$ and the computed ones based on the ENDF/B-III and GALAXY

nuclear data file. The comparison is between the results of the

same chamber and the same deposits and hence reflects any difference

between the two standard neutron fields. The transport computation

was only made for the ^{235}U (n,f) and ^{238}U (n,f) reaction rates in

NISUS and $\Sigma\Sigma$ (see Section 5.12), due to the lack of ^{239}Pu and ^{237}Np

cross sections in the GALAXY data file. The $\Sigma\Sigma$ computed fission

rates based on the ENDF/B-III file were taken from Ref. (6). Table

6.15 shows that the discrepancy between the NISUS and $\Sigma\Sigma$ fission rates

is about 0.2% and 0.5% for the ^{239}Pu (n,f) and ^{237}Np (n,f) fission

TABLE 6.14

Final fission ratio data for NISUS: mean values, precision and accuracy

Fission chamber	Ratio	Fission rate ratio					
		Monitor chamber			^{197}Au(n,γ) reaction		
		Value	Precision	Accuracy	Value	Precision	Accuracy
NBS[a]	^{239}Pu/^{238}U	20.72	± .44%	± 2.36%	20.52	± .63%	± 2.40%
	^{239}Pu/^{235}U	1.177	± .26%	± 2.06%	1.178	± .46%	± 2.10%
	^{237}Np/^{235}U	.3820	± .21%	± 2.43%	.3747	± .36%	± 2.45%
	^{238}U/^{235}U	.05735	± .39%	± 2.28%	.05650	± .50%	± 2.30%
ULRC[b]	^{238}U/^{235}U	.05533	± .17%	± 2.76%	.05525	± .25%	± 2.76%

Note: (a) Values corrected for chamber perturbation (1.006 ± .003 on threshold reactions) and epithermal streaming (.995 ± .005 on non-threshold reactions).

(b) Values uncorrected for chamber perturbation or epithermal streaming (i.e. true fission rates in the chamber).

TABLE   6.15

Comparison of fission ratios in NISUS and $\Sigma\Sigma$ by means of the NBS absolute fission chamber[*]

Reaction	NISUS		$\Sigma\Sigma$		
	Measured	Computed	Measured[(100)]	Computed	
		GALAXY		ENDF/B-III[(6)]	GALAXY
$^{239}Pu(n,f)$	1.177 ± .26%	–	1.175 ± .25%	1.114	–
$^{237}Np(n,f)$	.3820 ± .21%	–	.380 ± .7%	.367	–
$^{238}U(n,f)$	.05735 ± .39%	.05278	.05636 ± .22%	.0515	.05209
$^{235}U(n,f)$	1.000	1.000	1.000	1.000	1.000

Note: * All uncertainties random at 1 σ confidence level.

rates respectively.   The measured ^{238}U (n,f) fission rate in NISUS

is 1.7% higher than that in $\Sigma\Sigma$, compared with calculation which gives

1.3%.

7.   TRACK RECORDER MEASUREMENTS IN NISUS

The measurements of fission rates are performed by fission

foil activation technique, double fission chamber, and as recently

developed by solid-state track recorders.   The foil activation

measurement is carried out by irradiating foils and subsequently

gamma counting their fission product activity.   Gamma activity

ratios are related to true fission ratios by using a time-dependent

calibration factor which is measured in a separate measurement using

a double fission chamber.   This technique suffers from the disadvantage

that the calibration factor is spectrum dependent[16] and that is

subject to possible systematic errors.

The technique involving the use of solid-state track recorders

is based on the fact that the passage of fission *fragments* through a suitable

dielectric such as Makrofol cause narrow trails of radiation damage

in the material.   Fission rate measurements are made from the number

of tracks formed in the film when it is irradiated in intimate contact

with a fissionable material.   Among several advantages of SSTR compared

with other fission rate measurement techniques is its considerable

geometric flexibility.   Track recorders can be shaped to detect

fission fragments over an extended solid angle or can be reduced in

size to eliminate flux depression or flux perturbation.

7.1   Determination of the optical efficiency

The first part of the present track recorder measurements in

NISUS involved the determination of the optical efficiency of Makrofol

SSTR. When a track recorder is irradiated in contact with a
fissionable material, fission fragments that escape the source
create tracks in the SSTR. Consequently, fission rate measure-
ments with SSTR are surface observations of fission events occurring
within the top layers of the source. Ideally, one of the two fragments
resulting from each fission would produce an observable track when
the SSTR subtends 2π sr relative to the source. The ratio of the
number of observed tracks per unit area to the number of fission
fragments per unit area that escape the source is called the optical
efficiency.

7.1.1 Performance

Five experiments were carried out in NISUS with the ULRC fission
chamber and the Makrofol SSTR. One experiment was made with an
aluminium foil holder using solid uranium plug with no hole (Fig. 7.1),
and consequently no thermal neutron streaming[107]. In the edperiments
with fission chamber, the SSTR was placed on one of the two deposits
of the chamber and was secured between the two aluminium plates of
the deposit holder. This arrangement was made SSTR in intimate
contact with the deposit as it should be. In the experiment with the
aluminium foil holder, two track recorders were placed on the two
deposits for simultaneous irradiation. In this experiment, too,
the track recorders were kept tight with the deposits. Special care
was taken in placing and removing the SSTR on and from the deposit not
to damage the fissionable material. The diameter of the SSTR was
slightly bigger than that of the backing of the SSTR to make removing

Key

1. Specimen Support Ring
2. Specimen Holder
3. Support

NATURAL URANIUM

B₄C
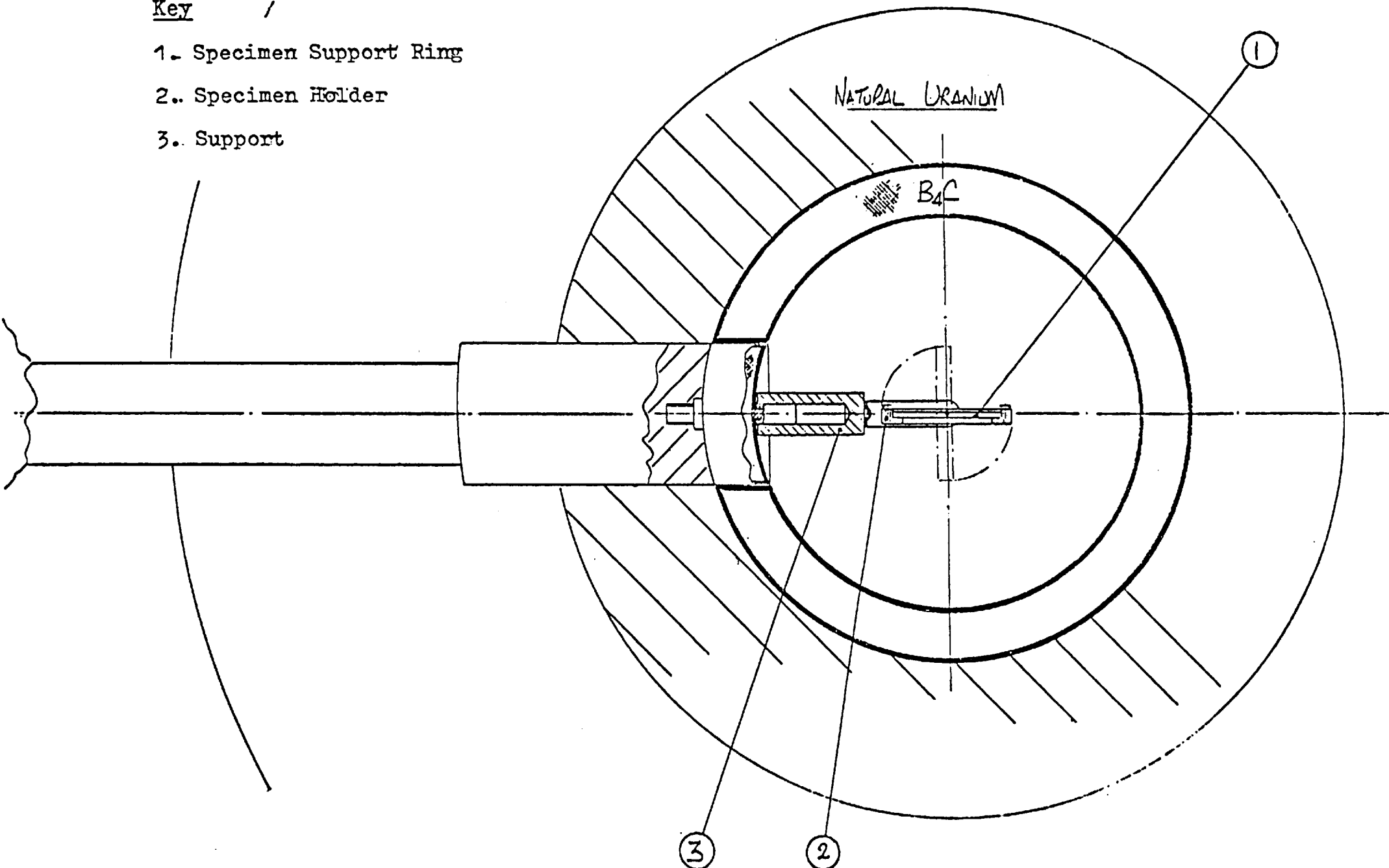
Fig. 7.1   NISUS facility with SSTR foil holder.

easier.

The track recorder experiments were carried out at low
reactor power or short irradiation time to avoid track pile-up
and excessive overlap. In order to get statistical error around
1% the reactor power and irradiation time were chosen to produce
about 2 x 10^4 tracks/cm^2. At the end of each run the reactor was
shut down and the samples were taken out of NISUS. This was
necessary because during the fission chamber measurements, it was
found that when the cadmium shutter is closed the NISUS facility is
not completely shut off from the reactor core. A 0.25% core leakage
was observed when the reactor was running at full power (100 kW).
The low reactor power and short irradiation times prevented other
experiments from being carried out on the reactor, and this is one
of the disadvantages with the SSTR technique.

7.1.2 Fission track counting

The Makrofol SSTR were etched at $60^{\circ}C$ for 30 min in an
alcoholic alkaline solution of 15% KOH and 40% C_2H_5OH diluted with
45% distilled water. The etched films were counted automatically
by the Quantimet 720. Since this set of samples were counted after
a few months' time interval with the previous films (see Section 4.10),
a new calibration was made using the same Leitz stage micrometer.
It was found that there are 143 picture points per 100 μm, resulting
in 0.559 x 0.437 mm field of view which is about 1.4% less in area
than the previous calibration. Apart from the re-calibration, the
grey level threshold setting, size setting, and track area distribution

were also found for this set of samples to set the right detection

conditions in track counting.

The grey level threshold setting was determined by plotting

the total number of tracks of several fields of view against the

threshold detection.   Table 7.1 shows the results of the two samples,

Film No. 806 and Film No. 808, irradiated in the ULRC fission chamber

with 23 $\mu g/cm^2$ and 103 $\mu g/cm^2$ enriched uranium deposits, respectively.

The films have the track density of about the same order of magnitude.

The threshold detection curves for these two films are shown in Fig.

7.2.

The size setting distribution, the longest chord of the tracks,

was found by plotting the total number of tracks in 23 fields of view

against the size when the threshold detection was kept constant at

the right setting.   Table 7.2 shows the results of the size setting

distribution for the Film Nos. 806 and 808.   The integral size

distribution curves of these two films are shown in Fig. 7.3.   The

differential histograms of the number of tracks as a function of

track size (longest chord) are shown in Figs. 7.4 and 7.5 for the

Film Nos. 806 and 808 respectively.

As it was described earlier (see Section 4.10.4) the experimental

estimate of P(X), the differential track area probability distribution,

is an essential aspect of automatic fission track counting.   This

distribution has been found for the Film No. 806 which was irradiated

in the ULRC fission chamber in contact with the thinnest source,

23 $\mu g/cm^2$ enriched uranium deposit.   Table 7.3 shows the variation

of the track area (in picture points) with the total number of tracks

TABLE 7.1

Threshold setting for two films irradiated in the ULRC fission chamber

Film No.   =   806

Source   =   23 $\mu gm/cm^2$ Enriched Uranium Deposit

Condition   =   100 kW   30 min

Threshold setting*	Total count of 23 frames	Threshold setting*	Total count of 23 frames	Threshold setting*	Total count of 23 frames
4.0	745	5.7	954	7.4	1024
4.1	763	5.8	950	7.5	1018
4.2	794	5.9	956	7.6	1015
4.3	815	6.0	959	7.7	1029
4.4	845	6.1	958	7.8	1066
4.5	865	6.2	969	7.9	1072
4.6	903	6.3	974	8.0	1094
4.7	911	6.4	973	8.1	1072
4.8	930	6.5	980	8.2	1092
4.9	937	6.6	984	8.3	1079
5.0	949	6.7	985	8.4	1133
5.1	955	6.8	1002	8.5	1128
5.2	939	6.9	995	8.6	1146
5.3	945	7.0	1013	8.7	1185
5.4	964	7.1	1003	8.8	1220
5.5	958	7.2	1008	8.9	1303
5.6	955	7.3	1009	9.0	1426

Note: * Size setting = 7

TABLE 7.1 (continued)

Threshold setting for two films irradiated in the ULRC fission chamber

Film No. = 808

Source = 103 $\mu gm/cm^2$ Enriched Uranium Deposit

Condition = 10 kW 70 min

Threshold setting*	Total count of 23 frames	Threshold setting*	Total count of 23 frames	Threshold setting*	Total count of 23 frames
3.0	79	5.0	1013	7.0	1089
3.2	159	5.2	1003	7.2	1067
3.4	388	5.4	1036	7.4	1068
3.6	571	5.6	1042	7.6	1102
3.8	691	5.8	1048	7.8	1103
4.0	776	6.0	1043	8.0	1146
4.2	851	6.2	1048	8.2	1251
4.4	877	6.4	1061	8.4	1386
4.6	916	6.6	1057		
4.8	928	6.8	1066		

Note: * Size setting = 7
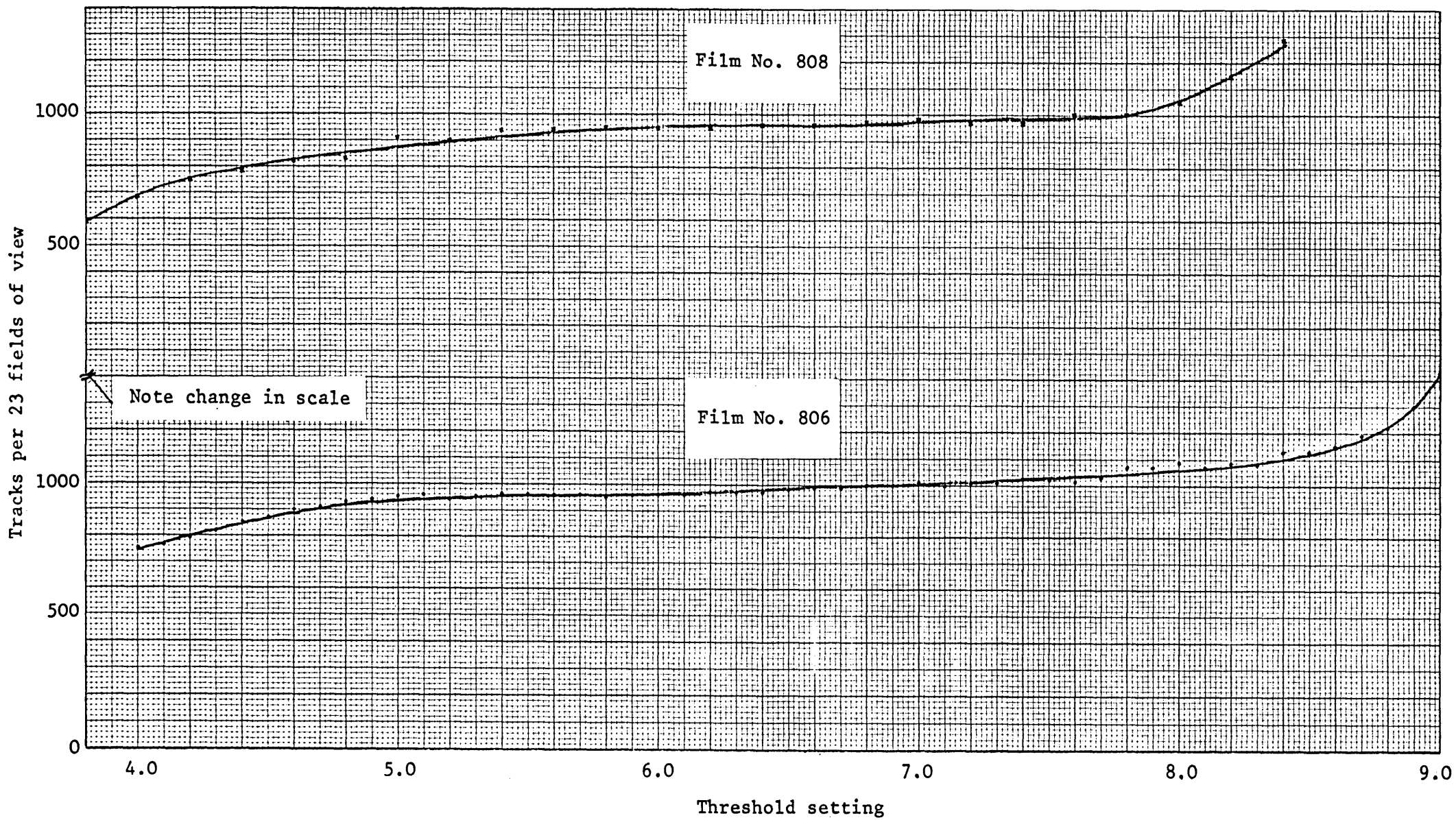
Fig. 7.2 Threshold detection curves for two films irradiated in the ULRC fission chamber.

TABLE 7.2

Size setting for two films irradiated in the ULRC fission chamber

Film No.   =   806

Source   =   23 μgm/cm^2 Enriched Uranium Deposit

Condition   =   100 kW   30 min

Size * setting (p.p.)	Total count of 23 frames	Δ C	Size * setting (p.p.)	Total count of 23 frames	Δ C
0	1522	-	16	441	103
1	1207	315	17	380	61
2	1179	28	18	326	54
3	1120	59	19	261	65
4	1071	49	20	239	22
5	1050	21	21	194	45
6	1005	45	22	150	44
7	976	29	23	122	28
·8	936	40	24	92	30
9	912	24	25	69	23
10	881	31	26	53	16
11	825	56	27	36	17
12	787	38	28	26	10
13	745	42	29	19	7
14	655	90	30	12	7
·15	544	111			

Note: * Threshold setting = 6.4

TABLE 7.2 (continued)

Size setting for two films irradiated in the ULRC fission chamber

Film No. = 808

Source = 103 $\mu gm/cm^2$ Enriched Uranium Deposit

Condition = 10 kW 70 min

Size setting* (p.p.)	Total count of 23 frames	Δ C	Size setting* (p.p.)	Total count of 23 frames	Δ C
0	1434	-	16	428	123
1	1208	226	17	374	54
2	1141	67	18	314	60
3	1132	9	19	255	59
4	1116	16	20	221	34
5	1088	28	21	179	42
6	1074	14	22	141	34
7	1046	28	23	91	50
8	1013	33	24	66	25
9	968	45	25	51	15
10	929	39	26	31	20
11	885	44	27	24	7
12	864	21	28	21	3
13	819	45	29	15	6
14	654	165	30	9	6
15	551	103			

Note: * Threshold setting = 6.4

Tracks per 23 fields of view
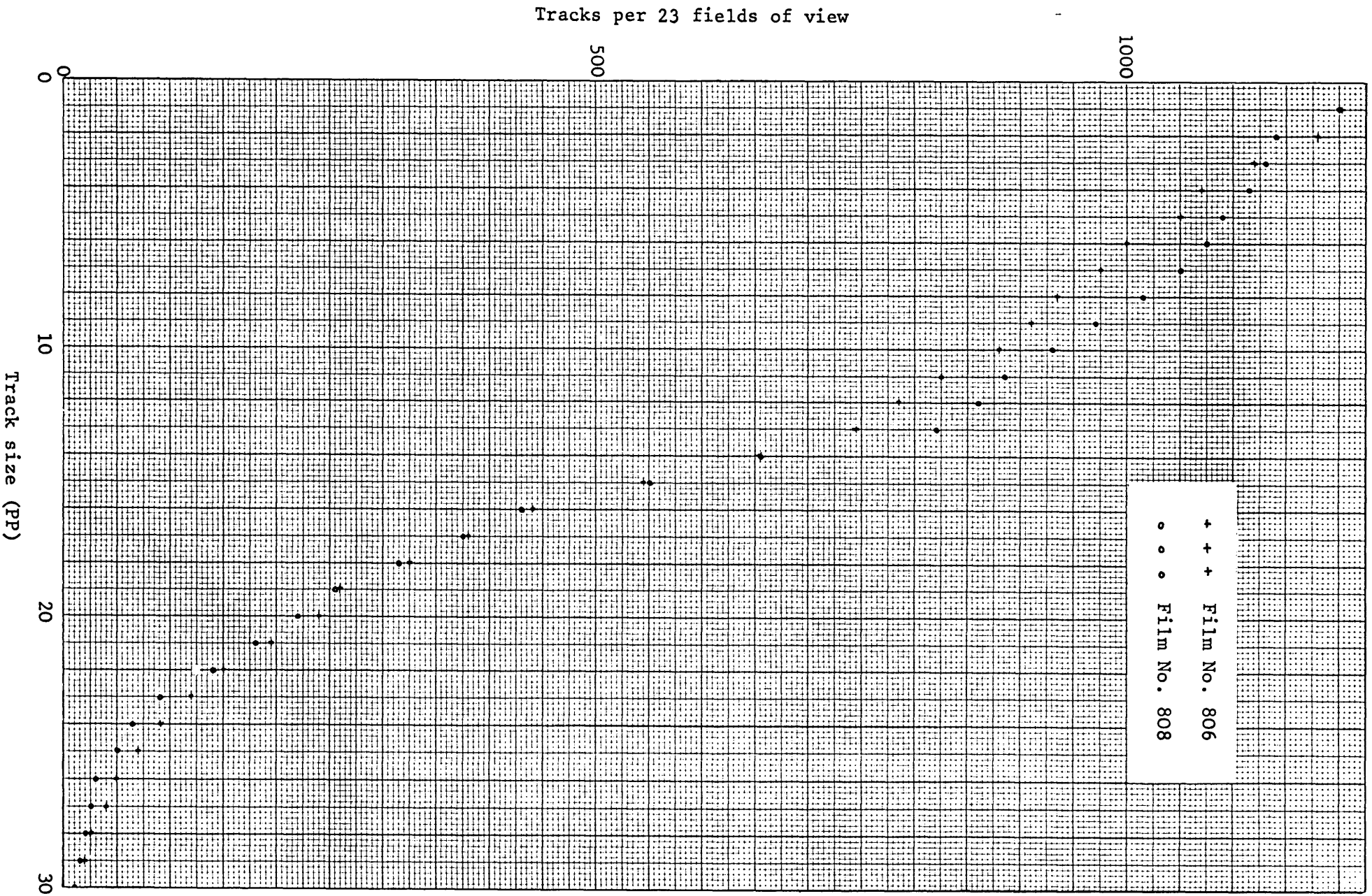
Fig. 7.3   Integral distribution curves for two films irradiated in the ULRC fission chamber.

295
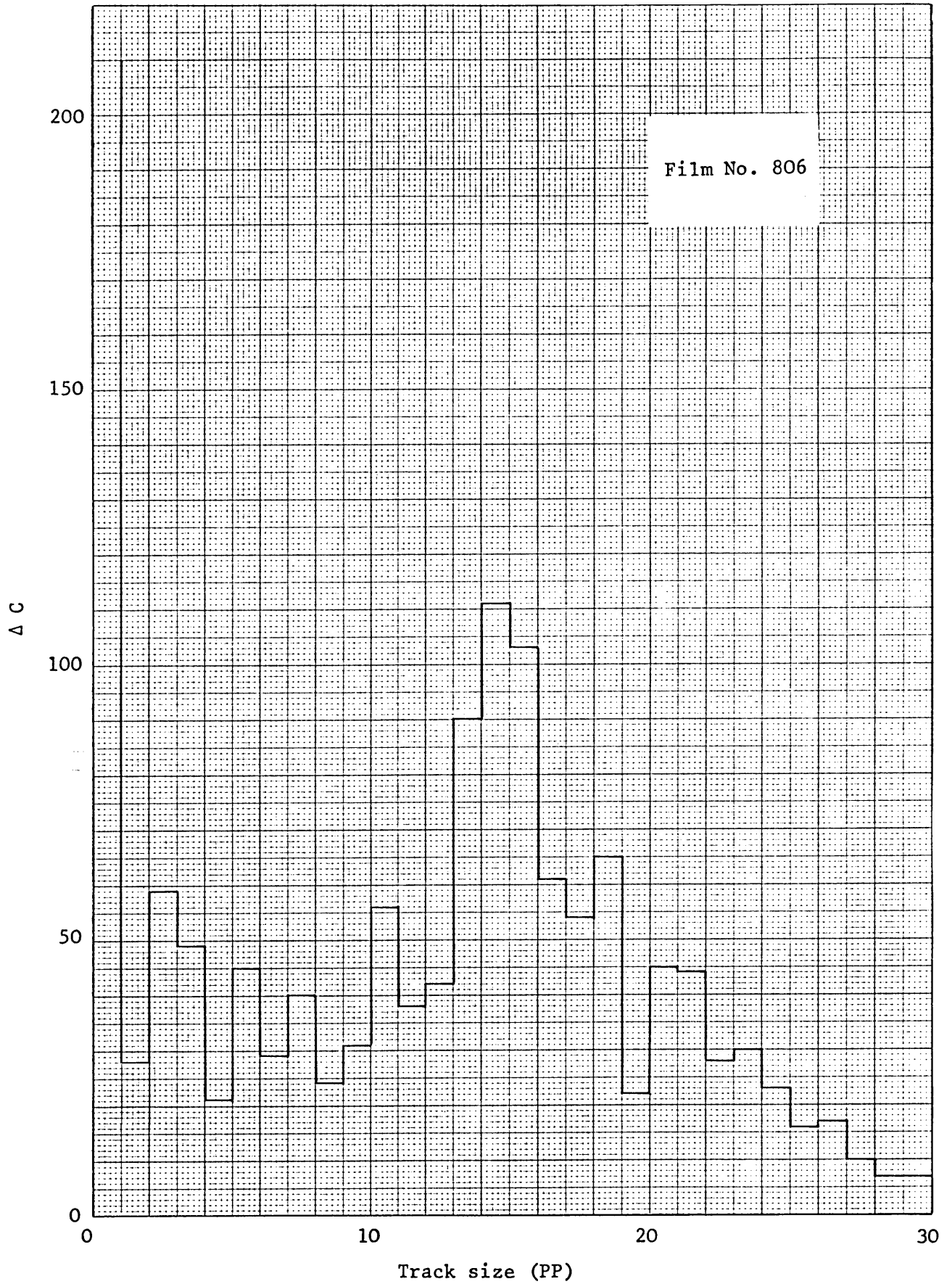
Fig. 7.4 Frequency histogram of the number of tracks as a function of
track size (longest chord).
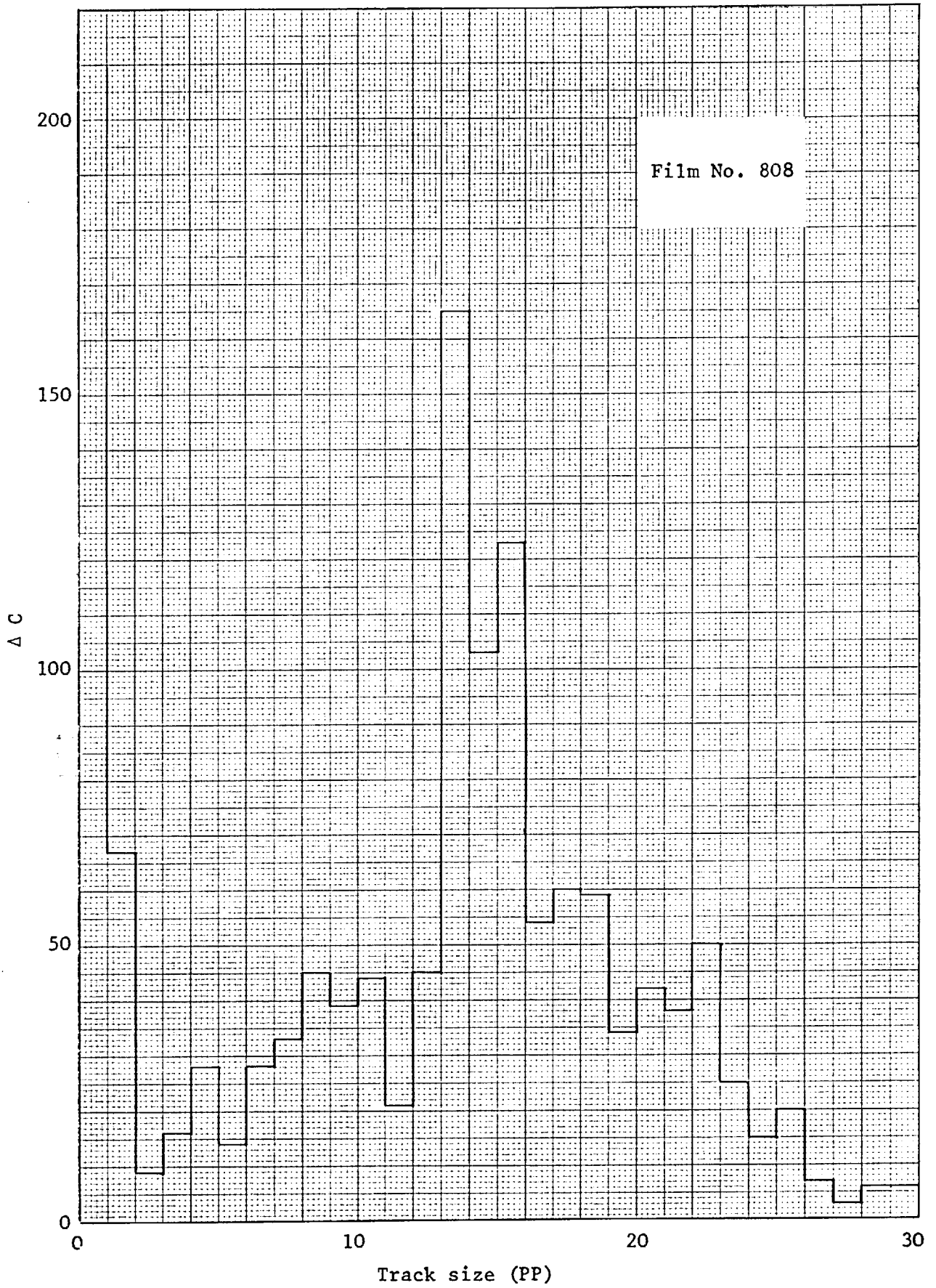
Fig. 7.5 Frequency histogram of the number of tracks as a function of

track size (longest chord).

TABLE 7.3

Track area distribution for the film irradiated with the
thinnest deposit in the ULRC fission chamber

Film No.   = 806

Source   = 23 µgm/cm^2 Enriched Uranium Deposit

Condition   = 100 kw   30 min

Area* (p.p.)	Total count of 31 frames	Area* (p.p.)	Total count of 31 frames
10	451	230	62
20	154	240	66
30	58	250	69
40	34	260	81
50	27	270	80
60	26	280	87
70	20	290	75
80	15	300	57
90	15	310	71
100	18	320	59
110	11	330	53
120	11	340	27
130	16	350	27
140	20	360	16
150	25	370	12
160	32	380	6
170	31	390	3
180	49	400	6
190	42	410	3
200	55	420	0
210	38	430	5
220	65		

Note: * Threshold setting = 6.4

per 31 fields of view. In Fig. 7.6 the frequency histogram of

the number of tracks as a function of track area of Film No. 806

is compared with that of the Film No. 206 (Table 4.7). Film No.

206 has been irradiated in contact with the asymptotically thick

source (NISUS natural uranium shell) and hence the comparison is

between the two limits of the available source thicknesses. It

is seen from Fig. 7.6 that the peak of the track area distribution

of the asymptotically thick source (Film No. 206) corresponds to

the area of 180 pp and that of the very thin deposit (Film No. 806)

to 280 pp. This means that the thicker the source the smaller the

tracks. The explanation is that the size of the damaged region

and the cone base of the etched pits in the SSTR depend on the

energy of the incident fission fragments. For energetic fragments

the rate of damage along the fragment path is high and thus for a

given etching condition the tracks of fragments with higher energies

are larger than those with lower energies. In asymptotically thick

source (NISUS uranium shell) most of the fragments lose their energies

before escaping the source and hence produce small tracks compared

with those of the thin source. Fig. 7.6 shows that the peak-to-

valley ratios of the track area distribution (analagous to fission

chamber pulse height distribution) vary from about 2 for Film No. 206

(thick source) to about 8 for Film No. 806 (thin source.)

7.1.3 Fission source evaluation

One important aspect of the fission rate measurement by SSTR

is the quality of the fission source. If the source is not uniform,
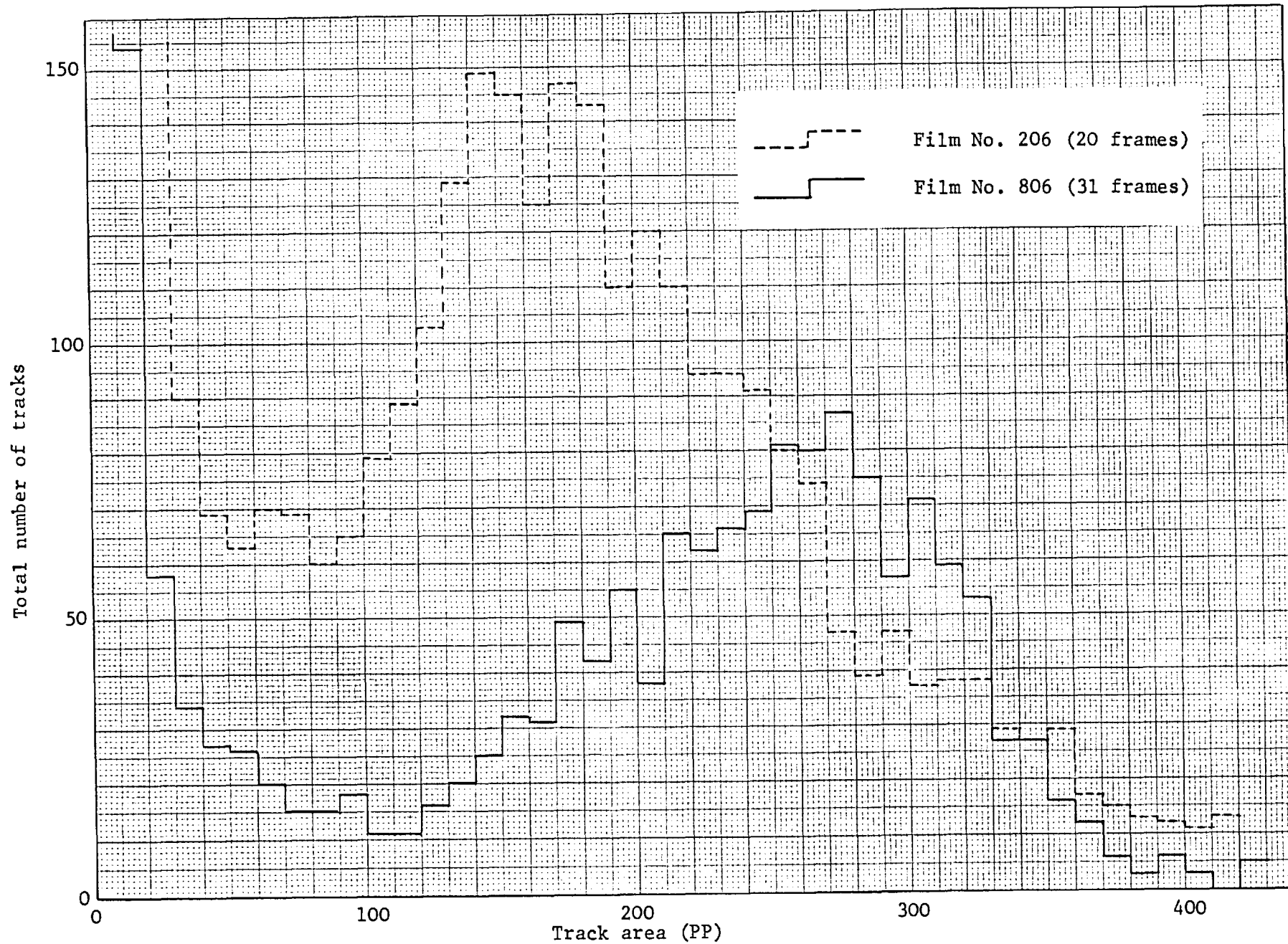
Fig. 7.6   Frequency histogram of the number of tracks as a function of track area.

then all tracks on the sample should be counted and the primary

difficulty arises in being assured of counting all the tracks.

On the other hand, counting all the tracks is much too time consuming

to be practical. It is, however, possible to move the microscope

stage such that a spot or a track on one boundary of the frame in

the field of view is moved to the opposite boundary. This method,

though applicable in track counting by eye, is not practical in

Quantimet track counting since it is difficult, time consuming and

expensive, in particular, when the fission souce diameter is large.

The alternative is to scan the SSTR in discrete steps, as it is done

by the Automatic Stage of the Quantimet 720, and find the average

number of tracks per field of view. In the present Quantimet track

counting, this method was followed and for each SSTR the number of

tracks per unit area determined. It is, however, clear that if the

fission source is not uniform in radial direction it could introduce

an error in track counting by scanning an insufficient area of the

SSTR. The radial uniformity of the fission sources was examined

by counting the tracks across a number of diameters. A typical

radial distribution of the observed tracks is shown in Fig. 7.7.

The results were obtained by the Quantimet 720 for the Makrofol SSTR

irradiated in the ULRC fission chamber in contact with the 103 $\mu g/cm^2$

enriched uranium deposit (Film No. 808). It is seen that the radial

distribution is uniform within the statistics.

The quality of fission sources can also be tested by examining

the specific track density, i.e. the number of observed tracks per

microgram of fissile material as a function of the source thickness.
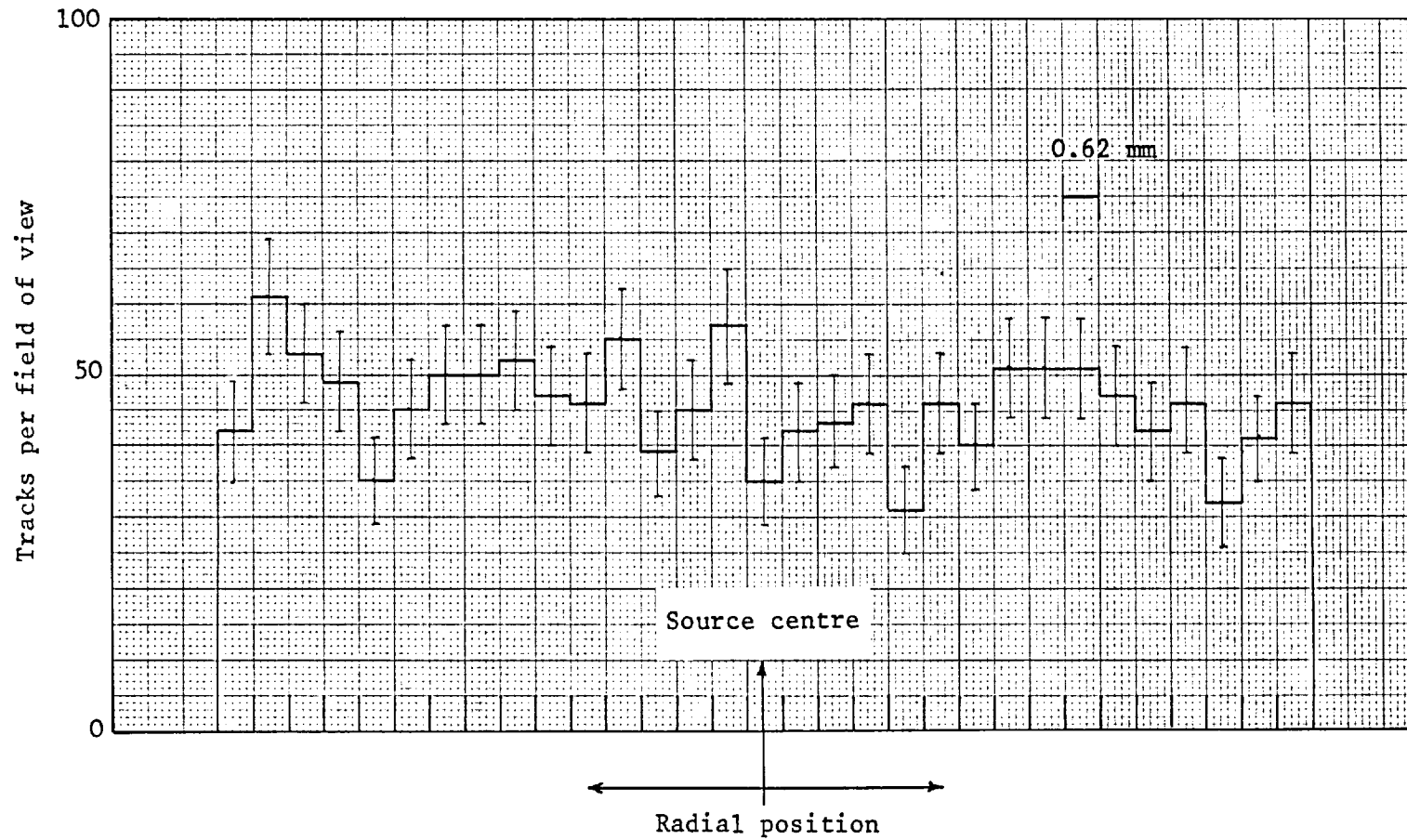
Fig. 7.7   Radial track density distribution obtained with Makrofol SSTR with 103 $\mu gm/cm^2$ enriched uranium deposit.

Gold et al[19] have shown that with an excellent approximation

the variation of specific track density with source thickess is

linear in the form of

$$T(\mu)/\mu = a + b \mu \qquad (7.1)$$

where $T(\mu)$ is the number of observed tracks per unit area and

μ is the thickness of the source in units of $\mu g/cm^2$.

In the present work the track recorders were irradiated at different

runs in contact with the ULRC deposits in the ULRC fission chamber.

The variation of specific track density with source thickness is

shown in Fig. 7.8. Since the reactor power and exposure time

were different, the quantity of number of observed tracks per cm^2

per sec per microgram per ^{197}Au (n,γ) reaction rate was taken

instead of simply the number of tracks per microgram. Moreover, the

data from the depleted deposits increased by a factor of F_5/F_8

to correspond to the same data for enriched deposits.

7.1.4 Optical efficiency

According to Gold et al[19] the optical efficiency of a SSTR

is the ratio of the number of observed tracks per unit area to the

number of fission fragments per unit area that escape the source.

This definition, however, differs from that of their total efficiency

which is the ratio of the number of observed tracks per unit area

to the true fission events in the source per unit area. They have

shown that the optical efficiency is a function of the source thickness
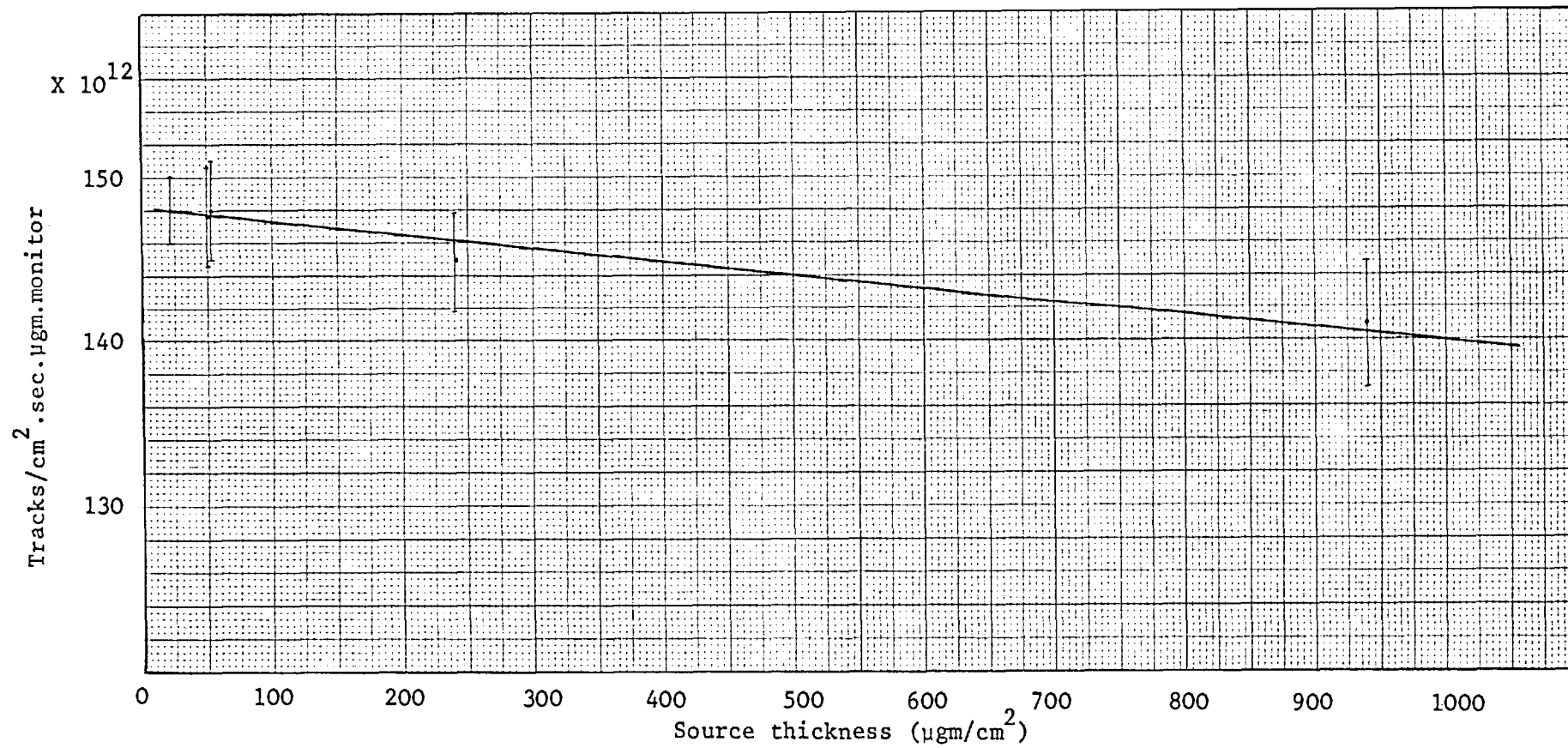
Fig. 7.8   Observed track density as a function of source thickness obtained with Makrofol SSTR.   The
smooth curve is a linear least-squares fit to the experimental data.

as well as the SSTR material, whereas the total efficiency depends only upon the detector and is independent of the fission source. It follows that for thin sources, the self-absorption effects can be neglected and the total efficiency reduces to optical efficiency. Khan and Durrani[12] have shown that the detection efficiency of a track recorder depends on the angle of incidence of the fission fragments. They have demonstrated that the track densities after having remained fairly constant over most of the angular interval, fall off to zero as the angle of incidence approaches the critical angle of etching on either side of the normal. It follows that the total efficiency is not constant either, since the angular distribution of the fission fragments impinging on the SSTR depends on the source thickness. Grundl et al[14] have defined the optical efficiency as the actual ratio of observed tracks to the true fission events. In the present work Gold's definition was adopted and both the optical efficiency and the total efficiency were determined.

To obtain the optical efficiency of the Makrofol SSTR, seven track recorders were irradiated in contact with the ULRC deposits at the centre of NISUS. Irradiations were performed such that the resulting track densities were about 2×10^4 tracks/cm^2 to get a minimum track overlap even under strong etching. The etched track recorders were counted by the Quantimet 720 when the gray level threshold and size (longest chord) were at the right settings. Table 7.4 shows the results of the track densities for seven Makrofol SSTR. The first five films were irradiated in the ULRC fission chamber and the last two (Run No. 30) with the aluminium foil holder. The overlap

TABLE 7.4

Track densities of Makrofol SSTR irradiated at NISUS centre

Run No.	Film No.	Reactor power (KW)	Irradiation time (sec)	Foil identification and principal isotope	Mass ($\mu g/cm^2$)	Track recorder			
						No. of frames	Total count	Tracks/cm^2	
								Observed	Overlap corrected
17	806	100	1800	ULRC-4 ^{235}U	23.3	430	20835	19835	20397
22	807	10	4200	ULRC-5 ^{235}U	101.7	430	21245	20225	20809
23	808	10	4200	ULRC-6 ^{235}U	102.8	450	22270	20259	20845
24	809	100	3000	ULRC-3 ^{238}U	241.2	450	21306	19382	19918
27	810	25	3000	ULRC-1 ^{238}U	943.5	480	21352	19745	20301
30	811	20	2100	ULRC-6 ^{235}U	102.8	480	24857	21199	21843
30	812	20	2100	ULRC-1 ^{238}U	943.5	460	12563	11180	11355

correction was made by using Equ. 4.3 and assuming the average track area of 280 PP, the value measured for Film No. 806 (Fig. 7.6). It was found that there is no significant difference in the track densities (through Au monitor) between Film Nos. 808 and 811, and also between Film Nos. 810 and 812. This means that thermal neutron streaming effect and flux perturbation due to fission chamber body is within the errors of the SSTR technique. Table 7.5 shows the summary of the count ratios of the ULRC deposits irradiated in the fission chamber and in contact with Makrofol SSTR. The values of optical efficiency η_o and total efficiency η_T are shown in Table 7.6. The results show that the detection efficiency for two thick deposits is near unity. This is attributable to uncertainty in the area of the source and non-uniformity of the fissionable material. In Table 7.7 is shown a comparison between the mean optical efficiency (thin deposits) obtained from Table 7.6 and those of References (19) and (12). The results indicate that the optical efficiency in this work is about 1% less than those reported by Gold et al[19] and Khan and Durrani[12]. This difference may be due to extensive etching in the present work, since the etching process removes surface from the polycarbonate resin (Makrofol) and the short fission tracks are lost and therefore the actual number of tracks reduced.

7.2 Fission ratio measurement

Solid-state track recorders have been used to measure the $^{238}U/^{235}U$ fission ratios with various degrees of accuracy. In

TABLE 7.5

Summary of the count ratios of the ULRC deposits exposed in the ULRC fission chamber and with Makrofol SSTR

Run No.	Foil identification and principal isotope		S_L (cps)	Tracks/cm^2	ETZ	Count ratio	Mean
14	ULRC-4	^{235}U	37.12 ± .07	—	1.02604 ± .00198	.22524 ± .29%	
	ULRC-6	^{235}U	164.15 ± .16	—	1.02390 ± .00068		
							.22590 ± .24%
15	ULRC-4	^{235}U	37.78 ± .11	—	1.01980 ± .00192	.22565 ± .39%	
	ULRC-6	^{235}U	165.30 ± .27	—	1.03290 ± .00076		
17	ULRC-4	^{235}U	SSTR	20397	—	.21289 ±1.00%	.21289 ±1.00%
	ULRC-6	^{235}U	163.32 ± .22	—	1.02390 ± .00106		
20	ULRC-5	^{235}U	159.03 ± .13	—	1.03054 ± .00086	.97893 ± .19%	.97893 ± .19%
	ULRC-6	^{235}U	163.76 ± .17	·—	1.02232 ± .00116		

TABLE 7.5 (continued)

Summary of the count ratios of the ULRC deposits exposed in the ULRC fission chamber and with Makrofol SSTR

Run No.	Foil identification and principal isotope		S_L (cps)	Tracks/cm^2	ETZ	Count ratio	Mean
22	ULRC-5	^{235}U	SSTR	20809	–		
	ULRC-6	^{235}U	16.41 ± .09	–	1.02562 ± .00178	.92482 ±1.13%	.92482 ±1.13%
23	ULRC-5	^{235}U	16.05 ± .08	–	1.02014 ± .00236		
	ULRC-6	^{235}U	SSTR	20845	–	1.03968 ±1.11%	1.03968 ±1.11%
16	ULRC-3	^{238}U	20.85 ± .06	–	1.04590 ± .00360		
	ULRC-6	^{235}U	163.78 ± .14	–	1.02238 ± .00322	.13023 ± .55%	
25	ULRC-3	^{238}U	20.77 ± .07	–	1.03184 ± .00230		.12939 ± .35%
	ULRC-6	^{235}U	160.98 ± .21	–	1.03560 ± .00084	.12855 ± .43%	

TABLE   7.5 (continued)

Summary of the count ratios of the ULRC deposits exposed in the ULRC fission chamber and with Makrofol SSTR

Run No.	Foil identification and principal isotope		S_L (cps)	Tracks/cm^2	ETZ	Count ratio	Mean
24	ULRC-3	^{238}U	SSTR	19918	-	.12999 ±1.57%	.12999 ±1.57%
	ULRC-6	^{235}U	161.92 ± .27	-	1.02090 ± .00146		
21	ULRC-1	^{238}U	75.23 ± .14	-	1.09206 ± .00706	3.78268 ± .75%	3.78268 ± .75%
	ULRC-3	^{238}U	20.80 ± .04	-	1.04416 ± .00286		
33	ULRC-1	^{238}U	74.40 ± .07	-	1.09696 ± .00432	2.16885 ± .61%	2.16885 ± .61%
	ULRC-4	^{235}U	36.89 ± .16	-	1.02006 ± .00164		
27	ULRC-1	^{238}U	SSTR	20301	-	.52266 ±2.24%	.52266 ±2.24%
	ULRC-6	^{235}U	41.75 ± .21	-	1.02358 ± .00174		

TABLE   7.6

Detection efficiency for Makrofol SSTR

Run No.	Foil identification and principal isotope		Efficiency[*]	
			Optical, η_o	Total, η_T
17	ULRC-4	^{235}U	.9424 ± 1.03%	.9409 ± 1.09%
22	ULRC-5	^{235}U	.9447 ± 1.15%	.9381 ± 1.20%
23	ULRC-6	^{235}U	.9416 ± 1.13%	.9350 ± 1.40%
24	ULRC-3	^{238}U	1.0046 ± 2.59%	.9882 ± 2.62%
27	ULRC-1	^{238}U	1.0668 ± 2.33%	1.0016 ± 2.79%

Note: * Total errors.

1968, Gold et al[19] reported that a limiting accuracy of close to within

1% is possible for uranium fission rate measurements with SSTR.

They concluded that the dominant contributing factor to this

uncertainty is not directly related to the SSTR method.   Instead,

the largest error by far arises in the determination of the mass

of fissionable material in a given uranium source or deposit.

TABLE   7.7

Comparison of optical efficiency of Makrofol SSTR

Optical efficiency %	Reference (19)	Reference (12)		This work *
		Expected	Observed	
η_o	95.2 ± .53	94.8	95.2	94.3 ± .64

Note: * Thin deposits.

It is, however, notable that the accuracy of close 1% has not

routinely   appeared in the subsequent literature for the

same types of measurements. Besant and Ipson[20] have measured

the $^{238}U/^{235}U$ fission ratio in the fast reactor ZEBRA with SSTR

and found an agreement to within the errors of ± 4.2% with

fission chamber measurements. In 1970, Jowitt[22]   reported

the results of the measurements of the $^{238}U/^{235}U$ fission ratios

with SSTR and the conventional foil activation technique in a

zero power fast reactor (ZEBRA). He has shown no significant

difference between the results obtained by the two methods since

each is subject to an error of about ± 2%. In the following year

Besant and Truch[21] measured the $^{238}U/^{235}U$ fission ratio in

ZEBRA with fission chamber and SSTR. They showed that the

fission chamber results were in agreement with those obtained

by SSTR to within ∿ 3%. Grundl et al[14], in 1975, reported

the results of $^{238}U/^{235}U$ fission ratio measurements in CFRMF

by fission chamber and track recorder. Although they have

developed the track recorder technique to accuracy levels no

better than 3% in fission rate measurements, they have shown

an agreement between the two techniques in the $^{238}U/^{235}U$ fission

ratio measurements and quoted an error of about 1.5% for each

method. Fabry et al[100] have measured the $^{238}U/^{235}U$ fission

ratio in ΣΣ by means of NBS fission chamber and ANL track recorders

and have found an agreement to within 3% between the results of

fission chamber and SSTR.

It seems that the accuracy of the order of 1.5% or better

in the absolute fission rate measurements by SSTR is hardly

achievable since the knowledge of the mass assay is subject to

an uncertainty of no better than 1% either by α or fission counting.

On the other hand the random error of the order of 1% puts another

limitation on the desired accuracy levels.   Similarly in the

fission ratio measurements one may get the accuracy of about

1.5% if the uncertainty of the mass assay of each deposit is at

the order of 1%.   Uncertainties in the fission fragment absorption

corrections in the deposits limit the overall accuracy in the

fission ratio measurements.

In the present work the $^{238}U/^{235}U$ fission ratio was measured

in the centre of NISUS using Makrofol SSTR.   The track recorders

were irradiated with the ULRC enriched and depleted uranium deposits

and after the etching they were counted by the Quantimet 720.   The

results of the track densities are shown in Table 7.4.   Table 7.8

shows the $^{238}U/^{235}U$ fission ratios obtained from Table 7.5.   The

comparison of the $^{238}U/^{235}U$ fission ratios in NISUS by fission

chamber and track recorder is shown in Table 7.9.   The results

show that the agreement between the fission chamber and SSTR

(irradiated with thin deposits) fission ratios is to within $\sim$ 3%.

7.3   Fission rate distribution in the NISUS uranium shell

The measurement of the fission rate distribution in the NISUS

natural uranium shell was made in the three orthogonal planes on the

TABLE 7.8

$^{238}U/^{235}U$ fission ratios measured in NISUS centre by track recorder

Run No.	Foil identification and principal isotope		Count ratio	$^{238}U/^{235}U$ fission ratios
24	ULRC-3	^{238}U	.12999 ± 1.57%	.05898 ± 3.1%
17	ULRC-4	^{235}U	.21289 ± 1.00%	
24	ULRC-3	^{238}U	.12999 ± 1.57%	.05926 ± 3.1%
22	ULRC-5	^{235}U	.92482 ± 1.13%	
27	ULRC-1	^{238}U	.52266 ± 2.24%	.06063 ± 4.4%
17	ULRC-4	^{235}U	.21289 ± 1.00%	
27	ULRC-1	^{238}U	.52266 ± 2.24%	.06092 ± 4.3%
22	ULRC-5	^{235}U	.92842 ± 1.13%	
30	ULRC-1	^{238}U	.51985 ± 1.09%	.05664 ± 3.7%
	ULRC-6	^{235}U		

inner and outer surfaces of the shell simultaneously. Since the

SSTR must be in intimate contact with the source and access to the

shell was only possible by dismantling NISUS which takes about a

normal working day, it was decided to prepare samples beforehand

to manage the irradiation in one day. This procedure allowed the

time required to stick the films on the shell   not to exceed a few

minutes. The simplest way was found to be to stick the SSTR on

the outer surface of the boron carbide shell and on a Sellotape,

for the inner and outer surface irradiations, respectively. When

TABLE 7.9

Comparison of fission ratios measured
by fission chamber and SSTR

Detector	$^{238}U/^{235}U$ fission ratios
Fission chamber	.05735 ± 2.3%
SSTR*	.05898 ± 3.1%

Note: * Irradiated with thin deposits.

the upper half of the uranium shell is removed the boron carbide

can be placed inside and the Sellotape stuck on the outer surface

of the uranium shell.   The problem associated with the SSTR to

be irradiated on the inner surface of the shell is not only that

the American boron carbide is in constant use in the NISUS assembly,

but that there is not enough space between this and the uranium

shell to put the SSTR, as the outside diameter of the boron carbide

shell is 157.4 ± 0.1 mm, the same as the inner diameter of the

uranium shell with a tolerance of 0.08 mm.   The alternative

was the use of the Belgian boron carbide shell with the outside

diameter of 144 ± 0.1 mm, leaving a gap of 6.7 mm between the boron

carbide and the uranium shells.   Although the gap was much smaller

than the mean range of fission fragments in air, $\sim$ 3 mg/cm^2[13], it

was necessary to irradiate SSTR in 2π geometry in order that the

scattered fission fragments, other than those from the surface

corresponding to the SSTR area, not are recorded.   The solution

was found by making three aluminium rings 16.0 mm wide with the

thickness of 6.3 mm, so that when they clamp together they make a

good arrangement for SSTR to stick on.   The gap between the aluminium

rings and the uranium shell is, therefore, 0.4 mm - almost the

thickness of SSTR and Sellotape together.   The films with diameter

of 15 mm were stuck to the surface of the aluminium rings by means of

a piece of Sellotape.   In each ring a hole of diameter 12 mm was

made to expose the SSTR.   The centres of the films were at a distance

apart of $d = \pi D/n$ where D = 157.48 mm is the inside diameter of the

uranium shell, and n = 12 is the number of films.

318

The preparation for the SSTR to be irradiated on the outer

surface of the uranium shell was made on a cloth-tape.   Three

cloth-tape ribbons were used for the three orthogonal circumferences,

each 79.8 cm long.   The position of the films were carefully marked

on the sticking side.   The films would be damaged when they were removed

if they were stuck directly to the sticking side of the tape.   So

some aluminium foils slightly bigger in diameter than the films were

put under the track recorders.   The films were then held by pieces

of Sellotape with   holes of diameter 12 mm, so that only an annular

with nominal width of less than 2 mm was in contact with the sticking

side of the Sellotape.   Fig. 7.9 shows the positions of the track

recorders on the NISUS uranium shell.

The measurement was carried out at the reactor power of 1 kW for

20 min.   The etched track recorders were then counted by the

Quantimet 720.   The results of track densities and fission rates/cm^2

of the films are shown in Tables 7.10, 7.11 and 7.12 for the planes

x = o, y = o and z = o respectively.   The overlap correction was

made by using Equ. 4.3 and assuming the average track area of 180 pp

(thick source).   The fission rates distributions on the outer and

inner surfaces of the NISUS uranium shell are shown in Figs. 7.10,

7.11 and 7.12 for three orthogonal planes x = o, y = o and z = o

respectively.   It is seen that in plane y = o (perpendicular to the

access hole axis) the fission rate distribution is almost constant,

whereas that in the other two planes is roughly cosine shape.   The cosine

shape of the fission rate distribution is due to non-uniformity of

thermal neutron source distribution in the graphite cavity block.

REACTOR CORE

Reactor core

REACTOR CORE

ACCESS HOLE

PLANE X=0

PLANE Y=0

ACCESS HOLE

PLANE Z=0
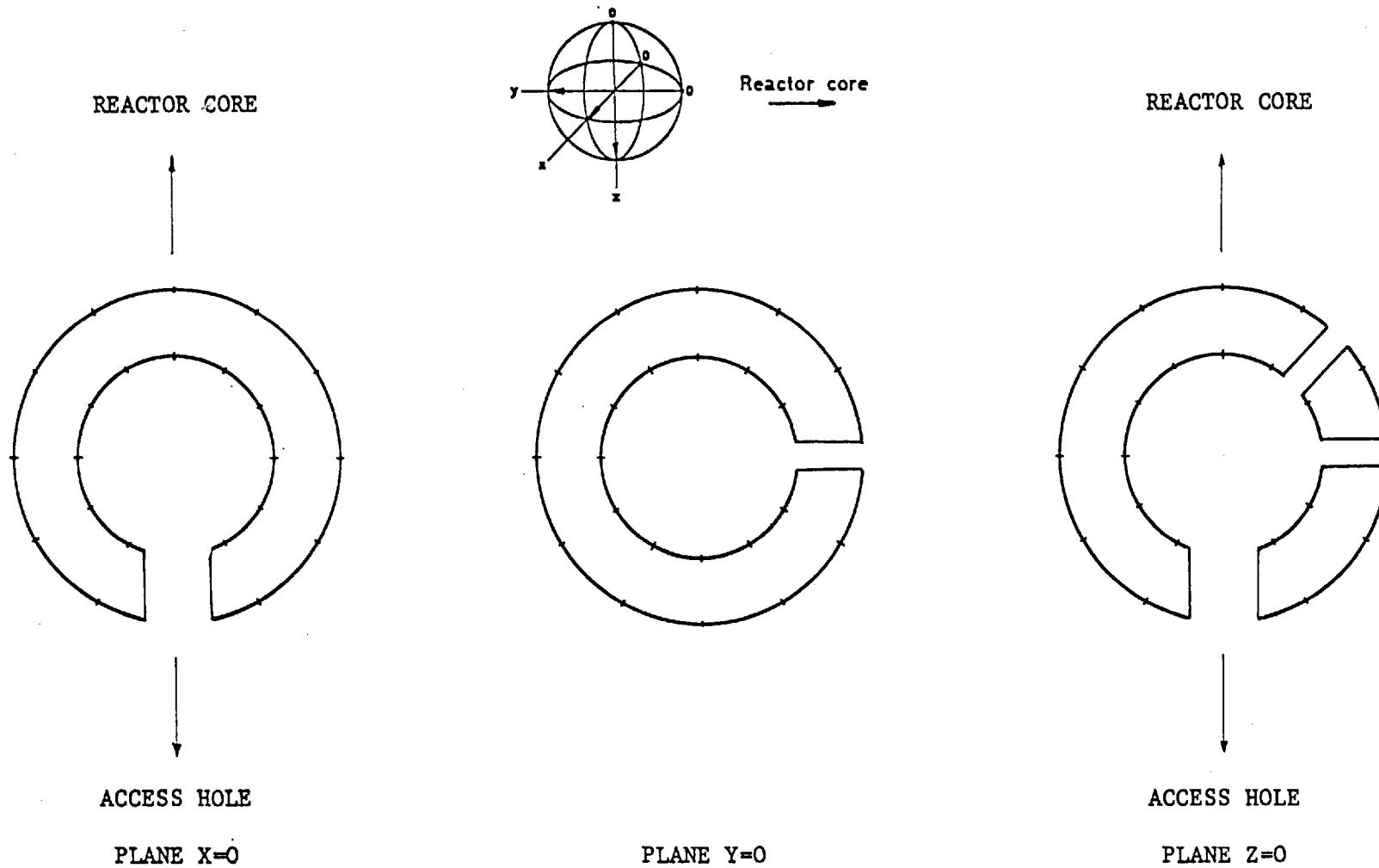
Fig. 7.9   Block diagram of the track recorder positions on the NISUS uranium shell.

TABLE 7.10

Track densities and fission rates for the SSTR irradiated on the
NISUS uranium shell in plane X=0

Position	Film No.	Angle β°	No. of frames	Total count	Tracks/cm^2		Fission/cm^2 sec
					Observed	Overlap corrected	
	-	0	-	-	-	-	-
	711	30	190	9722	20656	21047	16.539
	712	60	173	10516	24538	25093	19.719
	713	90	187	12640	27286	27976	21.984
	714	120	189	16261	34731	35858	28.178
Outer	715	150	218	23624	43746	45558	35.801
surface	705	180	225	27024	48485	50726	39.862
	716	210	191	20293	42890	44629	35.071
	717	240	146	13197	36489	37736	29.654
	-	270	-	-	-	-	-
	720	300	187	11399	24607	25165	19.775
	719	330	196	9988	20571	20959	16.470

TABLE   7.10 (continued)

Track densities and fission rates for the SSTR irradiated on the

NISUS uranium shell in plane X=0

Position	Film No.	Angle β°	No. of frames	Total count	Tracks/cm^2		Fission/cm^2 sec
					Observed	Overlap corrected	
Inner surface	–	0	–	–	–	–	–
	740	30	171	1164	2748	2755	2.165
	739	60	145	1058	2945	2953	2.321
	741	90	194	1453	3023	3031	2.382
	750	120	123	1098	3604	3616	2.842
	744	150	96	1001	4209	4225	3.320
	733	180	193	2087	4365	4382	3.444
	743	210	198	2030	4139	4154	3.264
	745	240	186	1734	3763	3776	2.967
	747	270	163	1285	3182	3191	2.508
	746	300	151	1116	2984	2991	2.350
	748	330	213	1439	2727	2734	2.148

TABLE 7.11

Track densities and fission rates for the SSTR irradiated on the
NISUS uranium shell in plane Y=0

| Position | Film No. | Angle $^\circ$ γ | No. of frames | Total count | Tracks/cm^2 | | Fission/cm^2 sec |
					Observed	Overlap corrected	
	708	0	169	12148	29017	29800	23.418
	727	30	186	13355	28985	29764	23.390
	728	60	119	8636	29296	30092	23.647
	713	90	187	12640	27286	27979	21.984
	721	120	206	15567	30505	31369	24.651
Outer	722	150	208	15422	29931	30763	24.175
surface	-	180	-	-	-	-	-
	723	210	210	15410	29622	30436	23.918
	724	240	230	17420	30574	31442	24.708
	-	270	-	-	-	-	-
	725	300	173	12304	28710	29474	23.162
	726	330	201	14855	29834	30660	24.094

TABLE 7.11 (continued)

Track densities and fission rates for the SSTR irradiated on the
NISUS uranium shell in plane Y=0

Position	Film No.	Angle γ°	No. of frames	Total count	Tracks/cm^2		Fission/cm^2 sec
					Observed	Overlap corrected	
	736	0	181	1403	3129	3137	2.465
	755	30	146	1068	2953	2961	2.327
	756	60	178	1316	2985	2993	2.352
	741	90	194	1453	3023	3031	2.382
	749	120	159	1237	3141	3149	2.475
Inner	742	150	123	926	3039	3047	2.394
surface	–	180	–	–	–	–	–
	751	210	160	1231	3106	3115	2.448
	752	240	146	1113	3077	3086	2.427
	747	270	163	1285	3182	3192	2.508
	751	300	141	1040	2978	2987	2.347
	754	330	190	1445	3070	3078	2.419

TABLE 7.12

Track densities and fission rates for the SSTR irradiated on the
NISUS uranium shell in plane Z=0

| Position | Film No. | Angle α° | No. of frames | Total count | Tracks/cm^2 | | Fission/cm^2 sec |
					Observed	Overlap corrected	
	-	0	-	-	-	-	-
	701	30	202	10658	21299	21715	17.064
	702	60	233	14388	24928	25501	20.040
	-	90	-	-	-	-	-
	703	120	235	20351	34959	36102	28.370
Outer	704	150	240	26404	44412	46281	36.369
surface	705	180	225	27024	48485	50726	39.862
	706	210	226	25429	45421	47379	37.232
	707	240	230	20542	36054	37271	29.289
	708	270	169	12148	29017	29800	23.418
	709	300	238	14411	24443	24993	19.640
	710	330	242	12843	21423	21844	17.166

TABLE 7.12 (continued)

Track densities and fission rates for the SSTR irradiated on the

NISUS uranium shell in plane Z=0

Position	Film No.	Angle α^o	No. of frames	Total count	Tracks/cm^2		Fission/cm^2 sec
					Observed	Overlap corrected	
Inner surface	–	0	–	–	–	–	–
	729	30	230	1559	2736	2743	2.156
	730	60	175	1289	2973	2981	2.343
	–	90	–	–	–	–	–
	731	120	186	1634	3546	3557	2.795
	732	150	219	2299	4238	4254	3.343
	733	180	193	2087	4365	4382	3.444
	734	210	211	2204	4217	4233	3.326
	735	240	194	1757	3656	3668	2.882
	736	270	181	1403	3129	3138	2.466
	737	300	218	1570	2907	2915	2.291
	738	330	195	1335	2764	2771	2.178
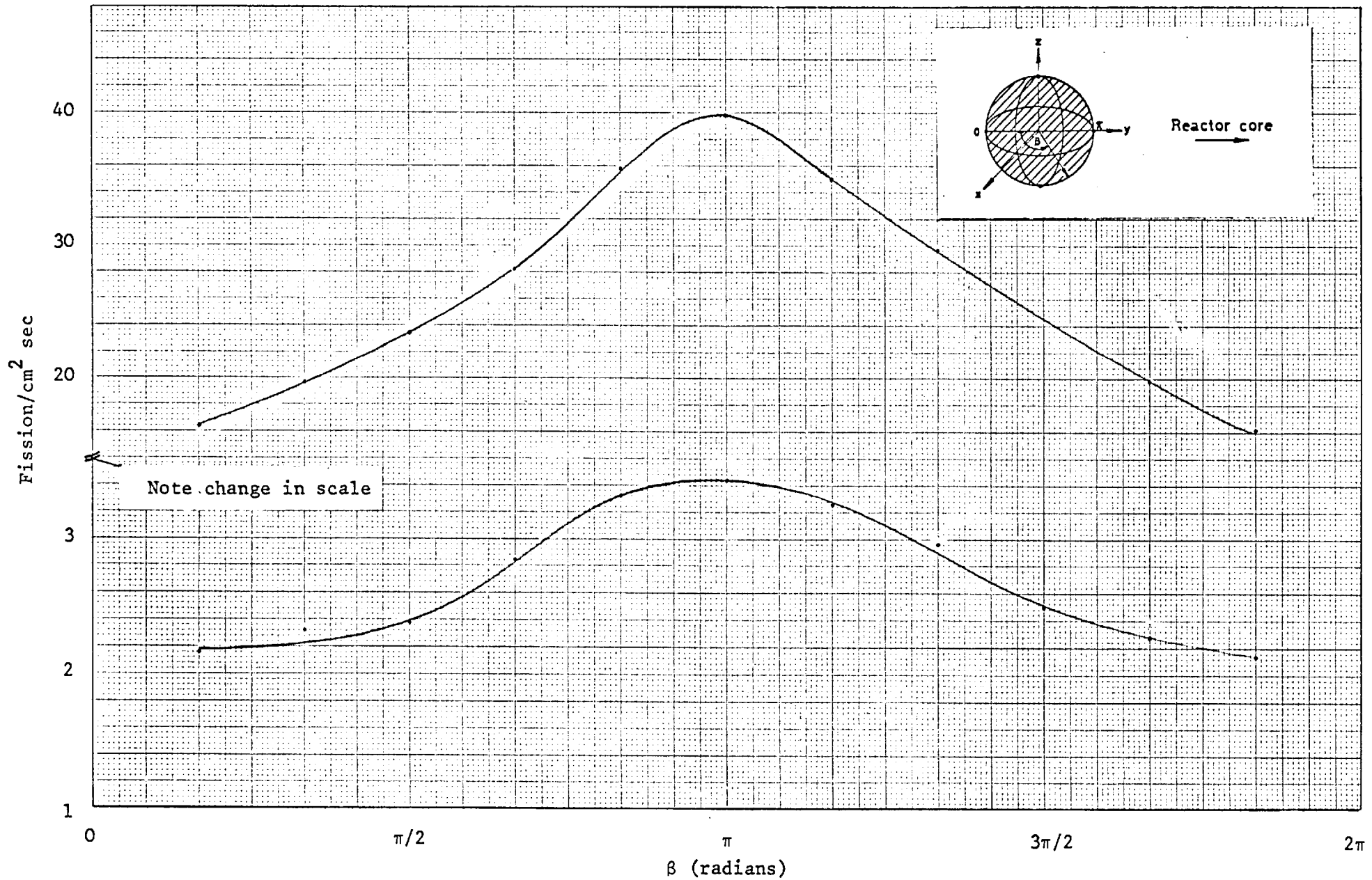
Fig. 7.10   Fission rate distribution on the NISUS uranium shell in plane X=0
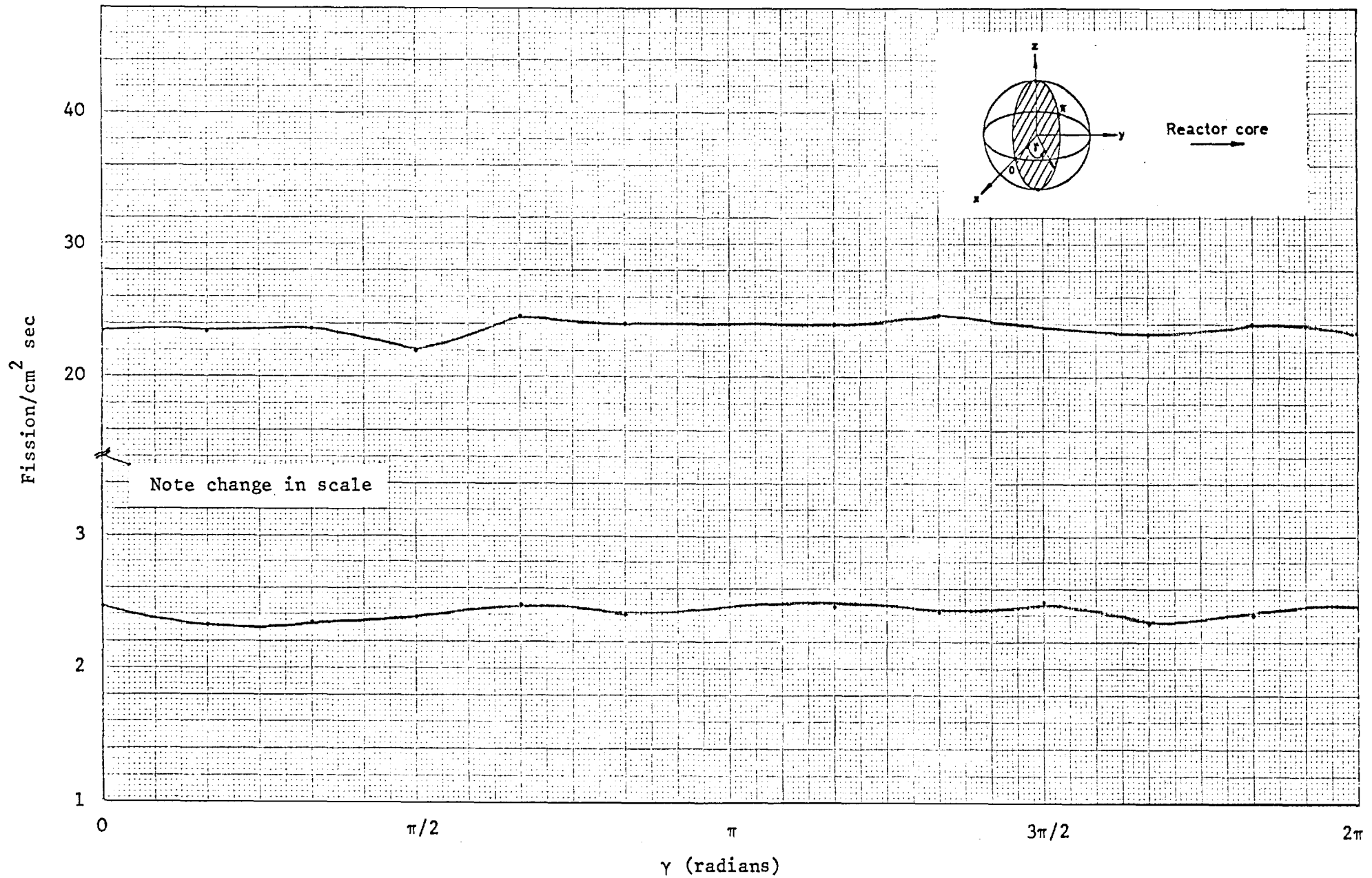
Fig. 7.11 Fission rate distribution on the NISUS uranium shell in plane Y=0

327
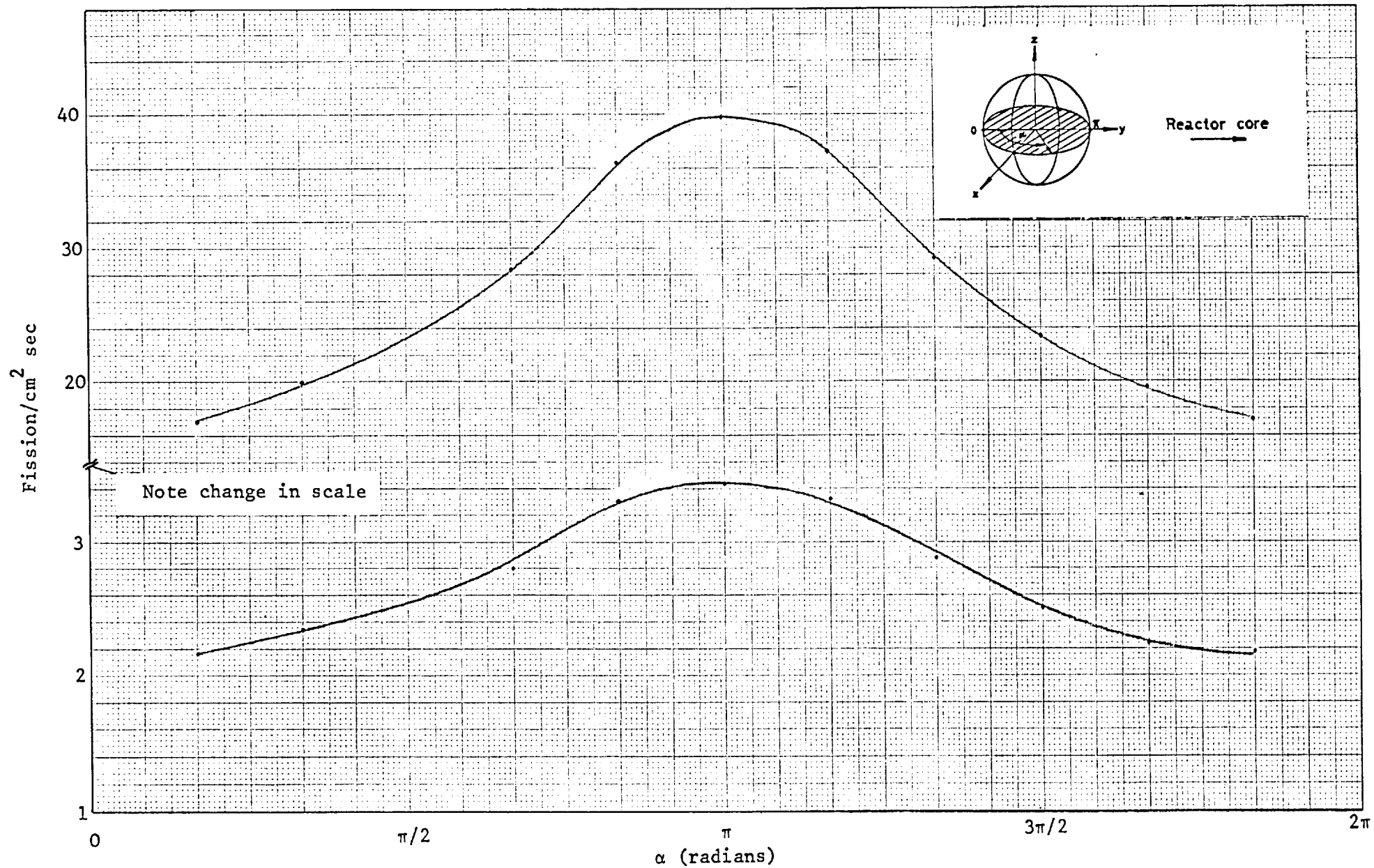
Fig. 7.12   Fission rate distribution on the NISUS uranium shell in plane Z=0

328

In both planes x = o and z = o the fission rates distributions are broader on the inner surface than on the outer surface. This is because of the neutron scattering and slowing down through the shell which makes the flux more uniform on the inner surface than on the outer. The peak-to-valley ratio of the fission rate distribution on the outer surface of the uranium shell is about 2.32. Fabry et al[108] have made a similar measurement by using thin copper foils placed only on the outer surface of the $\Sigma\Sigma$ uranium shell. They found that the maximum to minimum activity ratio is 2.3 and detailed data are associated to the overall gradient of the available thermal flux in the empty cavity.

The ratios of the fission rates of the outer surface to those of the inner surface for three othogonal planes are shown in Table 7.13. Fig. 7.13 shows the fission ratios distributions in the NISUS uranium shell. It is seen that these distributions are similar to those of fission rates in three orthogonal planes. This means that the fission ratio is not constant as it is predicted by the ANISN transport code. The ANISN calculation showed the value of 8.5 for the fission ratios in the NISUS uranium shell (see Fig. 5.7). It is, however, notable that ANISN prediction is an underestimate and this value approaches the true ratio upon increasing the number of mesh points in the uranium shell or upon extrapolating the relative fission rate to the outer diameter of the shell.

TABLE 7.13

Fission ratios in the NISUS uranium shell

in three orthogonal planes

Angle θ^o	Fission ratio		
	Plane X=0	Plane Y=0	Plane Z=0
0	–	9.50	–
30	7.64	10.05	7.92
60	8.50	10.05	8.56
90	9.23	9.23	–
120	9.92	9.96	10.15
150	10.78	10.09	10.88
180	11.58	–	11.58
210	10.74	9.77	11.19
240	9.99	10.19	10.16
270	–	–	9.50
300	8.41	9.87	8.57
330	7.67	9.96	7.88
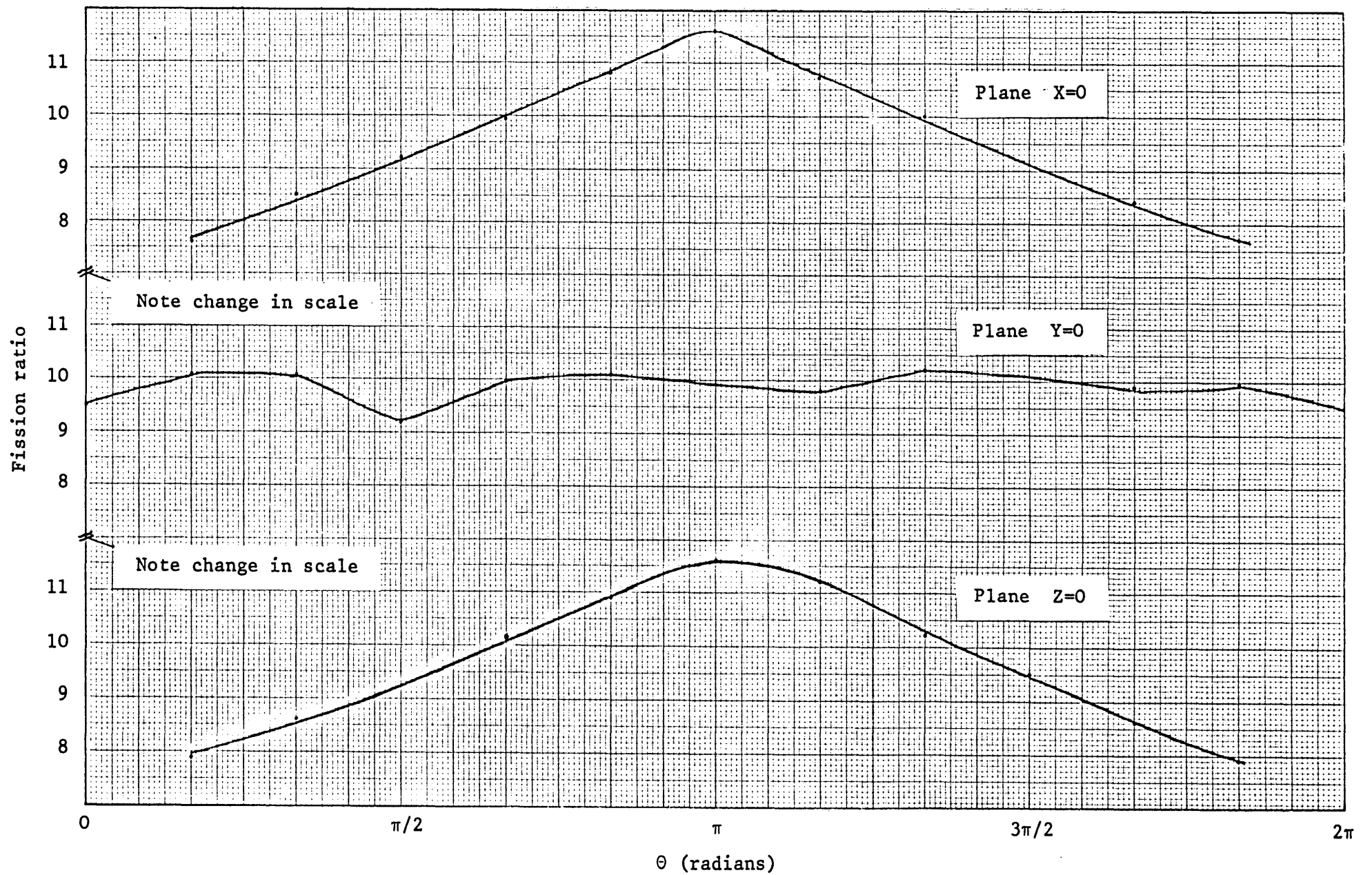
Fig. 7.13   Fission ratio distribution in the NISUS uranium shell in three orthogonal planes.

8.   SUMMARY AND CONCLUSIONS

The purpose of the research was to perform fission rate measurements in the Neutron Intermediate Standard Uranium Source (NISUS) with double fission chamber and solid-state track recorder and to compare the measurements with the one-dimensional discrete ordinates transport code ANISN.   Calculations were also made to investigate sensitivities of the central NISUS spectrum and reaction rate ratios to the uncertainties in the macroscopic configuration and nuclear data file used.   The effects of these uncertainties were studied by making a comparison between NISUS and MOL-$\Sigma\Sigma$ standard neutron fields.

At the first stage of the project an accurate and reproducible
                                    procedure
fission track counting using the Quantimet 720 was established.   This was made by a series of measurements in which SSTR were irradiated with the NISUS uranium plug and after etching, counted by eye and the Quantimet.   The track recorders   met all requirements for track counting, i.e. satisfactory track density, low background, high contrast, and uniformity of the features.   A wide range of track density was chosen, from about 1.3 x 10^3 tracks/cm^2 to about 6.6 x 10^4 tracks/cm^2, to study the performance and accuracy of the Quantimet 720 with eye counting.   The lower limit arises since the track density
          at this level
becomes too low for accurate measurements, while the upper limit comes from the practical limit of the overlapping problem.   The results of the fission track counting by eye and the Quantimet 720 showed that either method is capable of precision of ± 2% or better in fission

rate ratios. At this level of statistical accuracy no evidence has been found that the variance of the measurement exceeds that expected from random sampling errors provided that the track densities are not greater than 5×10^4 tracks/cm^2 for eye or Quantimet counting, or less than 2×10^3 tracks/cm^2 for eye counting. The relative efficiency of the Quantimet to eye counting was found to be .975 $\pm$ .005 (random). This value is subject to a systematic error of $\pm$ 2% attributable to the calibration of the fields of view in both methods.

The sensitivity of the central NISUS spectrum and reaction rates to the macroscopic parameters and cross sections were studied in detail using ANISN transport code with GALAXY 37 energy group structure. In the reaction rate calculations the response of 20 reactions were found relative to the most fundamental reaction rate, ^{235}U (n,f). The macroscopic uncertainties included density (of graphite, boron carbide and uranium), impurity (moisture and ^{10}B in graphite), abundance (^{10}B natural abundance) and tolerance (in Al cladding and B_4C shell). These macroscopic uncertainties were mainly based on the NISUS and $\Sigma\Sigma$ detailed material and geometrical data and consequently the comparison is between these two standard neutron fields. The uncertainties studies in the nuclear data file were those in the fission cross sections of ^{235}U and ^{238}U.

ANISN calculation showed that as far as central NISUS spectrum was concerned, the effect of uranium density variations is less than $\pm$ 0.4% above $\sim$ 70 keV, while those of graphite and boron carbide are about + 12% and + 1% respectively in the same energy range. The

effects of 250 ppm moisture and 0.4 ppm [10]B in graphite were found

to be to reduce the NISUS central flux in all groups by about 13%

and 38% respectively. However, the ratios of the flux in all groups

in the two spectra for both cases were constant *to* better than ± 1%.

The NISUS central flux was calculated for [10]B natural abundance of

19.78% (NISUS) and 18.37% ($\Sigma\Sigma$). It was found that so far as spectrum

measurement was concerned the abundance variation effect is negligible

(< 1%) above 70 keV, but it is significant in *the* thermal region. The

effects of tolerance of 1 mm in the B_4C shell and 0.5 mm in its Al

cladding were found to be about ± 1% or less in the NISUS central

spectrum above 70 keV.

The sensitivities of NISUS central flux to the [235]U and [238]U

fission cross sections were calculated by assuming a change of ± 2%

in the [235]U (n,f) cross sections and a change of ± 2% in the [238]U

(n,f) cross sections above threshold and ± 10% covering threshold

region respectively. The results showed that a change of — 2% in

the [235]U fission cross sections in all groups results in a *change*

of about — 4.6% in the total flux. The NISUS central spectrum is

less sensitive to the [238]U fission cross sections since the effects

of ± 2% change above threshold and ± 10% change covering threshold

region were found to be less than ± 1%.

In the reaction rate calculations the effect of uranium density

variation was found to be small for all reactions, i.e. less than

0.4%, and those of the graphite and boron carbide density are less

than 0.8% for the threshold detectors. The ANISN calculation

showed that for thermal detectors a decrease in graphite density from

1.722 gm/cm^3 (NISUS) to 1.60 gm/cm^3($\Sigma\Sigma$) corresponds to a decrease

of about 2.5% or less in the reaction rate ratios, while a decrease

in B$_4$C density from 1.58 gm/cm^3 (NISUS) to 1.49 gm/cm^3($\Sigma\Sigma$) results

in an increase of about 4% or less in the reaction rate ratios.

This means that the denser graphite and boron carbide shell in NISUS

than in $\Sigma\Sigma$ compensate each other in the reaction rate ratios so that

the net effect remains more or less unchanged. The effect of

impurities in graphite (moisture and ^{10}B) was found to be negligible

(< 0.2%) as far as reaction rate ratios are concerned. The effect

of variation in ^{10}B abundance from 19.78% (NISUS) to 18.37% ($\Sigma\Sigma$) is

about − 1% and + 4% in the reaction rate ratios for the threshold and

thermal detectors respectively. The reaction rate ratios are

insensitive to 0.5 mm tolerance of the Al cladding, but   the

the reaction ratios

tolerance of 1 mm in the B$_4$C shell   increases by about 4.5% or

less for thermal detectors. While no effect was observed for the

threshold detectors. The ANISN calculation showed that the reaction

rate ratios are insensitive to any change in the ^{235}U and ^{238}U fission

cross sections.

The NISUS and MOL-$\Sigma\Sigma$ central spectrum and reaction rate ratios

were calculated with GALAXY nuclear data file and were compared with

the aim to diagnose any difference between the two assemblies. It

was found that the NISUS and $\Sigma\Sigma$ central spectra are in agreement to

within 3% above $\sim$ 70 keV. The agreement departs sharply in the

lower tail of the spectrum due to differences in the boron carbide

density and ^{10}B abundance which have a great effect in this region

of the spectrum. The reaction rate ratios of the threshold detectors

in $\Sigma\Sigma$ were found to be less than 1.3% smaller than those in NISUS. It follows that the $^{238}U/^{235}U$ fission ratio in $\Sigma\Sigma$ is 1.3% less than that in NISUS, in good agreement with measurement which gives .05735 ± .39% in NISUS and .05636 ± .22% in $\Sigma\Sigma$ with the discrepancy of + 1.7%.

A set of experiments were carried out in NISUS by the NBS and ULRC double fission chambers and the results were compared with those of the $\Sigma\Sigma$. These measurements including ^{239}Pu, ^{237}Np, ^{235}U and ^{238}U fissionable deposits were performed with a dual triple-scaler counting system which monitors each side of the fission chamber independently. Two mutually independent monitor systems have been used for reactor powere monitoring during the course of fission rate measurements in NISUS: (i) two pulse fission chambers, and (ii) two Au foils in the graphite thermal column with the aim of checking the chambers' performance. It was found that the long term monitoring consistency may not be achieved with fission chambers due to drifting in electronic system. Because of this drawback, it was necessary to adjust the gain and/or the discriminator levels or both from time to time to obtain a consistent result. Nevertheless, the variation in the fission chamber monitor 1 was found to be ∿ 0.5%, and that of the monitor 2 about 2%. In the case of the Au foil monitors the variation for the foils in position A was 1.3% and that for the foils in position B was 1.5%. In the present fission rate measurements both fission chamber 1 and Au foil A monitors were taken for reactor power monitoring.

The central NISUS fission ratios measured by the NBS fission

chamber were compared with those of the $\Sigma\Sigma$. The same chamber and deposits

have already been exposed at the $\Sigma\Sigma$ centre and hence the comparison

was between the central fission ratios of the two assemblies. The

early $^{239}Pu/^{238}U$ fission ratio measurements in NISUS revealed a

discrepancy of $\sim + 2\%$ compared with that of $\Sigma\Sigma$. In subsequent measure-

ments the ^{235}U fission rates with bare chamber were found to be about

1% higher than those with the cadmium box. The higher fission rates

in ^{239}Pu and ^{235}U were found to be due to thermal neutron streaming

through the access hole. The measurements of $^{239}Pu/^{238}U$ fission

ratios with bare, the chamber, and with cadmium box and cadmium shield against thermal

neutron streaming showed that the thermal neutrons observed with the

bare chamber were indeed coming from the direction of the access hole.

The final results of the $^{239}Pu/^{238}U$, $^{239}Pu/^{235}U$ and $^{237}Np/^{235}U$ fission

ratios in the centre of NISUS showed an agreement of better than $\pm 0.6\%$

with those of $\Sigma\Sigma$. The $^{238}U/^{235}U$ fission ratio in NISUS

was found to be about 1.7% higher than that in $\Sigma\Sigma$, as it was predicted

by the ANISN transport code.

The measurements with the ULRC fission chamber were performed

with the NBS, AWRE and ULRC ^{235}U and ^{238}U fissionable deposits.

These measurements had three different feature: (i) to calibrate

the mass of the AWRE and ULRC deposits against those of the NBS,

(ii) to measure the central NISUS $^{238}U/^{235}U$ fission ratios, and

(iii) to determine the detection efficiency of the Makrofol SSTR

and to find the $^{238}U/^{235}U$ fission ratio by track recorder technique.

The mass assay of the NBS fissionable deposits originally used in

the Coupled Fast Reactivity Measurement Facility (CFRMF) has been determined by absolute alpha emission rate measurements complemented by fission comparison counting in the thermal neutron beam at the NBS Research Reactor and also at the centre of $\Sigma\Sigma$ standard neutron field. In the present work, however, the mass assay of the NBS deposits has been taken as reference. The measurements of the $^{238}U/^{235}U$ fission ratios by the ULRC chamber and with the NBS, AWRE and ULRC deposits showed that the agreement between these three sets of deposits with different mass and size is better than 0.6% for monitor chamber and $\sim$ 1.7% for the gold monitor. These variations reflect the consistency of the ULRC chamber performance for these deposits. The comparison between the $^{238}U/^{235}U$ fission ratios in NISUS obtained by the ULRC and NBS chambers with the same deposits showed that the value with the ULRC chamber is $\sim$ 3% less than that with the NBS chamber. This may be due to corrections applied for the epicadmium streaming and chamber moderation in the NBS chamber data. No comparable correction has been made for the ULRC chamber data since no effect has been demonstrated experimentally. Further work is needed to elucidate these corrections for the ULRC chamber measurements.

A set of experiments were carried out with track recorders to calibrate SSTR against fission chamber. In this calibration the detection efficiency of the Makrofol SSTR was found to be (94.3 $\pm$ .64)% for the thin deposits. The dominant uncertainties in the area of the thick deposits resulted in the detection efficiency of close to unity. Measurements of the diameter of the thick deposits both from the

track densities near the edge and from a microscope traverse along

the fission source, showed that the area of an approximately 1 mg/cm^2

fissionable deposit is subject to an uncertainty of $\sim \pm$ 3%. The

measurements of $^{238}U/^{235}U$ fission ratios with SSTR showed a discrepancy

of about 3% compared with those of the fission chamber. Nevertheless,

these measurements have provided valuable assurances of reliability

because of their systematic independence and added redundancy.

The fission rate distribution on the outer and inner surfaces

of the NISUS uranium shell has been measured in three orthogonal planes

using Makrofol SSTR. The results showed that the distribution on the

plane perpendicular to thermal column axis is constant, while in the that

other two planes is cosine shape. of roughly It has been shown that the fission

rate distributions are broader on the inner surface than on the outer

surface of the uranium shell. This means that the fission rate

distribution on the inner surface is more uniform than on the outer

surface due to neutron scattering and slowing down within the shell.

The fission ratios of the outer surface to the inner surface at different

positions are not constant as   is predicted by the ANISN one-dimensional

transport code. The fission ratios are constant in the plane

perpendicular to the thermal column axis, and have "cosine" shape

distributions on the other two orthogonal planes.

Finally it may be briefly concluded that:

(1)   it has been established that the automatic fission track

counting by a Quantimet 720 is an accurate and reproducible technique,

and that the precision of $\pm$ 2% is obtained in the fission ratios;

(2)   the NISUS and $\Sigma\Sigma$ standard neutron fields are very similar both

for the spectra (above ∿ 70 keV) and reaction rates if acceptable

accuracies are ± 3% and ± 2% respectively;

(3)   it has been proved that the fission chamber technique is a

very accurate means for measuring fission rates, and that a precision

level of betther than ± 1% has been obtained.   Accuracy levels

attained are of the order of ± 2.7% and are dominated by uncertainties

in the isotopic masses of the fissionable deposits.   These uncertainties

may be reduced to near ± 1% with further application of existing mass

assay techniques;

(4)   the track recorder technique may not, and probably cannot,

replace the fission chamber in fission rate measurements.   The

accuracy of this technique is limited because of (i)   track-counting

bias,   (ii)   inherent statistical limitations and   (ii)   etching

procedure.   These uncertainties combined with those of the mass and

area of the deposits result in an overall accuracy levels no better

than 3%.

REFERENCES

(1)   HUNT, S.E., Fission, Fusion and the Energy Crisis, Pergamon
        Press, (1974).

(2)   VAUGHAN, R.D., Uranium Conservation and the Role of the Gas
        Cooled Fast Breeder Reactor, J.Br.Nucl.Energy Soc. 14 (1975)
        105.

(3)   FARINELLI, U., The Role of Integral Experiments in the Production
        of Nuclear Data for Reactor Core and Shield Design and for
        Irradiation Experiments, in Nuclear Data in Science and
        Technology, (Proc.Symp., Paris, 1973), IAEA, Vienna 2 (1973)
        103.

(4)   CAMPBELL, C.G., and ROWLANDS, J.L., The Relationship of
        Microscopic and Integral Data, in Nuclear Data for Reactors,
        (Proc. 2nd Int. Conf., Helsinki, 1970) IAEA, Vienna, 2 (1970)
        391.

(5)   SCHMIDT, J.J., General Status of Nuclear Data Requirements,
        in Nuclear Data for Reactors (Proc. 2nd Int. Conf., Helsinki,
        1970) IAEA, Vienna, 1 (1970) 3.

(6)   FABRY, A., De LEEUW, G. and De LEEUW, S., The Secondary
        Intermediate-Energy Standard Neutron Field at the MOL-ΣΣ
        Facility, Nucl.Tech. 25 (1975) 349.

(7)   BESANT, C.B., EMMETT, J., CAMPBELL, C.G., KERRIDGE, M., and
        JONES, T.C., Design and Construction of a Fast Reactor Neutron
        Spectrum Generator - NISUS, Nucl.Eng.Int., May 1973.

(8)   GRANT, P.J., The London University Nuclear Reactor, CONSORT,
        Nature, 207 (1965) 911.

(9)   ASAD, S., BESANT, C.B., EMMETT, J., RICKARD, I.C., CAMPBELL, C.G.,
        JONES, T.C., KERRIDGE, M., PETR, J., and WILLIAMS, J.G.,
        NISUS - A Neutron Intermediate Standard Uranium Source, in
        Irradiation Facilities for Research Reactors (Proc. Symp.
        Tehran, 1972) IAEA, Vienna (1973) 185.

(10)   EMMETT, J., Ph.D. Thesis, University of London, I.C., In
        preparation.

(11)   PETR, J., Neutron Energy Spectrum Measurements in a Standard
        Fast Neutron Assembly, Ph.D. Thesis, University of London, I.C.
        (1973).

(12)   KHAN, H.A., and DURRANI, S.A., Efficiency Calibration of
         Solid-State Nuclear Track Detectors, Nucl.Inst.Methods
         98 (1972) 229.

(13)   PRICE, W.J., Nuclear Radiation Detection, McGraw-Hill,
         Second Edition (1964).

(14)   GRUNDL, J.A., GILLIAM, D.M., DUDEY, N.D., and POPEK, R.J.,
         Measurement of Absolute Fission Rates, Nucl.Tech. 25
         (1975) 237.

(15)   MARACCI, G., RUSTICHELLI, F., AIELLO, V., and De LILLO, T.,
         Absolute Neutron Flux Determination by a Back-to-Back Fission
         Chamber and Activation Detectors, Nucl. Inst. Methods.
         62 (1968) 57.

(16)   PAZIRANDEH, A., Reaction Rates in Fissile Material, Ph.D.
         Thesis, University of London, I.C., (1969).

(17)   AZAD, S., Fast Neutron Reaction-Rate and Spectrum Measurement,
         Ph.D. Thesis, University of London, I.C., (1973).

(18)   BARKAS, W.H., Nuclear Research Emulsions, Academic Press,
         N.Y. (1963).

(19)   GOLD, R., ARMANI, R.J., and ROBERTS, J.H., Absolute Fission
         Rate Measurements with Solid-State Track Recorders, Nucl.
         Sci. Eng. 34 (1968) 13.

(20)   BESANT, C.B., and IPSON, S.S., Measurement of Fission Ratios
         in Zero Power Reactors Using Solid-State Track Recorders,
         J. Nucl. Energy, 24 (1970) 59.

(21)   BESANT, C.B., and TRUCH, E.R., Automatic Image Analysis in
         Track Counting, Microscope, 20 (1972) 127.

(22)   JOWITT, D., Measurements of the $^{235}U/^{238}U$ Fission Ratios in
         ZEBRA using Solid-State Track Recorders, Nuc.Inst.Methods.
         92 (1971) 37.

(23)   SILK, E.C.H., and BARNES, R.S., Examination of Fission
         Fragment Tracks with an Electron Microscope, Phil. Mag.
         4 (1959) 970.

(24)   PRICE, P.B., and WALKER, R.M., Electron Microscope Observation
         of Etched Tracks from Spallation Recoils in Mica, Phys.Rev.
         Lett. 8 (1962) 217.

(25)   FLEISCHER, R.L., and PRICE, P.B., Charge Particle Tracks in
         Glass, J.App.Phys. 34 (1963) 2903.

(26)   FLEISCHER, R.L., PRICE, P.B., and WALKER, R.M., Solid-State
         Track Detectors: Application to Nuclear Science and Geophysics,
         Ann.Rev.Nucl.Sci. 15 (1965) 1.

(27)   PRICE, P.B., and FLEISCHER, R.L., Identification of Energetic
         Heavy Nuclei with Solid Dielectric Track Detectors, Ann.Rev.
         Nucl.Sci. 21 (1971) 295.

(28)   YOUNG, D.A., Etching of Radiation Damage in Lithium Fluoride,
         Nature, 182 (1958) 375.

(29)   ARMANI, R.J., and GOLD, R., Fast Neutron Personnel Dosimetry
         with Solid-State Track Recorders, Nucl.Inst.Methods 118
         (1974) 383.

(30)   BECKER, K., and RAZEK, A.B., Automatice Spark Counting of
         Fast-Neutron-Induced-Recoil-Particle Tracks in Polymer
         Films, Nucl.Inst. Methods 124 (1975) 557.

(31)   BENTON, E.V., and HENKE, R.P., Heavy Cosmic Ray Exposure of
         Apollo-17 Astronauts, Health Phys. 27 (1974) 79.

(32)   KHAN, H.A., ATTA, M.A., YAMEEN, S., and HAROON, M.R., The
         Effects of High Gamma Doses on the Response of Plastic
         Track Detectors, Nucl.Inst. Methods 127 (1975) 105.

(33)   SOMOGYI, G., and SZALAY, S.A., Track-Diameter Kinetics in
         Dielectric Track Detectors, Nucl.Inst. Methods 109 (1973)
         211.

(34)   VARNAGY, M., CSIKAI, J., and SZEGEDI, S., Effects of
         Electron and X-Rays on Alpha-Particle Registration in
         T-Cellit Detector, Nucl.Inst. Methods 119 (1974) 261.

(35)   GRIFFITH, R.V., Results of the 1972 Survey on Track
         Registration, California University, UCRL-51362, March
         1973.

(36)   COSTA-RIBERIO, C., and LOBAO, N., Testing of the LR-115
         Kodak-Pathe Red Dyed Cellulose Nitrate for Alpha Particle
         Detection, Health Phys. 28 (1975) 162.

(37)   CHING-SHEN SU, Diffusion of Uranium in Polyethylene
         Determined by Fission Track Detector, Nucl. Inst. Methods
         107 (1973) 29.

(38)   SPURNY, F., and LOCHMANOVA, J., Energy Dependence of Solid-
         State Track Detectors as Fast Neutron Dosimeters, NSA
         31-6061 (Feb. 1975).

(39) LÜCK, H.B., Investigation on Energy Resolution in Detecting Alpha Particles Using Cellulose Nitrate Detector, Nucl.Inst. Methods 124 (1975) 359.

(40) KORLEVA, V.P., SAMOVAROV, V.S., and CHERNOV, L.A., Investigation of the Characteristics of Lavsan Track Detectors, Sov..At. Energy (Eng. Transl.) 35 (1973) 1044.

(41) FLEISCHER, R.L., PRICE, P.B., and WALKER, R.M., Nuclear Tracks in Solids, California Press, Berkeley, September 1975.

(42) CARPENTER, B.S., Quantitative Applications of the Nuclear Track Technique, Microscope 20 (1972) 175.

(43) FLEISCHER, R.L., Particle Dosimetry by Track Etching, General Electric Company, Report No. 74 CRD-197, August 1974.

(44) BLOK, H., PATE, B.D., and PÉTER, J., Fission Fragment Spectroscopy by Measurements in Nuclear Track Detectors Applied to the Fission of Silver Induced by 80 MeV Alpha Particles, Nucl.Inst. Methods 122 (1974) 329.

(45) FRANK, A.L., BENTON, E.V., and ALBERGOTTI, J.C., A Passive Neutron Spectrometer using a Nuclear Track Detector, Nucl. Inst. Methods. 122 (1974) 433.

(46) LÜCK, H.B., Energy Spectrometry of Protons by Means of a Dielectric Track Detector, Nucl.Inst. Methods 119 (1974) 403.

(47) VARNAGY, M., CSIKAI, J., SZABO, J., SZEGEDI, S., and BANHALMI, J., Application of T-Cellit Detector for the Study of ^{6,7}Li (p,α) ^{3,4}He Reactions, Nucl.Inst. Methods 119 (1974) 451.

(48) FLEISCHER, R.L., PRICE, P.B., and WALKER, R.M., Ion Explosion Spike Mechanism for Formation of Charged-Particle Tracks in Solids, J.App.Phys. 36 (1965) 3645.

(49) CHADDERTON, L.T., and TORRENS, I.M., Fission Damage in Crystals, Methuen and Co. Ltd., London (1968).

(50) FLEISCHER, R.L., and PRICE, P.B., Glass Dating by Fission Fragment Tracks, J. Geophys. Res. 69 (1964) 331.

(51) SOMOGYI, G., VARNAGY, M., and MEDVECZKY, L., The Influence of Etching Parameters on the Sensitivity of Plastics, Int. Conf. Nucl.Track Reg., Clermount-Ferrand (1966).

(52) FLEISCHER, R.L., PRICE, P.B., WALKER, R.M., and HUBBARD, E.L., Criterion for Registration in Dielectric Track Detectors, Phys. Rev. 156 (1967) 353.

(53) BENTON, E.V., A Study of Charged Particle Tracks in Cellulose Nitrate, USNRDL-TR-68-14 (1968).

(54) KATZ, R., and KOBETICH, E.J., Formation of Etchable Tracks in Dielectrics, Phys. Rev. 170 (1968) 401.

(55) MORGAN, O.V., and VLIET, D.V., Charged Particle Tracks in Solids, Contemp.Phys. 11 (1970) 173.

(56) FLEISCHER, R.L., PRICE, P.B., and WALKER, R.M., Nuclear Tracks in Solids, Sci.Am. 220 No. 6 (1969) 30.

(57) BESANT, C.B., A High Spatial Resolution Fission Detector, Imperical College Report, IC/NP/102 (July 1970).

(58) WILKENING, L., LAL, D., and REID, A.M., The Evolution of the Kapoeta Howardite Based on Fossil Track Studies, Ann. Meeting of Meteoritical Society Oct. 1969, Houston, Texas.

(59) BOK, A.B., Le POOL, J.B., ROOS, J., and De LANG, H., Mirror Electron Microscopy, in Advances in Optical and Electron Microscopy, BARER, R., and COSSLETT, V.E. (Eds.), Vol. 4, Academic Press (1971).

(60) MALIK, S.R., Studies of Nuclear Track Detectors and their Applications to Materials of Terrestrial, Extra Terrestrial and Biological Origin, Ph.D. Thesis, University of Birmingham (1973).

(61) HAASE, G., and SCHOPPER, E., Tracks of Ionizing Particles in Silver Chloride Single Crystals, 6th Int.Conf. Corpus. Photo., Florence, July 1966.

(62) MAYBURY, P.C., and LIBBY, W.F., Non-Etching Optical Detection of Fission Tracks using Teflon, Nature 254 (1975) 209.

(63) PRICE, P.B., and WALKER, R.M., Chemical Etching of Charged-Particle Tracks in Solids, J.Appl. Phys. 33 (1962) 3407.

(64) FLEISCHER, R.L., PRICE, P.B., and WALKER, R.M., Tracks of Charged Particles in Solids, Science 149 (1965) 383.

(65) BLOK, J., HUMPHREY Jr., J.S., and NICHOLS, G.E., Hole Detection in Polymer Films and in Plastic Track Detectors, Rev.Sci.Inst. 40 (1969) 509.

(66)   SCHULTZ, WARNER W, Track Density Measurement in Dielectric
         Track Detectors with Scattered Light, Knolls Atomic Power
         Laboratory, Schenectady, N.Y. NSA : 22-37990 (Jan. 1968).

(67)   LARK, N.L., Spark Scanning Fission Fragment Tracks in Plastic
         Foils, Nuc.Inst. Methods 67 (1969) 137.

(68)   CONGEL, F.J., ROBERTS, J.H., DREIS, D., KASTNER, J.,
         OLTMAN, B.G., GOLD, R., and ARMANI, R.J., Automatic System
         for Counting Etched Holes in Thin Dielectric Plastics,
         Nucl.Inst. Methods 100 (1972) 247.

(69)   GEISLER, F., and PHILLIPS, P.R., An Improved Method for
         Locating Charged Particle Tracks in Thin Plastic Sheets,
         Rev.Sci.Inst. 43 (1972) 283.

(70)   GUNTHER, G., The Measurement of Fission Rate Microstructure
         with Plastic Foils, Leitz Scientific and Technical Information,
         Suppl. 1, 2, Wetzlar (July 1972).

(71)   OOSTERKAMP, W.J., SCHAAR, J., and VAN VELZE, P.L., Automatic
         Counting of Solid-State Fission Track Recorders, Trans.Amer.
         Nucl.Soc. 13 (1970) 526.

(72)   COHN, C.E., and GOLD, R., Computer Controlled Microscope for
         Automatic Scanning of Solid-State Nuclear Track Recorders,
         Rev.Sci.Inst. 43 (1972) 12.

(73)   Quantimet 720 Image Analysing Computer Instruction Manual,
         Image Analysing Computers Limited (IMANCO), Melbourn,
         Roystone, Herts, England.

(74)   MULLER, W., The LEITZ-Texture-Analysing-System (LEITZ-T.A.S.)
         Leitz Scientific and Technical Information Suppl. 1, 4
         (April 1974).

(75)   PRETRE, S., TOCHILIN, E., and GOLDSTEIN, N., A Standardized
         Method for Making Neutron Fluence Measurements by Fission
         Fragment Tracks in Plastics, USNRDL-TR-1089, U.S. Naval
         Radiological Defence Laboratory (1966).

(76)   KHAN, H.A., An Important Precaution in the Etching of
         Solid-State Nuclear Track Detectors, Nucl.Inst. Methods
         109 (1973) 515.

(77)   JOWITT, D., Private Communication to Dr. J.G. Williams.

(78)   TOMMASINO, L., Electrochemical Etching of Damaged Track
         Detectors by H.V. Pulse and Sinusoidal Waveforms, CENEN
         Report, RT/PROT (71) 1, 1970.

(79)   SOHRABI, M., The Amplification of Recoil Particle Tracks
        in Polymers and its Application in Fast Neutron Personnel
        Dosimetry, Health Physics 27 (1974) 598.

(80)   Interference Contrast Device T, Leitz Brochure No. 550-37a.

(81)   FISHER, C., The New Quantimet 720, Presented at INTER/MICRO-70,
        Chicago, Ill.

(82)   RICHMOND, R., and RÜEGGER, Application of Automatic Image
        Analysis to the Measurements of Fission Particle Track
        Densities, Presented at INTER/MICRO-71, Imperial College,
        London.

(83)   ENGLE Jr., W.W., A User's Manual for ANISN.   A One-Dimensional
        Discrete Ordinates Transport Code with Anistotropic Scattering,
        USAEC Report K-1693 (1967).

(84)   SPIEGEL, M.R., Theory and Problems of Statistics, Schaum's
        Outline Series, McGraw-Hill (1972).

(85)   KERR, W.M.M., PARKER, K., and WILLIAMS, D.V.J., The Calculation
        of Group Averaged Neutron Cross Sections, Report AWRE O-97/64
        (1965).

(86)   EMMETT, J., Internal Communications (1972)

(87)   Neutron Fluence Measurements, Technical Reports Series No. 107,
        IAEA, Vienna (1970).

(88)   STEHN, J.R., et al, Neutron Cross Sections, BNL-325 Second
        Edition, Supplement No. 2 (1964).

(89)   NIGHTINGALE, R.E., (Ed.) Nuclear Graphite, Academic Press
        (1969).

(90)   Reactor Physics Constants, ANL-5800, Second Edition, United
        States Atomic Energy Commission (1963).

(91)   GLASSTONE, S., and EDLUND, M.C., The Elements of Nuclear
        Reactor Theory, Van Norstrand (1952).

(92)   ETHERINGTON, H., (Ed.) Nuclear Engineering Handbook, McGraw-
        Hill (1958).

(93)   KAYE, G.W.C., and LABY, T.H., Tables of Physicals and Chemical
        Constants, Thirteenth Edition, Longman (1966).

(94)   Handbook of Chemistry and Physics, 51st Edition, CRC 1970-1971,
        The Chemical Rubber Co., Cleveland, Ohio (1970).

(95)   LEDERER, C.M., HOLLANDER, J.M. and PERLMAN, I., Table of
        Isotopes, Sixth Edition, John Wiley (1967).

(96)   Chart of Nuclides, Knolls Atomic Power Laboratory, Naval
        Reactors, USAEC, Eleventh Edition, (1972).

(97)   BESANT, C.B., and HEAD, J.L., Private Communications (1974).

(98)   Graviner Manufacturing Company Limited, Gosport Division,
        Gosport, Hants, England.

(99)   FARRAR IV, H., McELROY, W.N., and LIPPINCOTT, E.P., Helium
        Production Cross-Section of Boron for Fast Reactor Neutron
        Spectra, Nucl.Tech. $\underline{25}$ (1975) 305.

(100)   FABRY, A., COPS, F., GRUNDL, J.A., and GILLIAM, D., Fission
        Rates Measurements in the $\Sigma\Sigma$ Standard Neutron Field by means
        of the NBS Absolute Fission Chamber, Report AF/Sa, 61-606/75-
        02/C/a, (1975), Reactor Study, Reactor Physics, Mol, Belgium.

(101)   WHITE, P.H., Alpha and Fission Counting of Thin Foils of
        Fissile Material, Nucl.Inst.Methods $\underline{79}$ (1970) 1.

(102)   FABRY, A., Private Communications (1975).

(103)   HANNAN, A.H.M.A., Ph.D. Thesis, University of London, I.C.,
        To be submitted (1976).

(104)   WILLIAMS, J.G., Monitoring of Neutron Flux in the NISUS
        Thermal Column by means of Miniature Fission Chambers,
        ULRC Report, In preparation (1975).

(105)   ROUTTI, J.T., and PRUSSIN, S.G., Photopeak Method for the
        Computer Analysis of Gamma-Ray Spectra from Semiconductor
        Detectors, Nucl.Inst.Methods $\underline{72}$ (1969) 125.

(106)   FABRY, A., WILLIAMS, J.G., HANNAN, A.H.M.A., and AZIMI-GARAKANI, D.,
        Intercomparison of the Intermediate-Energy Standard Neutron
        Fields at the NISUS and MOL-$\Sigma\Sigma$ Facilities by means of NBS-Type
        Absolute Fission Chambers, to be published (1976).

(107)   AZIMI-GARAKANI, D., Measurements of Fast Fission Ratios using
        Solid-State Track Recorders, M.Sc., dissertation, University
        of London, I.C., (1973).

(108)   FABRY, A., DE LEEUW, G., and S., and DE COSTER, Survey of the
        Experiments Performed within the CEN/SCK Secondary Standard
        Neutron Spectrum Facility. Paper presented at the Meeting of
        Specialists held at the Argonne National Laboratory, November
        1970. Fast Reactor Spectrum Measurements and their Inter-
        pretation, IAEA-137, Vienna (1971).

(109)   KHAN, H.A., Solid-State Nuclear Track Detectors : Some Basic
        Parameters and Applications, Ph.D. Thesis, University of
        Birmingham (1972).

APPENDIX   A

Individual results of the fission chamber

irradiations at NISUS centre

TABLE A

Individual results of the fission chamber irradiations at NISUS centre

Run No.	Foil identification	S_L (cps)	S_U (cps)	S_{GC} (cps)	S_L/S_U	S_{GC}/S_U	Monitor chamber 1 (cps)	Monitor chamber 2 (cps)	Moni 2/ Moni 1
1[a]	NBS 49 I-1-1	64.17 ± .15	63.95 ± .12	32.94 ± .08	1.00339 +.00042	.51578 +.00370	1319.8 ± .8	_[b]	−
	NBS 28 N-5-2	20.13 ± .07	19.53 ± .07	9.67 ± .04	1.02570 +.00195	.49453 +.00458			
2	NBS 37 S-5-1	115.24 ± .11	113.87 ± .11	41.87 ± .07	1.01202 +.00071	.36771 +.00239	1323.1 ± .6	548.1 ± .5	.4143 +.0004
	NBS 25 S-2-3	111.07 ± .13	110.62 ± .15	49.04 ± .10	1.00557 +.00040	.44289 +.00258			
3[c]	NBS 37 S-5-1	57.39 ± .08	56.72 ± .08	20.90 ± .07	1.01190 +.00080	.36829 +.00300	1323.0 ± .8	548.4 ± .4	.4145 +.0004
	NBS 25 S-2-3	55.00 ± .10	54.70 ± .09	24.31 ± .07	1.00551 +.00037	.44445 +.00295			
4	NBS 28 HD-5-1	17.33 ± .06	17.07 ± .06	4.97 ± .04	1.01513 +.00158	.29035 +.00474	1321.9 ± .6	547.8 ±1.0	.4144 +.0020
	NBS 25 S-2-3	111.33 ± .12	110.78 ± .15	42.13 ± .27	1.00557 +.00046	.37478 +.00361			

350

TABLE A (continued)

Individual results of the fission chamber irradiations at NISUS centre.

Run No.	Foil identification	S_L (cps)	S_U (cps)	S_{GC} (cps)	S_L/S_U	S_{GC}/S_U	Monitor chamber 1 (cps)	Monitor chamber 2 (cps)	Moni 2/ Moni 1
6	NBS 25 S-2-3	110.68 ± .21	110.59 ± .21	97.96 ± .15	1.00998 ±.00051	.89440 ±.00189	1325.5 ± .6	546.9 ± .4	.4126 ±.0004
	AWRE 25	65.02 ± .11	64.62 ± .10	60.39 ± .09	1.00628 ±.00046	.93465 ±.00216			
7	NBS 49 I-1-1	62.60 ± .15	62.37 ± .15	25.92 ± .13	1.00375 ±.00041	.41554 ±.00465	1316.5 ± .6	_(b)	-
	NBS 28 N-5-2	_(b)	-	-	-	-			
8(c)	NBS 49 I-1-1	60.55 ± .11	60.31 ± .12	24.96 ± .09	1.00388 ±.00037	.41387 ±.00336	1313.3 ± .7	546.8 ± .4	.4163 ±.0004
	NBS 28 N-5-2	_(b)	-	-	-	-			
9(d)	NBS 49 I-1-1	61.04 ± .20	60.89 ± .15	29.03 ± .08	1.00449 ±.00020	.47880 ±.00386	1314.6 ± .8	547.2 ± .5	.4163 ±.0004
	NBS 28 N-5-2	19.81 ± .08	19.50 ± .09	9.98 ± .06	1.02665 ±.00124	.51145 ±.00644			

Individual results of the fission chamber irradiations at NISUS centre

Run No.	Foil identification	S_L (cps)	S_U (cps)	S_{GC} (cps)	S_L/S_U	S_{GC}/S_U	Monitor chamber 1 (cps)	Monitor chamber 2 (cps)	Moni 2/ Moni 1
12	NBS 28-N-5-2	16.79 ± .06	16.42 ± .05	11.05 ± .06	1.02288 ±.00195	.67409 ±.00849	1323.9 ± .8	543.9 ± .7	.4109 ±.0006
	ULRC-3 28	20.55 ± .09	20.05 ± .09	13.32 ± .06	1.02489 ±.00143	.66457 ±.00404			
14	ULRC-4 25	37.12 ± .07	36.64 ± .07	7.99 ± .04	1.01302 ±.00099	.21815 ±.00328	1319.3 ± .3	541.8 ± .3	.4107 ±.0009
	ULRC-6 25	164.15 ± .16	162.22 ± .15	45.62 ± .07	1.01195 ±.00034	.28124 ±.00134			
15	ULRC-6 25	165.30 ± .27	162.57 ± .29	33.51 ± .06	1.01645 ±.00038	.20609 ±.00080	1330.1 ± .6	549.0 ± .3	.4127 ±.0012
	ULRC-4 25	37.78 ± .11	37.36 ± .09	12.55 ± .04	1.00990 ±.00096	.33596 ±.00272			
16	ULRC-3 28	20.85 ± .06	20.37 ± .06	3.81 ± .03	1.02295 ±.00180	.18725 ±.00609	1343.9 ±2.4	550.0 ± .4	.4093 ±.0034
	ULRC-6 25	163.78 ± .14	161.91 ± .15	43.98 ± .08	1.01119 ±.00161	.27162 ±.00211			

Individual results of the fission chamber irradiations at NISUS centre

Run No.	Foil identification		S_L (cps)	S_U (cps)	S_{GC} (cps)	S_L/S_U	S_{GC}/S_U	Monitor chamber 1 (cps)	Monitor chamber 2 (cps)	Moni 2/ Moni 1
17	ULRC-4	25	SSTR	-	-	-	-	1331.7 ± .7	550.0 ±1.1	.4130 +.0015
	ULRC-6	25	163.32 ± .22	161.40 ± .25	44.70 ± .14	1.01195 +.00053	.27695 +.00190			
18	AWRE	25	64.12 ± .14	63.70 ± .07	14.02 ± .03	1.00813 +.00071	.22015 +.00289	1330.3 ± .5	552.5 ± .3	.4152 +.0025
	ULRC-6	25	163.48 ± .11	161.62 ± .11	48.74 ± .06	1.01182 +.00044	.30157 +.00231			
19	AWRE	28	34.86 ± .06	34.57 ± .05	11.47 ± .03	1.01036 +.00087	.33178 +.00529	1334.5 ± .3	568.2 ± .2	.4257 +.0012
	ULRC-3	28	20.78 ± .09	20.37 ± .04	3.75 ± .02	1.02210 +.00193	.18425 +.00545			
20	ULRC-5	25	159.03 ± .13	156.62 ± .13	33.00 ± .06	1.01527 +.00043	.21068 +.00200	1333.3 ± .7	551.3 ± .3	.4134 +.0014
	ULRC-6	25	163.76 ± .17	161.91 ± .16	54.04 ± .08	1.01116 +.00058	.33374 +.00198			

TABLE A (continued)

Individual results of the fission chamber irradiations at NISUS centre

Run No.	Foil identification		S_L (cps)	S_U (cps)	S_{GC} (cps)	S_L/S_U	S_{GC}/S_U	Monitor chamber 1 (cps)	Monitor chamber 2 (cps)	Moni 2/ Moni 1
21	U1RC-3	28	20.80 + .04	20.30 + .04	3.60 + .02	1.02208 +.00143	.17756 +.00382	1331.1 +1.5	550.1 + .5	.4135 +.0012
	ULRC-1	28	75.23 + .14	71.94 + .11	13.05 + .03	1.04602 +.00353	.18128 +.00234			
22[e]	U1RC-5	25	SSTR	–	–	–	–	–[b]	53.0 + .1	–
	ULRC-6	25	16.41 + .09	16.21 + .09	4.56 + .03	1.01281 +.00089	.28323 +.00354			
23[e]	ULRC-6	25	SSTR	–	–	–	–	–[b]	53.3 + .1	–
	ULRC-5	25	16.05 + .08	15.90 + .09	5.74 + .03	1.01007 +.00118	.36078 +.00442			
24	ULRC-3	28	SSTR	–	–	–	–	–[b]	523.3 + .8	–
	ULRC-6	25	161.92 + .29	160.24 + .26	56.82 + .18	1.01045 +.00073	.35461 +.00311			

TABLE A (continued)

Individual results of the fission chamber irradiations at NISUS centre

Run No.	Foil identification		S_L (cps)	S_U (cps)	S_{GC} (cps)	S_L/S_U	S_{GC}/S_U	Monitor chamber 1 (cps)	Monitor chamber 2 (cps)	Moni 2/ Moni 1
25	ULRC-3	28	20.77 ± .07	20.45 ± .07	5.99 ± .03	1.01592 +.00115	.29373 +.00427	1323.2 ± .4	525.1 ± .3	.3970 +.0013
	ULRC-6	25	160.98 ± .21	158.13 ± .20	25.84 ± .13	1.01780 +.00042	.16406 +.00257			
26	ULRC-2	28	72.75 ± .10	67.82 ± .09	5.13 ± .04	1.07351 +.00176	.07575 +.00229	1325.4 ± .5	526.3 ± .3	.3971 +.0014
	ULRC-3	28	20.75 ± .05	20.49 ± .05	5.80 ± .02	1.01651 +.00121	.28320 +.00374			
27[f]	ULRC-1	28	SSTR	−	−	−	−	337.6 ± .6	133.9 ± .4	.3967 +.0030
	ULRC-6	25	41.75 ± .21	41.16 ± .22	11.07 ± .06	1.01179 +.00087	.26909 +.00198			
28	ULRC-4	25	SSTR	−	−	−	−	1327.4 +2.1	526.3 ± .6	.3965 +.0012
	ULRC-6	25	163.72 ± ,34	161.95 ± .36	58.29 ± .17	1.01077 +.00086	.35987 +.00200			

Individual results of the fission chamber irradiations at NISUS centre

Run No.	Foil identification		S_L (cps)	S_U (cps)	S_{GC} (cps)	S_L/S_U	S_{GC}/S_U	Monitor chamber 1 (cps)	Monitor chamber 2 (cps)	Moni 2/ Moni 1
29	ULRC-3	28	SSTR	–	–	–	–	1327.3 +1.3	526.2 + .8	.3965 +.0009
	ULRC-6	25	163.05 + .33	161.58 + .31	60.13 + .16	1.01022 +.00034	.37240 +.00288			
31	ULRC-6	25	162.54 + .26	159.68 + .22	34.16 + .12	1.01751 +.00055	.21399 +.00222	1336.4 + .8	547.9 + .8	.4111 +.0068
	ULRC-3	28	21.01 + .06	20.81 + .11	6.09 + .04	1.01645 +.00161	.29272 +.00700			
33	ULRC-4	25	36.89 + .16	36.47 + .06	8.58 + .04	1.01003 +.00082	.23526 +.00654	1326.4 + .8	544.7 +1.5	.4151 +.0014
	ULRC-1	28	74.40 + .07	70.96 + .07	11.04 + .03	1.04848 +.00216	.15536 +.00238			

Note

(a)   The chamber was accidentally off-centred by 2.5 mm

(b)   Chamber malfunctioning

(c)   Cadmium box

(d)   Cadmium umbrella

(e)   Reactor power 10 kW

(f)   Reactor power 25 kW

356

APPENDIX B

Etching conditions for fission fragments in
solid-state track recorders [109]

TABLE B

Etching conditions for fission fragments

Note: Because of chemical variations within most minerals, glasses, or plastics of a given type, actual optimum conditions may vary from those given.

A. Etchants for minerals

Mineral	Etching conditions (temp. in °C)
allanite (H$_2$O·4(Ca, Fe)0.3(Al, Fe)$_2$O$_3$·6SiO$_2$)	50N NaOH, 2–60 min, 140°
apatite Ca$_5$(F, Cl) (PO$_4$)$_3$	conc HNO$_3$, 25 sec, 23° *
autunite (Ca(UO$_2$)$_2$P$_2$O$_8$·8H$_2$O or CaO 2UO$_3$·P$_2$O$_5$· 8H$_2$O)	10% HCl, 10–30 sec, 23°
barite (BaSO$_4$)	HNO$_3$, 3 hr, 100°
barysilite (Pb$_3$Si$_2$O$_7$)	HAc, 70 sec, 23°
beryl (Be$_3$Al$_2$Si$_6$O$_{18}$)	KOH(aq), 9 hr, 150°
bismutite (Bi$_2$O$_3$·CO$_2$·H$_2$O)	1(NaOH):1(H$_2$O), 50 min, 140°
calcite (CaCO$_3$)	10% HCl, 50 sec, 23°
cerussite (PbCO$_3$)	HAc, 10–30 min, 23°
clinochlore (a chlorite)	48% HF, 10 min, 23°
clinopyroxene (augite), Ca(Mg, Fe, Al) (Al, Si)$_2$O$_6$))	KOH(aq), 1 min, 220° 2 (48% HF): 1 (80% H$_2$SO$_4$): 4 (H$_2$O) 5-20 min, 23°

* Hexagons with symmetrical tracks on (0001); slits on (1010)

Etching conditions for fission fragments

Mineral	Etching conditions (temp. in °C)
clinopyroxene (diopside), $(CaMgSi_2O_6)$	KOH (aq), 15 min, 210° NaOH(aq), 10 min, 200°
clinopyroxene (pigeonite) $[(Mg, Fe)SiO_3]_t \cdot [CaMg(SiO_3)_2]_{1-t}$	KOH(aq), 15 min, 210°
epidote $(Ca_2(Al, Fe)_3(SiO_4)_3OH)$	5O N NaOH, 0.5–2 hr, 140°
eulytite $(Bi_4(SiO_4)_3)$	5% HCl, 60 sec, 23°
feldspar (albite), $(NaAlSi_3O_8)$	NaOH(aq), 4 mm, 195° 6 gm NaOH:4 gm H_2O, 23 min, boiling 6 gm NaOH:8 gm H_2O, 85 min, boiling
feldspar (anorthite), $(CaAl_2Si_2O_8)$	KOH(aq), 210°, 30 min 6 gm NaOH:4 gm H_2O, 5 min, boiling 6 gm NaOH:8 gm H_2O, 14 min, boiling
feldspar (bytownite), (An_8Ab_2)	KOH(aq), 15 min, 210° 6 gm NaOH:4 gm H_2O, 6 min, boiling 6 gm NaOH:8 gm H_2O, 19 min, boiling
feldspar (labradorite), (An_6Ab_4)	6 gm NaOH:4 gm H_2O, 13 min, boiling 6 gm NaOH:8 gm H_2O, 40 min, boiling
feldspar (microcline), $(KAlSi_3O_8)$	48% HF, 1–10 sec, 23° 5(KOH):1(H_2O), 80 min, 190°
feldspar (oligoclase), (An_2Ab_8)	6 gm NaOH:4 gm H_2O, 20 min, boiling 6 gm NaOH:8 gm H_2O, 75 min, boiling
feldspar (orthoclase), $(KAlSi_3O_8)$	48% HF, 10 sec, 23° 5(KOH):1(H_2O), 80 min, 190°
fluorite (CaF_2)	98% H_2SO_4, 10 min, 23°
garnet (pyrope), $(Mg_3Al_2(SiO_4)_3)$	KOH(aq), 2 hr, 150° 50 N NaOH, 0.5–2 hr, 140° KOH, 3 hr, 170°

Etching conditions for fission fragments

Mineral	Etching condition (temp. in °C)
glass (see separate list of etchants for glasses)	
gypsum $(CaSO_4 \cdot 2H_2O)$	5% HF, 5–10 sec, 23°
halite (NaCl)	1 gm/liter $HgCl_2$ in ethanol, 30 sec, 23° *
hardystonite $(Ca_{1.99}Pb_{.01}ZnSi_2O_7)$	1 NaOH:1 H_2O, 20 to 70 min, 140°
heulandite $((Ca, Na_2)O \cdot Al_2O_3 \cdot 9SiO_2 \cdot 6H_2O$, a zeolite)	10 (aqua regia):1(HF), 30 sec, 23°
hornblende $(Ca_2Na(Mg, Fe)_4(Al, Fe, Ti)_3Si_6O_{22})$	48% HF, 5–60 sec, 23–60°
kleinite (Hg-ammonium chloride)	37% HCl, 7 min, 23°
leuchtenbergite (low iron clinochlore)	49% HF, 10 min, 23°
lithium fluoride (LiF)	$H_2O + .13$ gm/liter LiF $+ 1/2$ ppm Fe ~ 1 min, 23°
margarite $(CaAl_4Si_2O_{10}(OH)_2)$	48% HF, 2 min, 23°
mica (biotite), $K(Mg, Fe)_3AlSi_3O_{10}(OH)_2$	20%, HF, 1 1/2 min, 23° 15% HF, 20 sec, 50° 48% HF, 3–20 sec, 23°
mica (lepidolite), $(K_2Li_3Al_4Si_7O_{21}(OH, F)_3)$	15% HF, 20 sec, 50° 48% HF, 3–70 sec, 23°
mica (muscovite), $(KAl_3Si_3O_{10}(OH)_2)$	20% HF, 2 hr, 23° 20% HF, 12 min, 52° 15% HF, 20 min, 50° 48% HF, 10–40 min, 23°
mica (phlogopite), $(KMg_2Al_2Si_3O_{10}(OH)_2)$	20% HF, 5 min 15% HF, 1 min, 50° 48% HF, 1–5 min, 23°

* Shallow pits

Etching conditions for fission fragments

Mineral	Etching conditions (temp. in °C)
monazite ((Ce, La, Di)PO_4)	conc H_2SO_4, 6–8 min, 23° *
nasonite ($Pb_4(PbOH)_2Ca_4(Si_2O_7)_3$)	1(NaOH):1(H_2O), 10 min, 137°
olivine ((Mg, $Fe)_2SiO_4$)	KOH(aq), 8 min, 220° 29 gm KOH:9 gm H_2O, 4 min, 160°+5% HF, 30 sec, 23° { KOH(aq), 8 min, 220° +48% HF, 5 sec, 23° † }
orthopyroxene (bronzite), ($Mg_{1-f}Fe_fSiO_3$) (.1>f>.2))	NaOH(aq), 6 min, 200° 6 gm NaOH:4 gm H_2O, 42 min, boiling
orthopyroxene (enstatite), ($MgSiO_3$)	NaOH aq, 15 min, 195° 6 gm NaOH:4 gm H_2O, 35 min, boiling
orthopyroxene (ferrohypersthene) ($Mg_{1-f}Fe_fSiO_3$, f>.5)	6 gm NaOH:4 gm H_2O, 70 min, boiling
orthopyroxene (hypersthene) ($Mg_{1-f}Fe_fSiO_3$, f>.2)	KOH(aq), 210°, 30 min NaOH(aq), 200–205°, 5 min 6 gm NaOH:4 gm H_2O, 42 min, boiling
pennine (a chlorite)	48% HF, 5 min, 23°
pollucite ($H_2O\cdot2Cs_2O\cdot2Al_2O_3\cdot9SiO_2$)	5% HF, 55 sec, 23°
pucherite ($BiVO_4$)	5% HCl, 90 sec, 23°
quartz (SiO_2)	KOH(aq), 3 hr, 150° 48% HF, 24 hr, 23°
raspite ($PbWO_4$)	6.25N NaOH, 4 min, 23°
scheelite ($CaWO_4$)	6.25N NaOH, 90 min, 95°
sphene ($CaTiSiO_5$)	conc HCl, 0.5–1.5 hr, 90° 1(49% HF):2(70% HNO_3):3(conc HCl):6H_2O, 1–3 min, 23°

* Large cone angle   † Alternated two or more cycles

Etching conditions for fission fragments

Mineral	Etching conditions (temp. in °C)
spodumene ($LiAlSi_2O_6$)	48% HF, 24 hr, 23°
stilbite ((Ca, Na_2)O $Al_2O_3 \cdot 6SiO_2 \cdot 6H_2O$), a zeolite)	1% HF, 60 sec, 23°
talc ($Mg_3Si_4O_{10}(OH)_2$)	48% HF, 15 min, 23°
thorite ($ThSiO_4$)	H_3PO_4, 1 min, 250°
torbernite ($Cu(UO_2)_2P_2O_8 \cdot 12H_2O$)	10% HCl, 10 min, 23°
tridymite (SiO_2)	10% HF, 1 hr, 23°
topaz ($Al_2SiO_4(F, OH)_2$)	KOH(aq), 100 min, 150°
tourmaline (complex silicate)	KOH(aq), 20 min, 220°
vermiculite (biotite derived)	48% HF, ~5–10 sec, 23°
whitlockite [$Ca_3(PO_4)_2$]	70% HNO_3, 10 sec, 23°
zircon ($ZrSiO_4$)	1(KOH):1(NaOH), 10 sec, 450°* H_3PO_4, few sec, 375–500° NaOH(aq), .25–5 hr, 220°

* Shallow pits

Etching conditions for fission fragments

B. Etchants for glasses

Type	Etching conditions (at 23 °C)
andesitic glass ($Ab_{60}An_{40}$)	5% HF, 3–5 min
borate glass	H_2O, 1 min
obsidian	48% HF, 30 sec
phosphate glass	48% HF, 5–20 min
pumice	5% HF, 500 sec
silica glass (fused quartz, Vicor, Libyan desert glass)	48% HF, 1 min
soda-lime (microscope slide; cover slip, window glass)	48% HF, 5 sec 5% HF, 2 min
tektite	48% HF, 30 sec
uranium-soda glass	48% HF, 5 sec
$V_2O_5(P_2O_5)_5$ (semiconducting glass)	48% HF, 10 sec

C. Etchants for plastics

Plastic (tade names)	Etching conditions (temp. in °C)
Amber	$KMnO_4$ sat. solution, 6.5 hr, 80° 30gm $K_2Cr_2O_7$ + 50cc conc H_2SO_4 + 100cc H_2O, 40hr, 28°
Cellulose acetate (Kodacel, Triafol T)	6.25 N NaOH 28% KOH 30 min. 60°
Cellulose acetate butyrate	6.25N NaOH, 12 min. 70° 28% KOH 60 min. 60°
Cellulose nitrate (Daicell, Nixon-Baldwin)	6.25N NaOH,* 2 min. 70°

* Any alkali earth hydroxide with appropriate etching time.

Etching conditions for fission fragments

Plastic (trade names)	Etching conditions (temp. in $^{\circ}$C)
Cellulose propionate (Cellidor) Cellulose triacetate (Kodacel TA401, Bayer TN)	6.25N NaOH, 4 min, 55° 6.25N NaOH, 2–4 hr, 23° 28% KOH, 30 min, 23° 28:KOH, 100 min, 60° 6.25 N NaOH 6.25N NaOH+15% NaClO (2:1 to 1:3) 40° 28% KOH 60 min, 60°
Formophenol (ambrolithe, phenoplaste)	NaOH, 1 hr, 40°+ HF, 30 sec, 40°, in sequence
HBpaIT (polyester, $C_{17}H_9O_2$) . Ionomeric polyethylene (Surlyn) Polyamide (H Film)	6·25N NaOH, 8 min, 70° 10 gm $K_2Cr_2O_7$+35cc 30% H_2SO_4, 1 hr. 50° $KMnO_4$ (25% aq), 1.5 hr, 100° NaOH solution
Polycarbonate (Lexan, Makrofol, Merlon)	6.25 NaOH*, 20 min, 50° 33cc 30%H_2SO+$K_2Cr_2O_7$(10 gm) 2 hr, 85° 1 (6.25N NaOH); 1 (ethanol), 2 hr, 23°
Polyethylene	6.25N NaOH+4% Benax†, 20 min, 70° 10 gm $K_2Cr_2O_2$+35cc, 30% H_2SO_4 30 min, 85° 10 gm $K_2Cr_2O_2$+5cc, 30% H_2SO_4+20 gm H_2O – 90°‡
Polyethylene terephthalate (Mylar, Chronar, Melinex) Polymethyl Methacrylate (Plexiglas, Lucite)	6.25N NaOH, 10 min, 70°C $KMnO_4$ (25%, aq), 1 hr, 55° 6 (aqua regia):1 (48% HF) sat $KMnO_4$, 6 min, 85° sat $KMnO_4$, 50 min, 85°
Polyoxymethylene (Delrin) Polyphenoxide Polyphenylene oxide (PPO) Polypropylene (Cryovac-y) Polystyrene	5% $KMnO_4$, 10 hr, 60° $KMnO_4$, (25% aq), 4 min, 100° $KMnO_4$ aq, 24 hr, 93° § 35cc (30% H_2SO_4):10 gm ($Cr_2K_2O_7$), 5 min, 94° sat $KMnO_4$, 2.5 hr, 85° 10 gm $K_2Cr_2O_7$+35cc, 30% H_2SO_4, 3 hr, 85°

* Any alkali earth hydroxide with appropriate etching time.   † Dow surfactant 2Al, Dowfax, Dow Corning.

‡ High density PE (Marlex SO) only.   § Large cone angle.

Etching conditions for fission fragments

Plastic (trade names)	Etching conditions (temp. in °C)
Polyvinylaceto chloride	$KMnO_4$ (25% aq) 30 min, 100°
Polyvinylchloride	sat. $KMnO_4$ 2.5 hr, 85°
	$KMnO_4$ (25% aq) 2 hr, 55°
Polyvinylidene chloride (Saran)	$KMnO_4$ (25% aq) 2 hr, 55°
	$KMnO_4$ sat aq 2 hr, 85°
Polyvinyl toluene	$KMnO_4$ sat aq 30 min, 100°
Silicone-polycarbonate copolymer	6.25N NaOH 20 min, 50°
Siloxane-cellulose copolymer	8N NaOH+Benax 3 hr, 85°